DISS. ETH NO. 28850

LIGHT STIMULATED MULTIFUNCTIONAL 3D PRINTED CELLULOSE NANOCOMPOSITES

Submitted to obtain the title of

DOCTOR OF SCIENCES ETH ZURICH

(Dr. sc. ETH Zurich)

Presented by

LUCA ALOIS EGON MÜLLER

Ing. Sc. Mat. Dipl. EPF

École Polytechnique Fédérale de Lausanne

born on *28.05.1990*

Citizen of Switzerland

Accepted on the recommendation of

Prof. Dr. Ingo Burgert, ETH Zürich, supervisor and examiner

Dr. Gilberto Siqueira, Empa, co-supervisor and co-examiners

Prof. Christoph Weder, Adolph Merkle Institute, co-examiner

Prof. Alain Dufresne, Grenoble INP - Pagora, UGA, co-examiner

2022

Abstract

With only a limited palette of ingredients, biological materials overcome the limitations of each single component's mechanical properties by organizing their structure in intricate and complex assemblies, which span from the nano to the macroscale. Common structuring strategies, like aligned building blocks and localized compositional changes, characterize such hierarchical assembly, conferring to natural composites, such as wood, bone and nacre, outstanding mechanical properties that greatly surpass the rule of mixture, as well as dynamic and adaptable responses to the external environment. Inspiration and emulation of these phenomena represents a strategy for the development of renewable materials that, presenting properties competitive with synthetic materials, will contribute to severing the dependence of our society on non-renewable resources. With the recent developments of 3D printing technologies, materials showing controlled microstructures of natural building blocks can be artificially produced. In particular, the direct ink writing (DIW) of materials containing anisotropic rod-like cellulose nanocrystals (CNC), demonstrated to allow local control over the alignment of such nanoparticles, promoting anisotropic reinforcement of the final printed composites. As a result, local tailoring of the mechanical properties allows to manufacture lightweight optimized devices for structural applications. However, the majority of 3D printed nanocellulose materials only present static properties. The development of complex 3D printed cellulose based materials presenting both intricate ordered structures as well as dynamic and reversible responses to external stimuli is still in its infancy and limited to few examples. Adaptable behaviors and movements as reaction to external stimuli are appealing features that would promote the spreading of nanocellulose based structures to applications ranging from sensors to actuators.

Owning to their renewability, biodegradability, biocompatibility, high surface area, ease of chemical functionalization and outstanding mechanical properties, CNC represent versatile reinforcing building blocks that allow the development of 3D printed devices with co-occurring mechanical optimization and smart photoresponsive behaviors. In order to tackle this challenge, this thesis proposes three approaches that introduce light triggered adaptable behaviors in 3D printable CNC based composites: photostiffening, shape changing and photosoftening.

The first approach leads to the development of a DIW 3D printing platform for the production of materials with locally tuneable mechanical properties. By engineering CNC particles and a compatible polyurethane matrix, both bearing cinnamate moieties, a processable ink with high solid contents (e.g. 30 wt%) could be produced and processed. The cinnamates functional groups into the printed and cured composites act as photoswitches. UV light (365 nm) triggers the [2,2] cycloaddition of the cinnamates creating covalent bonds between particles, particles and matrix, and into the matrix forming a secondary polymer network. This secondary polymer network is responsible to increase the Young's modulus from 15 MPa to 75 MPa depending on the irradiation dose. The stiffness of this material hence is tailored both by aligning the CNC along the printing direction and by illumination. Moreover, spatial control over the light source confers very high design freedom to finely tailor the mechanical behaviors since it allows to freely produce photopatterns of stiff domains in the printed material.

The second approach introduces 15 wt% of cellulose nanocrystals (CNC) into a liquid crystalline elastomer (LCE) in order to enable the printing process by DIW of shape changing structures. CNC, acting as rheology modifiers, facilitate the production of free-standing structures at room temperature, while by controlling the extrusion induced alignment of such nanoparticles, the LC mesogens of the matrix can be ordered in nematic phases. With the introduction in the composite of azobenzene photoswitches

after curing, photomechanical behaviors are conferred to the printed material. The *trans-cis-trans* photoisomerization of the azobenzene occurring under illumination (480 nm) generates the nematic to isotropic phase transition in the LCE, leading to the bending of the material. This approach results in soft composites, with an elastic modulus of 20 – 30 MPa, that present fully reversible photomechanical actuation occurring in less than 3 seconds. Moreover, the influence of methacrylated groups onto the CNC surface was investigated and revealed to allow improve both the photoactuation performances and the mechanical properties of the composites, improving stress transfer from the matrix to the particles.

In the last approach, anisotropic cellulose nanocrystals (CNC) are utilized as active reinforcement particles in DIW polymer ink formulations. By grafting azobenzene moieties onto the CNC surface, photoresponsive features depending on the polymer matrix are conferred to 3D printed complex structures. By using these CNC, the rheology influence of the modified particles on polymer resins allow DIW of self-standing structures, while the shear and extensional forces align the CNC leading to anisotropic mechanical properties. When treated CNC are introduced into polyurethane acrylate suspensions, up to 15 wt%, the 3D printing of the ink can be achieved successfully. Moreover, the printed structures present fast and reversible photosoftening, with longitudinal elastic modulus going from 30 to 16 MPa when illuminated, and a shape memory effect. In this case, the *trans-cis-trans* photoisomerization of the azobenzene generates heat that triggers the thermal properties of the polyurethane acrylate matrix.

Finally, the DIW of nanocellulosic materials demonstrates to allow fast prototyping of devices for a wide range of applications, such as optimized protective structures (photostiffening material), actuators (shape changing material) and dynamic energy absorptive structures (photosoftening material). The significant versatility and design freedom observed in these three approaches are expected to expand further the range of applications of the photoresponsive CNC composites.

Résumé

Avec seulement une palette limitée d'ingrédients, les matériaux biologiques surmontent les limites des propriétés mécaniques de chaque composant en organisant leur structure avec des assemblages étroitement imbriqués et complexes, qui s'étendent de l'échelle nano à l'échelle macro. Des stratégies de structuration, telles que des particules alignées et des changements localisés de la composition de la matière, caractérisent un tel assemblage hiérarchique. Ces assemblages confèrent aux matériaux composites naturels, tels que le bois, l'os et la nacre, des propriétés mécaniques exceptionnelles, qui dépassent largement la règle du mélange, ainsi que des propriétés adaptables et des réponses dynamiques à l'environnement extérieur. L'inspiration et l'émulation de ces phénomènes représentent une stratégie de développement de matériaux renouvelables qui, présentant des propriétés compétitives avec les matériaux synthétiques, contribueront à supprimer la dépendance de notre société vis-à-vis des ressources non renouvelables. Grace aux développements récents de technologies d'impression 3D, des matériaux présentant des microstructures contrôlées de blocs de construction naturels peuvent être produits artificiellement. En particulier, l'écriture directe d'encre, de l'anglais *Direct Ink Writing* (DIW), de matériaux contenant des nanocristaux de cellulose (NCC) en forme de tige ou d'aiguille, a démontrée qu'elle permettait un contrôle local de l'alignement de ces nanoparticules, favorisant le renforcement anisotrope des composites imprimés. L'adaptation locale des propriétés mécaniques d'un matériau permet de fabriquer des dispositifs légers, optimisés pour des applications structurelles. Cependant, la majorité des matériaux à base de nanocellulose imprimés en 3D ne présentent que des propriétés statiques. Le développement de matériaux à base de cellulose imprimés en 3D présentant à la fois des structures ordonnées et imbriquées, ainsi que des réponses dynamiques et réversibles à des stimuli externes, en est encore à son commencement, et est limité à quelques exemples. Des comportements et des mouvements adaptables, en réaction à des stimuli externes, sont des caractéristiques attrayantes qui favoriseraient la diffusion de structures à base de nanocellulose à des applications allant des capteurs aux actuateurs.

Les NCC sont issus de sources renouvelable et présentent biodégradabilité, biocompatibilité, une grande densité de surface, facilité de fonctionnalisation chimique et des propriétés mécaniques exceptionnelles. Grace à ces caractéristiques les NCC représentent des éléments de renforcement polyvalents qui permettent le développement de dispositifs imprimés en 3D avec une optimisation mécanique simultanée à des comportements photosensibles intelligents. Afin de relever ce défi, cette thèse propose trois approches qui introduisent des comportements adaptables déclenchés par la lumière dans des composites à base de NCC et imprimables en 3D : le photodurcissement, le changement de forme et le photo-adoucissement.

La première approche conduit au développement d'une plateforme d'impression 3D DIW pour la production de matériaux aux propriétés mécaniques localement ajustables. En concevant des particules NCC et une matrice de polyuréthane compatible, toutes deux portant des dérivés de l'acide cinnamique, une encre avec une teneur élevée en solides (par exemple 30 % en poids) pourrait être produite et imprimée. Les groupes fonctionnels cinnamiques, dans les composites imprimés et durcis, agissent comme des photocommutateurs. La lumière UV (365 nm) déclenche la [2,2] addition cyclique des dérivés cinnamiques créant des liaisons covalentes entre les particules, les particules et la matrice, et dans la matrice. Ceci forme un réseau polymère secondaire. Un tel réseau secondaire est responsable d'augmenter le module de Young des composites imprimées, de 15 MPa à 75 MPa, en fonction de la dose d'irradiation lumineuse. La rigidité de ce matériau est donc adaptée à la fois par l'alignement des NCC le long de la direction d'impression et par l'éclairage. De plus, le contrôle dans l'espace de la source lumineuse confère une très grande liberté de conception pour adapter finement les comportements mécaniques, puisqu'il permet de produire librement des motifs géométriques de domaines rigidifié dans le matériau imprimé.

La deuxième approche introduit 15 % en poids de NCC dans un élastomère à cristaux liquides (LCE) afin de permettre le processus d'impression par DIW de structures à changement de forme. Les NCC, agissant comme modificateurs de rhéologie, facilitent la production de structures imprimés à température ambiante, tandis qu'en contrôlant l'alignement de ces nanoparticules, induit par l'extrusion, les cristaux liquides de la matrice peuvent être ordonnés en phases nématiques. Avec l'introduction dans le composite de d'azobenzène comme photocommutateurs, après cuisson, des comportements photomécaniques sont conférés au matériau imprimé. La photoisomérisation *trans-cis-trans* des azobenzènes, se produisant sous illumination (480 nm), génère la transition de la phase nématique à la phase isotrope des cristaux liquides dans le LCE. Ce qui conduit à la flexion autonome du matériau. Cette approche aboutit à la production de composites souples, avec un module d'élasticité de 20 à 30 MPa, qui présentent un actionnement photomécanique entièrement réversible, se produisant en moins de 3 secondes. De plus, l'influence des groupes méthacrylés sur la surface des NCC a été étudiée et révèle de permettre d'améliorer à la fois les performances de photoactuation et les propriétés mécaniques des composites, améliorant le transfert de contraintes entre la matrice polymérique et les nanoparticules.

Dans la dernière approche, les NCC sont utilisés dans les formulations d'encre polymère par DIW comme particules actives de renforcement. En greffant des azobenzènes sur la surface des NCC, des caractéristiques photosensibles sont conférées aux structures complexes imprimées en 3D qui dépendent de la matrice polymère employé. En utilisant ces NCC, l'influence rhéologique sur les résines polymères des particules modifiées permet l'impression de structures par DIW, tandis que les forces de cisaillement et d'extension alignent le CNC, conduisant à des propriétés mécaniques anisotropes. Lorsque les CNC traités sont introduits dans des suspensions d'acrylate de polyuréthane, jusqu'à 15 % en poids, l'impression 3D de l'encre peut être réalisée avec succès. De plus, les structures imprimées présentent un photoramollissement rapide et réversible, avec un module d'élasticité longitudinal allant de 30 à 16 MPa, lorsqu'elles sont éclairées, et un effet de mémoire de forme. Dans ce cas, la photoisomérisation *trans-cis-trans* de l'azobenzène génère de la chaleur, qui déclenche les propriétés thermiques de la matrice polyuréthane acrylate.

Enfin, le DIW de matériaux intelligents, à base de NCC, démontre qu'il permet le prototypage rapide de dispositifs pour une large gamme d'applications, telles que des structures de protection mécaniquement optimisées (matériau photo-rigidifiant), des actionneurs (matériau à changement de forme) et des structures qui absorption d'énergie de façons dynamique (matériau photo-adoucissant). La grande polyvalence et liberté de conception, observées dans ces trois approches, devraient contribuer à élargir davantage la gamme d'applications des composites CNC photosensibles.

Acknowledgements

A PhD thesis is a long amazing journey and an adventure at the frontier of innovation and science discoveries. There are all kinds of moments in this journey, happiness, sadness, relaxation, stress, confidence and skepticism. I believe that such an adventure is impossible to undertake alone. Hence, I would like to express my gratitude to all the people that accompanied me in this scientific and human experience.

I would like to start thanking my supervisors, Ingo Burgert (ETHZ), Gilberto Siqueira, Gustav Nyström and Tanja Zimmermann (Empa) for having given me the opportunity to carry out this project, having accepted me in their respective groups, Wood Materials Science in ETHZ and Cellulose and Wood Materials Laboratory in Empa, and most importantly for the outstanding guidance, help and support that I received from them, both in science and life. It is thanks to everything you all taught me, from pursuing my own ideas with a strict methodology to expressing and sharing my works with project's outsiders, that I am the researcher I am today. I do not have enough words to say how grateful I am for this!

During my thesis I had not only the support from my supervisors, but also from my past and present colleagues of both groups, the Cellulose and Wood Materials Laboratory and the Wood Materials Science, with whom I had excellent scientific discussions that nourished my work and promoted the achievement of my research objectives, with whom I had fun and relaxing moments that allowed to keep the motivation when the experiments were not as successful, with whom I could tackle challenges in both my professional and private life. Thank you, Xavier Aeby, Nadia Ahmadi, Luana Amoroso, Katerina Andric, Silvia Campioni, Kevin De France, Christopher Dreimol, Roman Elsener, Thomas Geiger, Marc Grädel, Markus Heeb, Yijie Hu, Anja Huch, Tine Kalac, Sophie Koch, Nico Kummer, Tina Künninger, Mirko Lukovic, Danilo Menghini, Rossana Pitocchi, Javier Ribera, Mark Schubert, Paul-Antoine Spies, Anh Tran Ly, Xiaomei Yan, Alessia Pasqualini, Alexandre Poulin, Daniel Heer, Francis Schwarze, Hugh Morris, Marion Frey, Philippe Grönquist, Walter Risi, Alberto Giubilini, Debora França, Electra D'Emilio, Zhihui Zeng, Jingjang Wei, Tobias Tschichold, Katrin Hoffmann, Daniel Käch and Sefora Riillo.

A special thank you goes to all my office mates Rani Boons, Michael Hausmann, Sarah Lämmlein, Sandro Stucki, Tingting Wu, Carolina Reyes, Ming Liu, Thoma Janine and Ashutosh Sinha that kept me smiling and gave me another motivation to come every day in the office and that I was missing during the dark times of Covid's "lockdown". Further, I am grateful to Yannick Nagel and Patrick Zumsteg for the midday runs and the climbing evenings we had together that maintained me fit, as well as all the help they gave me during the development of some experiments.

Importantly, I am grateful to my one and only student, Anita Zingg, for the precious work she carried out during her master thesis that significantly contributed in the development and the progress of my third scientific publication. Moreover, I could learn from her how to improve my advisor skills.

I want to thank Joanne Vaucher, Adrien Demongeot and Yves Leterrier, from LPAC in EPFL, for being both my friends and collaborators and supporting me into the development of the shape changing materials. We were colleagues before I started my thesis in Empa, and I am glad we could continue to work together, since without their help I could not have carried out the PhotoDSC and PhotoDMA experiments. Additionally, I would also like to thank Jonathan Avaro, Marianne Liebi and Antonia Neels of the Empa's Center for X-Ray Analytics for spending time measuring and analyzing the SAXS and WAXS data from the shape changing materials. I am also glad to all these six people, for being my coauthors and for the valuable inputs they gave during the correction and revision of my second paper.

I am grateful to Andrea Arcifa for the help he gave me for the time he spent analyzing my samples with the XPS, as well as, Rowena Crockett for the experiments she conducted with the ToF-SIMS, which helped the writing of the third publication of this thesis.

The PhD Gatherings played an important role in the advancement of my thesis. These events that we organized together, allowed me to expand my network, share and develop ideas and improved my organization and presentation skills. I want hence to thank all my committee colleagues that were present and worked for keeping these meetings alive despite the pandemic. Many thanks to Michael Hausmann, Ryo Asakura, Emmanuel Billeter, Nadia Gomez, Rani Booms, Francesco Pagani and the new people that recently joined, Alexander Vogel, Claudia Masucci, Francesco Bernasconi, Yijie Hu, Meet Jaydeepkumar Oza, Filippo Longo and Ashutosh Sinha.

Outside of my doctorate life, I want to thank my friends, that tolerated me for more than ten years, going along with all my crazy ideas and believing I could pull off this thesis. Many thanks for still being my friends Jeremiah Albrecht, Nathaly Battaglia, Valênti De Praetère, Max Caduff and Basile Vaucher.

Most importantly, I thank my family, my parents, Valentino and Marie-Jo, my brothers, Gauthier and Alaric, for the great support I received daily during all my life. You provided me everything that was necessary to achieve such an accomplishment, from the education and the critical thinking to the confidence I could gain thanks to your teachings in life and the experiences we lived together. Everything you transmitted me stands at the base of my personal development as researcher and human being, making this journey in science possible. The last member of my family I want to thank is my beloved Luana. You could pass through all the happy and sad moments of my PhD journey tolerating my moods and supporting me unconditionally. Thank you for all of this!

Finally, from a more venial point of view, I want to thank and express my gratitude to the Swiss National Science Foundation for funding (200021_178941/1) received, without which, the MULTIFUN project could not be realized. I must say that the project brought honor to his name, it really was a lot of fun!

Table of Contents

1 Introduction

1.1 Motivation and Goals

Today's society shows a strong interest in severing the dependence on petroleum based materials. With an ever-increasing focus on sustainability, research and studies on materials issued from renewable resources are flourishing inspired by the astonishing properties of biological materials. Through millions of years of evolution, natural materials have optimized their structural organization in order to reach outstanding mechanical properties. Wood is one example where, common strategies such as sophisticated geometrical structural design, compositional changes and oriented hierarchical assemblies of reinforcing building blocks are used to finely tune mechanical properties [1]. Insect cuticles and spider fangs represent other interesting examples where these strategies are also applied; both are chitin-protein based composites, but with vastly different organizations. For spider fangs, a tip composed of highly crosslinked proteins with packed and oriented layers of chitin fibers [2], and an optimized macroscopic conical shape [3], allow for easy perforation of insect cuticles. Not limited only to present static physical and chemical properties, biological materials can also respond to external stimuli via various movements and dynamic shape transformations, as well as adaptation of their mechanical properties, in order to fulfill different biological functions. Some examples include the movements of *Mimosa pudica* leaves [4] used to repel predators, or the closure of *Dionaea muscipula* [5] for feeding on insects, or the reaction of wood tissues initiating mechanical self-optimization, as a response to external load cases [6]. Although the understanding of such mechanisms is progressing fast, the implementation of both optimization of mechanical properties and reaction to the environment in engineered synthetic materials remains challenging. Materials with optimized geometries, presenting tailored mechanical properties, allow decreasing the weight and accessing very personalized features for sustaining particular load cases. At the same time, dynamic materials triggered by external stimuli such as heat, light, pH or humidity [7]–[10] are very appealing in the production of actuators [11], sensors [12], [13] and soft robots [14], [15]. In particular, shape changing materials allow further weight and energy consumption reductions, especially by substituting hydraulic systems, hinges or engines. Within the biomedical domain [16], [17] such combination of properties is particularly appealing and would allow access to applications where fine adaptability is required, such stents, implants and prosthetics. As a matter of fact, the development of biocompatible and lightweight materials with tailored mechanical properties and dynamic responses is critical for several applications. However, the realization of such synthetic materials based on renewable resources remains a major challenge.

3D printing, an additive manufacturing technology, shows promise for the synthetic production of composite materials presenting controlled and determined microstructures [18]–[21], as well as shape changing materials with complex 3D geometries [9], [22], [23]. Bottom-up approaches such as 3D printing, furthermore, allow for high spatio-temporal resolution while maintaining control over natural building blocks and composition. The use of cellulose nanocrystals (CNC), a natural, biocompatible building block, extracted from biomass, has attracted great attention due to their potential in polymer composite applications as a reinforcement phase [24], [25] and rheology modifier [24], [26], [27], which allow material processing by extrusion-based 3D printing, such as direct ink writing (DIW). Indeed, DIW is a technique that additively manufactures self-standing 3D structures from inks requiring optimized rheo-

logical properties, with a layer-by-layer filamentary extrusion. The use of CNC in DIW inks demonstrated to confer both printability and a strong reinforcement effect in the final composite. One example is the printing of textured cellular architectures presenting spatially tailored elastic moduli [26]. The anisotropic CNC particles have shown a high degree of alignment along the extrusion directions, due to the strong shear and extensional forces experienced during printing [26], [28]. Thus CNC orientation is spatially controlled by DIW and confers anisotropic mechanical reinforcement. Moreover, with the same principle, DIW has demonstrated to be the 3D printing technique of choice for production of synthetic shape changing materials, especially because shear and extensional forces can also be used to impart control over molecular organization in liquid crystalline elastomers (LCE) [29]–[31]. Here, the spatial molecular control exerted by the extrusion printing determines the actuated movements [32], and by controlling the printing parameters (nozzle diameter, printing speed and temperature), LCE are nowadays produced as structures able to display deformations like a 2D disc evolving to a 3D cone [33].

Despite the developments obtained so far in both hierarchical organization for tuning of mechanical properties and stimuli responsive materials like shape changing, the production of 3D complex structures presenting both features by DIW is still far from the intricate complexity of natural materials. However, the recent use of CNC as building blocks for DIW and production of 3D devices presents a concrete potential to allow such development, although, stimuli responsive behaviors have so far only rarely been introduced in such 3D printed composites and are limited to humidity as a trigger [34].

Among the available stimuli that can be utilized for imparting physical and chemical responses to synthetic responsive materials, light emerges as a very advantageous stimulus with respect to its low energy requirement, its contactless nature and the high control of both its physical properties (wavelength, polarization, intensity) and its spatio-temporal structure. Hence, with a particular focus on light responsive functionalities, this work aims to produce 3D printable cellulose nanocomposites that present local anisotropy in mechanical properties and, at the same time, enables dynamic and reversible changes in such properties as well as shape transformations. Such materials would allow then the production of more renewable smart devices than the currently available synthetic solutions. Moreover, with tailored mechanical properties they would be suitable for a wide range of applications requiring dynamic adaptation and functions.

In order to achieve this aim, the following research goals are pursued:

- Exploration and development of strategies for the introduction of photoresponsive behaviors in CNC based composites, by functionalization of CNC and engineering of the polymer matrix.
- Investigation on the influence of the defined modifications, introducing photoresponsive behaviors in cellulose nanocomposites, over the manufacturing process by DIW and the resulting microstructures. Particular focus is brought on the rheological properties of the ink formulations and the induced alignment of the natural nanoparticles within the 3D printed filaments and resulting structures with tailored mechanical properties.
- In depth characterization of photoresponsive chemical, physical and mechanical properties of 3D printed composites and investigation of the interfacial properties of CNC with the polymer matrices. Establishment of the synergy between photoresponsive behaviors and extrusion induced alignment of CNC.
- Development and prototyping of photoresponsive devices demonstrating their potential applications.

1.2 Thesis Outline

The research work began with the establishment of the possible photoresponsive behaviors that can be introduced in 3D printed cellulose nanocomposites. As a result, three main materials were developed, each of them presenting different methods and concepts allowing light to be harnessed and transformed into stiffening, deforming and softening of 3D printed devices. This cumulative thesis features this work by collecting three scientific publications that report the advances achieved during these years of investigation (Figure 1.2-1). This thesis is hence structured in 5 chapters. Starting from the present Chapter 1, the main motivations and the research objectives that are at the fundaments of this work are explained. Chapter 2 provides the theory and the knowledge on nanocellulose materials required for the understanding of this work. In particular, Chapter 2 comprises a detailed description of the state-of-the-art of both 3D printing of CNC based materials and 3D printing of photoresponsive materials and composites. In order to present and describe the research gaps, this state of the art includes the main strategies for the development of light stimulated smart materials.

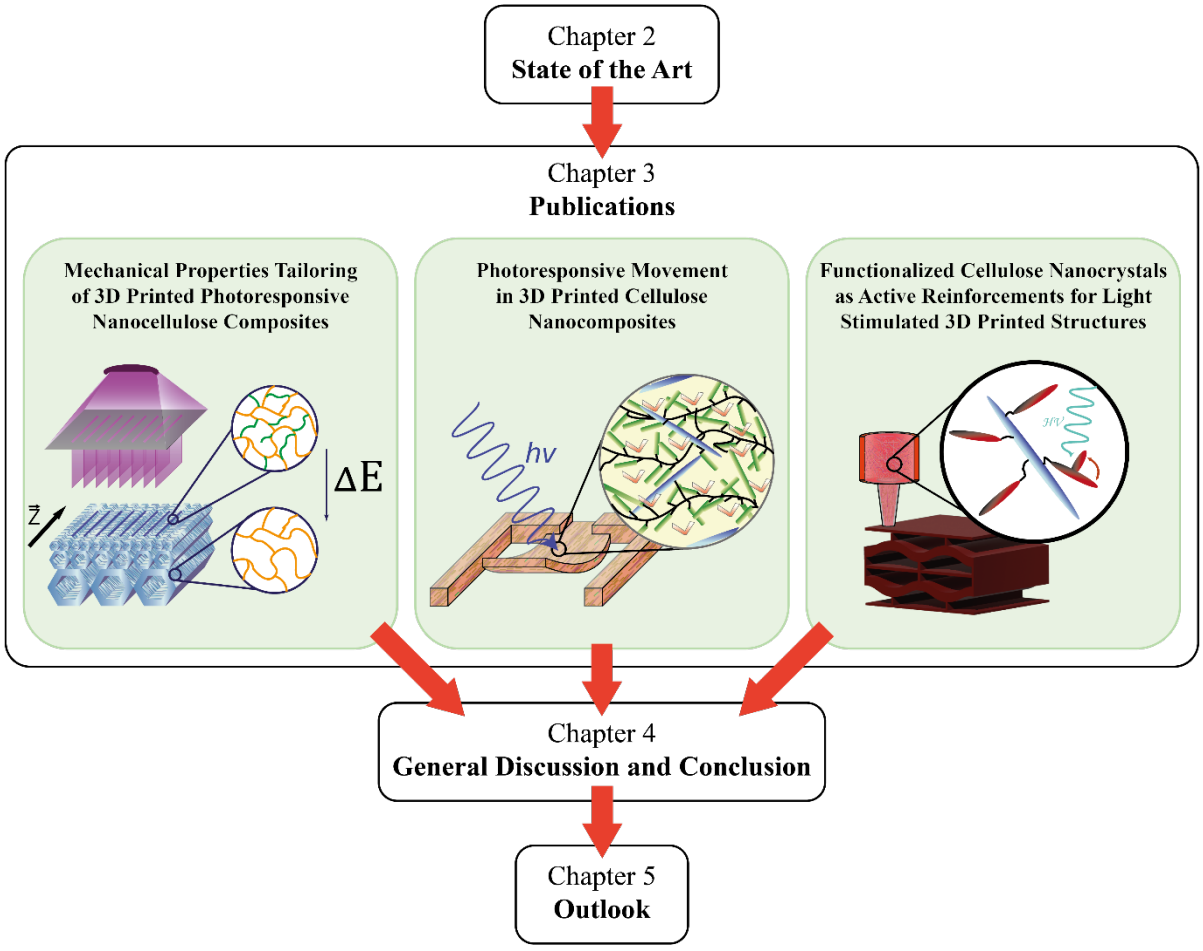

Figure 1.2-1 *Outline of the thesis.*

The three scientific articles are then illustrated in Chapter 3. They represent the main core of this research work and define guidelines that can be used to obtain smart materials composed of different elements:

- The first article "Mechanical Properties Tailoring of 3D Printed Photoresponsive Nanocellulose Composites" presents a strategy introducing photoresponsive stiffening into printed parts. This feature emerges with the creation of an on-demand secondary polymer network through modification of CNC and compatibilization with the polymer matrix.
- The second article "Photoresponsive Movement in 3D Printed Cellulose Nanocomposites" demonstrates a strategy allowing 3D printing of composite materials presenting a photomechanical effect, while investigating the role of CNC on the manufacturing process and the light triggered performance.
- The third article "Functionalized cellulose nanocrystals as active reinforcements for light stimulated 3D printed structures" introduces the last strategy, a modification of CNC that allows to widen the quantity of printable materials and has the potential to present multiple responses to a single illumination as a function of the matrix used.

The following Chapter 4 concludes the research work by providing a general discussion on the main achievements of this work, the limitations and current challenges, and the implications of the results presented in Chapter 3.

Finally, Chapter 5 provides perspectives and suggests future research paths that could be undertaken to progress in the field of CNC based smart materials that react to light.

1.3 References

[1] J. J. Harrington, "Hierarchical modelling of softwood hygro-elastic properties," 2002.

[2] Y. Politi *et al.*, "A Spider's Fang: How to Design an Injection Needle Using Chitin-Based Composite Material," *Adv. Funct. Mater.*, vol. 22, no. 12, pp. 2519–2528, Jun. 2012, doi: 10.1002/adfm.201200063.

[3] B. Bar-On, F. G. Barth, P. Fratzl, and Y. Politi, "Multiscale structural gradients enhance the biomechanical functionality of the spider fang," *Nat. Commun.*, vol. 5, no. 1, pp. 1–8, May 2014, doi: 10.1038/ncomms4894.

[4] S. N. Basir, H. Yussof, and N. I. Zahari, "Simulation Analysis of Mimosa Pudica Main Pulvinus Towards Biological Tactile Sensing Modelling," in *Procedia Computer Science*, 2015, vol. 76, pp. 425–429, doi: 10.1016/j.procs.2015.12.282.

[5] Y. Forterre, J. M. Skotheim, J. Dumals, and L. Mahadevan, "How the Venus flytrap snaps," *Nature*, vol. 433, no. 7024, pp. 421–425, Jan. 2005, doi: 10.1038/nature03185.

[6] C. Mattheck and I. Tesari, "The mechanical self-optimisation of trees," 2004. Accessed: 24-Jan-2022. [Online]. Available: www.witpress.com,.

[7] I. Navarro-Baena, J. M. Kenny, and L. Peponi, "Thermally-activated shape memory behaviour of bionanocomposites reinforced with cellulose nanocrystals," *Cellulose*, vol. 21, no. 6, pp. 4231–4246, Dec. 2014, doi: 10.1007/s10570-014-0446-5.

[8] M. Bodaghi, A. R. Damanpack, and W. H. Liao, "Triple shape memory polymers by 4D printing," *Smart Mater. Struct.*, vol. 27, no. 6, 2018, doi: 10.1088/1361-665X/aabc2a.

[9] A. Sydney Gladman, E. A. Matsumoto, R. G. Nuzzo, L. Mahadevan, and J. A. Lewis, "Biomimetic 4D printing," *Nat. Mater.*, vol. 15, no. 4, pp. 413–418, 2016, doi: 10.1038/nmat4544.

[10] Y. Li, H. Chen, D. Liu, W. Wang, Y. Liu, and S. Zhou, "PH-Responsive Shape Memory Poly(ethylene glycol)-Poly(ε-caprolactone)-based Polyurethane/Cellulose Nanocrystals Nanocomposite," *ACS Appl. Mater. Interfaces*, vol. 7, no. 23, pp. 12988–12999, Jun. 2015, doi: 10.1021/acsami.5b02940.

[11] D. Hua *et al.*, "3D printing of shape changing composites for constructing flexible paper-based photothermal bilayer actuators," *J. Mater. Chem. C*, vol. 6, no. 8, pp. 2123–2131, 2018, doi: 10.1039/c7tc05710e.

[12] T. Hiratani, O. Kose, W. Y. Hamad, and M. J. Maclachlan, "Stable and sensitive stimuli-responsive anisotropic hydrogels for sensing ionic strength and pressure," *Mater. Horizons*, vol. 5, no. 6, pp. 1076–1081, Nov. 2018, doi: 10.1039/c8mh00586a.

[13] H. Lu, K. Yu, Y. Liu, and J. Leng, "Sensing and actuating capabilities of a shape memory polymer composite integrated with hybrid filler," *Smart Mater. Struct.*, vol. 19, no. 6, p. 065014, May 2010, doi: 10.1088/0964-1726/19/6/065014.

[14] M. Pilz Da Cunha, E. A. J. Van Thoor, M. G. Debije, D. J. Broer, and A. P. H. J. Schenning, "Unravelling the photothermal and photomechanical contributions to actuation of azobenzene-doped liquid crystal polymers in air and water," *J. Mater. Chem. C*, vol. 7, no. 43, pp. 13502–13509, Nov. 2019, doi: 10.1039/c9tc04440j.

[15] P. Heidarian, A. Z. Kouzani, A. Kaynak, M. Paulino, and B. Nasri-Nasrabadi, "Dynamic Hydrogels and Polymers as Inks for Three-Dimensional Printing," *ACS Biomater. Sci. Eng.*, vol. 5, no. 6, pp. 2688–2707, Jun. 2019, doi: 10.1021/acsbiomaterials.9b00047.

[16] G. I. Peterson, A. V. Dobrynin, and M. L. Becker, "Biodegradable Shape Memory Polymers in Medicine," *Adv. Healthc. Mater.*, vol. 6, no. 21, pp. 1–16, 2017, doi: 10.1002/adhm.201700694.

[17] A. Kirillova and L. Ionov, "Shape-changing polymers for biomedical applications," *Journal of Materials Chemistry B*, vol. 7, no. 10. Royal Society of Chemistry, pp. 1597–1624, 2019, doi: 10.1039/c8tb02579g.

[18] A. R. Studart, "Additive manufacturing of biologically-inspired materials," *Chem. Soc. Rev.*, vol. 45, no. 2, pp. 359–376, Jan. 2016, doi: 10.1039/c5cs00836k.

[19] M. G. M. Marascio, J. Antons, D. P. Pioletti, and P.-E. Bourban, "3D Printing of Polymers with Hierarchical Continuous Porosity," *Adv. Mater. Technol.*, vol. 2, no. 11, p. 1700145, Nov. 2017, doi: 10.1002/admt.201700145.

[20] L. Alison *et al.*, "3D printing of sacrificial templates into hierarchical porous materials," *Sci. Rep.*, vol. 9, no. 1, Dec. 2019, doi: 10.1038/s41598-018-36789-z.

[21] M. Peng *et al.*, "3D Printing of Ultralight Biomimetic Hierarchical Graphene Materials with Exceptional Stiffness and Resilience," *Adv. Mater.*, vol. 31, no. 35, p. 1902930, Aug. 2019, doi: 10.1002/adma.201902930.

[22] S. Tibbits, "4D Printing: Multi-Material Shape Change," *Archit. Des.*, vol. 84, no. 1, pp. 116–121, Jan. 2014, doi: 10.1002/ad.1710.

[23] F. Momeni, S. M.Mehdi Hassani.N, X. Liu, and J. Ni, "A review of 4D printing," *Mater. Des.*, vol. 122, pp. 42–79, May 2017, doi: 10.1016/J.MATDES.2017.02.068.

[24] S. Sultan, G. Siqueira, T. Zimmermann, and A. P. Mathew, "3D printing of nano-cellulosic biomaterials for medical applications," *Curr. Opin. Biomed. Eng.*, vol. 2, pp. 29–34, 2017, doi: 10.1016/j.cobme.2017.06.002.

[25] W. Xu, X. Wang, N. Sandler, S. Willför, and C. Xu, "Three-Dimensional Printing of Wood-Derived Biopolymers: A Review Focused on Biomedical Applications," *ACS Sustain. Chem. Eng.*, vol. 6, no. 5, pp. 5663–5680, May 2018, doi: 10.1021/acssuschemeng.7b03924.

[26] G. Siqueira *et al.*, "Cellulose Nanocrystal Inks for 3D Printing of Textured Cellular Architectures," *Adv. Funct. Mater.*, vol. 27, no. 12, 2017, doi: 10.1002/adfm.201604619.

[27] L. Dai *et al.*, "3D printing using plant-derived cellulose and its derivatives: A review," *Carbohydrate Polymers*. 2019, doi: 10.1016/j.carbpol.2018.09.027.

[28] M. K. Hausmann *et al.*, "Dynamics of Cellulose Nanocrystal Alignment," *ACS Nano*, vol. 12, pp. 6926–6937, 2018, doi: 10.1021/acsnano.8b02366.

[29] S. Palagi *et al.*, "Structured light enables biomimetic swimming and versatile locomotion of photoresponsive soft microrobots," *Nat. Mater.*, vol. 15, no. 6, pp. 647–653, Jun. 2016, doi: 10.1038/nmat4569.

[30] T. Ube and T. Ikeda, "Photomobile Polymer Materials with Complex 3D Deformation, Continuous Motions, Self-Regulation, and Enhanced Processability," *Adv. Opt. Mater.*, vol. 7, no. 16, p. 1900380, Aug. 2019, doi: 10.1002/adom.201900380.

[31] S. Iamsaard *et al.*, "Conversion of light into macroscopic helical motion," *Nat. Chem.*, vol. 6, no. 3, pp. 229–235, 2014, doi: 10.1038/nchem.1859.

[32] Z. Wang, Z. Wang, Y. Zheng, Q. He, Y. Wang, and S. Cai, "Three-dimensional printing of functionally graded liquid crystal elastomer," *Sci. Adv.*, vol. 6, no. 39, p. eabc0034, Sep. 2020, doi: 10.1126/sciadv.abc0034.

[33] A. Kotikian, R. L. Truby, J. W. Boley, T. J. White, and J. A. Lewis, "3D Printing of Liquid Crystal Elastomeric Actuators with Spatially Programed Nematic Order," *Adv. Mater.*, vol. 30, no. 10, p. 1706164, Mar. 2018, doi: 10.1002/adma.201706164.

[34] O. Fourmann *et al.*, "3D printing of shape-morphing and antibacterial anisotropic nanocellulose hydrogels," *Carbohydr. Polym.*, vol. 259, p. 117716, May 2021, doi: 10.1016/j.carbpol.2021.117716.

2 State of the art

2.1 Nanocellulose as renewable building blocks

Cellulose is the most abundant polysaccharide present on Earth and can be found widely in trees, plants, algae, marine animal (tunicates) and can be produced by bacteria (e.g. *Acetobacter xylinum*). With an annual biomass production of 1.5×10^{12} tons [1], cellulose emerges as an attractive resource for the production of sustainable and ecofriendly devices and structures. Moreover, biocompatibility and biodegradability render this natural polymer an interesting alternative to non-degradable petroleum based polymers.[2] Cellulose is formed of high molecular mass homopolymer chains composed of β (1-4) linked D-glucose units. This polymer naturally presents degrees of polymerization ranging from 10000 to 15000 [3], depending on the source material. The cellobiose monomer comprises two anhydroglucose units holding three hydroxyl groups each (Figure 2.1) responsible for forming strong hydrogen bonds between adjacent glucose units and between the different chains. While intramolecular hydrogen bonding stabilizes the linkage and promotes a planar and linear chain configuration, intermolecular hydrogen bonding and Van der Waals interactions promote parallel stacking of several chains and formation of elementary fibrils presenting high axial stiffness [4]. These cellulose fibrils further aggregate in microfibrils with diameters lower than 100 nm and length of several microns [3]–[5]. Internally, cellulose microfibrils present two cellulose regions, one where cellulose chains are highly oriented and densely packed (crystalline cellulose) which provide strength and stiffness, and one disordered and loosely packed (disordered cellulose) that brings flexibility to the bulk material [6].

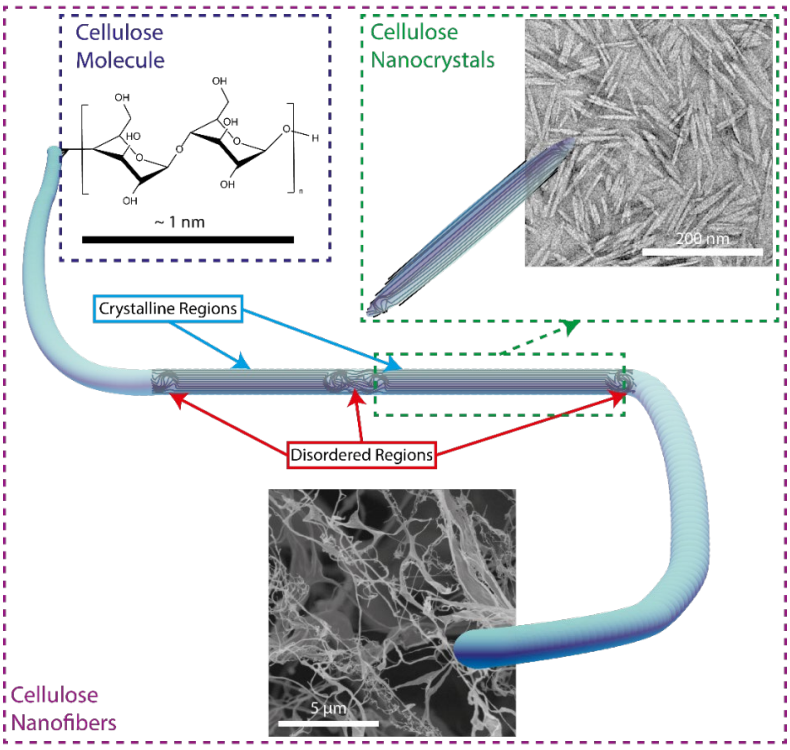

Figure 2.1 *Schematics representation of nanocellulose. Cellobiose unit (cellulose molecule) self assemble in elementary fibrils or cellulose nanofibers composed of crystalline and disordered regions. Cellulose nanocrystals, are the rigid, mainly ordered regions extracted form the cellulose nanofibers.*

The word nanocellulose generally refers to the elementary cellulose fibrils or microfibrils and their crystalline parts, namely known as cellulose nanofibrils (CNF) and cellulose nanocrystals (CNC), respectively. In particular, CNF are semi rigid elementary cellulose fibrils or microfibrils with diameters of a few, up to tens of nanometer, and lengths of few micrometers. They are composed of both crystalline and disordered regions, while CNC are the isolated needle, or rod-like, rigid crystalline parts with diameters of tens of nanometers and lengths of hundreds of nanometers, usually presenting high crystallinity (54-88%) [7]. Both CNF and CNC are the main natural building blocks forming the elementary cellulose fibrils constituting the cell walls in plants. Such fibrils are mainly responsible for conferring outstanding mechanical properties to wood and other biological materials by acting as reinforcement phases in hierarchically structured biopolymer composites. In particular, due to the high crystallinity, CNC present high stiffness and strength, chemical inertness, low density and a hydroxyl surface prone to functionalization [6]. Such nanoparticles are ideal for mimicking nature and to produce man-made synthetic renewable nanocomposites. Therefore, this thesis focuses especially on CNC and in the following, starting from an insight of the role of nanocellulose in wood, details on the extraction methods and properties of CNC are provided.

2.1.1 Role of nanocellulose in wood

To optimize their physical properties and ensure fulfillment of their biological functions in harsh environments, biological materials are often characterized by hierarchical assemblies of few building blocks spanning several length-scales. Such structures and designs are widely spread in nature, and can be seen in nacre [8], bone [9] and plants [10], to cite some examples. Cellulose constitutes an important building block in plants, including trees. In particular, wood, obtained from the tree stem, constitutes a complex hierarchical cellular biocomposite material, with 40 to 50 wt% of cellulose, occurring in nanocrystalline and amourphous states with around a 1:1 ratio [11]. The main sources of industrial nanocellulose are hence wood pulp and cotton fibers due to their abundance and relative low cost. An overview of wood hierarchy (Figure 2.2) and the role of cellulose such structure is presented in the following. However, cellulose is part of all plants and several other sources, such as jute, ramie, sisal, flax, hemp are also utilized for nanocellulose isolation [12].

In trees, cellulose is the main component of the cell walls. At the nanoscale, cellulose synthase (CESA) complexes synthetize cellulose microfibrils from glucose units in the plasma membrane and extrude them to the cell wall controlling their orientation [13]–[15]. Each CESA protein produces long cellulose chains that bundle and assemble in cellulose microfibrils by coalescence supported by Van der Waals forces and intermolecular hydrogen bonds interactions [13]. These microfibrils are formed of both crystalline and disordered cellulose regions and present a diameter around 3 - 4 nm [2], [10]. Surrounded by hemicelluloses, the stiff cellulose microfibrils further arrange into cellulose aggregates with diameters of 20 to 30 nm [16]. Microfibrils and cellulose aggregates are the reinforcement elements embedded in a matrix of hemicelluloses and lignin, forming the complex biocomposite that are cell walls. Such structural elements are packed in different layers, each with different compositions, and orientations defined by the microfibril angle (MFA) with the cell's longitudinal axis [17]. Cell walls layers are produced sequentially from the plasma membrane, inward. A primary external layer and up to 3 secondary layers usually constitute the cell walls of trees [18], providing the basic structural resistance of wood to internal and external stresses. The primary wall, in its initial stage, is a thin cell wall layer (30-100 nm) consisting of cellulose microfibrils, embedded in hemicelluloses and pectins [13], [19], [20]. Secondary cell walls are then built, inward, on the primary cell wall, generally when the cell reaches its final size and shape. With a higher portion of cellulose, secondary cell wall layers are thicker (up to 8 µm for the central S2

layer [20]) than primary walls and generally characterized by microfibrils oriented in parallel, embedded in a matrix of hemicelluloses and lignin. Going further up in the length-scale, each elongated hollow cell is attached to each other by the middle lamella (composed mainly of pectin and lignin) forming tissue structures arranged in alternating layers, the annual rings [21]. In conifers, annual rings are defined by successive layers of earlywood, with thin cell walls and wide lumina, and latewood, characterized by thick cell walls and narrow lumina [22].

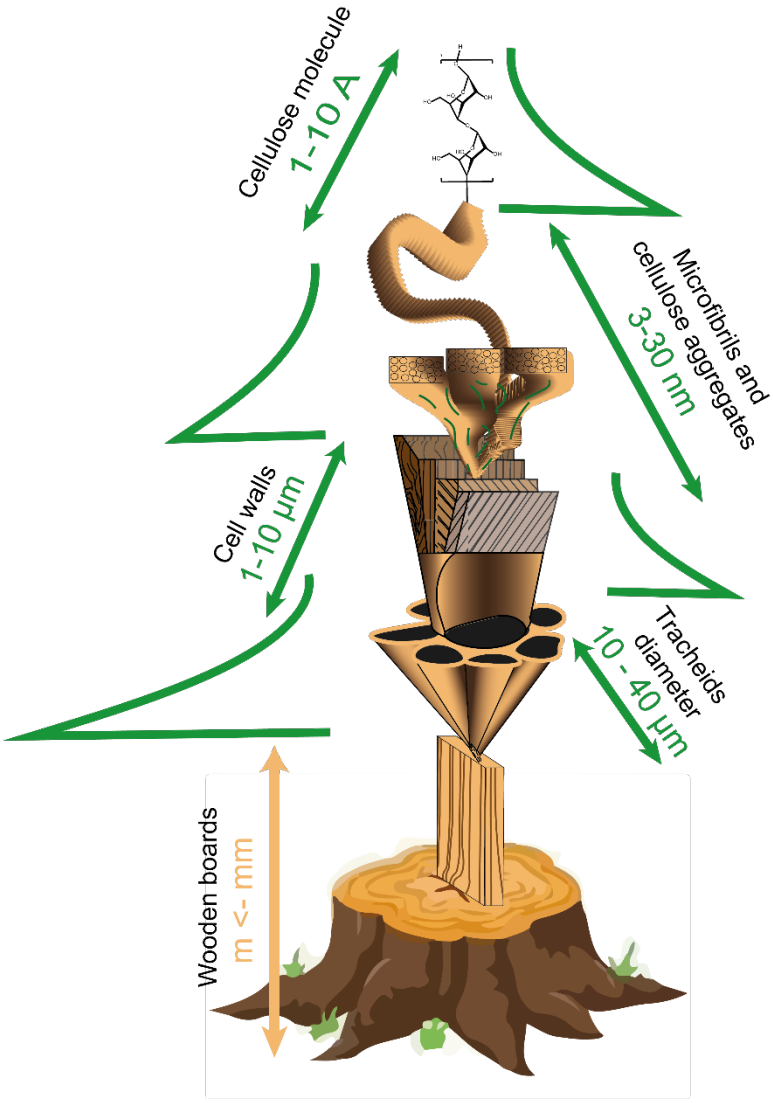

Figure 2.2 *Multiscale hierarchical arrangement of cellulose in softwood. From a cellulose molecule, cellulose self-assemble in microfibrils, which in their turn self-assemble in cellulose aggregates embedded in hemicelluloses and lignin. Such elements arrange further, forming the cell walls, in several packed layers characterized by different cellulose density and orientations, with respect to the main axis of the cell. The cellular structure characterizes the organization of wooden boards.*

With just four basic constitutive materials, i.e. cellulose, hemicelluloses, lignin and pectin, the wide variations and complexity of hierarchical assemblies, observed in different trees and plant tissues, generate a large palette of mechanical properties. For instance, materials like wood from different trees are composed of these constitutive materials, but present very different strengths and young moduli, covering a large range of values. The elastic modulus and tensile strength of parenchyma tissues can be as

low as 0.3 MPa, while the densest palms can reach values as high as 30 GPa for elastic modulus and 300 MPa for strength [10]. In addition, for the wood of the same species, the hierarchical structure renders such materials anisotropic, presenting different mechanical properties as a function of the loading directions (Figure 2.3).

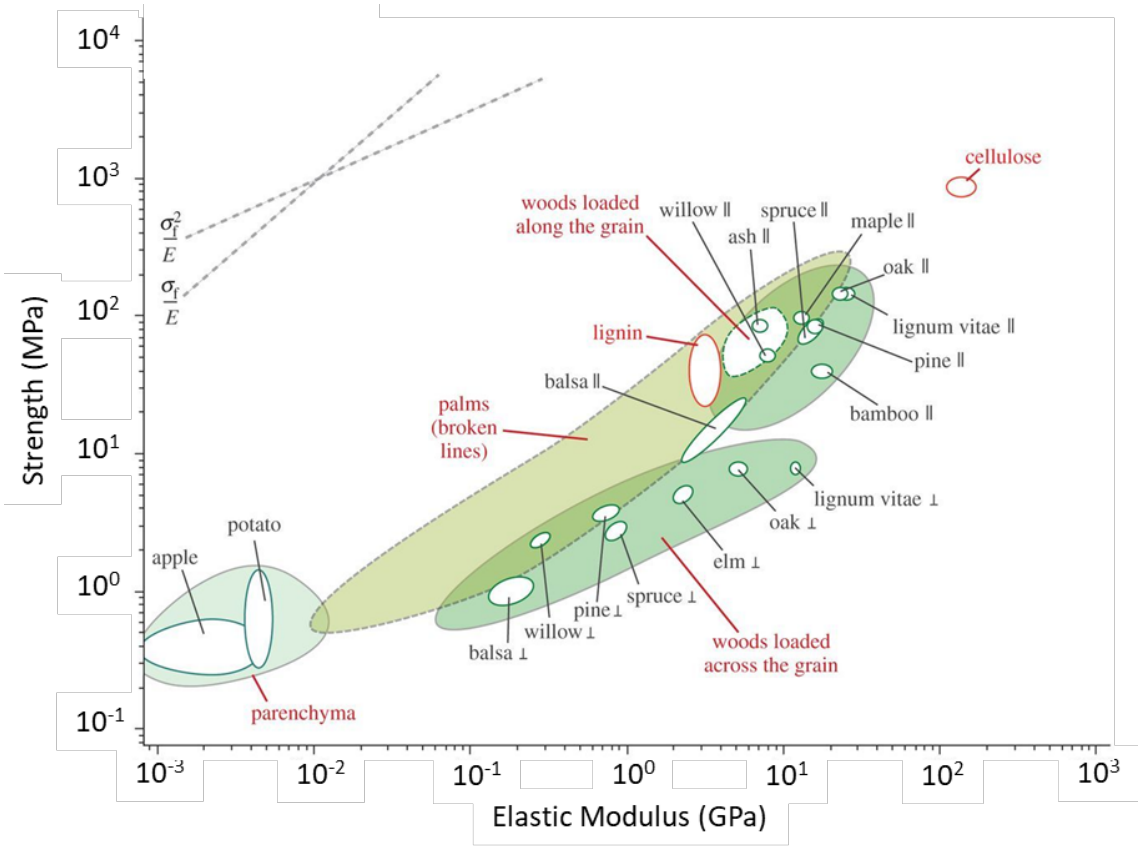

Figure 2.3 *Tensile strength in function of Young's modulus for diverse trees and plant materials composed of cellulose, hemicellulose and lignin and tested either parallel // or perpendicular ⊥ to the fiber orientation. Cellulose and lignin building blocks are indicated in red. Adapted from Gibson et al.*[10], *with kind permission from The Royal Society (U.K.).*

With local variations in the organization of the building blocks, occurring during the tree's growth, tree and other plants can even optimize and locally tune mechanical properties as a reaction to external load conditions like, for instance, the bending exerted by wind [23]. Structural optimization in trees emerges from design strategies executed at all levels of the hierarchical assembly. As a result of adaptive growth, the macroscopic shape of branches may present oval sections arising from eccentricity, in order to maximize bending stiffness [24]. The porous cellular structure of wood can be considered as a honeycomb structure and provides the high specific stiffness and strength demonstrated by these materials. Here, the tree can increase or decrease the thickness of cell walls and hence modify the relative density of the structure, promoting an increase or decrease, respectively, of the elastic modulus and strength [25], as well as, creating structural gradients minimizing shear stresses and inhomogeneities [19]. Moreover, the tubular and unidirectional porous structure of such assemblies is optimized for water and nutrient transport from the roots to the crown [26], [27].

The role of cellulose emerges at the nanoscale impacting all larger scales of the hierarchical structure. In the cell walls, cellulose fibrils play an important structural function acting as main high strength fibrous reinforcement phase. Optimization of the cell wall mechanical properties relies on the orientation

of such building blocks. By varying the microfibrils angle (MFA) with the cell axis in the different cell wall's layers, trees fine tune locally their mechanical properties, allowing for material adaptation during growth and promoting the strong mechanical anisotropy. Indeed, the longitudinal Young modulus of *Pinus Radiata* S2 secondary cell walls, measured by Cave et al. [28], drops from 45 GPa to 10 GPa when the MFA is increasing from 10° to 40°, respectively. The mechanical anisotropy, arising from cellulose microfibrils alignment in the cell wall, is also one of the factors that contributes in controlling the elastic or plastic deformations of the cells [29]. In cells with only primary cell walls, specific patterns of cellulose microfibril orientations dictate the anisotropic deformation behavior, due to generating an anisotropic response to the hydrostatic increase in volume of the cell, allowing easier deformation in a direction perpendicular than parallel to the fibrils axis [29], [30]. In addition to structural functions and mechanical adaptability, the oriented arrangements of nanocellulose are at the origin of passive hygroscopic movements in plant materials. In dead cells, when properly arranged, oriented cellulose layers can produce passive reversible movements as a function of the relative humidity due to transverse hygroscopic expansion or shrinking. In pine cones, scales are composed of two transversally oriented layers of lignocellulosic fibers that allow opening and release of the seeds when dry [31]. The hierarchical arrangement of specialized cells in *Delosperma nakurense* seed capsules [32] provides opening of a valve when wetted, to release the seeds. Combining the swelling of a layer of primarily cellulose in the hexagonal cells of a keel and a hydration dependent change in curvature in the valve backing, a huge deformation over 150° is obtained.

Finally, at the molecular scale, the optimization of the mechanical properties in hierarchical assemblies utilizes local variations in composition of the matrix, i.e. in the hemicelluloses and lignin content, as well as, in the polymerization of lignin [33]. Lignification of the secondary cell walls is responsible to structurally embed cellulose microfibrils, increasing the wall stiffness and rigidity [10]. The examples mentioned above describe mechanical optimization strategies, as a source of inspiration to produce efficient synthetic composite materials. Especially, those examples point out the role of nanocellulose as main building block of hierarchical assemblies in plants, specifically in trees, and provide models for stimulating and promoting the development of new engineered materials.

2.1.2 Extraction of cellulose nanocrystals from ligno-cellulosic resources

Being part of complex biopolymer composites, ligno-cellulosic feedstock used for CNC extraction generally undergoes pretreatments such as steam explosion [34] or alkaline and bleaching treatments [35], which allow removal of lignin and hemicelluloses and lead to purified cellulose pulp. Isolation and extraction of CNC from the cellulose pulp can then be achieved in several ways.

Acidic hydrolysis represents the most studied and industrially utilized process and includes the use of strong concentrated acids to hydrolyze and esterify cellulose. The most used approach relies on sulfuric acid and creates sulfate esters which promotes dispersion of CNC in aqueous media [36]. However hydrochloric, phosphoric and organic acids can also be employed for the hydrolysis [37]. During the process, the glycosidic bonds of disordered (amorphous) cellulose is attacked by the large concentration of protons, and broken faster than bonds within the crystalline cellulose regions. This results in a shortening of cellulose chains and decreasing of the polymerization degree, which continues until reaching the level-off degree of polymerization (LODP), which marks a strong decrease in the degradation kinetics [38]. When desired, the reaction is hindered by quenching and the CNC can be extracted by centrifugation and dialysis and successively redispersed in water by sonication. The resulting CNC will present different morphologies, degrees of crystallinity and surface chemistry as a function of the source used

for CNC extraction, as well as a function of process parameters (time, temperature) and the type of acid employed during the process [37], [39].

Due to the large quantities of acid waste other routes such as enzymatic hydrolysis, ionic liquid and deep eutectic solvents extraction are currently under investigation and development for industrial scale production [40]. Enzymatic hydrolysis consists in the degradation of the amorphous cellulose regions, of cellulose pulp, by enzymes such as cellulases. Under investigation, this process can be applied directly on pre-swollen wood pulp fibers by adding xylanase to the cellulases mixture of enzymes, in order to simultaneously degrading hemicelluloses and amourphous cellulose [41]. Enzymatic hydrolysis is still limited to low yields, however represent a concrete potential for an eco-friendly production process [40]. In addition, replacement of acids with ionic liquids or deep eutectic solvents may represent an alternative approach, due to the easy reusability of such solvents [42] even if the crystalline content of the obtained CNC is lower than the one of CNC prepared by sulfuric acid hydrolysis.

2.1.3 Properties of cellulose nanocrystals and their applications in composites

CNC present a wide range of interesting physical and chemical properties that render such particles appealing for a large palette of applications in polymer composite materials. At first, with the advantage of being renewable, biocompatible and biodegradable, CNC are very interesting reinforcing particles. Their outstanding mechanical properties, namely Young's moduli ranging from 105 to 220 GPa and tensile strengths as high as 8 GPa [4], [43], [44], coupled with a low density of 1.58 g/cm^3[4], make CNC competitive to well-established synthetic reinforcement fibers. For instance, glass fibers, the most produced (> 4 million tons per year) and employed reinforcing fibers in synthetic polymers, show elastic moduli and strengths spanning from 70 to 90 GPa and from 2 to 4.5 GPa, respectively, with a density around 2.5 g/cm^3 [45]. CNC may also compete with high performance polymer fibers, such as Kevlar® or Carbon fibers that present Young's moduli of 60 – 150 GPa and 200 – 900 GPa, strengths of 1.5 – 2.5 GPa and 2 – 7 GPa, densities of 1.4 and 1.7 – 2.2 g/cm^3, respectively [45], [46]. Consequently, the reinforcing effect of CNC in various polymer matrices has been studied intensively for the production of composites in the last decades. Dispersions of CNC in latex [47], epoxy [48], polyurethanes [49], polylactic acid (PLA) [50] and another wide variety of polymers [51], demonstrated the ability of improving elastic modulus and tensile strength of the final materials, while decreasing elongation at fracture. Such effects arise due to the strong mechanical properties of the CNC as well as the strong intermolecular interactions between particles and the polymer matrix promoting stress transfer [47]. The stress transfer from the polymer to the CNC strongly depends on the quality of the particles' dispersion and will be maximized with the formation of a percolating network of well dispersed particles [52]. Moreover, particle alignment within the composites microstructure may confer anisotropic properties and maximizes the reinforcing effect [53]. However, the great hydrophilicity of CNC limits and hinders their homogeneous dispersion in hydrophobic polymer matrices and leads to the formation of microscale aggregates, hindering the improvement of mechanical properties [54].

With a high surface to volume ratio and an important presence of hydroxyl groups, CNC particles can easily be modified to introduce functional groups allowing modification of their interactions with the environment. Acetylation, silanization and grafting of polymer chains [55] are among the available chemical treatments employed to increase the quality of the dispersion of CNC in hydrophobic matrices, further enhancing composite mechanical properties. For example, grafting of lactic acid on the CNC surfaces allows to obtain PLA-CNC composites with 20 wt % of particle content, reaching a 1.5 fold increase in storage modulus at 23° C and almost a 10 times improvement at 70° C, compared to the neat PLA. Moreover, modifying the surface of CNC and increasing compatibility of the particle with the

polymer matrix produce a decrease of the viscosity of the polymer melt or the suspension [51] promoting a better processability, when compared with unmodified particles.

The addition of pristine CNC in polymers has the direct consequence of increasing the viscosity of the matrix [56]. In addition, the presence of CNC in suspensions promotes nonlinear rheological properties. In particular, CNC have the ability to impart strong shear thinning behaviors to Newtonian fluids. In aqueous suspensions or low viscosity polymer resins with low CNC concentrations, particles are in an isotropic state and do not particularly influence the rheology. However, with an increase in concentration, suspensions present viscoelastic responses to deformation showing shear thinning, arising from the increasing shear induced alignment of the CNC. In concentrated suspensions, CNC form a percolated network, which confers elastic properties to the suspensions at low shear stresses. While increasing the shear stress, the CNC network is disrupted and the CNC particles can nematically align [57]. Thus, a strong decrease of the elastic properties is observed and a transition from solid to liquid like behavior is observed. This transition between states generally depends on concentration, shape and surface charge as well as the ionic strength of the media [58]–[60]. Importantly, the influence of CNC on suspension rheology is of particular interest for this thesis, because it allows the creation of printable inks, i.e. gels processable by DIW, allowing the production of customized self-standing 3D structures. More details about this particular application of CNC are provided in the next section. Nevertheless, other emerging applications of CNC as rheology modifiers are also explored in water based drilling fluids, cement pastes, paper coatings, lubricants, food additives and cosmetics [61].

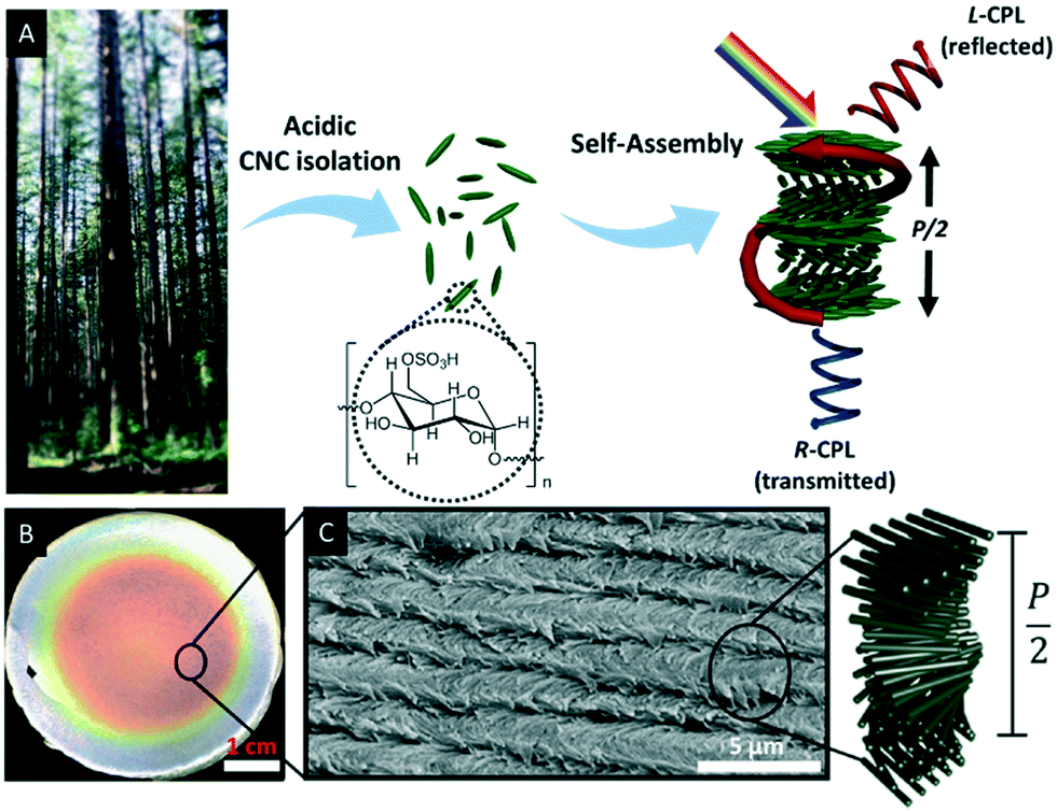

Figure 2.4 From the tree to iridescent colors. A) Isolation from wood and self assembly of CNC in the chiral nematic liquid crystalline structure. The structure is responsible for reflection of left hand circularly polarized light and transmission of right hand circularly polarized light, with wavelength dependent on the pitch dimensions (P/2). B) evaporation induced self-assembled film photograph. C) SEM of the layered structure. Used with permission of the Royal Society of Chemistry, from Giese et al. [70].

The technical interest in CNC for production of synthetic composite materials is not only limited to their mechanical properties and reinforcement effect. CNC are also interesting colloidal lyotropic liquid crystals, which present appealing optical properties for photonic applications. The directionality of the cellulose molecular assembly in CNC confers birefringence to the particles, i.e. CNC display anisotropic refractive indexes. At a wavelength of 589 nm, Iyer et al. [62] measured the refractive indexes of ramie crystalline cellulose I whiskers, being 1.603 and 1.523 for the extraordinary (parallel to the long axis) and ordinary (perpendicular to the long axis) indexes, respectively. As a consequence, composites with anisotropic orientation of CNC display an intrinsic birefringence [63], especially in nematically aligned regions. In addition, when CNC concentration is sufficiently high in aqueous suspensions, these particles self-assemble in a chiral nematic or cholesteric phase (Figure 2.4), presenting a left handed helicoidal structure composed of aligned pseudo layers slightly rotated along the helicoidal axis [64]–[66]. Such arrangements in CNC films obtained by slow evaporation of solvents, where the CNCs are dispersed, are responsible for structural colors and iridescence [67]. The concentration required for the self-assembly and the structural properties which influence the optical response can be controlled by particle aspect ratio, ionic strength, surface charge and polymer grafting [68]. The chiral nematic ordering of CNC can be imparted in composites and hence exploited to obtain mechanical reinforcement and interesting optical properties [69]. Therefore, cellulose nanocrystals and their composites are emerging as potential candidates also for decorative, photonic and counterfeiting applications [68].

The concurrence of their intrinsic physical and chemical properties with their ease of surface modification [71] renders CNC a valuable asset in the development of all kind of composites with added functionality. Owing to their low toxicity, biocompatibility, biodegradability large surface area and hydrophilicity CNC are widely included in hydrogels for biomedical applications. The surface of the particles can be easily adapted to transform CNC in effective drug nanocarriers for drug delivery. The strong hydrophilicity of CNC prevent drying of wounds and their surface may be equipped with antimicrobial functions during wound dressing or tissue engineering applications [72]. Despite the non-conductive behavior of CNC, with the appropriate polymer grafting procedure these particles can become highly conductive and be suitable for energy and electronic devices production [73]. In the last years, a growing interest in the scientific community arose on introducing stimuli responsive functionalities in CNC composites. Humidity triggered reactions can be easily introduced in polymers due to the strong hygroscopic effect of CNC. With swelling and shrinking of two perpendicularly aligned CNC polyN-isopropylacrylamide hydrogels bilayers, Fourmann et al. [74] demonstrated shape morphing behaviors upon wetting and drying cycles. A distinctive color change could be obtained by Lu et. al in CNC-Polyacrylamide films intended as humidity sensors [75]. There, the self-assembled CNC helicoidal structure undergoes swelling, which increases the pitch of the chiral nematic phase, leading to a red shift. Other triggers and functionalities were developed either by modifying the surface of CNC or by engineering suitable matrices. By grafting of polyacrylamide onto CNC surfaces, Zubik et al. [76] produced thermo responsive shrinking hydrogels employed for targeted drug release, demonstrating potential application for wound dressing. The introduction of carboxylate groups and amine groups onto the surface of CNC promotes pH sensitivity to CNC nanocomposite systems, leading to pH dependent swelling [77] or even shape memory effects [78]. Further stimuli responsive functionalizations of CNC composites exist, such as those triggered by light. For instance, mechanically switchable photo-responsiveness of CNC/ethylene oxide/epichlorohydrin composites was achieved either by grafting of benzophenones or coumarins on the CNC surface [79], [80]. However, the main efforts so far have been focused on introducing thermo and pH responsive functionalities while utilizing the CNC's intrinsic hygroscopic behaviors [81] rather than exploiting light as a stimulus. Nevertheless, CNC bear an important potential for the development

of smart and multifunctional "green" composites for high technological applications that requires dynamic reactions to the environment.

2.2 3D printing of cellulosic materials

Inspired by the mechanical designs of wood in trees, but also from other naturally available hierarchical structures such as nacre [8] or bone [9], scientists focused on production techniques of CNC reinforced composites that allows to control orientation of particles and create textured architectures that enhance composite mechanical properties and/or confer other functionalities. Such textured composites can be manufactured by solution casting of self-assembled structures [82], templating approaches [83], [84], shear casting or film drawing [85], [86], electrospinning [87], melt compounding and extrusion [54], or even with alignment induced by strong magnetic fields [88]. However, the obtained macroscopic shapes of the final composites produced in these ways remained often limited to simple 2D geometries, or simple 3D geometries defined by external molds. Differently, the emergence of 3D printing technologies has allowed providing geometrical freedom to the produced composites. Moreover, by adding materials instead of removing it from a monolithic block, 3D printing accounts also for a reduced waste of materials.

Nanocellulose based composites could be processed by stereolithography (SLA) [89], Fused Deposition Modeling (FDM) [90], [91] and DIW [92] in complex architectures. Extrusion based techniques are particularly interesting for the printing of materials with controlled hierarchical structures [93]. As mentioned above, with the shear and extensional stresses during printing, anisotropic particles align along the printing direction and precise local control can be exerted over the particles' orientation. In particular, DIW is a versatile bottom-up platform, virtually allowing to print layer by layer all kind of materials as soon as they display the correct rheological properties [94]. As a consequence, DIW revealed to be the perfect technology for manufacturing nanocellulose based composites due to the gel-like behavior of nanocellulose suspensions, their strong shear thinning and the fast post stress recovery [92] that allow printing 3D self-standing structures. DIW printing of composites based on CNC was not really spread and investigated until 2017 and was mainly limited to manufacturing of low concentration of CNF hydrogels and suspensions (<3wt% solid content) as bio-inks [95]. In 2017, Siqueira et al. [96] demonstrated the 3D printing of relatively high solid content of CNC (10 – 20 wt%) in polyurethanes matrices. There, CNC functioned in a dual role as rheology modifiers, allowing the printing, and as reinforcing agents. The alignment of CNC along the printing directions was observed by polarized optical microscopy and confirmed by 2D WAXS measurements indicating a degree of alignment around 84%. The control over the orientation of CNC resulted in anisotropic tailoring of the composites' mechanical properties, where a 10 fold increase in the Young's modulus was measured in the longitudinal direction, i.e. parallel to the printing direction, while a 8 fold increase was observed in the transverse direction, i.e. perpendicular to the printing direction. This work paved the way for the use of CNC as natural building blocks allowing the production of 3D printed lightweight devices that exhibit tailored mechanical responses, inspired by the hierarchical structures found in wood and other biological composites. Successive efforts, in 3D printing of CNC based composites, led to the fabrication of hydrogel structures suitable as scaffolds with porosity gradients controlled by the printing parameters [97]. Strong and lightweight structures like a hook supporting more than 700 times its own weight could be created exploiting the 3D printing of complex shaped CNC hydrogels [98]. With a first step, DIW conferred local alignment to the CNC while shaping the macroscopic complex shape of the hydrogel. Then, the printed

part underwent an infusion and densification process in order to allow production of composite structures with relatively high CNC volume fractions (27.35 vol%). DIW is hence a very powerful tool for the production of hierarchically structured materials.

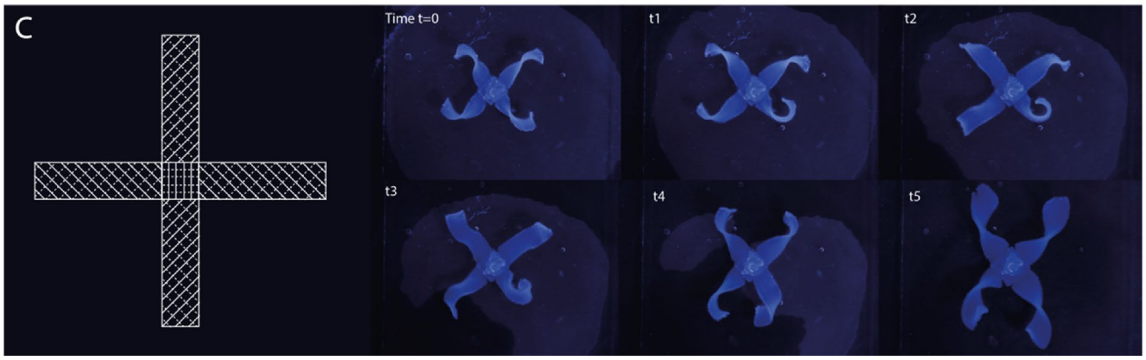

Figure 2.5 3D printed structures of nanocellulose-NIPAM hydrogels with swelling and anisotropic actuation behaviours. C) Combination of two bilayer strips produced by 3D printing of nanocellulose-NIPAM hydrogels (20 wt% CNC) leading to synthetic architectures that twist. On the left is the scheme of the printing pattern (45/135° filling) and on the left side,pictures of the evolution of the anisotropic actuation of the printed structures. Adapted from Fourmann et al. [74].

The complexity of the microstructures obtained by DIW need still to be improved in order to increase the range of physical behaviors and functionalities available in printed structures. So far, CNC are mainly employed in 3D printed devices for their reinforcement effect combined with their intrinsic biocompatibility biodegradability and low toxicity and follows CNF composites and hydrogels as scaffolds for tissue engineering and targeted biomedical applications [99]. Differently, latest developments of 3D printed CNC composites should focus on imparting multifunctionality and stimuli response to the printed device exploiting simultaneously anisotropy and surface state of CNC. Despite the increasing development of CNC smart and stimuli responsive composites, only few examples of materials processable by DIW are present and are still limited to soft hydrogels. Mostly, humidity triggered shape morphing behaviors have been explored. As an example, Fourmann et al. [74] developed antibacterial and shape morphing 3D printed CNC hydrogels (Figure 2.5). The printed material demonstrated reversible bending during cycles of swelling and de-swelling in water. Since DIW conferred the local CNC orientation to the printed layers, the shape morphing movements and directions can be predetermined. Water adsorbs on the CNC, generating a swelling of the hydrogel transversal to the orientation of cellulose nanoparticles.

The possibilities offered by printing CNC composites are currently in their infancy. The ordering and structuring of CNC in composites by DIW, could be exploited to create materials with stronger and tailored mechanical properties while CNC could be functionalized offering a series of different functions or responses to the environment, not yet limited to humidity changes. Thus, there is a need of broadening the quantity of 3D printable renewable CNC based materials as well as the application fields of smart devices reacting to different environmental stimuli.

2.3 Photoresponsive molecular switches and their effects

Photoresponsive polymers are materials that show a change in one of their physical or chemical properties upon irradiation with light. Switches, placed in the polymer are generally the main triggers for the

stimulated responses and can act irreversibly or reversibly on the material properties. Figure 2.6 illustrates some examples of common photoswitches and their phototriggered reactions. Irreversible switches are photolabile molecules, such as o-nitrobenzyl or benzophenones derivatives, that undergo cleavage reactions, producing either solubilization, depolymerization and degradation [100] or, inversely, generation of highly reactive radicals leading to crosslinking and further polymerization [101]. Reversible photoswitches consist of photochromic molecules, such as cinnamates and coumarins, that undergo reversible cycloaddtion reactions, or diarylethenes, spiropyran and azobenzenes, that undergo reversible light-driven isomerization, and generate different material behaviors related to their photostationary states [102]. These molecules can be dispersed in solutions, grafted in side chain positions or surfaces, or being part of a polymer backbone. Depending on their interactions with the immediate environment and its structure, the nanoscale isomerization is amplified to express a wide range of macroscale phototriggered functions as gel-sol transitions, motions, stimulated changes in stiffness, wettability transitions and optical responses [82], [102]–[105]. Amongst these photoresponses, on demand dynamic mechanical properties and motions display particular complementarity with 3D printing technologies, which could allow coupling of geometrical effects with the photoresponses. Consequently, the following reviews the principal strategies employed in the development of materials presenting photostiffening, photosoftening, and motions induced by the shape memory and photomechanical effect as well as the state of the art in the 3D printing of such materials.

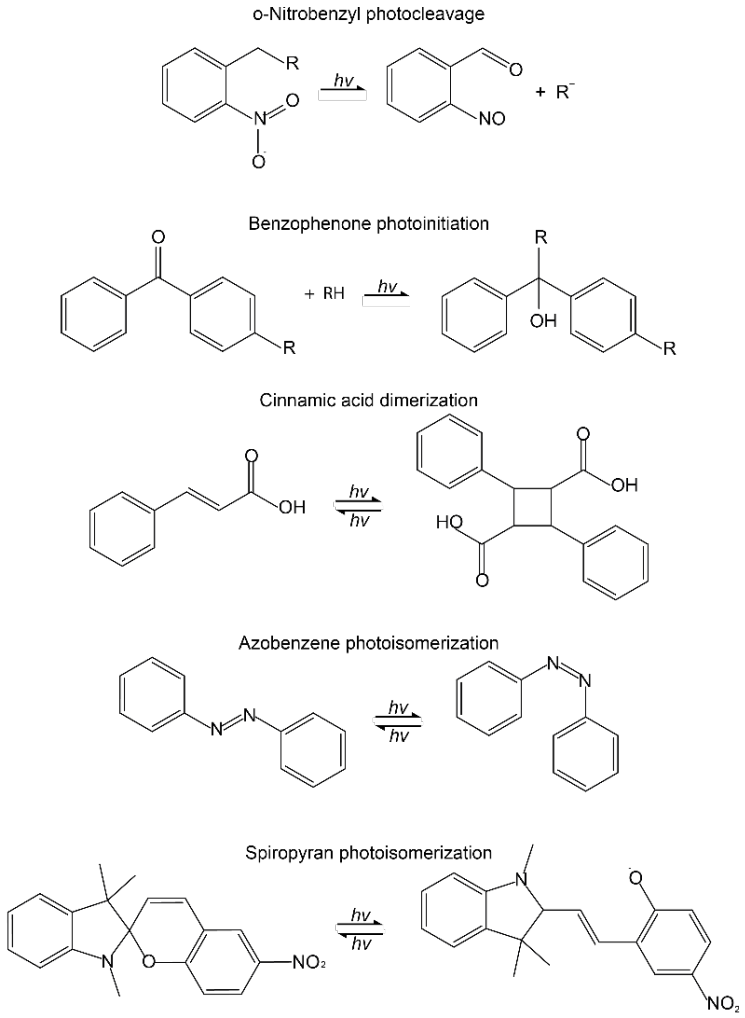

Figure 2.6 Examples of common photoswitches and their light triggered reaction.

2.3.1 Photostiffening and photosoftening

Light triggered mechanical property transformations on demand arise, after illumination, mainly because of irreversible reactions of photoresponsive functional groups. Indeed, the common strategies used to make phototriggered stiffening in polymers is achieved by increasing the density of crosslinks, i.e. increasing the quantity of covalent bonds between the main polymer chains, or by the creation of a secondary interpenetrated network. Photoinitiators as benzophenones, quinones, phosphine oxides and ammonium salts [106] are examples of molecules allowing such behavior. By dissolving the photoreactive species in the appropriate monomer solution, light triggers the creation of radicals (for acrylates) or the generation of acids (for epoxies) and leads to the transformation of a liquid resin into a stiff and solid crosslinked material. Such technology is nowadays widespread for coatings, adhesives, negative photoresists and 3D printing by stereolithography [107]. With the same principle, photoinitiators can be added into solid materials to provide light triggered secondary crosslinking. As mentioned above, Biyani et al. [79] could graft benzophenones to CNC and trigger with light, hydrogen abstraction from the ethylene oxide/epichlorohydrin matrix and thus generating particle/matrix covalent bonds that increased the stiffness of the composite. Lithium phenyl-2,4,6-trimethylbenzoylphosphinate (LAP), a visible light photoinitiator has been dispersed in methacrylated hyaluronic acid soft hydrogels produced by Michael-type addition [108]. When the hydrogels were illuminated with blue light, the unreacted methacrylic groups could then create a secondary network and increase the stiffness on demand.

Strategies promoting reversible photostiffening are currently under development. Replacing irreversible photoinitiators with molecules such as coumarins, that display a reversible photoresponsive [2+2] cycloaddition, allowed the formation of hyaluronic acid-coumarin grafted hydrogels switching on command from a supramolecular assembly to a covalently bonded and stiffer material [109]. With a different approach, photostiffening can be obtained reversibly also by introduction of free liquid crystals in azobenzene liquid crystalline elastomer (LCE) [110]. There, light triggers the isomerization of the azobenzene groups decreasing the solubility of the free liquid crystals. Thus elasto-capillary forces, opposing to the formation of interfacial area, resists against deformation. However, such effect depends strongly on the ratio of free liquid crystals to azobenzene, since below a certain threshold the opposite reaction, photosoftening, emerges.

As for light generated stiffening, photosoftening is a response primarly obtained irreversibly with the introduction of photolabile molecules as o-nitrobenzyl or in the polymer network but also reversibly with dynamic covalent bonds, or isomerizable moieties such as azobenzenes. In the irreversible approaches, the photoswitches are generally introduced in the main chain of the polymer and undergo photolysis leading to chain breakage. Such materials can be considered as photodegradable and find their main application as positive photoresists [111]. As an example, Giebler et al. synthetized epoxy terminates o-nitrobenzyl derivative and produced a thermally cured photodegradable materials [112]. Once illuminated with UV light, photocleavage of the nitrobenzyl group generates a decrease in T_g and hardness of the illuminated regions. Interestingly, the use of cinnamates and coumarins and their reversible photodimerization can be employed for the production of photodegradable materials when the main crosslink of the polymer network consists in the dimer of such molecules. Polyurethanes with grafted end chain coumarins [113] and poly(butylene adipate) diol with cinnamate end chains [114] display reversible phototriggered degradation that has been harvested for intrinsic self-healing. Indeed, such materials can degrade under illumination but can also create further crosslinks with the appropriate wavelength and thus close and heal cracks (Figure 2.7).

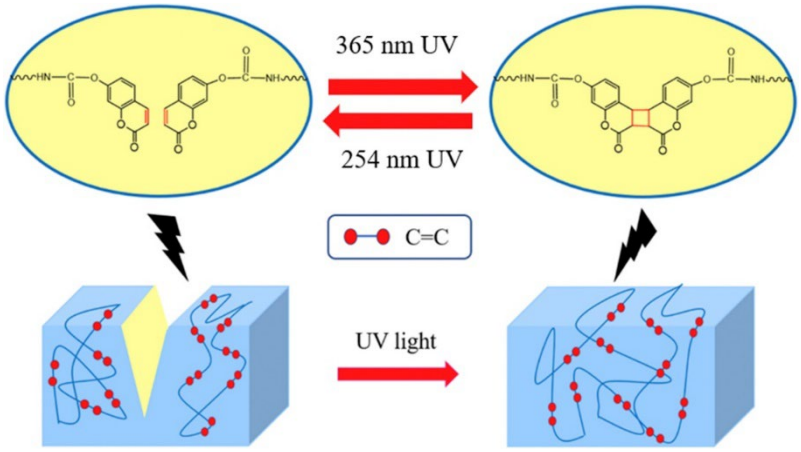

Figure 2.7 Schematic diagram of self-healable polyurethane based on the reversible light triggered cycloaddition of end chain coumarins. Reprinted from Wang et al. [113]*, with permission from Elsevier.*

Finally, reversible photosoftening is widely demonstrated by azobenzene based LCE [115]–[118]. When the photoisomerization of azobenzenes occurs as a fast oscillation between *E* and *Z* states, it triggers an increase in free volume [116], it generates heat [119], and can modify locally the microstructure of the crystalline phases [120]. Each effect contributes to the reversible softening of the crosslinked liquid crystalline material.

2.3.2 Shape memory effect

Separately, photostiffening and photosoftening are stimuli responsive behaviors that tailor the mechanical properties of smart materials on demand. Interestingly, their subsequent implementation is the main strategy generating motion due to shape transformations. Indeed, the incorporation of cinnamate, coumarins and anthracene moieties and their photodimerizetion [121] is at the origin of the main photoresponsive shape memory effect, i.e. the ability of a deformed material to return to its original shape upon illumination. These chromophores have been incorporated as pendant groups in n-butylacrylate (BA), HEMA and ethyleneglycol-1-acrylate-2-CA copolymers [104], polyurethane-PCL-polyL,L-Lactide (PLLA) multiblock copolymers [122] or in PCL [123]. As illustrated in Figure 2.8, each material can be mechanically deformed while illuminated at a wavelength of 365 nm (programming step), which activates the dimerization reaction, creating the secondary network of covalent bonds (photostiffening), which fixes the temporary shape. When illuminated by light with 254 nm wavelength, the chromophores undergo the *reversible reaction* breaking such covalent bonds (photosoftening), leading the materials to the recovery of their original shape and hence a photoactuated movement.

Another approach has been proved efficient in the development of light actuated *shape memory polymers*: the photothermal effect [124]. Indirect switches like metallic particles or carbon derived building blocks are introduced in temperature responsive polymers. The photoresponsive behaviors arise because these fillers are converting the incoming light radiation in thermal power that, in turn, triggers the thermo-responsive behavior of the polymer. As a relevant example for this thesis, CNC grafted with silver nanoparticles were shown to be used as photothermal elements and introduced into thermal shape memory PCL by Toncheva et al.[125]. Such reinforcing particles can generate heat when exposed to IR radiation, due to plasmonic resonance of the silver nanoparticles. The polymer can hence undergo thermo-reversible Diels–Alder reactions that trigger the shape memory [126], [127].

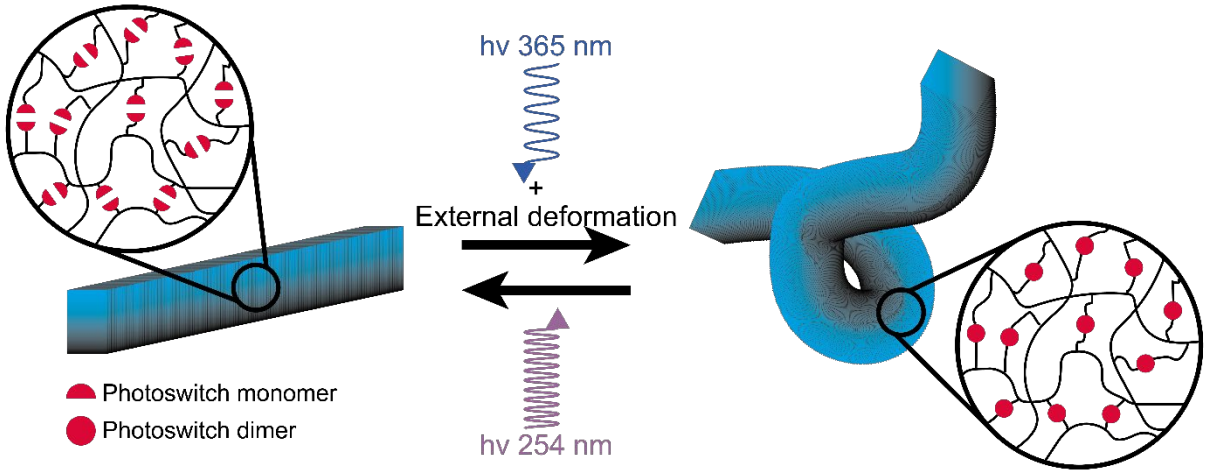

Figure 2.8 *Photoresponsive shape memory effect. From an initial shape the material is deformed and illuminated at the appropriate wavelength, which activate dimerization of photoswitches in order to fix a custom shape. Once illuminated at the second wavelength the temporary shape is released when the reverse isomerization reaction takes place and the initial shape recovered.*

2.3.3 Photomechanical effect

Direct transformation of light energy in movements is defined as the photomechanical effect. Materials demonstrating this behavior consist in a different class of photoresponsive materials called *shape-changing polymers*. These materials can actively undergo shape transformations upon illumination without requiring a programming step, i.e. external mechanical deformation. Thus, such photomechanical reactions being fully reversible, make *shape changing* materials potential candidates for the production of artificial muscles, soft robots and a large range of actuators or light fueled engines [128]–[130].

Dynamic shape changes arise from polymeric photoswitches undergoing reversible photoisomerization. Azobenzenes (Figure 2.6), undergoing *trans-cis* photoisomerization, are the most used in the field. Generally, these moieties strongly absorb in the UV region leading to the metastable *cis* state, while the stable *trans* form is recovered by both visible light absorption or thermal relaxation. The possibility to modify wavelengths of excitation and *cis* form lifetimes by substitution in para or ortho position of both aromatic rings led to the creation of a wide range of azobenzene derivatives [131], [132]. The conformational *trans-cis* change generates, in the azobenzene unit, a contraction of 3.5 Å [133] that can be harnessed and amplified to the macroscale (mm).

The straight-forward strategy for the production of a photomechanical polymer consists in the introduction of such molecules in a polymer network or by developing pendant side chain or main chain azopolymers. However, control and transfer of the nanoscale motion to the macroscale requires conferring order to the photoswitches, or their direct environment [134]. Indeed, azobenzenes present molecular anisotropy and can act as a liquid crystal mesogens due to their rigidity in the *trans* form, thus conferring a directionality to their pulling effect [135]. Therefore, in amorphous or isotropic polymer structures only small isotropic volume contractions were observed. In particular, nylon fibers dyed with an azobenzene derivative could undergo only a 0.1% volume contraction due to the isotropic orientation of the dyes [136]. A similar effect could be obtained by incorporating azobenzene units as crosslinks in poly(ethyl acrylate) networks, leading to a 0.2 % reversible volume contraction [133]. Increase in the azobenzene quantity showed to enhance volume contraction in crosslinked polymers, reaching a maximum value of 1 % [137]. Differently, when azobenzene moieties are nematically aligned (in azopoly-

mer) or incorporated in liquid crystalline elastomer (LCE) with nematically aligned liquid crystal mesogens the material's contraction becomes anisotropic and can reach values as high as 30 % [138] in the direction of the liquid crystal (LC) director. Here, the contraction of azobenzenes is amplified and their conformational changes trigger the nematic to isotropic phase transition of the LC mesogens [119], [139].

Two main manufacturing processes have been extensively used for the production of ordered LCE. Finkelmann et al. [140] demonstrated the first example of aligned photoresponsive LCE having a 20 % uniaxial contraction. A two-stage cross-linking process was applied to a side chain LC polysiloxane with azobenzene crosslinks. The first polymerization allows the formation of the main network, while the second polymerization is carried out during imposed tension to fix a strain induced nematic alignment. More complex LC arrangements are produced by introducing monomer solutions at nematic temperatures in conventional LC alignment cells exploiting rubbed alignment layers [130], [141]. There the mixture is photopolymerized to fix the nematic order.

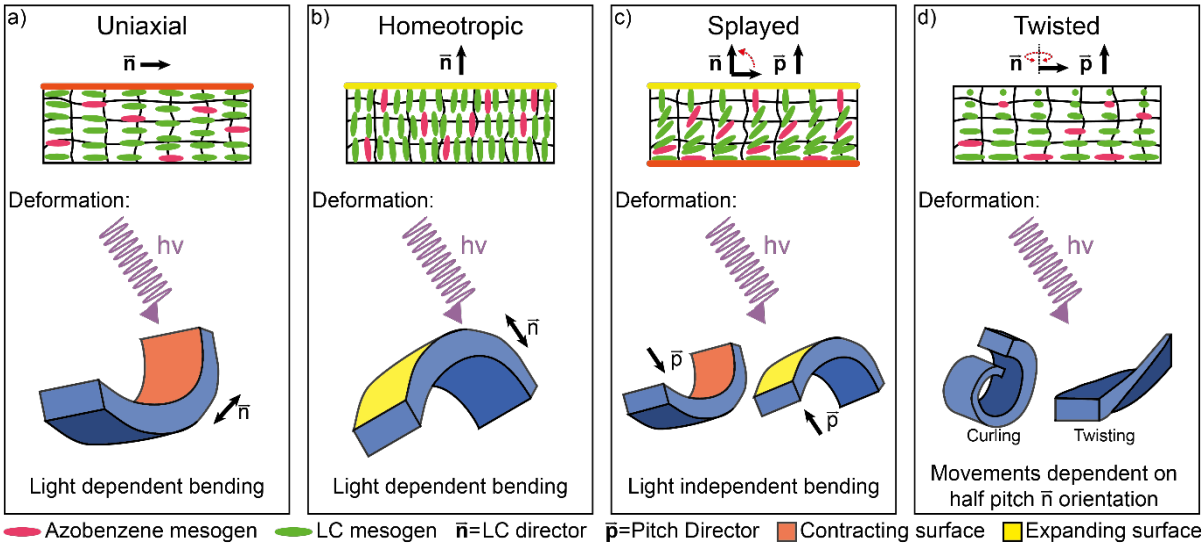

Figure 2.9 *Influence of LC mesogen nematic arrangements on the movements of photoresponsive LCE. Uniaxial nematic produce surface contraction where illuminated and successive bending (a). Homeotropic LC arrangements instead produce expansion of the illuminated region followed by a reverse bending (b). Splayed nematic LC arrangements promotes light independent bending depending on the splay director $\vec{p}$ direction (c). Twisted nematic present curling or twisting as movements that can be programmed by defining the LC director $\vec{n}$ orientation at half twist (45°) and by defining the right or left hand twist of the LC mesogens.*

The control over the LC director and type of phase in photoresponsive LCE is an important parameter that programs the out of plane or 3D motions of LCE films [142]–[144]. Generally, due to the high extinction coefficient of azobenzene molecules, the triggering light is absorbed through the thickness of the film. Thus, a gradient of activated switches is present: from a strongly activated illuminated surface of azobenzene based LCE films to a non-activated dark surface (Figure 2.9). In uniaxial aligned nematic LC arrangements, a contraction gradient translates to an out-of plane bending in the direction of the light source, while in uniaxial homeotropic LC phases the bending occurs in the other direction due to expansion gradients. Films with more complex nematic LC arrangements display behaviors that are more complex. A bending independent from the light direction is observed with splayed nematic phases [143], while curling and twisting arise from twisted nematic LC phases [145]. Additionally, light as a trigger offers the possibility to control movements of azobenzene-based LCE by either affecting its properties

or its spatial structure. Controlling the direction of linearly polarized light shining on a polydomain azopolymer allows to control the direction of the film's bending [146] due to the selective light absorption of azobenzenes aligned with the polarization. Instead, structuring the illumination spatially and temporally allows to create locomotion and to reproduce worm-like [138] or caterpillar-like [147] movements.

2.4 Photoresponsive CNC composites

Besides research on stimuli responsive CNC based composites triggered by humidity and temperature changes, the use of CNC nanocomposites that present photoresponsive behaviors has been also explored in 2D-shaped materials. Owning to the influence of CNC on mechanical properties of the composites, the photostiffening has been readily explored in CNC composites to improve the mechanical properties of such materials [79], [80], [148]. To obtain photostiffening, the renewable nanoparticles have been functionalized with indirect or direct photoactive elements, and used as active light stimulated elements. Fox et al. [148] achieved photostiffening behaviors in poly(vinylacetate)-CNC composites by functionalizing the nanocellulose particles' surfaces with allyl moieties and imbibing the material with a photoinitiator and a tetrathiol crosslinker, in a successive step. When illuminated with UV, the photoinitiator acts as direct photoactive element and triggers the reaction of allyl-CNC with the tetrathiol, creating a covalently bonded network of the reinforcing particles. This results in the stiffening of the polymer composites. In particular, this photoresponsive effect was used to hinder the plasticizing effect of water on the composite films when immersed in such solvent. Poly(vinylacetate) composites with 20 wt% of allyl CNC, presented the ability to increase their wet elastic modulus from ca. 60 to ca. 300 MPa after irradiation with UV light for 20 minutes. As mentioned in the previous sections, CNC-based composites demonstrating photostiffening were also produced by Biyani et al. by functionalizing CNC either with photoswitches as coumarin [80] or benzophenones [79]. Coumarin modified CNC react to UV light by undergoing dimerization of the coumarin groups, forming a covalently bonded network of CNC particles inside the composite. A rubbery ethylene oxide–epichlorohydrin copolymer matrix presenting 10 wt% of coumarin modified CNC presents a photoactivated increase of its tensile storage modulus at 25°C from 199 to 291 MPa in the dry state, as well as from 38 to 80 MPa in the wet state. Differently, benzophenone modified CNC allow to create both covalent bonds between the CNC and in-between CNC and the polymer matrix. This is achieved by triggering benzophenone's hydrogen abstraction with UV light. Light can hence trigger the increase of tensile storage modulus in composites, of an ethylene oxide–epichlorohydrin copolymer containing 20 wt% of benzophenone modified CNC, from 407 to 508 MPa at 25°C in the dry state.

The photostiffening observed in CNC composites has been used mainly to hinder the negative influence of water on the mechanical properties of the materials. However, photostiffening also offers the possibility to obtain multiple functions originating from the orthogonal stimulation of light and water. For instance, the approach of Fox et al. [148] allows to locally control the crosslinking density with illumination time, and hence to create mechanical gradients. Combining such gradients with the plasticizing effect of water confers to the wet poly(vinylacetate)-allyl CNC composites enhanced mechanical contrast across the length of the film. This would allow adapting the stiffness of the composites in order to interface soft biological tissues with stiff therapeutic interventions. In the example of benzophenone modified CNC composites of Biyani et al. [79], the strong hygroscopic behavior of CNC can be combined with local photostiffening to modify the behavior of water triggered shape memory effects of the materials. Swelling of the benzophenone modified CNC composites in distilled water, allows deforming

the material in a temporary shape that is fixed upon drying. By selectively photostiffening defined regions of the deformed material, hindering the shape recovery of these regions can be achieved, resulting in modification of the composite movement, when the shape memory effect is triggered by wetting the samples. Furthermore, it has recently been shown that the photostiffening of CNC composites can help to improve and control water barrier properties. Vijay et al. [149] demonstrated that the functionalization of CNC with coumarin moieties allows to create composite films presenting an increase the water barrier performances as the degree of crosslinks arising from coumarin dimerization increases due to UV illumination.

Besides photostiffening, self-healing and shape memory functions could be conferred to CNC composites by modifying either the polymer matrix and/or the reinforcing particles with photothermal agents that would trigger temperature dependent responses of the surrounding polymer. Biyani et al. [150] produced a supramolecular CNC composite by decorating a telechelic poly(ethylene-*co*-butylene) matrix and CNC with hydrogen-bonding ureidopyrimidone. When these materials are illuminated with light at 282 nm of wavelength, the ureidopyrimidone binding motifs generate heat causing the disengagement of their hydrogen-bonding interactions. This results in a strong softening of the composites due to the decrease of molecular weight and viscosity of the polymer, which allows to fill defects and close interfaces. In particular, defects like scratches and cuts that were deliberately introduced in the materials, could be optically healed efficiently, especially at high solid content of CNC (15 and 20 wt%). A similar result could be obtained by end functionalizing telechelic poly(ethylene-*co*-butylene) with 2,6-bis(1′-methylbenzimidazolyl) pyridine (Mebip) ligands and $Zn(NTf_2)_2$ [151]. In this work, CNC were introduced into the matrix to reinforce the self-healing polymer matrix. It was demonstrated that CNC can bind to the Zn^{2+} used to assemble the metallosupramolecular polymer fulfilling their reinforcement effect without modifying the morphology of the polymer nor the optical self-healing. When illuminated, the metal-ligand absorbs UV light, dissociating and making the polymer liquefy. In this way, defects can be filled and as soon as the irradiation stops, the material comes back to its solid form and recovers its mechanical properties. With a similar principle, shape memory of CNC composites could be generated as already mentioned. By grafting silver nanoparticles onto surfaces of CNC, Toncheva et al. [125] produced a PCL-CNC composite that demonstrates shape memory effect when illuminated with IR radiation. The silver nanoparticles modified CNC convert the incoming radiation into heat due to their plasmonic properties, triggering the thermo-responsive reversible Diels-Adler reactions that release the fixed temporary shape of the materials.

The development of CNC composites with various photoresponses is still progressing. Liu et al. [152] formed composite films grafting poly{6-[4-(4-methoxyphenylazo) phenoxy]hexyl methacrylate} onto CNC. The azobenzene group being part of the polymer graft allows the material to change color during UV illumination due to the *trans-cis* photoisomerization of the azobenzene. However, further responses of this material, as the typical photomechanical effect associated with the azobenzene photoisomerization, were not investigated.

2.5 3D printing of photoresponsive materials

Conventional manufacturing techniques limited the production of stimuli responsive materials to one- or two-dimensional simple shapes. Complex assembly steps would allow the development of intricate 3D geometries. Differently, 3D printing technologies allows to overcome such drawbacks. The manufacture of complex shaped devices in a single additive step offers easy, fast and reliable ways to produce lightweight smart devices. Since the first demonstration of 3D printed thermo-responsive shape memory

polymers in 2014 [148], a large variety of stimuli-responsive materials and 3D printing technologies were investigated. However, the majority of the works reported so far are mainly focused on the development of thermo-responsive shape memory materials and devices [149]. Common examples are the thermo-responsive stents printed by Zarek et al. [150] manufactured in methacrylated polycaprolactone (M-PCL) by SLA printing. By Fused Deposition Modeling (FDM) Yang et al. [151] shaped a commercially available thermoplastic polyurethane (PU) elastomer in grippers which closed in function of the temperature and were able to lift small non uniform objects like pens.

The 3D printing of photo-responsive devices has also been investigated and focused mainly on shape memory materials or shape-changing materials (Figure 2.10). However, due to the extensive research carried out on thermo-responsive 3D printed materials, the commonly employed approach is based on the photo-thermal effect [149], [155]. Shape memory structures could be activated by NIR or IR irradiation by incorporating photoheating elements. FDM printing of a PU embedding carbon black nanocomposite could be achieved for the production of cubic structures [152] unfolding during illumination, or poly(lactic-co-glycolic) (PLGA) loaded with gold nanoparticles could be printed as shell for drug release capsules [156]. Moreover, with the advantage of programming the LCE molecular order along printing directions [157], [158], the recent DIW of LCE further allowed the printing of photothermally activated shape-changing materials. For instance, Ambulo et al.[159] produced an acrylate-terminated LCE embedding eutectic Ga-In liquid metal droplets. Such a material can convert both electric current (joule effect) or NIR irradiation (photothermal effect) in heat, which triggers contractions and bending of the printed films.

Despite these investigations, the 3D printing of materials with direct photoresponsive and photochemical effects is a very recent development. First efforts were made by Roppolo et al. in 2017 [115]. They created photo-responsive microcantilevers with an SLA printer by incorporating azobenzene dyes in the polymer bath to act both as resolution enhancers and photoswitching elements. The printed parts showed photo-tuneable Young's modulus, however only slight light-induced volume changes were observed. Indeed, SLA printing did not allow for controlling the orientation of LC phases as required to obtain directional photo-induced movements [115]. Anisotropic contractions, out-of-plane bending and movements have been achieved with the printing of LCE by DIW, which, as mentioned above, allows control over the molecular order of the LC phase. Hagaman et al. [160] created bilayer actuators by printing azobenzene side chains polysiloxanes on a polyimide film. The final actuators were able to carry out light triggered bending independently from the light direction. Ceamanos et al. [153] created an LCE embedding azobenzenes in the main chain as part of the polymer backbone. By printing at 60°C and successively curing the ink for locking the LC phase (aligned to the printing direction) they conferred both films with phototriggered bending movements and muscle-like contractions, which generated up to 12 J/kg of specific work. As for previously developed thermo-responsive LCE [157], more complex deformations like a 2D disc evolving into a 3D cone could be demonstrated by Lu et al. [154] for 3D printed phototriggered Braille-like actuators. Interestingly, the authors created an LCE comprising acrylated crosslinked LC mesogens, azobenzene units, UPy and *Diels-Adler* adducts that allows the light actuation to occur while being fixed by supramolecular interactions and reconfigurable crosslinks. Tackling hence the challenge of *cis-trans* isomerization relaxation of the azobenzene. As the process is fully reversible, the initial shape of the actuator could be recovered by heating the printed parts at 65°C.

Only few examples of 3D printable photoresponsive materials are available nowadays. Increasing the number of these materials would contribute to further advance the field and to widen achievable light triggered functionalities. As a matter of fact, new materials with the potential to lead to more complex shapes and shape deformations, as well as, the potential to demonstrate adaptable chemical and mechanical properties are required in order to exploit fully the potential of non-contact light actuation.

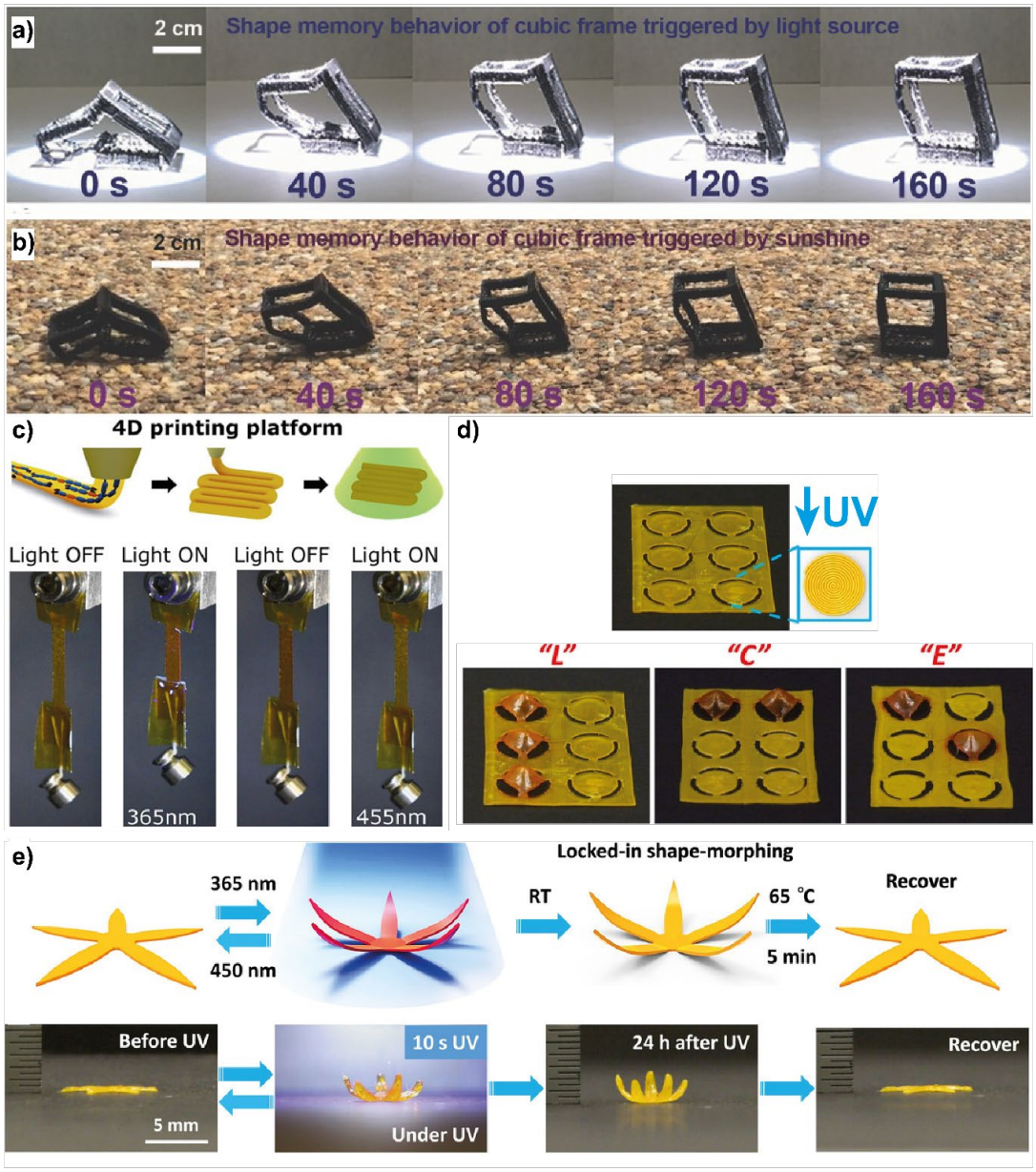

Figure 2.10 *Examples of photoresponsive 3D printed materials. a) and b) Unfolding cube under UV light and sunlight respectively, adapted from Yang et al.* [152], *with permission from John Wiley and Sons. Muscle like photoinduced contraction (c) adapted from Ceamanos et al.* [153]. *Braille-like actuators responding to UV and locking their actuated state (d). Principle of photoactuation of a flower like device and its recovery either with blu light or by heating. d) and e) adapted from Ware et al.* [154], *with permission from John Wiley and Sons*

2.6 References

[1] D. Klemm, B. Heublein, H. P. Fink, and A. Bohn, "Cellulose: Fascinating biopolymer and sustainable raw material," *Angew. Chemie - Int. Ed.*, vol. 44, no. 22, pp. 3358–3393, 2005, doi: 10.1002/anie.200460587.

[2] J. George and S. N. Sabapathi, "Cellulose nanocrystals: Synthesis, functional properties, and applications," *Nanotechnol. Sci. Appl.*, vol. 8, pp. 45–54, Nov. 2015, doi: 10.2147/NSA.S64386.

[3] R. A. Shanks, "Chemistry and structure of cellulosic fibres as reinforcements in natural fibre composites," in *Natural Fibre Composites: Materials, Processes and Applications*, Elsevier Inc., 2013, pp. 66–83.

[4] R. J. Moon, A. Martini, J. Nairn, J. Simonsen, and J. Youngblood, "Cellulose nanomaterials review: Structure, properties and nanocomposites," *Chemical Society Reviews*, vol. 40, no. 7. The Royal Society of Chemistry, pp. 3941–3994, 20-Jul-2011, doi: 10.1039/c0cs00108b.

[5] V. Kumar *et al.*, "Comparison of nano- and microfibrillated cellulose films," *Cellulose*, 2014, doi: 10.1007/s10570-014-0357-5.

[6] A. Dufresne, "Nanocellulose: Potential Reinforcement in Composites," .

[7] P. Phanthong, P. Reubroycharoen, X. Hao, G. Xu, A. Abudula, and G. Guan, "Nanocellulose: Extraction and application," *Carbon Resour. Convers.*, vol. 1, no. 1, pp. 32–43, Apr. 2018, doi: 10.1016/j.crcon.2018.05.004.

[8] F. Barthelat, H. Tang, P. D. Zavattieri, C. M. Li, and H. D. Espinosa, "On the mechanics of mother-of-pearl: A key feature in the material hierarchical structure," *J. Mech. Phys. Solids*, vol. 55, no. 2, pp. 306–337, 2007, doi: 10.1016/j.jmps.2006.07.007.

[9] Y. Liu, D. Luo, and T. Wang, "Hierarchical Structures of Bone and Bioinspired Bone Tissue Engineering," *Small*, vol. 12, no. 34, pp. 4611–4632, Sep. 2016, doi: 10.1002/smll.201600626.

[10] L. J. Gibson, "The hierarchical structure and mechanics of plant materials," *Journal of the Royal Society Interface*, vol. 9, no. 76. Royal Society, pp. 2749–2766, 07-Nov-2012, doi: 10.1098/rsif.2012.0341.

[11] A. Dufresne, "Nanocellulose: From Nature to High Performance Tailored Materials - Alain Dufresne - Google Books," *Library of Congress Cataloging*, 2012. https://books.google.com.my/books?hl=en&lr=&id=vElADwAAQBAJ&oi=fnd&pg=PR7&dq=nanocellulose+and+swelling&ots=E7vrjw9rtt&sig=Nbs5tImQtL6M3KP8WBeP3HOml4g&redir_esc=y#v=onepage&q=nanocellulose and swelling&f=false (accessed Jun. 10, 2020).

[12] S. J. Eichhorn *et al.*, "Current international research into cellulosic fibres and composites," *Journal of Materials Science*, vol. 36, no. 9. Springer, pp. 2107–2131, 01-May-2001, doi: 10.1023/A:1017512029696.

[13] D. J. Cosgrove, "Growth of the plant cell wall," *Nat. Rev. Mol. Cell Biol.*, vol. 6, no. 11, pp. 850–861, Nov. 2005, doi: 10.1038/nrm1746.

[14] A. M. C. Emons, H. Höfte, and B. M. Mulder, "Microtubules and cellulose microfibrils: how intimate is their relationship?," *Trends in Plant Science*, vol. 12, no. 7. Elsevier Current Trends, pp. 279–281, 01-Jul-2007, doi: 10.1016/j.tplants.2007.06.002.

[15] A. R. Paredez, C. R. Somerville, and D. W. Ehrhardt, "Visualization of cellulose synthase demonstrates functional association with microtubules," *Science (80-.).*, vol. 312, no. 5779, pp. 1491–1495, Jun. 2006, doi: 10.1126/science.1126551.

[16] J. Fahlén and L. Salmén, "Cross-sectional structure of the secondary wall of wood fibers as affected by processing," *J. Mater. Sci.*, vol. 38, no. 1, pp. 119–126, 2003, doi: 10.1023/A:1021174118468.

[17] M. Mitov, "Cholesteric liquid crystals in living matter," *Soft Matter*, vol. 13, no. 23. Royal Society of Chemistry, pp. 4176–4209, 14-Jun-2017, doi: 10.1039/c7sm00384f.

[18] C. Plomion, G. Leprovost, and A. Stokes, "Wood formation in trees," *Plant Physiology*, vol. 127, no. 4. American Society of Plant Biologists, pp. 1513–1523, 2001, doi: 10.1104/pp.010816.

[19] T. Speck and I. Burgert, "Plant Stems: Functional Design and Mechanics," *Annu. Rev. Mater. Res.*, vol. 41, no. 1, pp. 169–193, Aug. 2011, doi: 10.1146/annurev-matsci-062910-100425.

[20] M. N. Belgacem and A. Gandini, *Monomers, Polymers and Composites from Renewable Resources*. 2008.

[21] C. Mattheck and K. Bethge, "The structural optimization of trees," *Naturwissenschaften*, vol. 85, no. 1. Springer, pp. 1–10, 02-Mar-1998, doi: 10.1007/s001140050443.

[22] L. A. Berglund and I. Burgert, "Bioinspired Wood Nanotechnology for Functional Materials," *Adv. Mater.*, vol. 30, no. 19, p. 1704285, May 2018, doi: 10.1002/adma.201704285.

[23] C. Mattheck and H. Kubler, *Kubler Wood - The Internal Optimization of Trees*, Second. Springer, 1995.

[24] C. Mattheck and I. Tesari, "The mechanical self-optimisation of trees," 2004. Accessed: 24-Jan-2022. [Online]. Available: www.witpress.com,.

[25] L. J. Gibson and M. F. Ashby, *Cellular solids: Structure & properties*, vol. 9, no. 2. Oxford: Pergamon Press, 1989.
[26] J. S. Sperry, U. G. Hacke, and J. Pittermann, "Size and function in conifer tracheids and angiosperm vessels," *Am. J. Bot.*, vol. 93, no. 10, pp. 1490–1500, Oct. 2006, doi: 10.3732/ajb.93.10.1490.
[27] K. A. McCulloh, J. S. Sperry, and F. R. Adler, "Water transport in plants obeys Murray's law," *Nature*, vol. 421, no. 6926, pp. 939–942, Feb. 2003, doi: 10.1038/nature01444.
[28] I. D. Cave, "The longitudinal Young's modulus of Pinus radiata," *Wood Sci. Technol.*, vol. 3, no. 1, pp. 40–48, Mar. 1969, doi: 10.1007/BF00349983.
[29] T. I. Baskin, "Anisotropic expansion of the plant cell wall," *Annual Review of Cell and Developmental Biology*, vol. 21. pp. 203–222, 2005, doi: 10.1146/annurev.cellbio.20.082503.103053.
[30] I. Burgert and J. W. C. Dunlop, "Micromechanics of Cell Walls," Springer, Berlin, Heidelberg, 2011, pp. 27–52.
[31] C. Dawson, J. F. V. Vincent, and A. M. Rocca, "How pine cones open," *Nature*, vol. 390, no. 6661. Nature Publishing Group, p. 668, 1997, doi: 10.1038/37745.
[32] M. J. Harrington *et al.*, "Origami-like unfolding of hydro-actuated ice plant seed capsules," *Nat. Commun.*, vol. 2, no. 1, pp. 1–7, Jun. 2011, doi: 10.1038/ncomms1336.
[33] W. Boerjan, J. Ralph, and M. Baucher, "Lignin Biosynthesis," *Annual Review of Plant Biology*, vol. 54. pp. 519–546, 2003, doi: 10.1146/annurev.arplant.54.031902.134938.
[34] I. Hongrattanavichit and D. Aht-Ong, "Nanofibrillation and characterization of sugarcane bagasse agro-waste using water-based steam explosion and high-pressure homogenization," *J. Clean. Prod.*, vol. 277, p. 123471, Dec. 2020, doi: 10.1016/j.jclepro.2020.123471.
[35] E. Pinto *et al.*, "Cellulose processing from biomass and its derivatization into carboxymethylcellulose: A review," *Sci. African*, vol. 15, p. e01078, Mar. 2022, doi: 10.1016/j.sciaf.2021.e01078.
[36] D. Trache *et al.*, "Nanocellulose: From Fundamentals to Advanced Applications," *Frontiers in Chemistry*, vol. 8. Frontiers Media S.A., p. 392, 06-May-2020, doi: 10.3389/fchem.2020.00392.
[37] O. M. Vanderfleet and E. D. Cranston, "Production routes to tailor the performance of cellulose nanocrystals," *Nature Reviews Materials*, vol. 6, no. 2. Nature Research, pp. 124–144, 01-Feb-2021, doi: 10.1038/s41578-020-00239-y.
[38] O. A. Battista, S. Coppick, J. A. Howsmon, F. F. Morehead, and W. A. Sisson, "Level-Off Degree of Polymerization," *Ind. Eng. Chem.*, vol. 48, no. 2, pp. 333–335, Feb. 1956, doi: 10.1021/ie50554a046.
[39] L. Chen, Q. Wang, K. Hirth, C. Baez, U. P. Agarwal, and J. Y. Zhu, "Tailoring the yield and characteristics of wood cellulose nanocrystals (CNC) using concentrated acid hydrolysis," *Cellulose*, vol. 22, no. 3, pp. 1753–1762, Jun. 2015, doi: 10.1007/s10570-015-0615-1.
[40] M. Raza and B. Abu-Jdayil, "Cellulose nanocrystals from lignocellulosic feedstock: a review of production technology and surface chemistry modification," *Cellulose*, vol. 2019, no. 1–9, p. 4751827, Jan. 2022, doi: 10.1007/s10570-021-04371-y.
[41] X. Tong, W. Shen, X. Chen, M. Jia, and J. Roux, "Preparation and mechanism analysis of morphology-controlled cellulose nanocrystals via compound enzymatic hydrolysis of eucalyptus pulp," *J. Appl. Polym. Sci.*, vol. 137, no. 9, p. 48407, Mar. 2020, doi: 10.1002/app.48407.
[42] H. Abushammala, I. Krossing, and M. P. Laborie, "Ionic liquid-mediated technology to produce cellulose nanocrystals directly from wood," *Carbohydr. Polym.*, vol. 134, pp. 609–616, Aug. 2015, doi: 10.1016/j.carbpol.2015.07.079.
[43] S. Iwamoto, W. Kai, A. Isogai, and T. Iwata, "Elastic modulus of single cellulose microfibrils from tunicate measured by atomic force microscopy," *Biomacromolecules*, vol. 10, no. 9, pp. 2571–2576, Sep. 2009, doi: 10.1021/bm900520n.
[44] A. Šturcová, G. R. Davies, and S. J. Eichhorn, "Elastic modulus and stress-transfer properties of tunicate cellulose whiskers," *Biomacromolecules*, vol. 6, no. 2, pp. 1055–1061, Mar. 2005, doi: 10.1021/bm049291k.
[45] D. Pico and W. Steinmann, "Synthetic Fibres for Composite Applications," Springer, Singapore, 2016, pp. 135–170.
[46] M. Minus and S. Kumar, "The Processing, Properties, and Structure of Carbon Fibers:"
[47] V. Favier, G. R. Canova, J. Y. Cavaillé, H. Chanzy, A. Dufresne, and C. Gauthier, "Nanocomposite materials from latex and cellulose whiskers," *Polym. Adv. Technol.*, vol. 6, no. 5, pp. 351–355, May 1995, doi: 10.1002/pat.1995.220060514.

[48] S. Xu, N. Girouard, G. Schueneman, M. L. Shofner, and J. C. Meredith, "Mechanical and thermal properties of waterborne epoxy composites containing cellulose nanocrystals," *Polymer (Guildf).*, vol. 54, no. 24, pp. 6589–6598, Nov. 2013, doi: 10.1016/j.polymer.2013.10.011.

[49] A. Santamaria-Echart, L. Ugarte, C. García-Astrain, A. Arbelaiz, M. A. Corcuera, and A. Eceiza, "Cellulose nanocrystals reinforced environmentally-friendly waterborne polyurethane nanocomposites," *Carbohydr. Polym.*, vol. 151, pp. 1203–1209, Oct. 2016, doi: 10.1016/j.carbpol.2016.06.069.

[50] S. Spinella *et al.*, "Modification of cellulose nanocrystals with lactic acid for direct melt blending with PLA," in *AIP Conference Proceedings*, 2015, vol. 1664, no. 1, p. 070019, doi: 10.1063/1.4918454.

[51] J. Shojaeiarani, D. S. Bajwa, and S. Chanda, "Cellulose nanocrystal based composites: A review," *Composites Part C: Open Access*, vol. 5. Elsevier B.V., p. 100164, 01-Jul-2021, doi: 10.1016/j.jcomc.2021.100164.

[52] Y. Chen, L. Gan, J. Huang, and A. Dufresne, "Reinforcing Mechanism of Cellulose Nanocrystals in Nanocomposites," in *Nanocellulose*, Wiley, 2019, pp. 201–249.

[53] M. Shishehbor, H. Son, M. Nuruddin, J. P. Youngblood, C. Davis, and P. D. Zavattieri, "Influence of alignment and microstructure features on the mechanical properties and failure mechanisms of cellulose nanocrystals (CNC) films," *J. Mech. Behav. Biomed. Mater.*, vol. 118, p. 104399, Jun. 2021, doi: 10.1016/j.jmbbm.2021.104399.

[54] A. P. Mathew, A. Chakraborty, K. Oksman, and M. Sain, "The structure and mechanical properties of cellulose nanocomposites prepared by twin screw extrusion," in *ACS Symposium Series*, 2006, vol. 938, pp. 114–131, doi: 10.1021/bk-2006-0938.ch009.

[55] A. Dufresne, "Chemical modification of nanocellulose," in *Nanocellulose*, 2012, pp. 147–192.

[56] Y. Wang *et al.*, "Rheology of the cellulose nanocrystals filled poly(ε-caprolactone) biocomposites," *Polymer (Guildf).*, vol. 140, pp. 167–178, Mar. 2018, doi: 10.1016/j.polymer.2018.02.050.

[57] M. K. Hausmann *et al.*, "Dynamics of Cellulose Nanocrystal Alignment," *ACS Nano*, vol. 12, pp. 6926–6937, 2018, doi: 10.1021/acsnano.8b02366.

[58] S. Shafiei-Sabet, W. Y. Hamad, and S. G. Hatzikiriakos, "Rheology of nanocrystalline cellulose aqueous suspensions," *Langmuir*, vol. 28, no. 49, pp. 17124–17133, Dec. 2012, doi: 10.1021/la303380v.

[59] C. Qiao, G. Chen, J. Zhang, and J. Yao, "Structure and rheological properties of cellulose nanocrystals suspension," *Food Hydrocoll.*, vol. 55, pp. 19–25, Apr. 2016, doi: 10.1016/j.foodhyd.2015.11.005.

[60] R. Nigmatullin *et al.*, "Mechanically Robust Gels Formed from Hydrophobized Cellulose Nanocrystals," *ACS Appl. Mater. Interfaces*, vol. 10, no. 23, pp. 19318–19322, Jun. 2018, doi: 10.1021/acsami.8b05067.

[61] M. Li, Q. Wu, R. J. Moon, M. A. Hubbe, and M. J. Bortner, "Rheological Aspects of Cellulose Nanomaterials: Governing Factors and Emerging Applications," *Adv. Mater.*, vol. 33, no. 21, p. 2006052, May 2021, doi: 10.1002/adma.202006052.

[62] K. R. K. Iyer, P. Neelakantan, and T. Radhakrishnan, "Birefringence of native cellulosic fibers. I. Untreated cotton and ramie," *J. Polym. Sci. Part A-2 Polym. Phys.*, vol. 6, no. 10, pp. 1747–1758, Oct. 1968, doi: 10.1002/pol.1968.160061005.

[63] E. D. Cranston and D. G. Gray, "Birefringence in spin-coated films containing cellulose nanocrystals," *Colloids Surfaces A Physicochem. Eng. Asp.*, vol. 325, no. 1–2, pp. 44–51, Jul. 2008, doi: 10.1016/j.colsurfa.2008.04.042.

[64] K. Fleming, D. G. Gray, and S. Matthews, "Cellulose Crystallites," *Chemistry (Easton).*, vol. 7, no. 9, pp. 1831–1836, May 2001, doi: 10.1002/1521-3765(20010504)7:9<1831::AID-CHEM1831>3.0.CO;2-S.

[65] A. G. Dumanli *et al.*, "Digital color in cellulose nanocrystal films," *ACS Appl. Mater. Interfaces*, vol. 6, no. 15, pp. 12302–12306, Aug. 2014, doi: 10.1021/am501995e.

[66] N. Lin, J. Huang, and A. Dufresne, "Preparation, properties and applications of polysaccharide nanocrystals in advanced functional nanomaterials: a review," doi: 10.1039/c2nr30260h.

[67] R. M. Parker *et al.*, "The Self-Assembly of Cellulose Nanocrystals: Hierarchical Design of Visual Appearance," *Adv. Mater.*, vol. 30, no. 19, p. 1704477, May 2018, doi: 10.1002/adma.201704477.

[68] K. De France, Z. Zeng, T. Wu, and G. Nyström, "Functional Materials from Nanocellulose: Utilizing Structure–Property Relationships in Bottom-Up Fabrication," *Adv. Mater.*, vol. 33, no. 28, p. 2000657, Jul. 2021, doi: 10.1002/adma.202000657.

[69] J. O. Zoppe, L. Grosset, and J. Seppälä, "Liquid crystalline thermosets based on anisotropic phases of cellulose nanocrystals," *Cellulose*, vol. 20, no. 5, pp. 2569–2582, Oct. 2013, doi: 10.1007/s10570-013-0008-2.

[70] M. Giese and M. Spengler, "Cellulose nanocrystals in nanoarchitectonics-towards photonic functional materials," *Molecular Systems Design and Engineering*, vol. 4, no. 1. Royal Society of Chemistry, pp. 29–48, 01-Feb-2019, doi: 10.1039/c8me00065d.

[71] L. Thompson, J. Azadmanjiri, M. Nikzad, I. Sbarski, J. Wang, and A. Yu, "Cellulose nanocrystals: Production, functionalization and advanced applications," *Rev. Adv. Mater. Sci.*, vol. 58, no. 1, pp. 1–16, 2019, doi: 10.1515/rams-2019-0001.

[72] T. V. Patil, D. K. Patel, S. D. Dutta, K. Ganguly, T. S. Santra, and K. T. Lim, "Nanocellulose, a versatile platform: From the delivery of active molecules to tissue engineering applications," *Bioactive Materials*, vol. 9. KeAi Communications Co., pp. 566–589, 01-Mar-2022, doi: 10.1016/j.bioactmat.2021.07.006.

[73] O. A. T. Dias, S. Konar, A. L. Leão, W. Yang, J. Tjong, and M. Sain, "Current State of Applications of Nanocellulose in Flexible Energy and Electronic Devices," *Frontiers in Chemistry*, vol. 8. Frontiers Media S.A., p. 420, 21-May-2020, doi: 10.3389/fchem.2020.00420.

[74] O. Fourmann *et al.*, "3D printing of shape-morphing and antibacterial anisotropic nanocellulose hydrogels," *Carbohydr. Polym.*, vol. 259, p. 117716, May 2021, doi: 10.1016/j.carbpol.2021.117716.

[75] T. Lu *et al.*, "Cellulose Nanocrystals/Polyacrylamide Composites of High Sensitivity and Cycling Performance to Gauge Humidity," *ACS Appl. Mater. Interfaces*, vol. 9, no. 21, pp. 18231–18237, May 2017, doi: 10.1021/acsami.7b04590.

[76] K. Zubik, P. Singhsa, Y. Wang, H. Manuspiya, and R. Narain, "Thermo-responsive poly(N-isopropylacrylamide)-cellulose nanocrystals hybrid hydrogels for wound dressing," *Polymers (Basel).*, vol. 9, no. 4, p. 119, Mar. 2017, doi: 10.3390/polym9040119.

[77] R. Cha, Z. He, and Y. Ni, "Preparation and characterization of thermal/pH-sensitive hydrogel from carboxylated nanocrystalline cellulose," *Carbohydr. Polym.*, vol. 88, no. 2, pp. 713–718, Apr. 2012, doi: 10.1016/j.carbpol.2012.01.026.

[78] Y. Li, H. Chen, D. Liu, W. Wang, Y. Liu, and S. Zhou, "PH-Responsive Shape Memory Poly(ethylene glycol)-Poly(ε-caprolactone)-based Polyurethane/Cellulose Nanocrystals Nanocomposite," *ACS Appl. Mater. Interfaces*, vol. 7, no. 23, pp. 12988–12999, Jun. 2015, doi: 10.1021/acsami.5b02940.

[79] M. V. Biyani, M. Jorfi, C. Weder, and E. J. Foster, "Light-stimulated mechanically switchable, photopatternable cellulose nanocomposites," *Polym. Chem.*, vol. 5, no. 19, pp. 5716–5724, 2014, doi: 10.1039/c4py00487f.

[80] M. V. Biyani, C. Weder, and E. J. Foster, "Photoswitchable nanocomposites made from coumarin-functionalized cellulose nanocrystals," *Polym. Chem.*, vol. 5, no. 18, pp. 5501–5508, Sep. 2014, doi: 10.1039/c4py00486h.

[81] R. Nasseri, C. P. Deutschman, L. Han, M. A. Pope, and K. C. Tam, "Cellulose nanocrystals in smart and stimuli-responsive materials: a review," *Materials Today Advances*, vol. 5. Elsevier Ltd, p. 100055, 01-Mar-2020, doi: 10.1016/j.mtadv.2020.100055.

[82] P. R. Anusuyadevi *et al.*, "Photoresponsive and Polarization-Sensitive Structural Colors from Cellulose/Liquid Crystal Nanophotonic Structures," *Adv. Mater.*, vol. 33, no. 36, p. 2101519, Sep. 2021, doi: 10.1002/adma.202101519.

[83] J. Yang, X.-M. Zhang, and F. Xu, "Design of Cellulose Nanocrystals Template-Assisted Composite Hydrogels: Insights from Static to Dynamic Alignment," 2015, doi: 10.1021/ma5026175.

[84] K. L. Dagnon, K. Shanmuganathan, C. Weder, and S. J. Rowan, "Water-triggered modulus changes of cellulose nanofiber nanocomposites with hydrophobic polymer matrices," *Macromolecules*, vol. 45, no. 11, pp. 4707–4715, Jun. 2012, doi: 10.1021/ma300463y.

[85] A. B. Reising, R. J. Moon, and J. P. Youngblood, "Effect of particle alignment on mechanical properties of neat cellulose nanocrystal films," 2012.

[86] T. M. Ejara, S. Balakrishnan, and J. C. Kim, "Nanocomposites of PVA/cellulose nanocrystals: Comparative and stretch drawn properties," *SPE Polym.*, vol. 2, no. 4, pp. 288–296, Oct. 2021, doi: 10.1002/pls2.10057.

[87] A. Redondo, D. Jang, L. S. T. J. Korley, I. Gunkel, and U. Steiner, "Electrospinning of cellulose nanocrystal-reinforced polyurethane fibrous mats," *Polymers (Basel).*, vol. 12, no. 5, May 2020, doi: 10.3390/POLYM12051021.

[88] T. Pullawan, A. N. Wilkinson, and S. J. Eichhorn, "Influence of magnetic field alignment of cellulose whiskers on the mechanics of all-cellulose nanocomposites," *Biomacromolecules*, vol. 13, no. 8, pp. 2528–2536, Aug. 2012, doi: 10.1021/bm300746r.

[89] N. B. Palaganas *et al.*, "3D Printing of Photocurable Cellulose Nanocrystal Composite for Fabrication of Complex Architectures via Stereolithography," *ACS Appl. Mater. Interfaces*, vol. 9, no. 39, pp. 34314–34324, Oct. 2017, doi: 10.1021/acsami.7b09223.

[90] Kusmono and O. E. R. Wiratma, "Fabrication and Characterization of PLA/Nanocrystalline Cellulose Nanocomposite Filaments for 3D Printing Application," *IOP Conf. Ser. Mater. Sci. Eng.*, vol. 1096, no. 1, p. 012055, Mar. 2021, doi: 10.1088/1757-899x/1096/1/012055.

[91] A. Giubilini *et al.*, "3D-Printing Nanocellulose-Poly(3-hydroxybutyrate- co-3-hydroxyhexanoate) Biodegradable Composites by Fused Deposition Modeling," *ACS Sustain. Chem. Eng.*, vol. 8, no. 27, pp. 10292–10302, Jul. 2020, doi: 10.1021/acssuschemeng.0c03385.

[92] S. Sultan, G. Siqueira, T. Zimmermann, and A. P. Mathew, "3D printing of nano-cellulosic biomaterials for medical applications," *Curr. Opin. Biomed. Eng.*, vol. 2, pp. 29–34, 2017, doi: 10.1016/j.cobme.2017.06.002.

[93] A. R. Studart, "Additive manufacturing of biologically-inspired materials," *Chem. Soc. Rev.*, vol. 45, no. 2, pp. 359–376, Jan. 2016, doi: 10.1039/c5cs00836k.

[94] J. E. Smay, J. Cesarano, and J. A. Lewis, "Colloidal inks for directed assembly of 3-D periodic structures," *Langmuir*, vol. 18, no. 14, pp. 5429–5437, Jul. 2002, doi: 10.1021/la0257135.

[95] L. Dai *et al.*, "3D printing using plant-derived cellulose and its derivatives: A review," *Carbohydrate Polymers*. 2019, doi: 10.1016/j.carbpol.2018.09.027.

[96] G. Siqueira *et al.*, "Cellulose Nanocrystal Inks for 3D Printing of Textured Cellular Architectures," *Adv. Funct. Mater.*, vol. 27, no. 12, 2017, doi: 10.1002/adfm.201604619.

[97] S. Sultan and A. P. Mathew, "3D printed scaffolds with gradient porosity based on a cellulose nanocrystal hydrogel," *Nanoscale*, vol. 10, no. 9, pp. 4421–4431, Mar. 2018, doi: 10.1039/c7nr08966j.

[98] M. K. Hausmann *et al.*, "Complex-Shaped Cellulose Composites Made by Wet Densification of 3D Printed Scaffolds," *Adv. Funct. Mater.*, vol. 30, no. 4, p. 1904127, Jan. 2020, doi: 10.1002/adfm.201904127.

[99] W. Xu, X. Wang, N. Sandler, S. Willför, and C. Xu, "Three-Dimensional Printing of Wood-Derived Biopolymers: A Review Focused on Biomedical Applications," *ACS Sustain. Chem. Eng.*, vol. 6, no. 5, pp. 5663–5680, May 2018, doi: 10.1021/acssuschemeng.7b03924.

[100] Y. Zhao, "Photocontrollable block copolymer micelles: What can we control?," *J. Mater. Chem.*, vol. 19, no. 28, pp. 4887–4895, Jul. 2009, doi: 10.1039/b819968j.

[101] S. Arumugam and V. V. Popik, "Light-induced hetero-diels-alder cycloaddition: A facile and selective photoclick reaction," *J. Am. Chem. Soc.*, vol. 133, no. 14, pp. 5573–5579, Apr. 2011, doi: 10.1021/ja200356f.

[102] A. Goulet-Hanssens, F. Eisenreich, and S. Hecht, "Enlightening Materials with Photoswitches," *Adv. Mater.*, vol. 32, no. 20, p. 1905966, May 2020, doi: 10.1002/adma.201905966.

[103] M. Camacho-Lopez, H. Finkelmann, P. Palffy-Muhoray, and M. Shelley, "Fast liquid-crystal elastomer swims into the dark," *Nat. Mater.*, vol. 3, no. 5, pp. 307–310, 2004, doi: 10.1038/nmat1118.

[104] A. Lendlein, H. Jiang, O. Jünger, and R. Langer, "Light-induced shape-memory polymers," *Nature*, vol. 434, pp. 879–882, 2005, doi: 10.1038/nature03438.1.

[105] N. Wagner and P. Theato, "Light-induced wettability changes on polymer surfaces," *Polymer (United Kingdom)*, vol. 55, no. 16. Elsevier, pp. 3436–3453, 05-Aug-2014, doi: 10.1016/j.polymer.2014.05.033.

[106] N. S. Allen, "Photoinitiators for UV and visible curing of coatings: Mechanisms and properties," *J. Photochem. Photobiol. A Chem.*, vol. 100, no. 1–3, pp. 101–107, 1996, doi: 10.1016/S1010-6030(96)04426-7.

[107] A. Polykarpov and A. Tiwari, "Chapter 1. Photocured Materials: A General Perspective," Royal Society of Chemistry, 2014, pp. 1–14.

[108] S. R. Caliari *et al.*, "Stiffening hydrogels for investigating the dynamics of hepatic stellate cell mechanotransduction during myofibroblast activation," *Sci. Rep.*, vol. 6, no. 1, pp. 1–10, Feb. 2016, doi: 10.1038/srep21387.

[109] A. Tabet, R. A. Forster, C. C. Parkins, G. Wu, and O. A. Scherman, "Modulating stiffness with photo-switchable supramolecular hydrogels," *Polym. Chem.*, vol. 10, no. 4, pp. 467–472, Jan. 2019, doi: 10.1039/c8py01554f.

[110] F. Lancia, A. Ryabchun, A. D. Nguindjel, S. Kwangmettatam, and N. Katsonis, "Mechanical adaptability of artificial muscles from nanoscale molecular action," *Nat. Commun.*, vol. 10, no. 1, pp. 1–8, Dec. 2019, doi: 10.1038/s41467-019-12786-2.

[111] S. Chen *et al.*, "Photoresponsive dynamic covalent bond based on addition-fragmentation chain transfer of allyl selenides," *Polym. Chem.*, vol. 12, no. 11, pp. 1622–1626, Mar. 2021, doi: 10.1039/d0py01730b.
[112] M. Giebler, S. Radl, T. Ules, T. Griesser, and S. Schlögl, "Photopatternable Epoxy-Based Thermosets," *Materials (Basel).*, vol. 12, no. 15, p. 2350, Jul. 2019, doi: 10.3390/ma12152350.
[113] Y. Wang *et al.*, "UV-triggered self-healing polyurethane with enhanced stretchability and elasticity," *Polymer (Guildf).*, vol. 172, pp. 187–195, May 2019, doi: 10.1016/j.polymer.2019.03.045.
[114] N. Oya, P. Sukarsaatmadja, K. Ishida, and N. Yoshie, "Photoinduced mendable network polymer from poly(butylene adipate) end-functionalized with cinnamoyl groups," *Polym. J.*, vol. 44, no. 7, pp. 724–729, Jul. 2012, doi: 10.1038/pj.2012.18.
[115] I. Roppolo *et al.*, "3D printable light-responsive polymers," *Mater. Horizons*, vol. 4, no. 3, pp. 396–401, 2017, doi: 10.1039/c7mh00072c.
[116] H.-K. Kim *et al.*, "Reversible Photo-Mechanical Switching Behavior of Azobenzene-Containing Semi-Interpenetrating Network under UV and Visible Light Irradiation," *Macromol. Chem. Phys.*, vol. 206, no. 20, pp. 2106–2111, Oct. 2005, doi: 10.1002/macp.200500241.
[117] J. Vapaavuori, A. Laventure, C. G. Bazuin, O. Lebel, and C. Pellerin, "Submolecular Plasticization Induced by Photons in Azobenzene Materials," *J. Am. Chem. Soc.*, vol. 137, no. 42, pp. 13510–13517, Oct. 2015, doi: 10.1021/jacs.5b06611.
[118] K. Kumar, A. P. H. J. Schenning, D. J. Broer, and D. Liu, "Regulating the modulus of a chiral liquid crystal polymer network by light," *Soft Matter*, vol. 12, no. 13, pp. 3196–3201, Mar. 2016, doi: 10.1039/c6sm00114a.
[119] M. Pilz Da Cunha, E. A. J. Van Thoor, M. G. Debije, D. J. Broer, and A. P. H. J. Schenning, "Unravelling the photothermal and photomechanical contributions to actuation of azobenzene-doped liquid crystal polymers in air and water," *J. Mater. Chem. C*, vol. 7, no. 43, pp. 13502–13509, Nov. 2019, doi: 10.1039/c9tc04440j.
[120] A. Shimamura *et al.*, "Simultaneous analysis of optical and mechanical properties of cross-linked azobenzene-containing liquid-crystalline polymer films," *ACS Appl. Mater. Interfaces*, vol. 3, no. 11, pp. 4190–4196, Nov. 2011, doi: 10.1021/am200621j.
[121] G. Kaur, P. Johnston, and K. Saito, "Photo-reversible dimerisation reactions and their applications in polymeric systems," *Polym. Chem.*, vol. 5, no. 7, pp. 2171–2186, 2014, doi: 10.1039/c3py01234d.
[122] L. Wu, C. Jin, and X. Sun, "Synthesis, Properties, and Light-Induced Shape Memory Effect of Multiblock Polyesterurethanes Containing Biodegradable Segments and Pendant Cinnamamide Groups," *Biomacromolecules*, vol. 12, no. 1, pp. 235–241, Jan. 2011, doi: 10.1021/bm1012162.
[123] T. Defize *et al.*, "Photo-Cross-Linkable Coumarin-Based Poly(ε-caprolactone) for Light-Controlled Design and Reconfiguration of Shape-Memory Polymer Networks," *Macromolecules*, vol. 52, no. 2, pp. 444–456, Jan. 2019, doi: 10.1021/acs.macromol.8b02188.
[124] M. Herath, J. Epaarachchi, M. Islam, L. Fang, and J. Leng, "Light activated shape memory polymers and composites: A review," *European Polymer Journal*, vol. 136. Elsevier Ltd, p. 109912, 05-Aug-2020, doi: 10.1016/j.eurpolymj.2020.109912.
[125] A. Toncheva *et al.*, "Fast IR-Actuated Shape-Memory Polymers Using in Situ Silver Nanoparticle-Grafted Cellulose Nanocrystals," *ACS Appl. Mater. Interfaces*, vol. 10, no. 35, pp. 29933–29942, Sep. 2018, doi: 10.1021/acsami.8b10159.
[126] F. Orozco *et al.*, "Diels-Alder-based thermo-reversibly crosslinked polymers: Interplay of crosslinking density, network mobility, kinetics and stereoisomerism," *Eur. Polym. J.*, vol. 135, p. 109882, Jul. 2020, doi: 10.1016/j.eurpolymj.2020.109882.
[127] A. Gandini, "The furan/maleimide Diels-Alder reaction: A versatile click-unclick tool in macromolecular synthesis," *Progress in Polymer Science*, vol. 38, no. 1. Pergamon, pp. 1–29, 01-Jan-2013, doi: 10.1016/j.progpolymsci.2012.04.002.
[128] M. P. M. Dicker *et al.*, "Light-Triggered Soft Artificial Muscles: Molecular-Level Amplification of Actuation Control Signals," *Sci. Rep.*, vol. 7, no. 1, p. 9197, Dec. 2017, doi: 10.1038/s41598-017-08777-2.
[129] H. Shahsavan *et al.*, "Bioinspired underwater locomotion of light-driven liquid crystal gels.," *Proc. Natl. Acad. Sci. U. S. A.*, Feb. 2020, doi: 10.1073/pnas.1917952117.
[130] M. Yamada *et al.*, "Photomobile polymer materials: Towards light-driven plastic motors," *Angew. Chemie - Int. Ed.*, vol. 47, no. 27, pp. 4986–4988, 2008, doi: 10.1002/anie.200800760.
[131] H. M. D. Bandara and S. C. Burdette, "Photoisomerization in different classes of azobenzene," *Chem. Soc. Rev.*, vol. 41, no. 5, pp. 1809–1825, 2012, doi: 10.1039/c1cs15179g.

[132] H. Rau, "Photoisomerization of azobenzenes," *Photochem. photophysics*, vol. 2, pp. 119–141, 1990.
[133] C. D. Eisenbach, "Isomerization of aromatic azo chromophores in poly(ethyl acrylate) networks and photomechanical effect," *Polym. (United Kingdom)*, vol. 21, no. 10, pp. 1175–1179, Oct. 1980, doi: 10.1016/0032-3861(80)90083-X.
[134] T. Kim, L. Zhu, R. O. Al-Kaysi, and C. J. Bardeen, "Organic photomechanical materials," *ChemPhysChem*, vol. 15, no. 3. Wiley-VCH Verlag, pp. 400–414, 24-Feb-2014, doi: 10.1002/cphc.201300906.
[135] Z. Mahimwalla, K. G. Yager, J. I. Mamiya, A. Shishido, A. Priimagi, and C. J. Barrett, *Azobenzene photomechanics: Prospects and potential applications*, vol. 69, no. 8. 2012.
[136] E. Merian, "Steric Factors Influencing the Dyeing of Hydrophobic. Fibers," *Text. Res. J.*, vol. 36, no. 7, pp. 612–618, Jul. 1966, doi: 10.1177/004051756603600704.
[137] L. Matějka, M. Ilavský, K. Dušek, and O. Wichterle, "Photomechanical effects in crosslinked photochromic polymers," *Polymer (Guildf).*, vol. 22, no. 11, pp. 1511–1515, Nov. 1981, doi: 10.1016/0032-3861(81)90321-9.
[138] S. Palagi *et al.*, "Structured light enables biomimetic swimming and versatile locomotion of photoresponsive soft microrobots," *Nat. Mater.*, vol. 15, no. 6, pp. 647–653, Jun. 2016, doi: 10.1038/nmat4569.
[139] M. Kondo *et al.*, "Photomechanical properties of azobenzene liquid-crystalline elastomers," *Liq. Cryst.*, vol. 36, no. 10–11, pp. 1289–1293, 2009, doi: 10.1080/02678290903138711.
[140] H. Finkelmann, E. Nishikawa, G. G. Pereira, and M. Warner, "A New Opto-Mechanical Effect in Solids," *Phys. Rev. Lett.*, vol. 87, no. 1, 2001, doi: 10.1103/PhysRevLett.87.015501.
[141] O. M. Wani, H. Zeng, and A. Priimagi, "A light-driven artificial flytrap," *Nat. Commun.*, vol. 8, no. 1, pp. 1–7, May 2017, doi: 10.1038/ncomms15546.
[142] S. L. Oscurato, M. Salvatore, P. Maddalena, and A. Ambrosio, "From nanoscopic to macroscopic photo-driven motion in azobenzene-containing materials," *Nanophotonics*, vol. 7, no. 8, pp. 1387–1422, 2018, doi: 10.1515/nanoph-2018-0040.
[143] C. L. Van Oosten, K. D. Harris, C. W. M. Bastiaansen, and D. J. Broer, "Glassy photomechanical liquid-crystal network actuators for microscale devices ⋆," *Eur. Phys. J. E*, vol. 23, pp. 329–336, 2007, doi: 10.1140/epje/i2007-10196-1.
[144] M. Kondo, Y. Yu, and T. Ikeda, "How Does the Initial Alignment of Mesogens Affect the Photoinduced Bending Behavior of Liquid-Crystalline Elastomers?," *Angew. Chemie*, vol. 118, no. 9, pp. 1406–1410, Feb. 2006, doi: 10.1002/ange.200503684.
[145] S. Iamsaard *et al.*, "Conversion of light into macroscopic helical motion," *Nat. Chem.*, vol. 6, no. 3, pp. 229–235, 2014, doi: 10.1038/nchem.1859.
[146] Y. Yu, M. Nakano, and T. Ikeda, "Directed bending of a polymer film by light," *Nature*, vol. 425, no. 6954, pp. 145–145, Sep. 2003, doi: 10.1038/425145a.
[147] A. H. Gelebart *et al.*, "Making waves in a photoactive polymer film," *Nature*, vol. 546, no. 7660, pp. 632–636, 2017, doi: 10.1038/nature22987.
[148] J. D. Fox, J. R. Capadona, P. D. Marasco, and S. J. Rowan, "Bioinspired water-enhanced mechanical gradient nanocomposite films that mimic the architecture and properties of the squid beak," *J. Am. Chem. Soc.*, vol. 135, no. 13, pp. 5167–5174, Apr. 2013, doi: 10.1021/ja4002713.
[149] P. Vijay, W. Batchelor, and K. Saito, "Preparation of coumarin polymer grafted nanocellulose films to form high performance, photoresponsive barrier layers," *J. Polym. Sci.*, Jul. 2022, doi: 10.1002/pol.20220248.
[150] M. V. Biyani, E. J. Foster, and C. Weder, "Light-healable supramolecular nanocomposites based on modified cellulose nanocrystals," *ACS Macro Lett.*, vol. 2, no. 3, pp. 236–240, Mar. 2013, doi: 10.1021/mz400059w.
[151] S. Coulibaly *et al.*, "Reinforcement of optically healable supramolecular polymers with cellulose nanocrystals," *Macromolecules*, vol. 47, no. 1, pp. 152–160, Jan. 2014, doi: 10.1021/ma402143c.
[152] X. Liu, M. Li, X. Zheng, E. Retulainen, and S. Fu, "Dual light- and pH-responsive composite of polyazo-derivative grafted cellulose nanocrystals," *Materials (Basel).*, vol. 11, no. 9, Sep. 2018, doi: 10.3390/ma11091725.
[153] S. Tibbits, "4D Printing: Multi-Material Shape Change," *Archit. Des.*, vol. 84, no. 1, pp. 116–121, Jan. 2014, doi: 10.1002/ad.1710.
[154] A. J. Boydston *et al.*, "Additive manufacturing with stimuli-responsive materials," *J. Mater. Chem. A*, pp. 20621–20645, 2018, doi: 10.1039/C8TA07716A.

[155] M. Zarek, M. Layani, I. Cooperstein, E. Sachyani, D. Cohn, and S. Magdassi, "3D Printing: 3D Printing of Shape Memory Polymers for Flexible Electronic Devices (Adv. Mater. 22/2016)," *Adv. Mater.*, vol. 28, no. 22, p. 4166, 2016, doi: 10.1002/adma.201670148.

[156] Y. Yang, Y. Chen, Y. Wei, and Y. Li, "3D printing of shape memory polymer for functional part fabrication," *Int. J. Adv. Manuf. Technol.*, vol. 84, no. 9–12, pp. 2079–2095, 2016, doi: 10.1007/s00170-015-7843-2.

[157] H. Yang *et al.*, "3D Printed Photoresponsive Devices Based on Shape Memory Composites," *Adv. Mater.*, vol. 29, no. 33, pp. 1–7, 2017, doi: 10.1002/adma.201701627.

[158] L. Ceamanos, Z. Kahveci, M. Lopez-Valdeolivas, D. Liu, D. J. Broer, and C. Sanchez-Somolinos, "Four-dimensional printed liquid crystalline elastomer actuators with fast photoinduced mechanical response toward light-driven robotic functions," *ACS Appl. Mater. Interfaces*, vol. 12, no. 39, pp. 44195–44204, Sep. 2020, doi: 10.1021/acsami.0c13341.

[159] X. Lu *et al.*, "4D-Printing of Photoswitchable Actuators," no. 10, Mar. 2021, Accessed: 23-Apr-2021. [Online]. Available: https://onlinelibrary.wiley.com/doi/10.1002/ange.202012618.

[160] M. Nadgorny and A. Ameli, "Functional Polymers and Nanocomposites for 3D Printing of Smart Structures and Devices," *ACS Appl. Mater. Interfaces*, vol. 10, no. 21, pp. 17489–17507, 2018, doi: 10.1021/acsami.8b01786.

[161] M. K. Gupta *et al.*, "3D Printed Programmable Release Capsules," *Nano Lett.*, vol. 15, no. 8, pp. 5321–5329, Aug. 2015, doi: 10.1021/acs.nanolett.5b01688.

[162] A. Kotikian, R. L. Truby, J. W. Boley, T. J. White, and J. A. Lewis, "3D Printing of Liquid Crystal Elastomeric Actuators with Spatially Programed Nematic Order," *Adv. Mater.*, vol. 30, no. 10, Mar. 2018, doi: 10.1002/adma.201706164.

[163] E. C. Davidson, A. Kotikian, S. Li, J. Aizenberg, and J. A. Lewis, "3D Printable and Reconfigurable Liquid Crystal Elastomers with Light-Induced Shape Memory via Dynamic Bond Exchange," *Adv. Mater.*, vol. 32, no. 1, pp. 1–6, 2020, doi: 10.1002/adma.201905682.

[164] C. P. Ambulo, M. J. Ford, K. Searles, C. Majidi, and T. H. Ware, "4D-Printable Liquid Metal-Liquid Crystal Elastomer Composites," *ACS Appl. Mater. Interfaces*, vol. 13, pp. 12805–12813, 2021, doi: 10.1021/acsami.0c19051.

[165] D. E. Hagaman, S. Leist, J. Zhou, and H. F. Ji, "Photoactivated Polymeric Bilayer Actuators Fabricated via 3D Printing," *ACS Appl. Mater. Interfaces*, vol. 10, no. 32, pp. 27308–27315, Aug. 2018, doi: 10.1021/acsami.8b08503.

3 Publications

This cumulative thesis builds his discussion on the following three first-author scientific publications:

1) **L. A. E. Müller**, T. Zimmermann, G. Nyström, I. Burgert, and G. Siqueira*, "Mechanical Properties Tailoring of 3D Printed Photoresponsive Nanocellulose Composites," *Adv. Funct. Mater.*, vol. 2002914, pp. 1–9, 2020, doi: 10.1002/adfm.202002914.

Author Contributions: LM, TZ, GN, IB and GS designed and planned the study. LM carried out all the experiments, analyzed the data, organized the figures and wrote the manuscript. All authors revised and commented the paper.

2) **L. A. E. Müller**, Adrien Demongeot, Joanne Vaucher, Yves Leterrier, Jonathan Avaro, Marianne Liebi, Antonia Neels, Ingo Burgert, Tanja Zimmermann, Gustav Nyström* and Gilberto Siqueira*, "Photoresponsive Movement in 3D Printed Cellulose Nanocomposites," *ACS Appl. Mater. Interfaces*, p. acsami.2c02154, Apr. 2022, doi: 10.1021/acsami.2c02154.

Authors Contributions: Experiments were designed and coordinated by L.M., T.Z., G.N., I.B., and G.S., and were conducted by L.M. The photoresponsive differential scanning calorimetry (photo-DSC) and photoresponsive DMA temperature sweeps analyses were conducted by J.V., A.D., and Y.L.. The X-ray analyses were performed by J.A., M.L., and A.N.. Figure graphic designs were prepared by L.M. who also wrote the manuscript with input from all coauthors. All authors reviewed and commented on the manuscript.

3) **L. A. E. Müller*,** Anita Zingg*, Andrea Arcifa, Tanja Zimmermann, Gustav Nyström, Ingo Burgert, Gilberto Siqueira. " Functionalized cellulose nanocrystals as active reinforcements for light stimulated 3D printed structures", *ACS Nano*, 2022, doi: 10.1021/acsnano.2c05628

*Luca Müller and Anita Zingg, Master student of D-MATL ETHZ (2021), share the first co-authorship

Authors Contributions: The study was designed and planned by LM, AZ, TZ, GN, IB and GS. AZ carried out the FTIR, UV-Vis spectroscopy, rheology and DMA characterizations of the materials and analyzed the data under the supervision of LM. LM performed AFM imaging, tensile tests, produced the honeycomb structures and carried out all compression measurements under selective illumination, analyzed the data and coordinated the manuscript. LM and AZ cowrote the manuscript and organized the figures. All authors reviewed and commented on the manuscript.

These scientific papers have been formatted from the published and submitted versions to fit the format of this thesis.

3.1 Mechanical Properties Tailoring of 3D Printed Photoresponsive Nanocellulose Composites

*Luca A. E. Müller[1], Tanja Zimmermann[1], Gustav Nyström[1], Ingo Burgert[2], and Gilberto Siqueira[1]**

[1]Cellulose and Wood Materials Laboratory, Empa, Swiss Federal Laboratories for Materials Science and Technology, 8600 Dübendorf, Switzerland

[2]Wood Materials Science, Institute for Building Materials, ETH-Zürich, 8093 Zürich, Switzerland

*Corresponding author: Gilberto Siqueira

E-Mail address: gilberto.siqueira@empa.ch

3.1.1 Abstract

3D printing technologies allow control over the alignment of building blocks in synthetic materials, but compositional changes often require complex multimaterial printing steps. Here, 3D printable materials showing locally tunable mechanical properties are produced in a single printing step of Direct Ink Writing. These new inks consist of a polymer matrix bearing biocompatible photoreactive cinnamate derivatives and up to 30 wt% of anisotropic cellulose nanocrystals. The printed materials are mechanically versatile and can undergo further crosslinking upon illumination. When illuminating the material and controlling the irradiation doses, the Young's moduli can be adjusted between 15 and 75 MPa. Moreover, spatially controlled illumination allows patterning stiff geometries, resulting in 3D printed structures with segments of different mechanical properties tailoring the mechanical behavior under compression. The high design freedom implemented by 3D printing and photopatternability opens the venue to rapid manufacturing of devices for applications such as prosthetics or soft robotics where the 3D shapes and mechanical properties must be tailored for personalized load cases.

Keywords: *cellulose nanocrystals, direct ink writing, mechanical adaptation, photoresponsiveness, secondary crosslinking*

3.1.2 Introduction

The development of biocompatible and lightweight materials, presenting tailored and adaptable mechanical properties for production of devices utilized in biomedical, soft robotics and other applications, is a compelling issue in a technological world moving toward increased sustainability. In nature, biological materials have optimized their structural organization, reaching extraordinary mechanical properties for specific load cases. Sophisticated geometric structural designs, compositional changes and oriented hierarchical assemblies of reinforcing building blocks, are the common strategies employed to achieve such fine tailoring of the mechanical properties. For instance, insect cuticles and spider fangs are both chitin-protein based composites, but the presence of highly crosslinked proteins at the tip forming packed layers with determined orientations of chitin fibers [1], assembled into an optimized conical shape [2], makes the spider fangs able to easily perforate the insect cuticle. Despite the fact that these structural and chemical optimizations are well known and observed in many exemplary materials in

nature, their implementation in synthetic composite materials for the production of optimized devices remains challenging.

Additive manufacturing technologies, however, and in particular 3D printing, show promising results for the artificial production of synthetic composite materials with controlled microstructures [3]–[6]. With a bottom-up approach, these technologies allow for a high geometrical freedom and an efficient spatial control over natural building blocks and composition. In particular, natural and biocompatible anisotropic building blocks, such as cellulose nanocrystals (CNC), have attracted great interest from the scientific community due to their reinforcing properties and high potential in biomedical applications [7],[8]. Shear and extensional forces experienced during extrusion based 3D printing, such as Direct Ink Writing (DIW), allow to obtain textured cellular architectures where CNC have high alignment along the printing directions [9],[10], hence spatially tailoring the Young's modulus of the produced structures. However, local compositional changes in the matrix as well as local density patterns are still difficult to produce with single-nozzle DIW printing since they require in situ mixing of materials with different viscoelastic responses [11]. Such features might be achieved via multimaterial 3D printing approaches [12], but these are usually time consuming due to the complexity of manufacturing and require careful selection of compatible materials. Indeed, multimaterial printing often introduces incoherent interfaces with abrupt changes of elastic modulus between materials to the manufactured composites, hence leading to stress concentration sites and defects that weaken the printed structure [13].

With a surface chemistry that enables specific functionalization, CNC represent interesting reinforcement particles for the production of devices with compositional changes in single material printing. The high quantity of hydroxyl groups on their surface is suitable for grafting specific functional groups to increase matrix-reinforcement interactions [9] and adaptive properties [14] in response to external stimuli. In particular, light responsive cellulose based materials are highly interesting for biomedical applications with the need to operate in closed systems without addition of chemicals. Such materials offer the possibility to obtain both improved matrix-reinforcement interactions and adaptability. Active cellulose nanocomposites capable of improving their mechanical properties upon illumination could be produced by grafting coumarin or benzophenone moieties on the surface of the reinforcing CNC [15],[16]. When irradiated with defined wavelengths, these materials presented the ability to create strong covalent bonds between cellulose nanoparticles and matrix, therefore increasing the crosslink density and consequently the mechanical properties. Specifically, by illuminating defined parts, i.e. photopatterning, of the sample, it is possible to have a spatial control and create materials composed of soft and stiff domains combined by continuous interfaces [16]. However, such responsive materials were so far only produced in two dimensions. By grafting phosphane oxides on CNC to promote photopolymerization between CNC and PEG, it was possible to produce 3D structures by stereolithography printing [17]. Nevertheless, the produced parts did not present further light responsivity after printing. Moreover, differently than extrusion based 3D printing, where an orientation of CNC up to 84% was demonstrated along the printing directions [9], one shortcoming was that control over alignment of CNC could not be obtained. As a matter of fact, there is no research yet combining the influence of cellulose nanoparticles orientation with an additional photoresponsive tuning of mechanical properties.

Here, we present an elegant solution that enables production of 3D structures with mechanically adaptable nanocellulose composites. Our method combines CNC alignment and light responsive tuning of mechanical properties for enhanced tailoring of the final composite. The surface of the CNC is chemically modified by grafting of biocompatible photoreactive cinnamates [18], which have the property to undergo reversible cycloaddition upon illumination with wavelength > 300 nm. Successively, functionalized CNC can be dispersed in a polymer matrix also containing coupling cinnamate moieties (Figure 3.1-1). Being naturally rheology modifiers, CNC in the dispersion ensure the formation of a printable

ink that can be processed by DIW and thus, shaped into complex 3D structures. In addition, the modification of CNC allows the formation of a secondary polymer network, responsible for the increase of elastic modulus upon illumination. With spatially controlled irradiation of the material, designs combining soft and stiff regions can be achieved using a single material during printing. This approach decreases the quantity of interfacial defects between soft and stiff domains and limits the abrupt stiffness changes. Finally, combining 3D printing with spatially controlled illumination adds design freedom to the produced parts, which can be fine-tuned for a wide range of applications. Single material devices presenting complex structures with mechanical gradients ensuring energy dissipation, Young modulus matching for adhesion and highly personalized load cases could be easily produced as impact absorbing devices, substrates for flexible electronics or biomedical prosthesis.

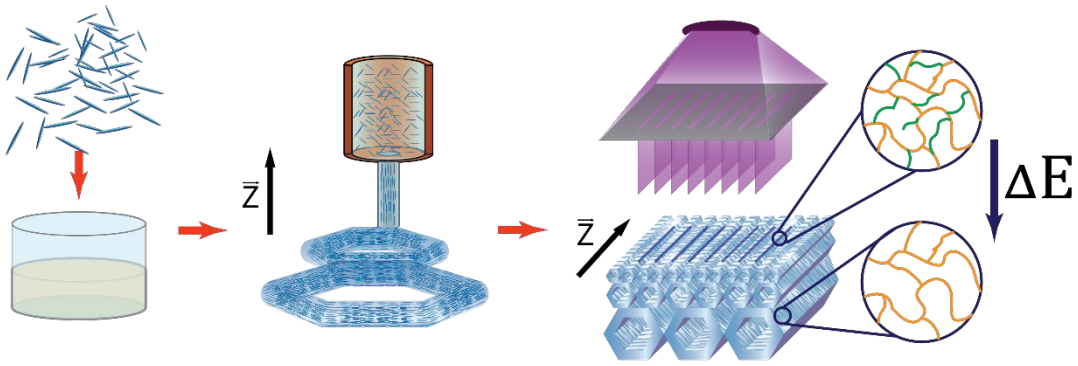

Figure 3.1-1 *Schematic approach for the manufacture of hierarchical structures showing functional gradients. Combination of CNC and reactive monomers enables the 3D printing of complex architectures where CNC reinforcements are oriented during the extrusion. After solidification, spatially controlled photostiffening is obtained by photocuring.*

3.1.3 Results and Discussion

3.1.3.1 Cellulose Nanocrystal Functionalization

Incorporation of cinnamate moieties in the matrix and on the CNC surface introduces photoresponsiveness features to the composite parts. The [2,2] photoactivated cycloaddition of cinnamates results in covalent bond formation in between CNC particles, and between CNC and the matrix, thus forming a secondary polymer network, which further improves the elastic modulus of the composites, on demand, by increasing locally their crosslinking densities and particle-matrix interfacial strength. While vinyl cinnamate (VCA) was directly incorporated in the polymer network of the polyurethane acrylate (PUA) matrix during polymerization, CNC were modified by grafting of cinnamoyl chloride on their surface.

The chemical reaction was successfully achieved as reported in Figure 3.1-2 and the comparison between Fourier transform infrared spectroscopy (FT-IR) spectra of unmodified CNC and cinnamate CNC (cin-CNC) after 1 h of reaction (Figure 3.1-2a) allowed to assess qualitatively the final reaction product. The appearance of the cinnamate carbonyl C=O stretching peak at 1715 cm^{-1} and the aromatic C-H bend at 765 cm^{-1} proves the presence of cinnamates on the surfaces of cin-CNC. Moreover, the decrease of the hydroxyl peak in the region 3000-3500 cm^{-1} and the relative increase of the acyl C-O stretching peak at 1062 cm^{-1} show the transformation of cellulose hydroxyl groups into ester groups, emphasizing the success of the reaction. Initially, the chemical reaction lasted 24 h, however the total disappearance of the hydroxyl group peaks (Figure S3.1-2, Supporting Information) indicates that CNC underwent bulk

transformation and the crystalline structure might be damaged during the process. Therefore, the structural integrity of cin-CNC and their relative crystallinity content changes were obtained from powder X-ray diffraction (XRD) patterns. Figure 3.1-2b illustrates the results for the modified CNC after 1 h of reaction. Respective crystalline indexes of CNC and cin-CNC were calculated by deconvolution of the peak patterns. The chemical treatment decreases the crystallinity indexes from around 80% for unmodified CNC to around 70% for cin-CNC. The pattern peaks become broader with longer reaction time, indicating that the grafting process was actually modifying the structure of CNC. Sampling the chemical reaction products from 1 to 24 h for XRD measurements confirms that the crystal structure of cellulose I is destroyed as the treatment continues, until an amorphous material was obtained after 24 h (Figure S3.1-3, Supporting Information).

In order to not compromise the anisotropic nature of CNC after modification (i.e. of cin-CNC), the particle morphology was characterized by atomic force microscopy (AFM), as illustrated in Figure 3.1-2c.

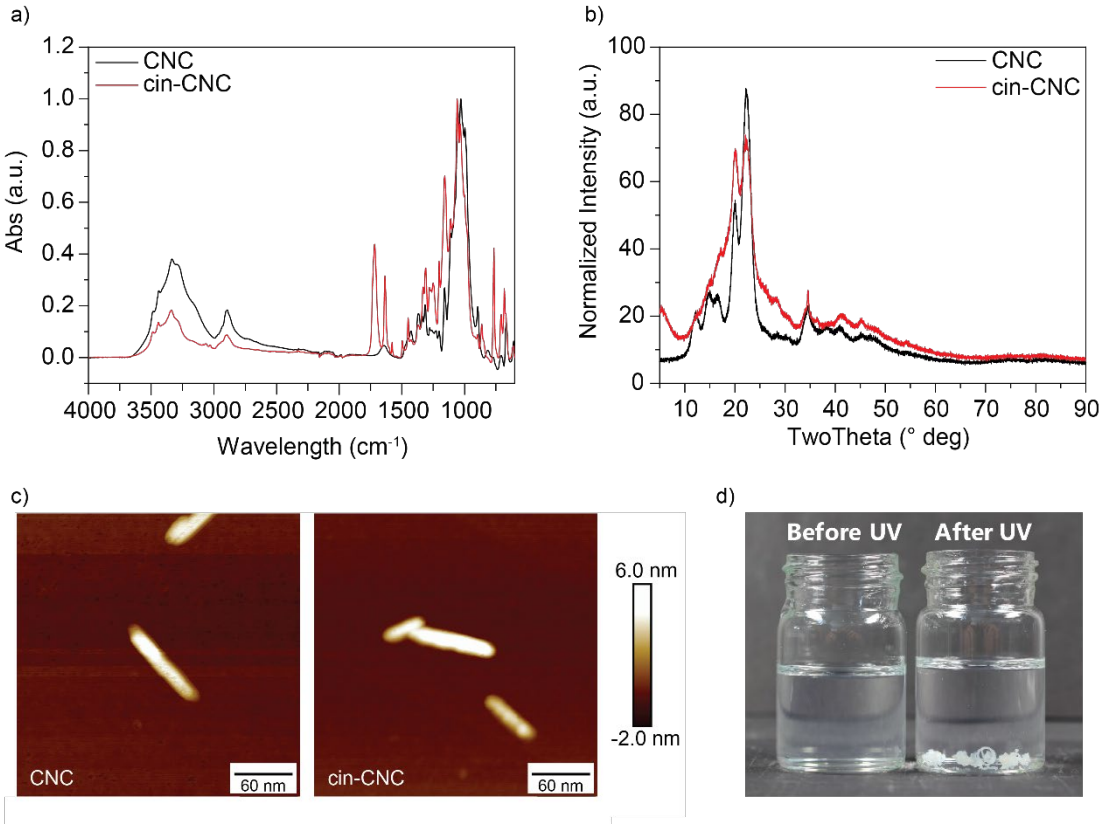

Figure 3.1-2 *a) FT-IR analysis of cinnamoyl chloride grafting on the CNC surfaces. b) XRD analysis of cellulose nanocrystals before and after 1 h of chemical functionalization. c) AFM pictographs comparing CNC and cin-CNC. d) Left vial: fully dispersed, not UV irradiated cin-CNC in NN'-dimethylformamide; right vial: cin-CNC, previously UV irradiated do not disperse in the same solvent.*

Despite the slight decrease of crystallinity index indicated by the XRD analysis after 1 h of reaction, AFM pictographs do not show a substantial difference of the CNC sizes before and after chemical modification. In both cases, cellulose nanoparticles remain anisotropic with widths ranging between 5 to 10 nm and lengths between 70 to 140 nm. However, as for the crystallinity of CNC structure, the particle's morphology strongly depend on reaction time since AFM images of longer reaction times show disappearance of the CNC anisotropic nature (Figure S3.1-4, Supporting Information).

Shaping the responsive material into an extruded filament and immersing it into pure N,N-dimethylformamide (DMF) (Figure 3.1-2d) demonstrates the cin-CNC's ability to create crosslinks between cellulose particles when illuminated. Indeed, when the material is not subjected to UV illumination, the filaments swell and disperse homogeneously as soon as they are in contact with the solvent. On the contrary, when the cin-CNC is previously irradiated for 30 min with UV light, the immersed filament keeps its shape and precipitates immediately. Moreover, the specimen resisted 30 min in an ultrasonic bath before failure of the filamentary shape and the resulting filament parts do not disperse. Consequently, the chemical treatment of CNC is limited to 1 h of reaction since this time demonstrated to be a valid compromise between safeguarding of particle's anisotropy and achieving a strong functionalization. Thus, in all the following experiments, cin-CNC refers to modified CNC obtained after 1 h of reaction.

3.1.3.2 Printable Ink Preparation

To fabricate composites with a DIW set-up, the extruded ink should show determined rheological properties, known as printability requirements, namely a strong shear thinning behavior, a storage (G') and loss (G'') modulus superior than a few kPa and a dynamic yield stress (τ_y) higher than a few hundred Pa [9],[19]. CNC are known rheology modifiers widely used for the production of biocompatible 3D printable inks [7],[10], since they allow obtaining shear thinning gels from Newtonian liquids.

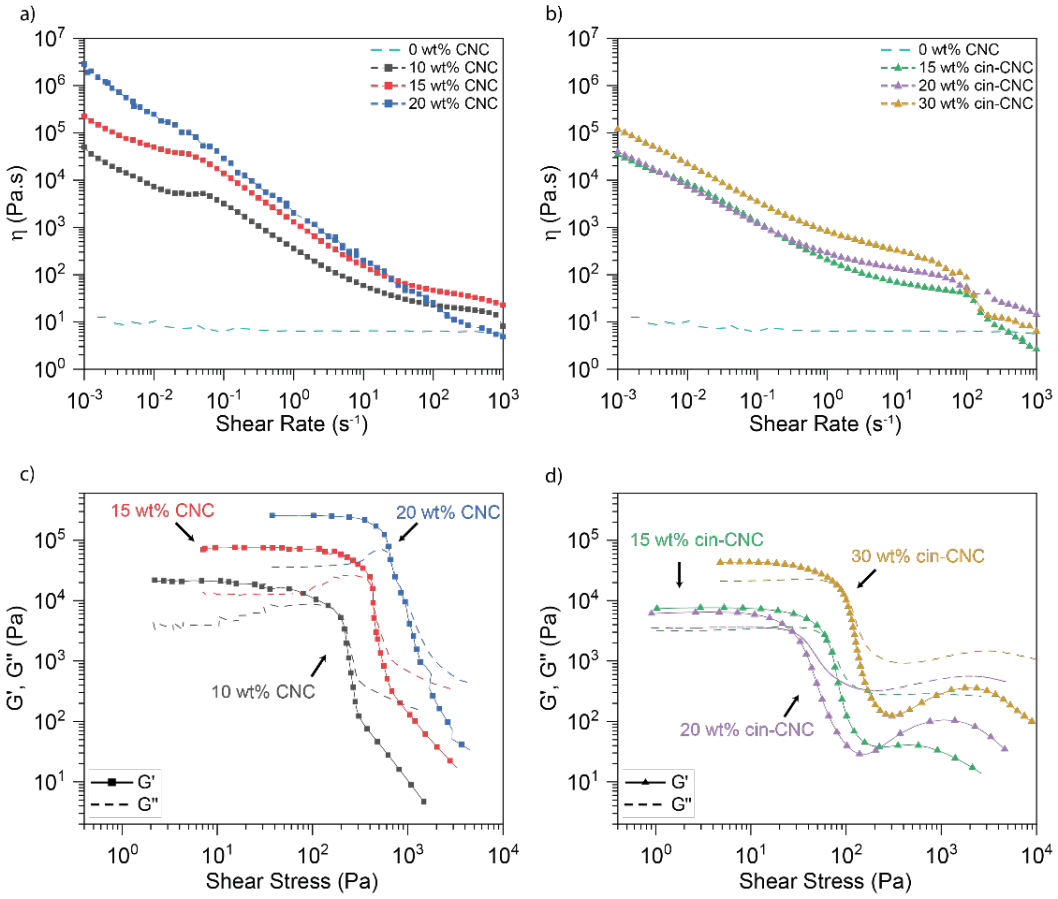

Figure 3.1-3 *Rheological behavior of CNC composite suspensions with a,c) unmodified and b,d) modified surfaces observed under a,b) flow and c,d) oscillatory conditions.*

In the present case, the addition of CNC and cin-CNC into a resin composed of 50-50 weight PUA-VCA monomers does not only target mechanical reinforcement but also enables tailoring of rheological

properties of the inks for meeting the requirements of 3D printability. Adding at least 10 wt% of CNC into the resin has the direct consequence of modifying the Newtonian behavior of the pure matrix resulting in a strong shear thinning. While, further increasing the CNC concentration within the composites increments the viscosity as well as the apparent yield stress of the inks. In particular, rotational rheology experiments (Figure 3.1-3 a, b) show that the measured viscosity (η) of composite inks increases from 10 Pa s (neat matrix viscosity) to more than 10^4 Pa s with the addition of at least 10 wt% cellulose nanocrystals. Then, η decreases several order of magnitude as the shear rate increases from 0.01 to 100 s^{-1} (typical applied range during DIW). Although both CNC and cin-CNC have a similar influence on the ink's viscosity, cin-CNC present a weaker effect. While the addition of 20 wt% of pristine CNC increases the viscosity of the ink up to 10^6 Pa s at low shear rates, the inks with 20 wt% cin-CNC show viscosities that are one order of magnitude smaller. The different surface chemistry of the cin-CNC influences both the electrostatic and hydrophilic particle-particle and particle-matrix interactions. More precisely, the decreased amount of hydroxyl groups on the cellulose surface results in less hydrogen bonds between crystals, reducing aggregation. Instead, the presence of hydrophobic aromatic groups mainly promotes the stable dispersion of CNC in the matrix, thus allowing higher solid content inks. This reduces the amount of processing steps required for the ink preparation, such as mechanical mixing and ultrasonic bath cycles, as it is easier to disperse cin-CNC in the PUA matrix.

Oscillatory rheology experiments (Figure 3.1-3 c, d) were used to characterize the elastic and viscous components of the ink's modulus and to determine the ink's dynamic yield stress. All tested modified and unmodified ink formulations present similar rheological behavior. At low shear stresses, an equilibrium region with $G' > G''$ confirms the stability of the inks as well as their solid-like elastic response. At higher shear stress, shear thinning appears due to alignment and ordering of the particles [20]. At the yield shear stress, when $G' = G''$, the inks present the transition between solid to liquid-like behavior as G'' becomes higher than G' and both drop several orders of magnitude. Particularly, higher solid content in the ink formulations produces a shift to higher moduli and shear stresses for both types of inks. Instead, the grafting of cinnamates on CNC surface shifts the curves in the opposite direction and induces the appearance of a light shear thickening at high shear stresses. Indeed, all CNC inks present $G' > 10$ kPa and $\tau_y > 100$ Pa while for cin-CNC a concentration of 30 wt% is needed to overcome those values. Moreover, the light shear thickening effect is appearing for the 20 and 30 wt% cin-CNC inks at high oscillating shear stresses. This result is typical for fumed silica dispersions and leads to the suggestion that cin-CNC can form disordered clusters due to π stacking of cinnamate aromatic rings, jamming the movement of the particles and creating a slight increase in the storage modulus of the ink [21].

Formulations containing 10, 15 wt% of pristine CNC and 30 wt% cin-CNC could be printed in 3D structures with high shape fidelity (Figure S3.1-5**,** Supporting Information) since printability requirements were met (i.e. the inks presented the required rheological properties). For inks with 20 wt% CNC, the high yield stress renders the extruding pressure too high for the used DIW and they could not be printed. Even though inks with 15 and 20 wt% cin-CNC could be printed, only 2D parts were possible, because 3D geometries were collapsing. In the following, we focused on 15 wt% cin-CNC printed flat sheets to better understand the effect of functionalization on the mechanical properties of cured composites after printing.

3.1.3.3 Photoresponse of Printed Composites and Evolution of Mechanical Properties

To understand how the addition of CNC and cin-CNC influences the elastic moduli and strength behavior of the polymer composites, and to compare the photoresponsive behavior of such fillers, 15 wt%

inks were printed as single layers and were analyzed by dynamic mechanical analysis (DMA) and tensile tests measurements. All printed composites were tested by loading in longitudinal direction to the particle orientation. DMA on not-illuminated samples showed that the presence of anisotropic nano-reinforcement improved the storage modulus E' of the composites compared to the pure matrix (Figure S3.1-6, Supporting Information), from 2 to around 15 MPa at 25 °C for both types of cellulose nano-reinforcements. This result is in agreement with previously reported studies by our group [9],[10] on the CNC alignment by DIW extrusion and its influence on mechanical properties. Consequently, other loading directions were not investigated and the attention was focused on the photoresponse of the materials.

Irradiation with UV light at wavelengths > 300 nm allows improving the Young's modulus of both CNC and cin-CNC composites, and to tune it by varying the irradiation time (Figure 3.1-4a). The DMA measurements show that, by increasing the irradiation time, all composites present an improved elastic component E' of the modulus over a wide range of temperatures. CNC and cin-CNC composites have a similar behavior when not illuminated, with E' values of 17 and 15 MPa at 25 °C, respectively. However, starting from 30 °C, cin-CNC composites become weaker, following the behavior of the neat polymer matrix, probably due to weak particle-particle interactions coming from the reduced available amount of hydroxyl groups on their surfaces. When CNC and cin-CNC composites are illuminated, E' increases faster for the pristine CNC composites. These materials double the value of storage modulus, $E' = 34$ MPa at 25 °C in 30 min of illumination, while cin-CNC samples reach a lower value, from 15 to 23 MPa at 25 °C. The photoreactive groups on the surface of CNC are most likely responsible for this behavior since they compete with the reactive moieties of the matrix for the energy required in the photoreaction. Thus, cin-CNC composites require more energy to achieve the secondary crosslinked network. Indeed, after 90 min of irradiation, E' of CNC specimens improves slightly from 34 to 40 MPa at 25 °C, meaning that the materials are reaching the conversion of all cinnamate groups. Differently, after the extended illumination, cin-CNC samples show a strong improvement of the storage modulus to the highest measured value of 67 MPa at 25 °C. In agreement with previous studies on similar photoreactive cellulose nanocomposites [15],[16], the photoinduced improvement of the storage modulus in the CNC composites qualitatively demonstrates the ability of the cinnamate functional groups to dimerize, creating covalent bonds that in-crease the polymer's crosslink density. Instead, the larger storage modulus improvement observed in cin-CNC indicates the formation of covalent bonds between modified fillers and matrix, improving the filler-matrix interfacial strength.

As a direct consequence of photostiffening, the developed materials present the ability of shape-fixing (Figure 3.1-4b). A flat printed beam of cin-CNC composite was rolled around a glass tube and UV irradiated for 90 min while deformed. As a result, due to the creation of the secondary cinnamate's crosslink network, the beam keeps its deformed shape after removal of the external stresses. This shape fixing ability allows for printing simple geometries, in a first step, and shaping them later into complex and application-specific geometries. This can reduce the amount of sacrificial structures (hence material waste) during the 3D printing process. Moreover, cinnamate moieties can undergo reversible photoreaction when illuminated with wave-lengths < 300 nm and this process can be repeated for several cycles [22]. This feature might be observed also in the developed materials. Modified cin-CNC would enable the production of complex 3D stimuli responsive actuating devices, such as shape memory structures. However, reversibility of the reaction in the cellulose composites was not investigated in the present work as the focus was on spatially controlling the illumination of the composites.

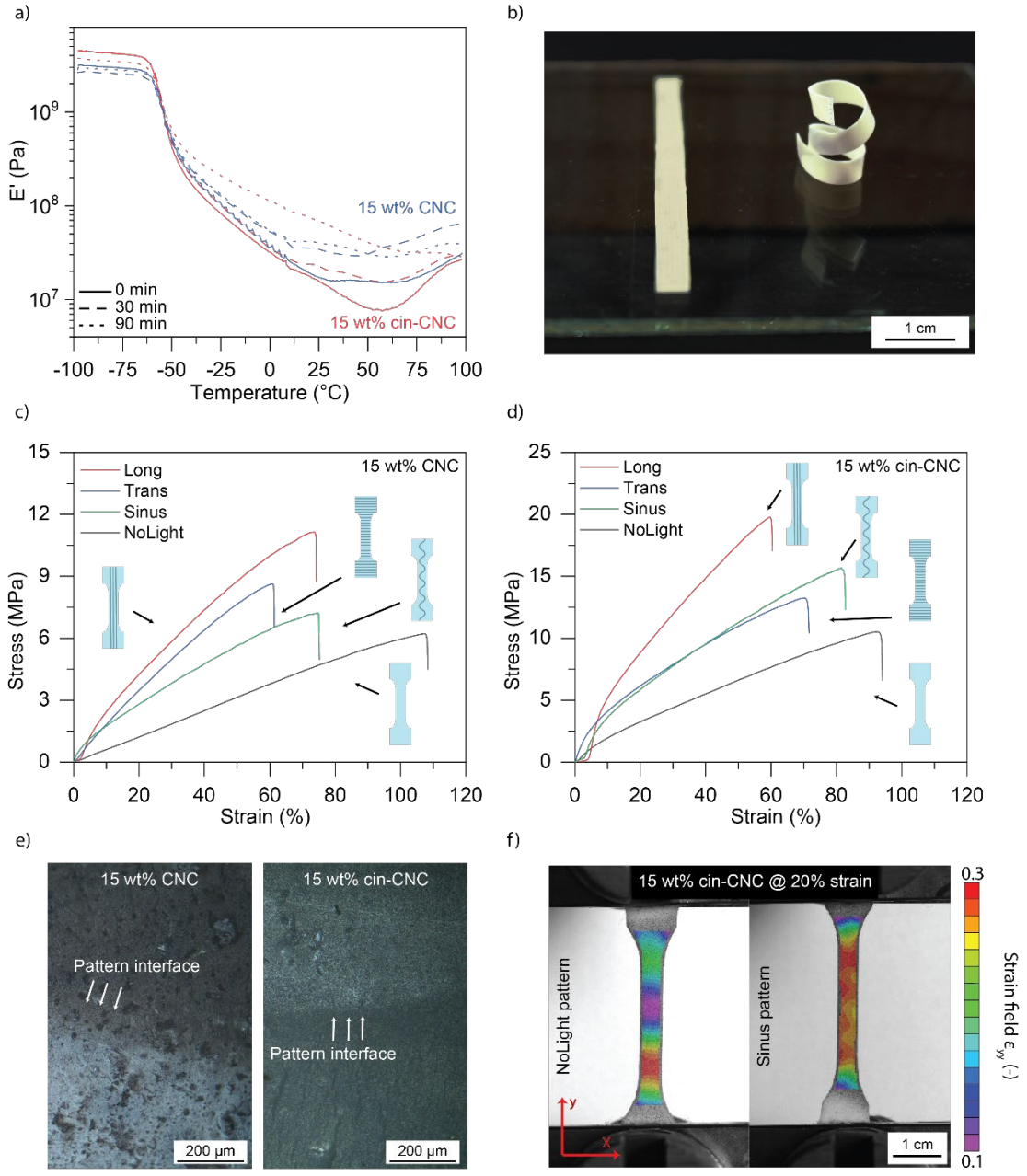

Figure 3.1-4 *Light responsiveness of the 15 wt% cellulose based materials and influence of the photopatterning on the composite mechanical properties. a) DMA measurement showing the photostiffening response for both CNC composites and its dependence to irradiation time. b) Left, original printed sample; right, shape fixing ability of the composite after illumination. c,d) Tensile measurements of photopatterned CNC and cin-CNC composites, respectively. In the legend of the graphs, Long, Trans, and Sinus stand for longitudinal, transversal, and sinusoidal pattern, respectively. e) Microscopy image illustrating the interface of the photostiffened patterns for CNC (left) and cin-CNC composites. f) Comparison of strain fields at 20% deformation between a nonilluminated cin-CNC composite and the same material with a sinusoidal photopattern.*

To study the effects of photopatterning on the mechanical response of the materials, different sample regions were selectively irradiated for 90 min with application of a photomask to create patterned regions. Tensile tests of samples with stiffer straight lines (longitudinal and transverse to the loading direction) or sinusoidal patterns show the results of versatile control over the mechanical properties of

these light responsive composites (Figure 3.1-4 c and d). In static measurements, cin-CNC samples present a stronger reinforcement effect than CNC, with a Young's modulus mean value of 35 MPa compared to 7 MPa and a strength of 12 MPa compared to 6 MPa for un-patterned samples (Figure S 3.1-7, Supporting Information). While dynamic tests were carried out in nitrogen atmosphere, tensile tests were carried out at 60% RH atmosphere. Due to the high hydrophilicity and hygroscopicity of pristine CNC, the CNC compo-sites might absorb atmospheric water. As demonstrated in a recent study [23], this would weaken the CNC-CNC hydrogen bonds in the composites, lowering their mechanical properties. Instead, after modification, cin-CNC presented a strongly decreased affinity to water (Figure S3.1-8, Supporting Information) and this would prevent the plasticizing effect of the relative humidity. Nevertheless, both not-illuminated composites show a similar general behavior. The stress strain curves illustrate an almost linear deformation. Differently, patterned samples present a reduced linearity and the appearance of an initial elastic regime with a yield point between 5% and 10% strain. The different pattern geometries lead to improvements in Young's moduli and tensile strengths, while lowering elongations at break compared to un-patterned samples. Specimens with longitudinal straight lines patterns reached the highest values with a Young modulus of 30 and 101 MPa and a strength of 10 and 17 MPa for CNC and cin-CNC composites, respectively. The samples of cin-CNC with transverse patterns, having the same illuminated volume fraction (50%) of the longitudinal ones, present an intermediate stress-strain behavior. Interestingly, patterning the cin-CNC composite with a sinusoidal line along the loading direction with an illuminated volume fraction of 25% leads to a similar behavior as transverse patterning but with 15% higher strain at failure.

While sinusoidal patterns provide an intermediate tensile response for both composite materials, transverse patterns on CNC composites show a behavior very close to the longitudinal ones. Despite the fact that the illuminated volume fractions of longitudinal and transverse patterns are theoretically the same (50%), the result is not in agreement with the rule of mixture, suggesting that larger volumes were irradiated. Observations of the patterned CNC composites with optical microscopy (Figure 3.1-4e) confirm that the interfaces between irradiated and nonirradiated regions were shady and blunted compared to the cin-CNC composites. Moreover, the deformation of cin-CNC samples with sinusoidal patterns could be observed by analyzing the strain filed in the loading direction with digital image correlation (DIC), illustrated in Figure 3.1-4f, while CNC samples did not show any defined deformation pattern. The difference of the interfaces between CNC and cin-CNC samples might be due to light absorption of the particles. Indeed, CNC are transparent to the used UV wavelengths and act as scattering centers for the incoming light increasing the size of the illuminated volumes. With the photomask's pattern width of around 544 ± 15 µm, CNC composites presented patterns widths of around 650 ± 25 µm (Figure S 3.1-9, Supporting Information). On the contrary, cin-CNC presented a photopattern width of 545 ± 8 µm, which corresponds to the mask dimensions. This behavior arise from the greater light absorption of cin-CNC , which reduces the scattering. This suggests the need for a more complete investigation focused on optimizing the light interaction with the cin-CNC, since a small penetration depth of the light would increase the photopattern resolution while limiting the maximum size of cin-CNC 3D printed parts.

The addition of functionalized cin-CNC within the polymer matrix allows tuning the mechanical response of 3D structured parts by locally patterning the material. To demonstrate how local photostiffening influences the deformation during compression of the parts, we compressed 3D printed honeycomb and grid-like composite structures, of 4 mm height, with 30 wt% cin-CNC, as shown in Figure 3.1-5. Such geometries represent a suitable example to illustrate the versatility of our approach. 3D printing is used to manufacture structures showing high out-of-plane specific stiffness, while photopatterning improves and tailors their in-plane response and deformation. The printed structures were illu-

minated for 3.5 h and successively loaded with different weights within the DMA apparatus. The pictures were taken 10 s after loading. The hexagonal honeycomb parts printed in a squared frame (Figure 3.1-5 a-c) present the most pronounced difference: while the nonilluminated sample shows a substantial compression, the sample with a vertical line of illuminated hexagons sustains the weight, thus limiting the deformation of the printed structure. By illuminating the center of the same hexagonal honeycomb pattern, but in a circular frame (Figure 3.1-5 d-f), another effect can be observed. For a similar deformation of the whole structures, 48% and 46% for unpatterned and patterned samples respectively, the unpatterned structures suffer a bigger internal deformation for a lower load, which makes the inner geometry collapse. Differently, the central hexagons of the patterned sample support the same load without collapsing. Finally, this effect is also observed for a squared grid-like structure in a circular frame (Figure 3.1-5 g-i) with a central illuminated circle. The selective photostiffening hinders the deformation of the inner structure in comparison to the unpatterned sample. Importantly, this last sample shows a strong buckling for loads higher than 250 g while the illuminated counterpart displays a light buckling after 300 g. These first results demonstrate the versatility and the design freedom that can be achieved combining 3D printing processes with a photopatternable material. In particular, this property could allow embedding and protection of sensitive electronics in structures that shall deform as in the case of soft robotics, where incorporation of sensors, which do not influence the macroscopic deformation of the device remains an open challenge [24]. Further investigation of high contents of functionalized cellulose nanocrystals (cin-CNC) within the polymer matrix, with a focus on tailoring mechanical properties by increasing complexity of both the 3D printed structures and the photostiffened patterns is expected to open up for a wide range of applications such as medical prosthetics or soft robotics where specific local load case requirements are needed.

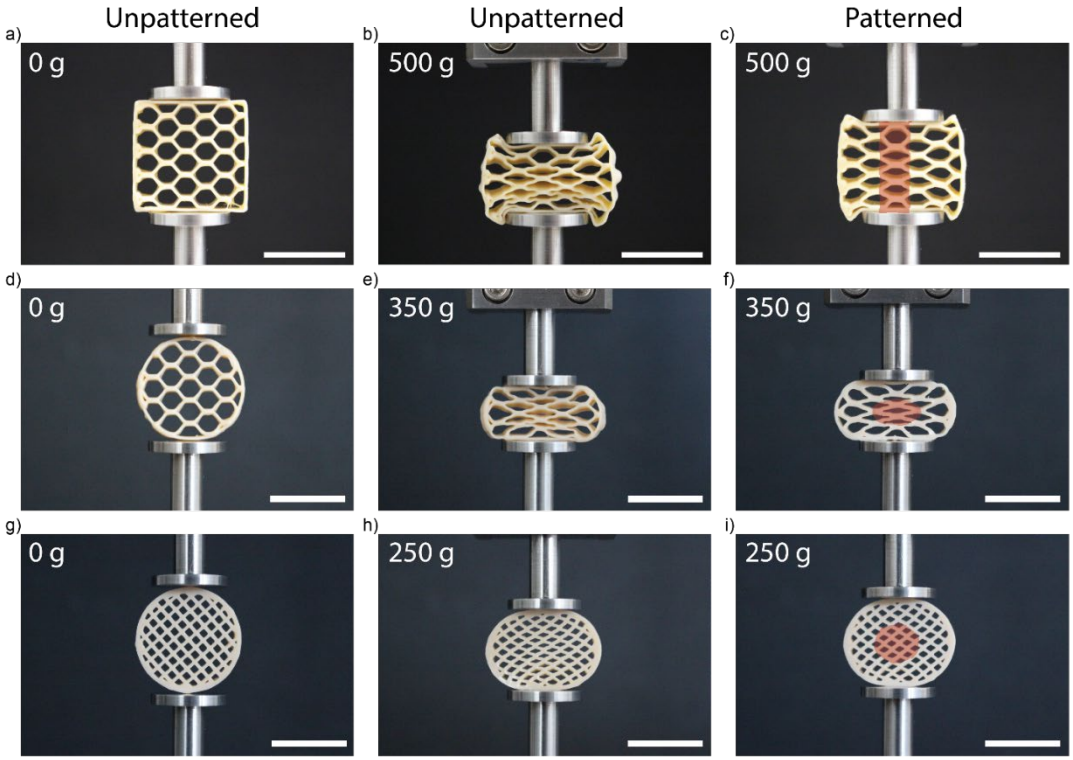

Figure 3.1-5 *Compression of 3D structures printed with an ink formulation containing 30 wt% of cin-CNC. The pictures (a), (d), and (g) represent unpatterned samples without load while the pictures (b), (e), and (h) are the same samples after compressive loading. In the right column (c,f,i), the pictures demonstrate the effect of selectively photocrosslinked regions (illustrated by the red shapes) on the deformation of the samples for the same load case. The white scale bars represent 15 mm.*

3.1.4 Conclusion

We developed an approach to produce mechanically adaptable 3D structures by DIW process, where the mechanical response is tailored upon UV illumination. This method introduces the photostiffening to the produced parts by incorporating biocompatible photocrosslinkable cinnamates on the surface of reinforcing anisotropic nanocellulose particles and into the PUA matrix. The strength of our approach lies in the design freedom arising from the combination of DIW structuring and photopatterning while keeping the simplicity of single material printing. To demonstrate the versatility of the method and possible mechanical responses, produced composites were fully or locally illuminated. Total illumination led to general stiffening and shape fixing ability, while spatial control over illumination led to the formation of localized patterns of soft and rigid domains in the composites, which allowed tailoring both their tensile response and compressive deformation behaviors. Further effects on the mechanical properties of the composites may be accessible by increasing the complexity of patterned designs as well as by varying the light intensity or the illumination time to produce, for instance, graded Young's moduli through the sample. Therefore, combination of light triggered phenomena with the alignment and the concentration of cin-CNC offer vast potential for the development of bioinspired functional graded materials, which can be adapted to particular load cases, required in impact absorbing structures in soft robotic applications or in biomedical prosthetics, sensing and adhesion structures for flexible electronics.

3.1.5 Experimental Section

Materials: Cellulose Nanocrystals (CNC), obtained from Eucalyptus pulp via sulfuric acid hydrolysis, were purchased from University of Maine (Orono, Maine, USA). Cinnamoyl chloride (predominantly trans, 98%) and pyridine (99%) were purchased from VWR while vinyl cinnamate (VCA) (trans, 98%) and DMF (≥99.5% synthesis) were purchased from Sigma Aldrich and Roth AG, respectively. Dymax kindly supplied the polymer matrix, the difunctional polyurethane acrylate (PUA) BR3741A. The photoinitiator, bis(2,4,6-trimethylbenzoyl)-phenylphosphineoxide (Irgacure 819) was acquired from BASF.

cin-CNC production: Grafting of cinnamoyl chloride on the surface of CNC was achieved by esterification of cellulose hydroxyl groups. Freeze dried CNC were dispersed in DMF to obtain a 20 wt% gel. Dispersion and homogenization were achieved by placing the dispersion in a SpeedMixer (DAC 150.1 FVZ) for 5 min at 2000 and 3500 rpm, resting overnight at 5 °C and mixed again before use. 25g of gel CNC/DMF were added to 225g of DMF and stirred for 30 min. The mixture was heated at 70 °C in a three-neck reactor equipped with condenser and previously flushed three times with nitrogen. Excess amount of both cinnamoyl chloride (50 g) and pyridine (50 g) was added to the dispersion and the reaction was carried out for 1 h. The reactor was then immersed in an ice bath to stop the reaction. Modified CNC (cin-CNC) were washed with excess methanol for two times and finally with isopropanol two times. The washing procedure was conducted using a centrifuge (ROTINA-380, Hettich) at 5000 rpm for 10 min for each step. Cin-CNC were finally stored in isopropanol to avoid drying and subsequent undesired agglomeration. All steps of the process were carried out in dark to avoid unwanted photoreactions.

Ink production: Printable gels with CNC or cin-CNC were obtained with variable concentrations of nano-reinforcements. CNC inks were produced in the following way: CNC/DMF dispersion was solvent exchanged with isopropanol by centrifugation (4 times, 5 min at 5000 rpm). In the resulting CNC-isopropanol mixture, the required amount of matrix (BR3741A and vinyl cinnamate with a 50-50 weight

ratio) was added. The solution was stirred overnight and placed in an ultrasonic bath (TUC-150, TEL-SONIC) for 15 min before evaporating all the solvent with a rotary evaporator (Rotovapor R-215, BÜCHI) at 100 mbar and 45 °C. Finally, the photoinitiator, Irgacure 819, was added with 2 wt% in respect to the matrix amount. The obtained gel was mixed twice in the speed mixer at 2500 rpm for 5 min and twice at 3500 rpm for 5 min to obtain a homogeneous ink. Cin-CNC inks were obtained with the same procedure as above, starting directly from the isopropanol dispersion.

3D printing: All composite samples were manufactured with a Direct Ink Writing printer (3D-Bioplotter "Manufacturer Series", EnvisionTEC, Germany). Prior to printing, inks were loaded into 30cc UV shielding cartridges and centrifuged at 2500 rpm for 10 min to remove air bubbles. After loading the cartridge into the printer, the ink was pneumatically extruded with pressures ranging between 1 to 3 bar, through conical nozzles with inner diameter of 0.41 mm. The filaments were deposited on hydrophobized glass slides at speed ranging between 10 and 15 mm s^{-1}. After printing, the produced parts were cured under UV irradiation in nitrogen atmosphere for 20 min. The illuminating set-up was a self-made chamber composed of 5 monochromatic LEDs (410 nm wavelength, 3W).

Photopatterning: Secondary UV illumination of cured printed parts was achieved by placing the samples 13 cm from a flood high pressure mercury lamp (UVASPOT 400/T, Dr Hönle) equipped with an UVC filter (H2 filter, Dr. Hönle) presenting maximum emission peak at 365 nm of wavelength. Photopatterning was carried out using masks positioned directly on the samples. Photopatterning masks were 3D printed with a Fused Deposition Modeling printer (Ultimaker 2+, Ultimaker) in a commercial UV resistant polymer (ASA-X Black - 3mm, Dutch Filaments). The filament was extruded through a 0.40 mm nozzle at a speed of 40 mm s^{-1}. Nozzle and bed temperatures were set to 245 °C and 85 °C, respectively.

Fourier Transform Infrared Spectroscopy (FT-IR): Synthesis of cin-CNC was followed qualitatively with a FT-IR spectroscope (Tensor 27 IR, Bruker) equipped with a ZnSe crystal Attenuated Total Reflectance (ATR) cell. CNC and cin-CNC were characterized as dried powder. Evaporation of isopropanol from cin-CNC solution was achieved in an oven at 60° for 24 h. Measurements were carried out three times per sample in dark and the representative spectrum was selected. Spectra were recorded from 600 to 4000 cm^{-1}, with a resolution of 4 cm^{-1} and 64 scans. Finally, spectra were normalized in respect to the C-O stretching vibration frequency (1060 cm^{-1}) of the β-glucose units since not affected by the chemical reaction [25].

Powder X-Ray Diffraction (XRD): Diffraction patterns of both types of CNC were acquired using an X'Pert Pro XRD system from Panalytical equipped with a Cu Kα monochromator (λ= 1.5418 Å). CNC were dried as explained above and placed on a silicon single crystal holder. Diffraction angles (2θ) from 5° to 90° with step size of 0.016° were used for all XRD characterizations. Crystallinity index of cellulose was then calculated by deconvolution of XRD patterns as reported in [26].

Transmission Electron Microscopy (TEM): The morphology of unmodified CNC was examined using a JEM-2200FS microscope from JEOL with acceleration voltage of 200 kV. CNC were dispersed in water by bath ultrasonication (30 min) and overnight mechanical stirring with a concentration of 0.01 wt%. Carbon coated grid surface was cleaned with 10s of oxygen plasma. A drop of the dilute solution was then deposited on the grid for 60 s before washing with MillQ water. A drop of 2 wt% of uranyl acetate was successively deposited on the samples for 2 min to stain the cellulose nanocrystals. Samples were finally washed again with MillQ water and stored overnight in a desiccator under vacuum.

Atomic Force Microscopy (AFM): Pictographs were acquired in soft tapping mode using an ICON3 AFM from Bruker where commercially available silicon tips (RTESPA-150, Bruker) were

mounted. Samples were prepared according to the procedure used in [27]. CNC and cin-CNC were dispersed in water with a concentration of 2 mg/L and deposited on freshly cleaved mica for 30 s. Positive surface charge of the mica was previously obtained by pouring a 20 µL drop of 0.05 vol% of (3-aminopropyl)triethoxysilane (APTES) for 60 s, rinsed with MilliQ water and dried with pressurized air. The samples were stored under vacuum in a desiccator to avoid contamination prior to measurements. Images were lightly processed to remove bows with the software NanoScope Analysis from Bruker. Diameters of the CNC were measured by the height displacement of the cantilever tip.

Rheological characterization of printing inks: The rheological behavior of all the produced inks was characterized at room temperature with an MCR 302 Anton Paar rheometer in a plate-plate geometry with 25 mm of diameter and 0.5 mm of gap. Flow viscosity was obtained by changing rotational shear rate from 0.001 to 1000 s^{-1} with a logarithmic sweep. While, storage and loss modulus were measured with oscillatory strain variations from 0.01 to 1000 % at a frequency of 1 Hz with logarithmic sweep. Apparent yield stress was defined as the shear stress when storage and loss moduli intersect i.e. the gelation point. Three samples per ink were measured.

Dynamic mechanical analysis (DMA): was carried out using a RSA 3 analyzer from TA Instruments in tensile mode, equipped with liquid nitrogen cooler. Tests were conducted with an initial clamp distance of 20 mm. The measurements were carried out with a frequency of 1 Hz, a strain of 0.04%, from -100 °C to 100 °C and a temperature rate of 3 °C/min. Tested samples were 35 mm x 5mm x 0.35 mm strips cut from a single layer sheet of the printed composites. All samples were tested in printing direction longitudinal to loading direction. For pure matrix samples, the sheets were produced with doctor blade (0.5 mm). Secondary UV illumination occurred right before sample measurement. Measurements were repeated three to five times for each samples condition.

Tensile tests were carried out in an universal mechanical instrument (AGS-X Shimadzu) equipped with a 100 N load cell. Samples were tested at a speed of 5mm min^{-1} at 25 °C and 60% RH. Dog bone specimens with a tested region being 30 mm x 4 mm were obtained by cutting printed single layer sheets with thicknesses around 0.35 mm. As for DMA measurements, printing direction was longitudinal to the loading direction. Photopatterned samples were illuminated for 90 min, stored in a desiccator under vacuum and conditioned for 48 h to measurement room conditions (25 °C and 60% RH) prior testing. A minimum of four measurements per sample was tested. Tensile tests were coupled with digital image correlation (DIC) analysis by recording the sample deformation with a 9 Mpx Manta G-917 camera from Allied Vision Technologies GmbH. Speckle patterns on the samples were made using an Iwata CM-B-SB Airbrush with an acrylic black paint. Image analysis was carried out with the commercial software VIC2D. Only one sample per condition was analyzed as demonstration.

3.1.6 Additional Information

Supporting Information

Supporting Information is available from the Wiley Online Library or from the author.

Acknowledgements

The authors thank A. Huch for the TEM imaging of CNC suspension, R. Boons for x-ray experiments of CNC and MSc. Y. Nagel for the support on the tensile tests and digital image correlation (DCI) of the CNC-based composites. The authors greatly acknowledge the financial support from the Swiss National Science Foundation (grant Nr. 200021_178941/1).

The authors declare no conflicts of interest.

3.1.7 References

[1] Y. Politi, M. Priewasser, E. Pippel, P. Zaslansky, J. Hartmann, S. Siegel, C. Li, F. G. Barth, P. Fratzl, *Adv. Funct. Mater.* **2012**, *22*, 2519.

[2] B. Bar-On, F. G. Barth, P. Fratzl, Y. Politi, *Nat. Commun.* **2014**, *5*, 1.

[3] A. R. Studart, *Chem. Soc. Rev.* **2016**, *45*, 359.

[4] M. G. M. Marascio, J. Antons, D. P. Pioletti, P.-E. Bourban, *Adv. Mater. Technol.* **2017**, *2*, 1700145.

[5] L. Alison, S. Menasce, F. Bouville, E. Tervoort, I. Mattich, A. Ofner, A. R. Studart, *Sci. Rep.* **2019**, *9*.

[6] M. Peng, Z. Wen, L. Xie, J. Cheng, Z. Jia, D. Shi, H. Zeng, B. Zhao, Z. Liang, T. Li, L. Jiang, *Adv. Mater.* **2019**, *31*, 1902930.

[7] S. Sultan, G. Siqueira, T. Zimmermann, A. P. Mathew, *Curr. Opin. Biomed. Eng.* **2017**, *2*, 29.

[8] W. Xu, X. Wang, N. Sandler, S. Willför, C. Xu, *ACS Sustain. Chem. Eng.* **2018**, *6*, 5663.

[9] G. Siqueira, D. Kokkinis, R. Libanori, M. K. Hausmann, A. S. Gladman, A. Neels, P. Tingaut, T. Zimmermann, J. A. Lewis, A. R. Studart, *Adv. Funct. Mater.* **2017**, *27*.

[10] M. K. Hausmann, P. A. Rühs, G. Siqueira, J. Läuger, R. Libanori, T. Zimmermann, A. R. Studart, *ACS Nano* **2018**, *12*, 6926.

[11] D. T. Nguyen, T. D. Yee, N. A. Dudukovic, K. Sasan, A. W. Jaycox, A. M. Golobic, E. B. Duoss, R. Dylla-Spears, *Adv. Mater. Technol.* **2019**, *4*, 1900784.

[12] A. Bandyopadhyay, B. Heer, *Additive manufacturing of multi-material structures*; Elsevier Ltd, 2018; Vol. 129.

[13] L. R. Lopes, A. F. Silva, O. S. Carneiro, *Addit. Manuf.* **2018**, *23*, 45.

[14] K. Bethke, S. Palantöken, V. Andrei, M. Roß, V. S. Raghuwanshi, F. Kettemann, K. Greis, T. T. K. Ingber, J. B. Stückrath, S. Valiyaveettil, K. Rademann, *Adv. Funct. Mater.* **2018**, *28*, 1800409.

[15] M. V. Biyani, C. Weder, E. J. Foster, *Polym. Chem.* **2014**, *5*, 5501.

[16] M. V. Biyani, M. Jorfi, C. Weder, E. J. Foster, *Polym. Chem.* **2014**, *5*, 5716.

[17] J. Wang, A. Chiappone, I. Roppolo, F. Shao, E. Fantino, M. Lorusso, D. Rentsch, K. Dietliker, C. F. Pirri, H. Grützmacher, *Angew. Chemie Int. Ed.* **2018**, *57*, 2353.

[18] C. Zhu, S. R. Kustra, C. J. Bettinger, *Acta Biomater.* **2013**, *9*, 7362.

[19] J. E. Smay, J. Cesarano, J. A. Lewis, *Langmuir* **2002**, *18*, 5429.

[20] F. Pinto, M. Meo, *Appl. Compos. Mater.* **2017**, *24*, 643.

[21] S. Khandavalli, J. P. Rothstein, *Rheol. Acta* **2015**, *54*, 601.

[22] A. Lendlein, H. Jiang, O. Jünger, R. Langer, *Nature* **2005**, *434*, 879.

[23] B. Wang, J. Zhou, Z. Wang, S. Mu, R. Wu, Z. Wang, *Carbohydr. Polym.* **2020**, *231*, 115739.

[24] H. Wang, M. Totaro, L. Beccai, *Adv. Sci.* **2018**, *5*, 1800541.

[25] M. Planes, J. Brand, S. Lewandowski, S. Remaury, S. Solé, C. Le Coz, S. Carlotti, G. Sèbe, *ACS Appl. Mater. Interfaces* **2016**, *8*, 28030.

[26] S. Park, J. O. Baker, M. E. Himmel, P. A. Parilla, D. K. Johnson, *Biotechnol. Biofuels* **2010**, *3*.

[27] M. Arcari, E. Zuccarella, R. Axelrod, J. Adamcik, A. Sánchez-Ferrer, R. Mezzenga, G. Nyström, *Biomacromolecules* **2019**, *20*, 1288.

3.1.8 Supporting Information

Mechanical properties tailoring of 3D printed photo-responsive nanocellulose composites

*Luca A. E. Müller, Tanja Zimmermann, Gustav Nyström, Ingo Burgert, Gilberto Siqueira**

DOI: 10.1002/adfm.202002914

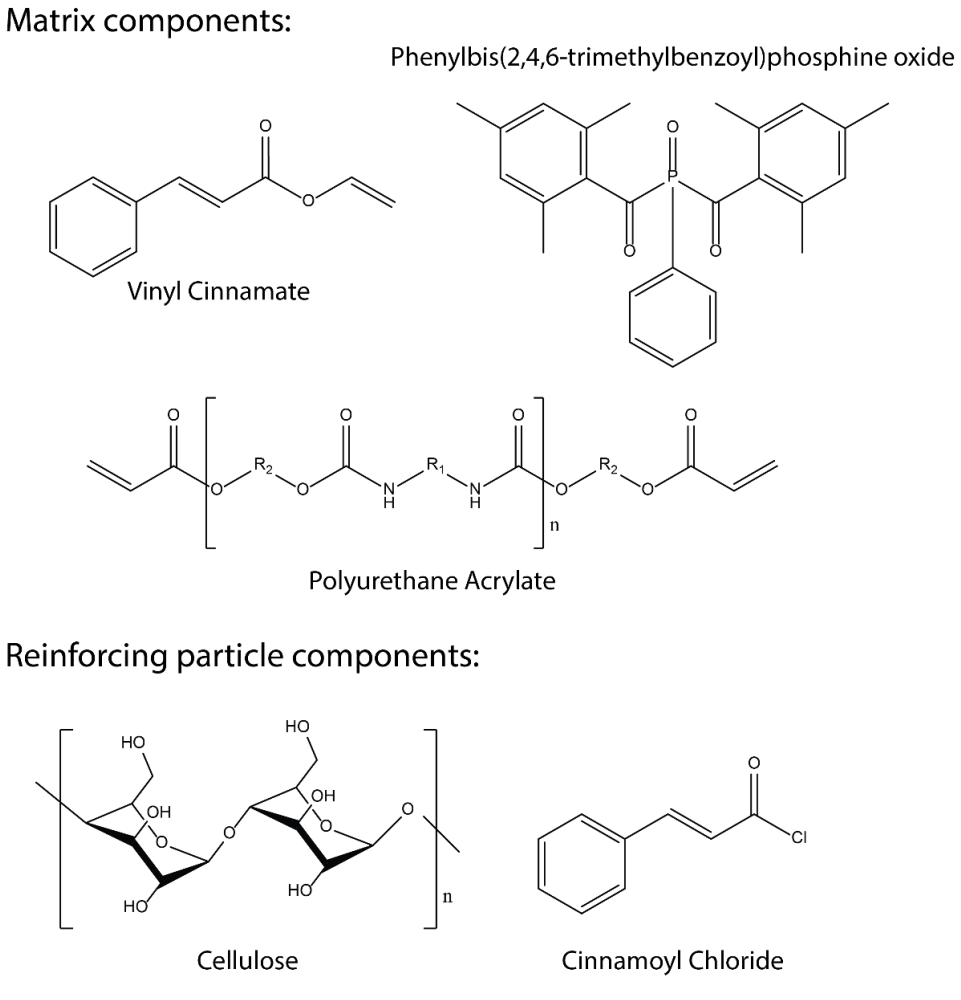

Figure S3.1-1 *Chemical structure of main chemicals composing both matrix and reinforcing particles.*

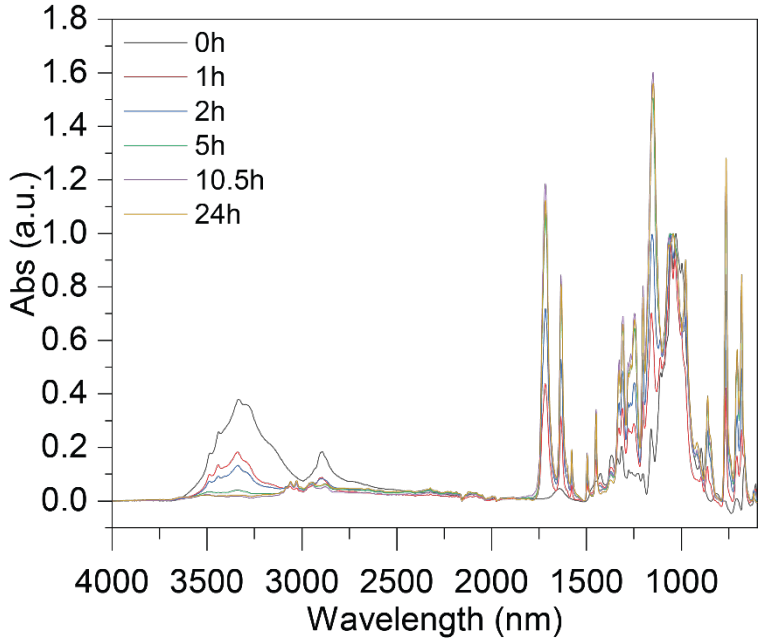

Figure S3.1-2 *FTIR spectra of CNC in function of reaction time during the process of Cinnamoyl chloride grafting.*

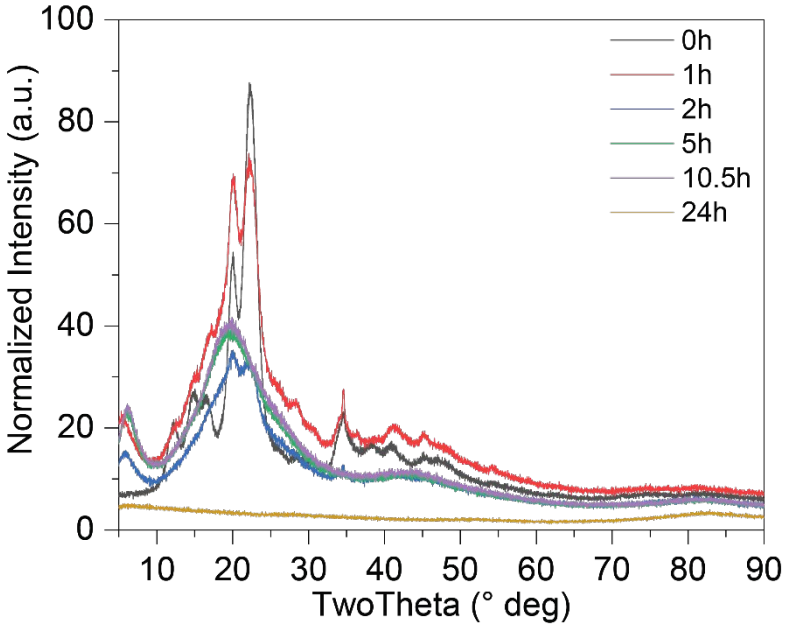

Figure S3.1-3 *XRD pattern of CNC in function of reaction time during the process of Cinnamoyl chloride grafting.*

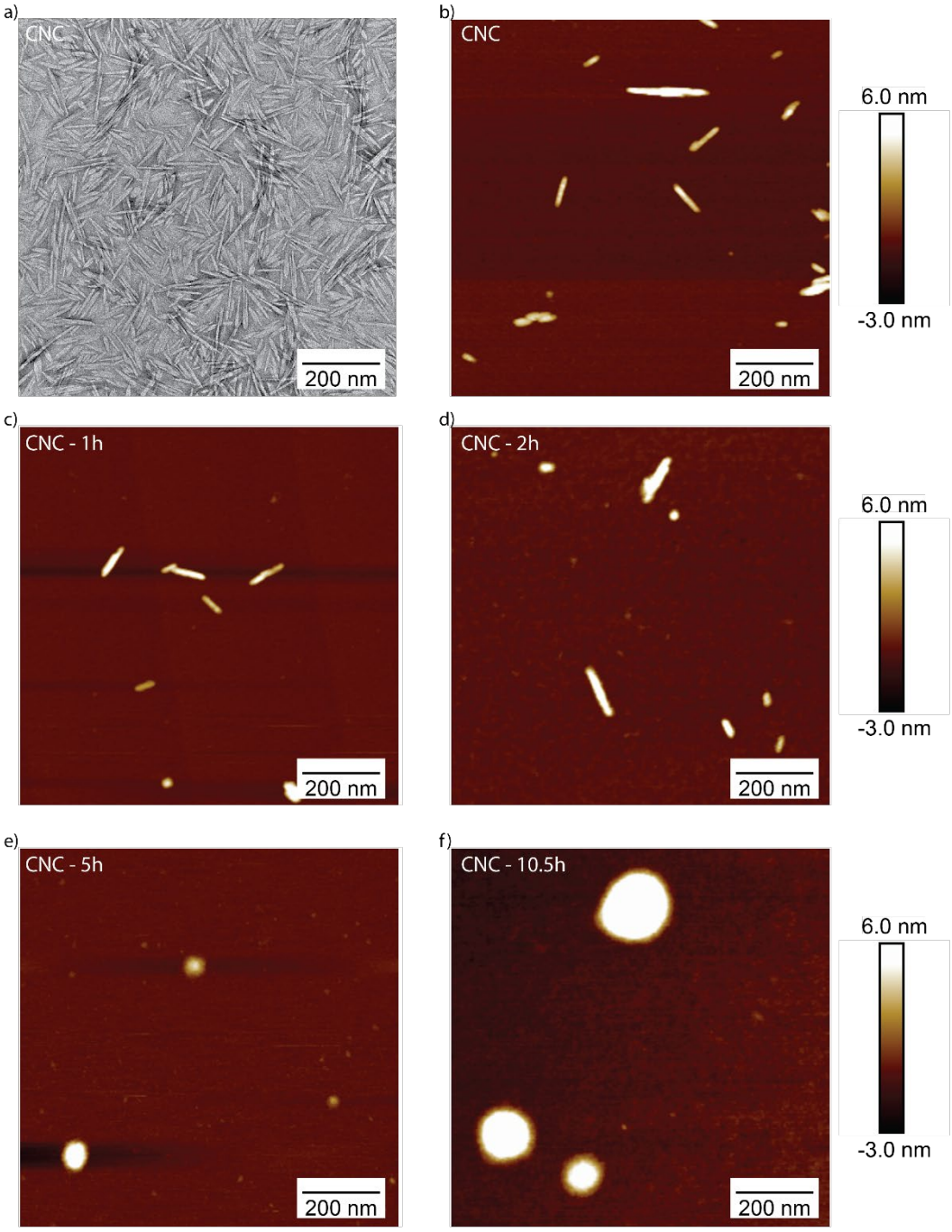

Figure S3.1-4 *a) TEM pictograph of CNC before modification. b) AFM image of CNC before modification. c to d) in order, AFM representing cin-CNC morphology after 1, 2, 5 and 10.5 h of reaction time during modification. Note that the 24h sample could not be observed by AFM measurements.*

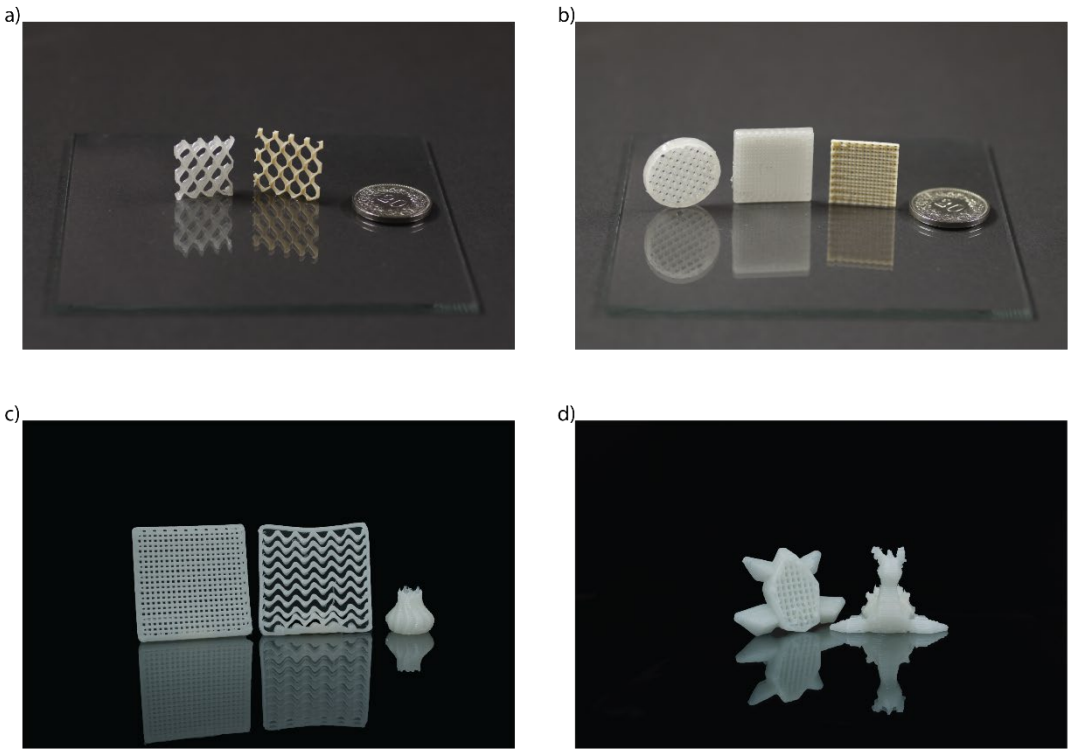

Figure S3.1-5 *Demonstration of 3D printed structures processed by DIW of 15 wt% CNC inks (whitish colored) and 30 wt% of cin-CNC inks (beige-brownish colored).*

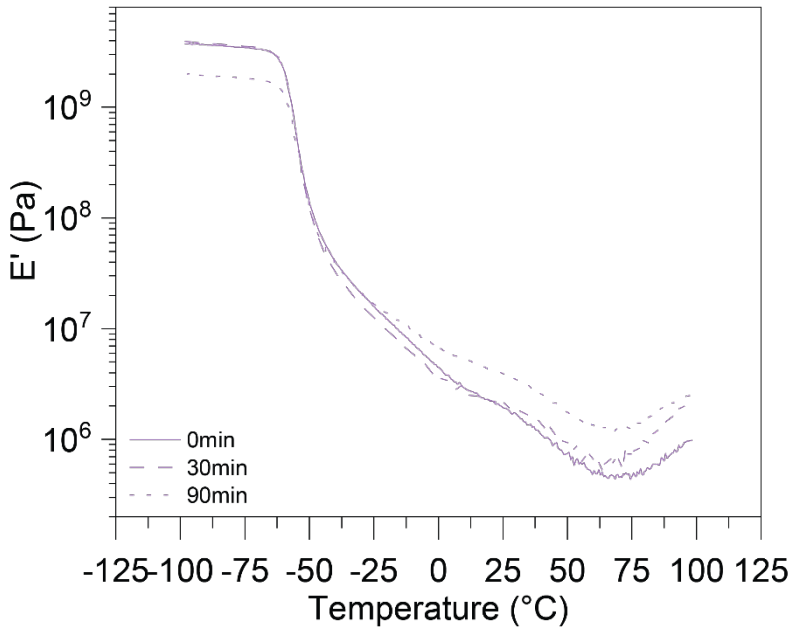

Figure S3.1-6 *DMA measurements of pure matrix in function of secondary UV illumination time.*

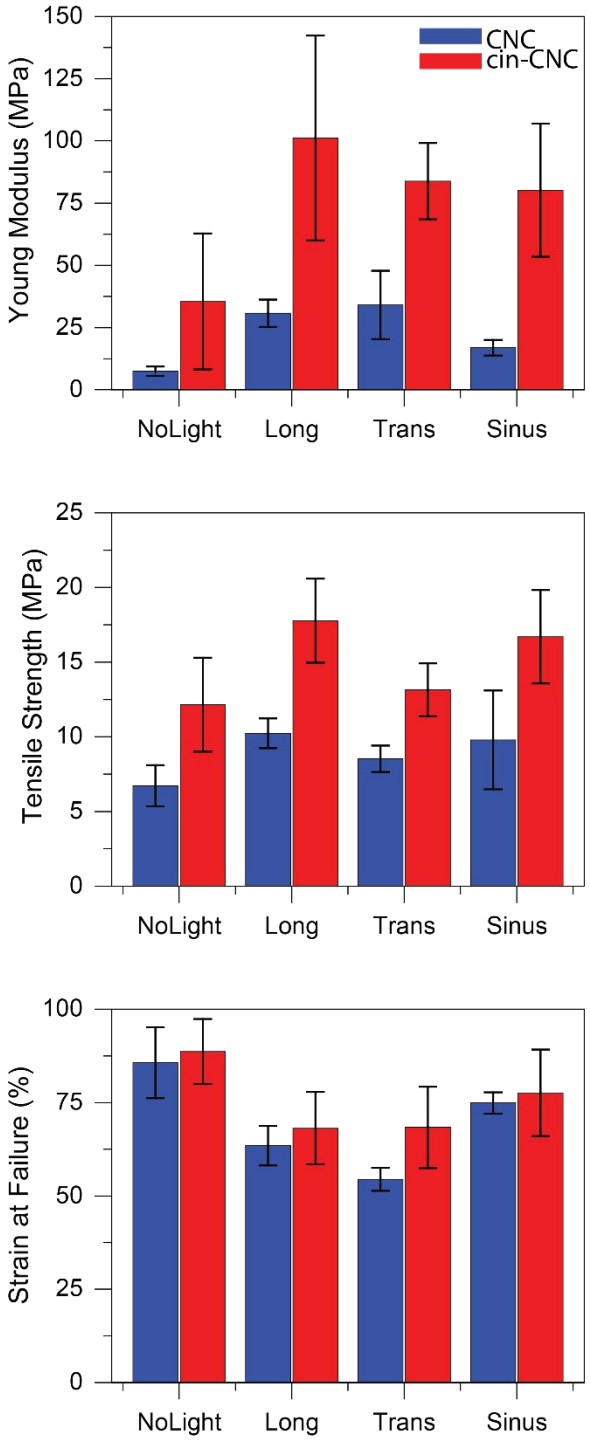

Figure S 3.1-7 *Values obtained by tensile tests for Young modulus, tensile strength and strain at failure of composites with 15 wt% of CNC or cin-CNC. Values represent measurements of 4 samples.*

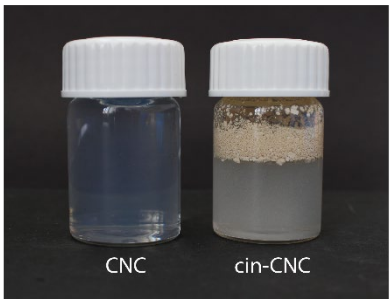

Figure S3.1-8 *CNC and cin-CNC in water after 30 minutes of stirring. The chemical modification strongly decreased the cin-CNC affinity to water, since the particle do not disperse and stay at the air water interface.*

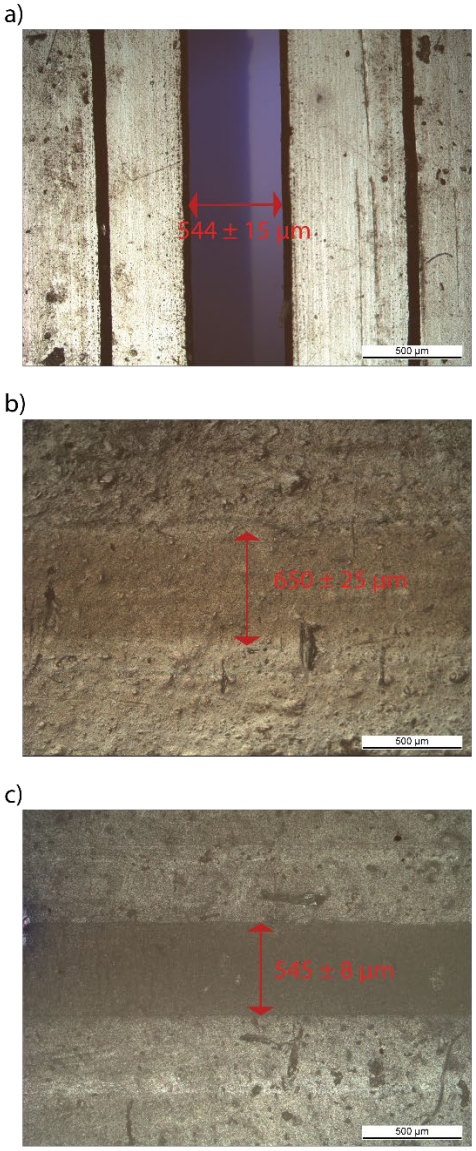

Figure S 3.1-9 *a) Micrograph of the photomask employed to photopattern the longitudinal patterns on (b) 15 wt% CNC composites and (c) 15 wt% cin-CNC composites. The width of the illuminated pattern was estimated from the micrographs.*

3.2 Photoresponsive Movement in 3D Printed Cellulose Nanocomposites

Luca A. E. Müller[1,4], Adrien Demongeot,[2] Joanne Vaucher,[2] Yves Leterrier,[2] Jonathan Avaro,[3] Marianne Liebi,[3] Antonia Neels,[3] Ingo Burgert,[4] Tanja Zimmermann,[1] Gustav Nyström,[1,5] Gilberto Siqueira**

[1]Cellulose and Wood Materials Laboratory, Empa, Swiss Federal Laboratories for Materials Science and Technology, 8600 Dübendorf, Switzerland.

[2]Laboratory for Processing of Advanced Composites (LPAC), Ecole Polytechnique Fédérale de Lausanne, EPFL-STI-IMX-LPAC, Station 12, CH-1015 Lausanne, Switzerland.

[3]Center for X-ray Analytics, Empa, Swiss Federal Laboratories for Materials Science and Technology, 8600 Dübendorf, Switzerland.

[4]Wood Materials Science, Institute for Building Materials, ETH-Zürich, 8093 Zürich, Switzerland.

[5]Department of Health Sciences and Technology, ETH Zürich, 8092 Zürich, Switzerland.

*Corresponding authors: Gustav Nyström, Gilberto Siqueira

E-Mail addresses: gustav.nystroem@empa.ch , gilberto.siqueira@empa.ch

3.2.1 Abstract

Photoresponsive soft liquid crystalline elastomers (LCEs) transform light's energy into dynamic shape changes and are considered promising candidates for production of soft robotic or muscle-like devices. 3D printing allows access to elaborated geometries as well as control of the photoactuated movements; however, this development is still in its infancy and only a limited choice of LCE is yet available. Herein, we propose to introduce biocompatible and sustainable cellulose nanocrystals (CNC) into an LCE in order to facilitate the printing process by direct ink writing (DIW) and to benefit from the anisotropic mechanical properties resulting from the extrusion-induced alignment of such nanoparticles. After a first printing step where the rheological influence of CNC allows the production of self-standing structures, a doping process introduces the azobenzene photoswitches in the composite, conferring photomechanical behaviors to the printed material. This approach results in soft composites, with an elastic modulus around 20-30 MPa, that present fully reversible photosoftening of 35% and photomechanical actuation occurring less than 3 s after illumination. The presence of CNC as reinforcement particles allows precise tailoring of mechanical properties, rendering such phototriggered materials suitable candidates for the production of actuators and 3D structures with particular and dynamic load cases.

Keywords: *cellulose nanocrystals, photoresponsive elastomers, azobenzene, 3D printing, shape-changing*

3.2.2 Introduction

Dynamic shape transformations, leading to motion, are widely observed in living creatures. From the movements of Mimosa pudica leaves [1], the closure of Venus flytraps [2], to the skeletal muscle's active contractions [3] and beyond, all these astonishing examples are an important source of inspiration in the development of smart shape changing materials triggered by external stimuli such as heat, light, pH or humidity [4]-[7]. The efficient translation of a stimulus into motion, without the use of hydraulic systems, hinges, or engines, is very appealing in the production of lightweight devices such as actuators

[8], sensors [9],[10], and soft robots [11],[12]. Furthermore, such materials could open the venue to applications where fine adaptability is required, like within the biomedical domain [13],[14]. Among the large variety of existing shape changing materials, light triggered liquid crystalline elastomers (LCEs) have been extensively investigated [15],[16]. LCEs have emerged as promising candidates for the development of fast and reliable actuators since they generally present a rapid and reversible response. The main mechanism of photoresponsive actuation in LCEs lies in the trans-cis photoisomerization of azobenzene derivatives. When an LCE, presenting an aligned nematic LC phase with incorporated azobenzenes is illuminated with the appropriate wavelength, the azobenzenes change from trans to cis conformation and reduce their size. This consequently decreases the order of the aligned LC mesogens, triggers the LC phase transition from nematic to isotropic, and hence, leads to a strong contraction (up to 30%) [17] along the LC director direction. Control over the LC arrangement determines the direction and type of movement exhibited by the LCE and complex 3D deformations such as bending, twisting, and curling can be obtained [18],[19]. Since light is a noncontact stimulus, it allows remote actuation with precise spatial and temporal control. Structuring the light, as well as tuning its properties (wavelength, intensity, polarization), allows control over the LCE movements and leads to different actuating responses within the same material [17]. The recent advances in the production of photomobile LCE allows the occurrence of nonreciprocal and reprogrammable movements [20] by combining different azobenzenes within the polymer network. Although such interesting and complex movements can be obtained with simple geometries such as tubules and films, the inherent need for aligning the LC mesogens in the polymer network with strain induced alignment [21] or LC alignment cells [22] strongly limits the achievable shapes to 2D configurations.

With the advent of additive manufacturing, and in particular, the development of 3D printing technologies, important progress has been made in the manufacturing of all kinds of shape changing materials with complex 3D shapes [6],[23],[24]. Indeed, 3D printing is a versatile platform that produces 3D structures in a bottom up approach. Thus, it presents a great geometrical freedom and spatial control over the material's composition, making these technologies suitable for the production of functional materials [25]. In particular, direct ink writing (DIW) has been demonstrated as the printing technique of choice for the production of thermally actuated LCEs 3D elements [26]−[29]. Here, uncured main chain LCE inks at temperatures higher than the nematic to isotropic transition can be deposited as filaments by extrusion through a nozzle and subsequent immediate photocuring to fix the polymer network. The shear and extensional stresses experienced by the ink during the extrusion are responsible for the alignment of the LC mesogens along the printing direction. These stresses impart precise control over the LC director and determine the actuated movements [28]. Hence, by controlling the printing design and parameters like nozzle diameter, printing speed, and temperature, LCEs have been manufactured in thermally activated structures able to display predetermined deformations like a 2D disc evolving to a 3D cone [26]. Instead, the additive manufacturing of photomechanical LCE containing azobenzene derivatives is a recent development. Based on the same approach as for thermally activated LCE, the introduction of pendant azobenzene groups in a polysiloxane backbone [30] or as main chain in LCE [31] prior to printing, enables the creation of 3D printed LCE actuators presenting bending in the printing direction and muscle-like contractions [31] as a response to illumination. Nevertheless, this emerging technology is still in its infancy, and the choice of available materials is still very limited, leaving space for the development of new materials for tailored applications.

Up to now, the 3D printing of photomechanical LCEs has been mainly focused on processing "pure" LCEs, that is, materials without reinforcement phases. The use of reinforcements would allow further tuning of the mechanical properties of such materials, opening the venue for photoresponsive 3D structures. The DIW not only allows control over the LC director and hence predetermines the photoactuated

movements, but it also allows the production of synthetic materials with controlled microstructures that begin to mimic the complexity of biological materials and their outstanding mechanical properties [25]. In particular, DIW of polyurethanes with natural building blocks, such as cellulose nanocrystals (CNC), demonstrated the production of cellular structures with spatially tailored mechanical properties [32], which presented up to a 10-fold increase in stiffness (along the printing direction) compared to the bare matrix. The tailored mechanical properties are obtained due to CNC's anisotropic shape: CNC experiencing shear and extensional flows during printing are aligned along the printing direction [32]−[34], promoting spatial control over the stiffness anisotropy. While CNC are suitable biocompatible and biodegradable reinforcements, they are also colloids that modify the rheological behavior of dispersions creating shear-thinning gels, processable by DIW printing [32],[35],[36]. However, addition of such natural building blocks in a 3D printed photomechanical LCE has been reported only for small amounts (<4 wt %), exploiting mainly the particles' ability of improving LC mesogens ordering during extrusion [37]. The development of lightweight devices combining tailored mechanical properties with photomechanical actuation presents a certain potential for the future of soft robotics and for biomedical applications, where both properties and stimulus responses shall be highly customized in order to sustain specific load cases.

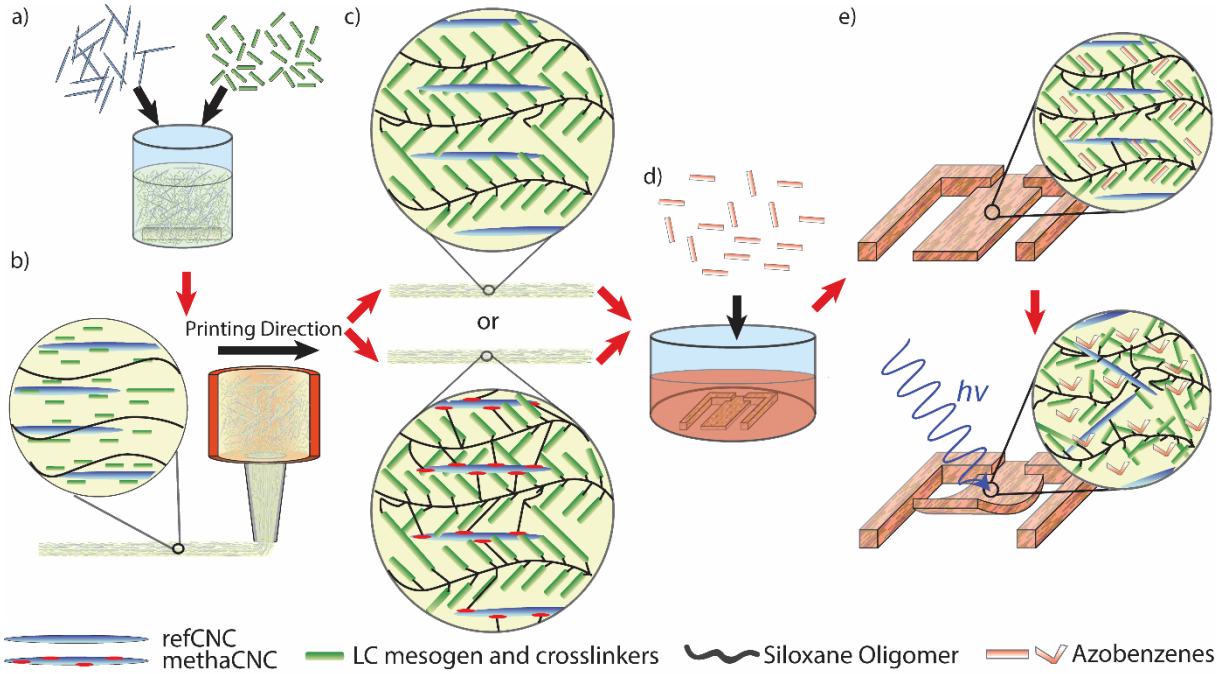

Figure 3.2-1 *Schematic illustration of the approach utilized in preparation of cellulose-based inks and composites. LC mesogens, cross-linkers, and CNC are added in the poly(mercaptopropyl)methylsiloxane (PMMS) matrix for the preparation of the printable ink (a). When the inks are prepared, they are printed by DIW. Here the LC mesogens and the CNC align along the printing direction (b). After curing the materials, unmodified CNC (refCNC) remain dispersed into the polymer without being linked to the matrix, while methacrylated CNC (methaCNC) can form bonds with the matrix (c). The 3D printed structures are immersed in an acetone/DR1 bath in order to allow the inclusion of the azobenzene (d). The printed structures consist of a side chain LCE that is illuminated, the presence of azobenzene triggers the LC nematic to isotropic phase transition and increases the LC disorder, resulting in a macroscopic bending (e).*

In order to tackle these challenges and to increase the available palette of 3D printable photoresponsive composites, we propose a novel approach allowing 3D printing of photoactuated CNC based LCE nanocomposites, which undergo reversible bending as well as dynamic softening when irradiated with

blue/green light. By introducing CNC in an LCE polymer matrix, we intend to harness the well-known rheological influences of such natural building blocks to allow printing of self-standing structures, promoting LC alignment while reducing the total amounts of LC mesogens. Furthermore, in order to evaluate the influence of particles' surface chemistry on the printed LCE's processability and properties, we study two types of CNC, one unmodified (named refCNC) and one functionalized with methacrylate groups (named methaCNC) that allow covalent bonding between the matrix and the particles. Hence, the printable inks consist respectively of one type of CNC dispersed in a mixture of unreacted polysiloxane backbone with mercaptopropyl groups as the main oligomer and acrylated LC mesogens and cross-linkers, forming the side chain LCE matrix. After a simple one-pot mixture of all the components, the inks can be printed at room temperature into 3D structures (Figure 3.2-1). We evaluated how the effect of CNC on the dispersion's rheology promotes the printing of self-supporting structures that are successively photocured. We also investigated whether the high pressures applied during printing allow for the alignment of both LC mesogens (required for the photoactuated movements) and CNC, tuning the mechanical properties of the final composite. In our method, the photoswitching azobenzene molecules are dispersed into the cured LCE network in a further doping step by immersing the printed structure in an azobenzene/acetone solution. The doped 3D structures can then be irradiated with 480 nm light causing the trans-cis azobenzenes' photoisomerization that leads to a decrease in the LC and CNC order and triggers the photoactuated movement. Finally, this approach results in the production of composite devices with 3D complex geometries that can dynamically respond to light, either with movements or with changes in their mechanical properties. Such functionalized materials could find application as photomobile modules and actuators or 3D adaptive structures for mechanical dampers or vibration absorbers where an instantaneous light activated softening is beneficial.

3.2.3 Results and Discussion

3.2.3.1 3D Printing of Composite LCE.

The first step in the production of 3D printed photomechanical structures consists of the production of a printable ink that can be processed by DIW. In particular, such inks shall satisfy three main rheological conditions known as printability requirements [25],[32],[34],[35], namely a strong shear thinning, storage (G'), and loss (G'') moduli higher than few kPa and the apparent yield stress τy, defined as shear stress when $G' = G''$ is higher than 100 Pa. Anisotropic CNC have already been widely used as mechanical reinforcements and demonstrated their ability to act as reinforcing agents as well as rheology modifiers in 3D printed biocompatible structures [6],[32],[35]. In the present work, unmodified CNC, referred as refCNC, and CNC presenting methacrylate groups on their surfaces [32], referred to as methaCNC, were employed in order to establish the differences in the photomechanical behavior between composites with unlinked particles or particles covalently bonded to the polymer matrix. The two types of particles were then separately incorporated into a mixture comprising a thiolene polysiloxane oligomer (poly(mercaptopropyl)- methylsiloxane homopolymer), acrylated LC mesogens (4- Methoxybenzoic acid 4-(6-acryloyloxyhexyloxy)phenyl), and cross-linkers (1,4-Bis-[4-(3-acryloyloxypropyloxy)benzoyloxy]- 2-methylbenzene), and a photoinitiator (Irgacure 819) (Supporting Information (SI) Figure S 3.2-1), leading to the formation of a side chain LCE matrix after polymerization.

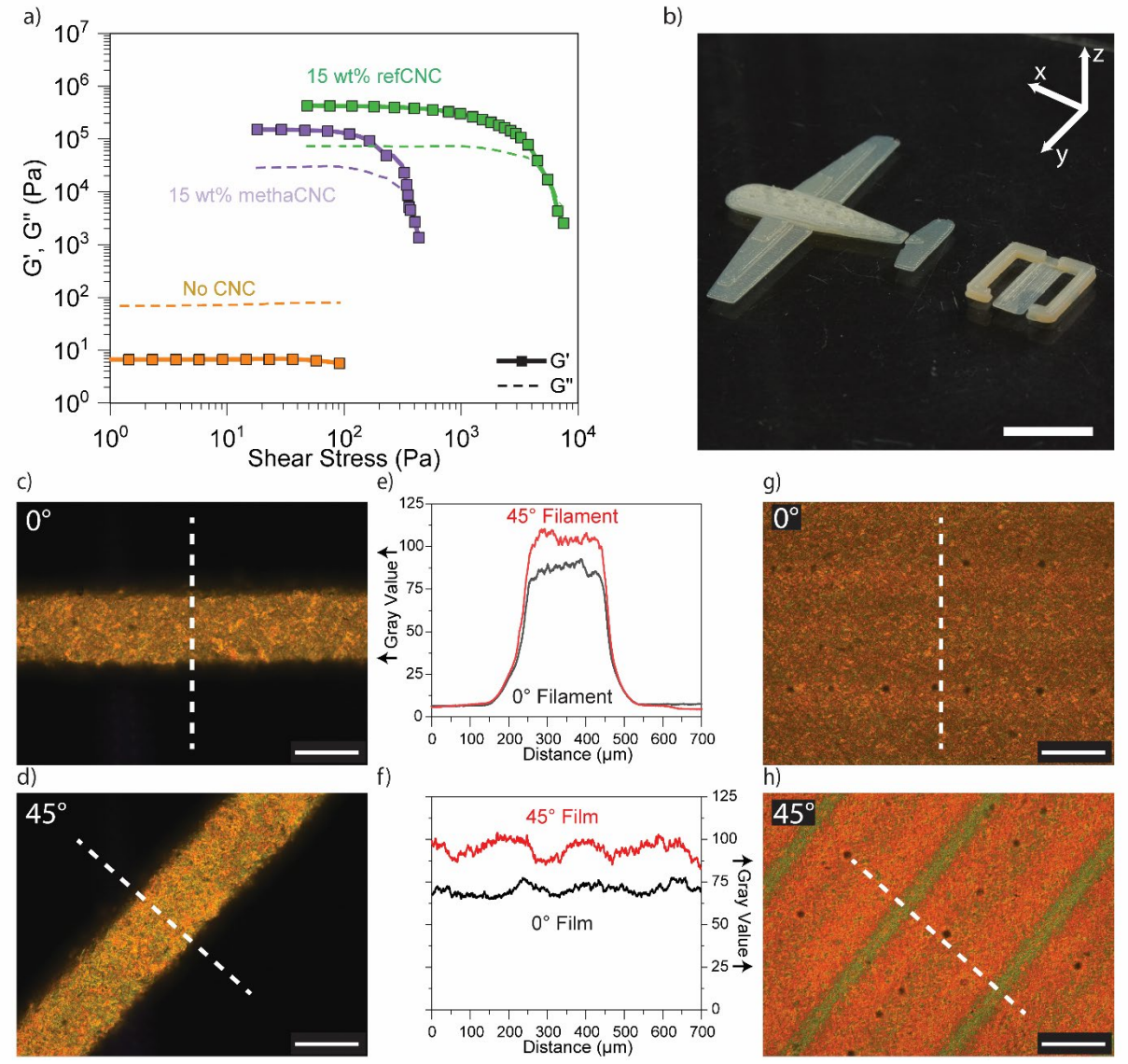

Figure 3.2-2 *Rheology of the inks allows printing of 3D parts with crystals (CNC and LC mesogens) oriented along the printing direction. (a) Oscillatory rheology (1 Hz) of the 15 wt % inks and the bare matrix. (b) 3D printed structures after photocuring (scale bar 10 mm). (c) and (d) 10× cross polarizer micrographs of methaCNC based printed filaments with printing direction at 0° and 45° with respect to light polarization, respectively. (e) Graph representing the gray value estimated from (c) and (d) along the white dotted lines. (f) Graph representing the gray value estimated from (g) and (h) along the white dotted lines. (g) and (h) 10× cross polarizer micrographs of printed films with printing direction at 0° and 45° with respect to light polarization, respectively. The scale bars of all micrographs represent 200 µm.*

The addition of 15 wt % of both types of CNC into the liquid crystalline matrix (Figure 3.2-2) successfully allows the production of 3D structures by DIW, presenting a determined alignment of crystals along the printing directions. Importantly, with the employed DIW setup, 15 wt % of CNC was the only concentration allowing printing. Lower concentrations of CNC could not be printed in the Z direction while higher concentrations reached prohibitive pressures. Since the effect of concentration on suspension rheology is well established and reported elsewhere [32],[34], we focused on this single concentration (15 wt %) to investigate the influence of CNC surface chemistry on the suspension properties. Oscillatory rheological experiments (Figure 3.2-2a) confirm the role of refCNC and methaCNC on transforming the bare liquid crystalline matrix into printable inks. The bare resin presents a liquid-like Newtonian behavior across the full range of tested shear stresses, with G″ around 70 Pa and G′ around 7 Pa. In contrast, both inks containing 15 wt % of CNC reinforcements present a solid-like behavior (at

low shear stresses) followed by a strong shear thinning (at high shear stresses). Due to the CNC's anisotropic shape, refCNC, and methaCNC form a percolating network at rest [32]−[34]. This imparts the elastic response to the inks, increasing G′ of several orders of magnitude, going from 7 Pa for the pure matrix to few hundreds kPa for the composites. When the shear stress reaches the inks' yield stress, the percolating network of cellulose nanocrystals start to disrupt. The particles align due to shear and extensional forces [33], providing the strong observed shear thinning behavior of the inks, with power law exponents of 0.2 and 0.1 for refCNC and methaCNC, respectively. Despite the similar changes that both types of CNC provide to the rheology of the matrix, refCNC present the strongest influence on storage modulus and yield stress. While methaCNC samples show a G′ around 150 kPa at low shear stresses (<100 Pa), refCNC inks possess a storage modulus around 425 kPa at similar shear stress. Moreover, τy is highly influenced by the CNC surface chemistry. In particular, methaCNC inks have a lower τy (350 Pa) compared to the one of refCNC (6000 Pa). The increased compatibility of methaCNC with the acrylate LC matrix and the reduction of available OH groups on their surfaces, due to the methacrylation reaction, explain this difference [32],[34]. It is important to note that the lower storage modulus and apparent yield stress presented by methaCNC inks resulted in easier printing with lower pressure values (2.5-3 bar) when compared to the materials prepared with refCNC inks (3.5- 4.5 bar). Furthermore, refCNC inks show frequent clogging of the nozzle during printing, probably due to the greater presence of hydroxyl groups, promoting CNC aggregation via nanocellulose particles hydrogen bonding. Comparing the cross sections of cured filaments for the two types of CNC by SEM (SI Figure S 3.2-2) revealed a larger number of agglomerates for refCNC composites. Such agglomerates are attributed as cellulose clusters and might arise more in refCNC due to the abundant presence of hydroxyl groups on the particle surface [32]. With the observed rheological properties, both inks could be successfully printed in custom 3D structures, and the parts' shape was successively fixed by 10 min of photocuring at 405 nm wavelength, followed by 30 min post cure with a high pressure mercury lamp (main emission peak at 365 nm). An example of cured printed parts is illustrated in Figure 3.2-2b for the methaCNC formulation.

In order to qualitatively access the alignment of CNC and LC mesogens along the printing direction, cured filaments and single layer films were printed by DIW and observed with an optical microscope equipped with cross-polarized filters, while the sample was rotated from 0° to 45° with respect to the polarizer direction, as shown in Figure 3.2-2c-h. Polarized optical microscopy has been widely used to study the structure of liquid crystalline phases, since they present birefringence [41]−[43]. In a liquid crystalline material nematically aligned parallel to the polarizer (0°), the incoming light (polarized parallel to the LC director) is transmitted undisturbed, successively canceled by the analyzer, leading to a dark image. Differently, when the nematic phase is observed at 45° with the polarizer, a maximum scattering of light is achieved, maximizing light transmittance through the analyzer, thus producing a brighter image. Hence, according to Figure 3.2-2c,d our printed filaments indicate a nematic alignment of crystalline components along the printing direction. Moreover, in printed films, illustrated in Figure 3.2-2g,h, in addition to a change in light intensity, a strong color change, is observed when turning the sample. Despite quantitatively observing the general alignment with the micrographs and further confirming by integrating the pixel's gray values transversally to the printing direction (Figure 2e,f), it was not possible to distinguish the LC mesogens alignment from the well-established alignment of the cellulose particles [32],[33],[44],[45]. Nevertheless, samples that were cured at 60 °C, above the nematic to isotropic phase transition temperature (T_{NI}) of the uncured resin, presented only a slight change in light intensity when analyzed at a 45° angle with respect to the polarizer. This change is assumed to come from the alignment of CNC, indicating that the isotropic LC mesogens did not present an overall

alignment (SI Figure S 3.2-3). Importantly, the samples cured with the isotropic LC mesogens did not show any photomechanical responses after the introduction of the photoswitching molecule.

3.2.3.2 Introduction of Photoswitches in the Printed Materials.

Disperse Red 1 (DR1) (SI Figure S 3.2-4) was chosen as the photoswitching molecule due to its very fast isomerization and short cis lifetime leading to fast actuation (seconds) under illumination and reverse actuation in dark conditions [46]−[48]. The dispersion of such a component into the printed composites was achieved after printing with acetone/ DR1 solutions. A similar process was reported by Camacho- Lopez et al., [49] who dispersed Disperse Orange 1 in a polysiloxane side chain LCE. This resulted in a photoactuated material with very fast response to light stimulation in the order of milliseconds. We adopted this approach in order to facilitate the printing process. Although initial attempts, with DR1 directly incorporated in the ink before printing, were successful, the printed structures were limited to a single layer. The curing depth of such samples did not allow thicker structures to cure homogeneously during the photopolymerization. Differently, in the second approach, doping of 3D structures with DR1 was successfully achieved by swelling and impregnating the already 3D printed parts in an acetone/DR1 solution for 24 h at room temperature. Two concentrations of DR1 in acetone were utilized, 0.5 mg mL^{-1} and 5 mg mL^{-1}. For simplicity, the samples issued from this doping bath are named Azo05 and Azo5, respectively, while samples without DR1 are referred as NoAzo. Following the doping bath, samples were dried at room temperature under vacuum overnight.

The azobenzene dye has been successfully dispersed in the composites (Figure 3.2-3). A strong red color indicates the presence of DR1 in the composites due to the strong absorbance of the azobenzene in the blue/green region of the visible spectrum (Figure 3.2-3a,b). A UV-vis spectrophotometer equipped with integrating sphere was used to confirm the dispersion of DR1 in the printed composites. Figure 3.2-3a shows the absorption of the single layer samples normalized by their thickness. Both refCNC and methaCNC composites only present an absorption peak from 350 to 450 nm, which was attributed to unreacted photoinitiator. Differently, Azo05 samples show a second peak in the visible range, with absorption maxima at 524 and 508 nm for refCNC and methaCNC respectively, while Azo5 samples presented the same peaks with a very strong absorption that could not be measured by the instrument. Previous observations of DR1 in acetone (SI Figure S 3.2-4) show a UV-vis spectrum with a main peak at 488 nm and a second minor peak at 285 nm. Interestingly, when DR 1 is dispersed into our composites, it undergoes a red shift, which is also observed between methaCNC composites and refCNC samples. This solvatochromism was previously observed for DR1 [46] and is explained by the strong dipole moment of the molecule in the ground state, which presents an electron acceptor group and an electron donor group substituted on the two aromatic rings. When the photoisomerization occurs, DR1 conserves its dipole moment, in the same direction, becoming more polar. The hydroxyl groups of the cellulose nanoparticles may stabilize the excited state of DR1 by hydrogen bonding leading to the positive red shift, and it explains why such shift is more important in the refCNC than in the methaCNC samples. Nevertheless, the concentration of DR1 in the Azo05 composites could be calculated from the UV-vis spectra and amounts to around 0.15 and 0.10 wt % for refCNC and methaCNC respectively.

In Figure 3.2-3c, the DSC analysis shows that introduction of the azobenzene molecules into the polymer network does not influence the samples' phase transitions. For both refCNC and methaCNC NoAzo composites, DSC curves show a glass transition temperature (Tg) between 4° and 6 °C and a change of the heat flow slope occurring between 60° and 65 °C, which was attributed to the nematic to isotropic phase transition of the side chain LC mesogens and is in agreement with DSC measurements carried out on the bare 4-methoxybenzoic acid 4-(6-acryloyloxyhexyloxy)phenyl and on uncured inks (SI Figure S

3.2-5). Accordingly, Azo05 and Azo5 composites of both CNC surface chemistries possess the same features indicating that both, the presence and the concentration of DR1, do not alter the phase transition temperatures of the materials.

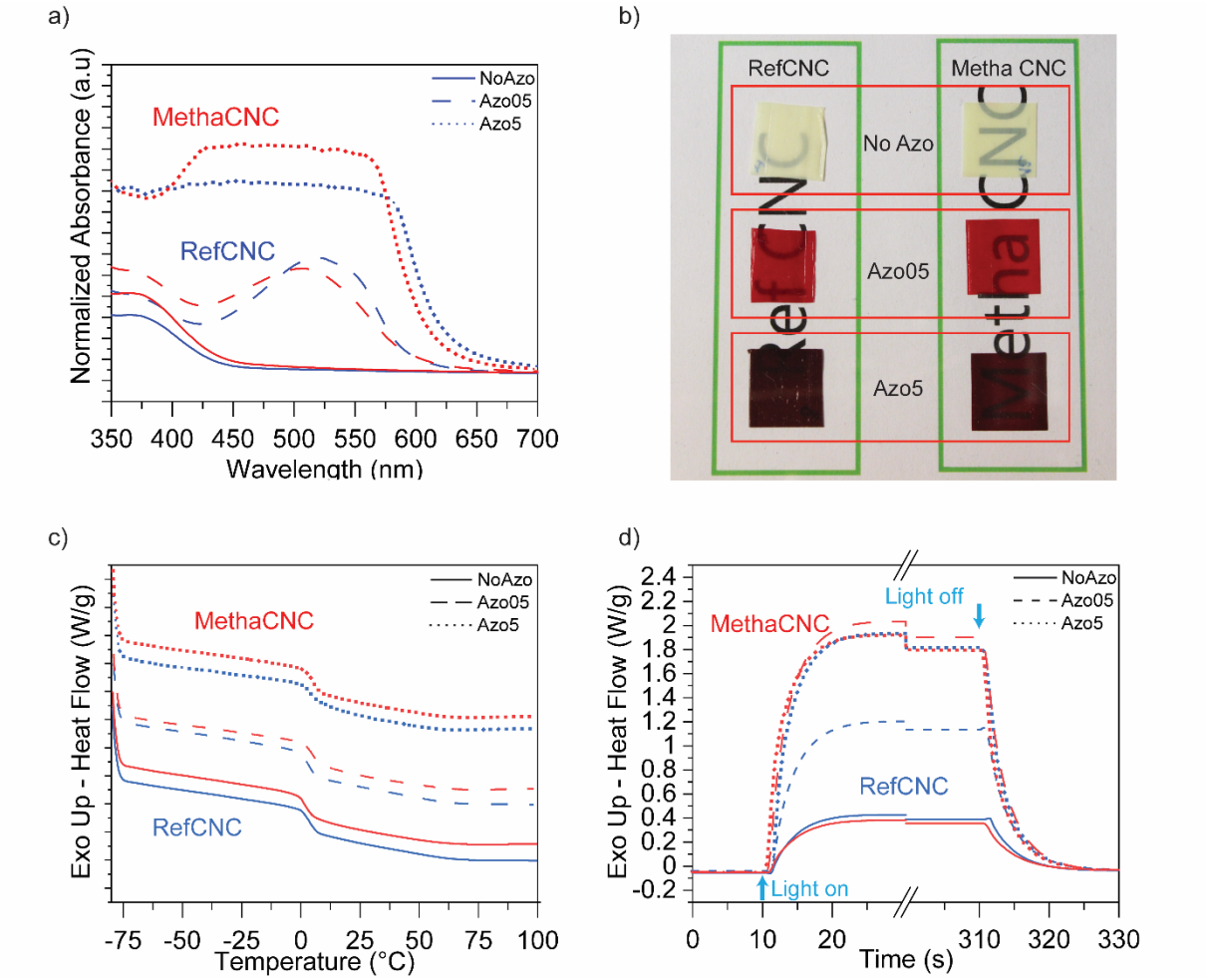

Figure 3.2-3 *Influence of azobenzene dyes on optical properties and polymer network of the composites. (a) UV-vis spectroscopy of printed films illustrated in (b). (c) Second heating cycle of differential scanning calorimetry measurements of printed composites in dark conditions. (d) Exothermic reaction to light illumination of printed composites observed by time dependent differential scanning calorimetry (DSC), the light has been switched on at 10 s and off at 310 s.*

Despite the fact that DR1 molecules did not impart substantial changes to the materials so far, a first photoresponse could be observed. Due to the strong light absorption of azobenzene derivatives, their photoisomerization occurs along with a strong photothermal effect [11],[50]−[52]. To monitor the time evolution of the photochemical reaction in the composites and confirming its effectiveness, photo-DSC measurements were performed (Figure 3.2-3d). Here, the samples at 25 °C were placed in an open pan and irradiated after 10 s with two LED sources (480 nm, 3W) placed at 45 mm from the sample. The illumination was maintained for 5 min in order to reach the equilibrium of the photoreaction. The results show that both NoAzo composites present a light photoabsorption generating an exothermic heat flow of 0.39 W g^{-1}. This is probably the consequence of the temperature increase in the chamber due to the LED being switched on. However, samples containing DR1 show a strong exothermic behavior reaching a maximum exothermic heat flow after 20 s of illumination and having a heat flow decay of 20 s after

switching off the light sources. While the photothermal behavior is clearly observed, the photoisomerization reaction can be noticed by comparing the values of the heat flow after 20 s of illumination with the heat flows values after 300 s. This drop was quantified to be systematic in all Azo samples around 0.10 W g^{-1} indicating that, at the current light intensity, the same amount of DR1 reacts in all samples, independent of the overall concentration of dye. Interestingly, for refCNC materials, Azo05 shows an intermediate behavior, reaching a maximum of 1.21 W g^{-1}, while Azo5 reach a maximum of 1.93 W g^{-1}. Differently, both Azo05 and Azo5 samples of methaCNC composites react to light with a strong exothermicity of 2.03 and 1.91 W g^{-1}, accordingly. The different behavior of refCNC Azo05 is attributed to the haziness of the sample. As illustrated in Figure 3.2-3b, refCNC generate scattering of light, making the film hazy and more blurry than the methaCNC counterparts. Consequently, when light penetrates into the sample, it is scattered and less photons can reach the bottom layer, thus exciting a smaller volume of DR1 localized at the surface of the sample. Therefore, the generated heat is not optimally transferred to the aluminum pan of the instrument, reducing the magnitude of the heat flow. In the case of Azo05 methaCNC samples, the higher transparency may facilitate light penetration and help the excitation of larger volumes, resulting in a more homogeneous heat generation and conduction to the measuring sensor. This could also explain the similar values of heat generated by the Azo5 samples with higher DR1 concentration. Indeed, the stronger absorption of these samples would allow excitation of smaller volumes compared to Azo05 samples and mainly localized to the surface.

3.2.3.3 Photoresponsive Behaviors and Properties of 3D Printed Composites.

After the successful DR1 dispersion in the printed parts, all the composites presenting birefringence show photomechanical bending when irradiated with light at 480 nm and reverse to the original shape as soon as the irradiation stops. Characterization of the movement of single printed filaments was carried out and is shown in Figure 3.2-4. DIW printed filaments with a thickness of 200 µm were placed at a distance of 2 mm from the light source with the tip of the sample at 5 mm from the axis of the LED. The actuated deformation was then recorded for both forward actuation during illumination (Figure 3.2-4a,b) and reverse actuation in the dark (Figure 3.2-4e,f). By tracking the movement of the filament's tip, the displacement normalized by the filament length from the axis of the LED and the strain rate of actuation could be characterized. Movement during irradiation occurs in less than 3 s for all sample categories (Figure 3.2-4c,d). A slight difference in the normalized displacement and the strain rate is present between the composites, in function of the particle's surface chemistries. RefCNC composites show an average normalized displacement of 0.20 and a maximum mean strain rate around 0.15 s^{-1}, while methaCNC filaments reach an average normalized displacement of 0.25 and a maximum mean strain rate of 0.25 s^{-1}. This slight improvement might arise from the better dispersion of methaCNC in the composite. This allows for improving the penetration of light, which can activate a slightly bigger volume of material. Differently, the concentrations of azobenzene in the composite filaments do not influence their actuation, suggesting an optimum value has already been reached with Azo05. The strong light absorption of DR1 would limit the light penetration in the sample, reducing the activated volume and localizing it to the surface, in the case of higher concentrations. This can also be observed from the big standard deviation of the refCNC Azo5 in Figure 3.2-4g. The heat generated by the LED source was not considered to influence the movement of the filaments since samples without DR1 doping did not show any deformation when illuminated. Interestingly, the photoactuated movements of all the printed samples were not dependent on the light direction and include a bending in the opposite direction of the printing substrate. This would not be the case if the filaments presented a uniaxial and homogeneous nematic phase [53], since the strong absorption of azobenzene would create a gradient of contraction localized

in the surface of the polymer resulting in a bending toward the light source. Differently, it has been already widely reported for other similar phototriggered [22],[54]−[56] LCEs, that when the polymers present a twisted or splayed nematic phase the actuated movement is independent from the light direction. In order to investigate the actual structure and orientation of mesogens and nanoparticles, SAXS analyses were carried out on printed samples (SI Figure S 3.2-6). The orientation analysis for refCNC and methaCNC composites was quantified as described by Bunk et al. [39]. In short, a cosine function was fitted to the azimuthal intensity at the chosen qranges. The degree of orientation was calculated based on the ratio of asymmetric/symmetric intensity extracted from the fast Fourier transforms. Despite a general orientation along the printing direction, it was not possible to define the actual LC phase orientation. The CNC signal could be isolated and nanoparticles in both refCNC and methaCNC samples show a degree of orientation of around 0.40 and 0.27, respectively. Such a difference may be explained by the surface chemistry of the particles. As mentioned above, the hydroxyl groups of refCNC render their inks quite more viscous than methaCNC inks, requiring more pressure to be extruded, thus promoting higher alignment [33]. Differently, the signal from LC mesogens could not be separated due to the superposition with the CNC signal in the same q-range, which appeared to dominate the scattering response of the material. Such relatively low degree of axial orientation (0.65 being previously achieved by DIW for CNC) [32] combined with the photoactuated behavior mentioned above, suggest the presence of nematic LC phases more complex than uniaxially aligned. Previous researches on the printing of LCEs [28],[57], as well as on CNC alignment during filament extrusion [32],[33], observed the presence of a gradient in the alignment degree of mesogens and particles, from well aligned external surfaces to an isotropic center of the filament. This might lead to the creation of asymmetric LC nematic phases promoting light-orientation independent movements of the printed filaments. Nevertheless, the role of CNC alignment on LC orientation is indirectly observed by comparing the normalized displacement of filaments from 15 wt % refCNC Azo05 composite with Azo05 filaments accounting 10 wt % refCNC (SI Figure S 3.2-7). No difference in the actuation behavior can be observed. Since the quantity of LC mesogen is lower in the 15 wt % refCNC while the composite stiffness slightly increases, an unchanged actuation behavior suggests that the LC mesogen can orient better with higher particle content. Most probably, this is due to the higher viscosity of the 15 wt % refCNC ink that leads to higher shear stress during printing and hinders the reorganization movements of the LC mesogen after extrusion. Especially, due to the lower viscosity presented by the 10 wt % inks, they could not be printed in the Z direction, limiting their application to production of single layer devices.

The analysis of the reverse deformation, depicted in Figure 3.2-4g, shows that all tested materials can recover their original shape in less than 3 s, independent from the type of particle or the concentration of DR1. However, a close look at the speed of reverse deformation (Figure 3.2-4h) points to a faster response of methaCNC composites, reaching a maximum strain rate of 0.5 s^{-1} for Azo05 methaCNC filaments. This is most probably a consequence of the covalent bonds between CNC and the polymer matrix. MethaCNC composites shall demonstrate a higher Young's modulus than refCNC material, which would translate in larger elastic energy stored into the material when deformed [58]. As soon as illumination stops this elastic energy is released and leads to a faster response, reaching a maximum strain rate of 0.5 s^{-1}, with respect to the maximum strain rate of 0.15 s^{-1} observed for refCNC composites.

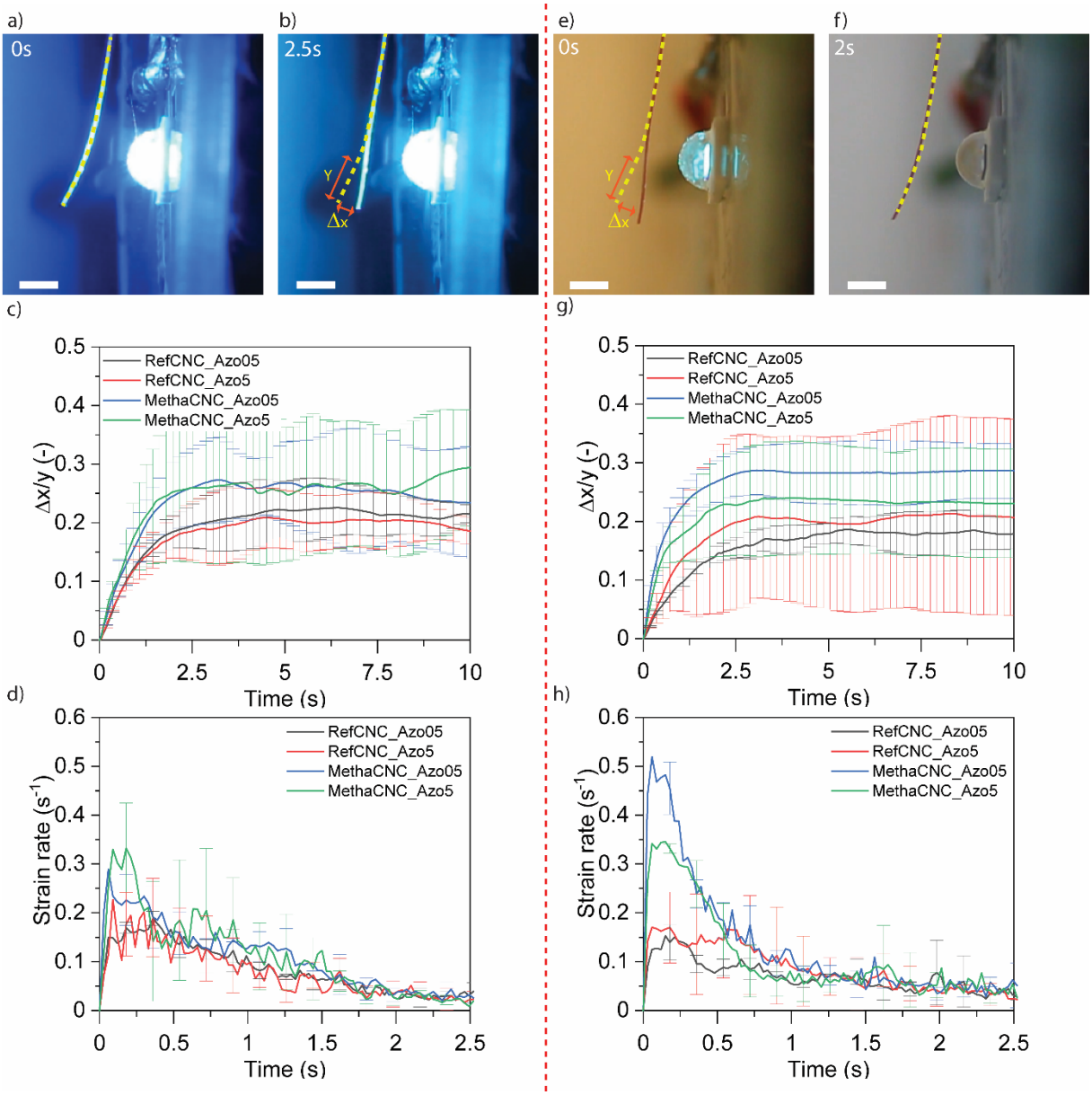

Figure 3.2-4 *Analysis of the printed filaments photoactuated movements. (a) and (b) represent the initial moment of illumination and the final moment of deformation under illumination, respectively, while (e) and (f) the counterparts for the recovery deformation in dark, the dashed line indicates the original position of the filament (Scale bars present 2.5 mm). (c) and (g) Measurements of the displacement of the filament tip normalized by the length y, as a function of time for the photoactuation and for the recovery motion, respectively. (d) and (h) Measurements of the strain rate of the filament tip as a function of time for the photoactuation and the recovery motion, respectively. For each experiment three samples were characterized.*

To demonstrate the influence of refCNC and methaCNC on the mechanical properties of the 3D printed composites, we performed tensile and DMA tests on the printed filaments with and without blue/green light illumination. The higher Young's modulus of methaCNC samples was confirmed with mechanical tests in tensile mode (Figure 3.2-5). The presence of DR1 in the polymer composites' networks leads to dynamic photoresponsive changes in their mechanical behavior. In particular, a pronounced photosoftening is observed. The mechanical properties of printed single filaments, for both CNC surface chemistries, were evaluated by microtensile tests (Figure 3.2-5a,c) and time sweep DMA (Figure 3.2-5b,d) at 25 °C in dark and under illumination at a wavelength of 480 nm. Tensile tests were carried out with a custom-made microtensile setup for the measurements of fibers already reported elsewhere [38], while the illumination source was placed at 10 mm distance from the sample (SI Figure S 3.2-8). As illustrated

in Figure 3.2-5a,c both types of reinforcement show a similar mechanical behavior in dark. Generally, all samples have a soft elastic response to the deformation followed by a stiffness increase. This effect is ascribed to strain induced alignment of LC mesogens in the composites [59]. However, with a Young's modulus of 2 MPa and a strength of 2 MPa, NoAzo refCNC are weaker than their methaCNC counterpart, which reaches an elastic modulus of 9 MPa and a strength of 3 MPa.

In agreement with previously reported experiments [32], this observation further confirms the successful methacrylation of methaCNC and their ability to covalently bond to the polymer matrix. In particular, the methaCNC surface does not influence the curing behavior of the polymer matrix as both types of composite display a similar relative degree of conversion around 50% (SI Figure S 3.2-9) when measured on single layer films (200 μm thick). This emphasizes that methaCNC composites are stiffer and stronger than refCNC composites, due to a higher cross-link density and an enhanced stress transfer from matrix to particles. The quantity of DR1 also influences the mechanical properties with the same trend for both CNC types. A first increase in the concentration makes the Azo05 samples stiffer and stronger than NoAzo samples, while increasing the elongation at break. This indicates that DR1 molecules might act like a LC mesogen and align along the filament main axis when intruding the material. In particular, Azo05 refCNC present an increase of 100% in both stiffness and strength, while Azo05 methaCNC have an increase of 100% in stiffness and 130% in strength. Although the more concentrated Azo5 samples show only a slight weakening of strength and elongation at break for refCNC composites, with respect to Azo05, methaCNC Azo5 show an important decrease in strength from 7 to 4 MPa, as well as a further decrease in the elongation at break. Indeed, according to SI Figure S 3.2-6, the increase in concentration of azobenzene in the methaCNC composites results in a slight decrease of the nanoparticles' orientation, which might be responsible for the observed weakening in Azo5 samples.

When the light shines on the samples, a strong photosoftening can be observed. Although NoAzo samples of both CNC typologies are slightly affected by the operating light source, probably due to the difficult heat dissipation of the testing setup, Azo05 and Azo5 samples are heavily influenced by the illumination. Azo05 and Azo5 refCNC composites reach both a Young's modulus of 2 MPa and both show a reduction of their strength, reaching 1.5 and 1 MPa, respectively. Moreover, illumination imparts a strong reduction of the toughness of the refCNC samples, observed from the decreased elongation at break, passing from around 0.57 in dark to 0.35 under irradiation. Differently, methaCNC did not show such clear effect, further confirming the stronger interfacial interactions they have with the polymer matrix. Nonetheless, Azo05 and Azo5 methaCNC materials, with elastic moduli going from 18 and 12 MPa in dark, soften under illumination reaching elastic moduli of 6 and 5 MPa, respectively. Similarly, strengths decrease from 8 and 4 MPa to 4 and 2 MPa, respectively, for Azo05 and Azo5 methaCNC composites (SI Figure S 3.2-10). Interestingly, Azo5 doping produces the same effect on both composites, resulting in illuminated materials of the same tensile properties than the illuminated NoAzo. The higher photoresponse of methacrylated CNC materials may still be explained by the lower haziness of methaCNC with respect to refCNC, which display more scattering that may reduce the size of the excited volume.

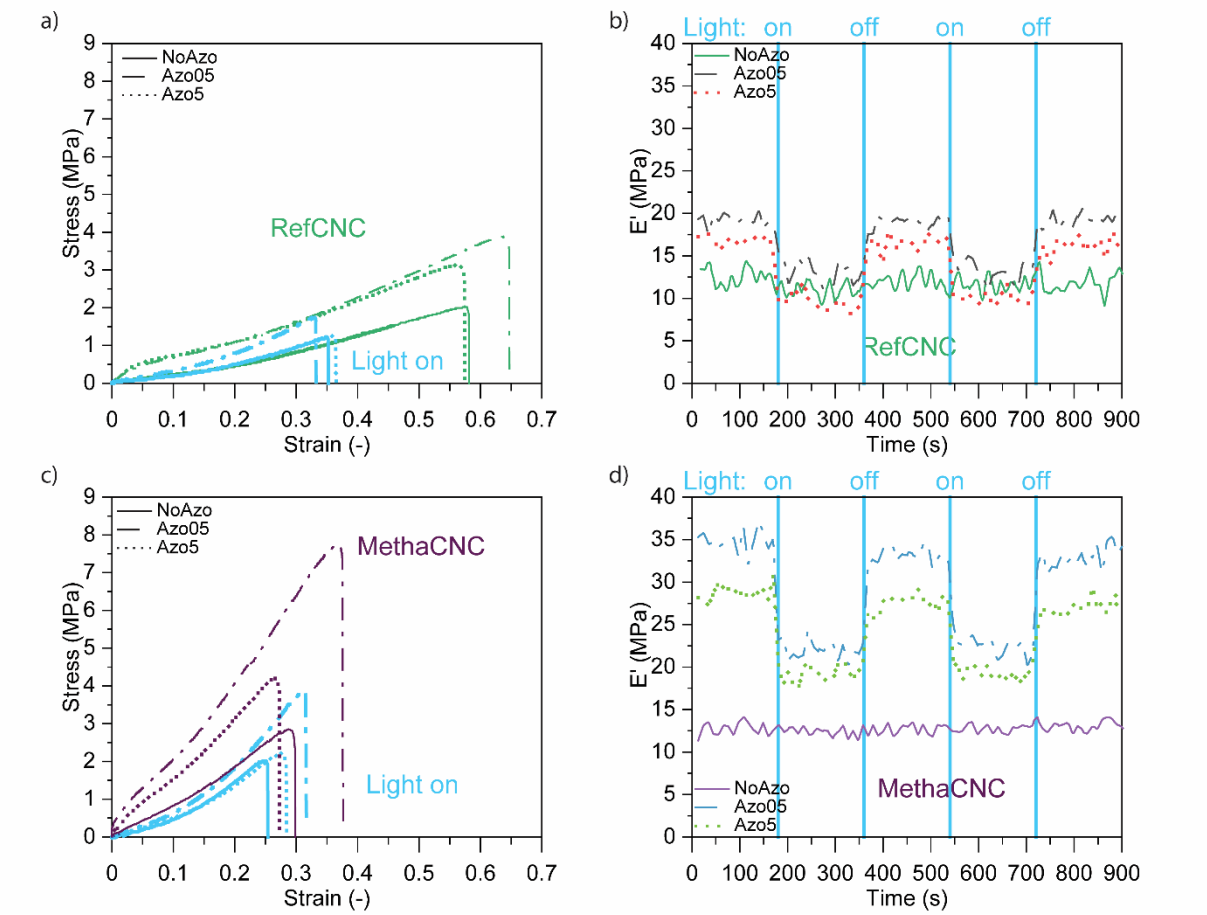

Figure 3.2-5 *Mechanical properties of printed filaments. (a) and (c) are the results of microtensile tests in dark and under illumination of refCNC and methaCNC composites, respectively. (b) and (d) represent the effect of light illumination on the storage modulus of the refCNC and methaCNC composites respectively, obtained by time sweep in DMA at 25 °C.*

Observation of the photosoftening and its reversibility was carried out by adapting the same light source (480 nm wavelength) at 10 mm from the sample in a DMA setup. Measurements were conducted in tensile mode with 0.04% strain and 1 Hz frequency at a fixed temperature of 23 °C (Figure 3.2-5b,c). The sample properties were measured in dark for 180 s and the light was switched on periodically for 180 s each 180 s. Two consecutive illumination cycles are illustrated here in order to highlight the reversible photosoftening. However, the tested materials could undergo more than five cycles without showing fatigue. Contrary to the microtensile tests, NoAzo refCNC and methaCNC tested by DMA measurements do not show any photoresponse in their storage modulus, due to a more efficient dispersion of the heat generated by the LED in the used setup. Instead, Azo05 and Azo5 of both refCNC and methaCNC filaments show a similar stiffening trend when compared with the samples tested with the microtensile setup. Azo05 doping treatment corroborates to improve the storage modulus (E') of the samples when compared to the ones prepared without Azo (NoAzo samples) from 11 to 20 MPa for refCNC composites and from 12 to 35 MPa for methaCNC, while Azo5 samples reach 17 MPa for refCNC and 28 MPa for methaCNC. In the present case, Azo05 and Azo5 refCNC samples show a softening of 36% and 33% respectively. Similarly, Azo05 and Azo5 methaCNC present a slightly more pronounced softening of 37-38% and 34%, respectively. This observed photosoftening effect has been investigated for similar azobenzene based materials [11],[51],[52]. Such effect arises from a combination of photothermal and photochemical effects. By comparing the tan(δ) of Azo05 and Azo5 materials (for both CNC types) during a temperature sweep between -20° and 80 °C in dark with a sweep carried

out during illumination (SI Figure S 3.2-11), an insight into the materials' phase transitions occurring during illumination could be obtained. There, all the irradiated materials show a ~25 °C drop of the Tg, decreasing from 15 °C to -10 °C. When comparing the storage moduli of the same composite, it is observed that the room temperature (23 °C) photosoftened elastic modulus reaches the same value as the nonirradiated modulus when the environmental temperature is around 48 °C. This corresponds to a ~ 25 °C increase in the sample temperature. Observations of surface temperature with an IR camera confirmed this increase in the samples' temperatures (SI Figure S 3.2-12), indicating that the photothermal effect of DR1 is mainly responsible for the softening of the materials. However, the overall increase in temperature is not enough to trigger the nematic to isotropic transition of the LC mesogens, located around 60 °C (in dark), and needed for the photoactivated deformation. Moreover, when light shines on the samples, the T_{NI} peak of DMA's loss factors in SI Figure S 3.2-11 strongly decreases for all DR1 doped samples, suggesting that the illuminated materials are partially in the LC isotropic phase at temperatures lower than T_{NI}. Hence, the photoisomerization of DR1 may mainly be responsible for the photoactuation by triggering the LC phase transition, while the generated heat promotes a photosoftening of the polymer network. Therefore, this facilitates the shape transformation, decreasing the amount of elastic energy required for the deformation.

The comparison between refCNC and methaCNC compositions revealed that functionalization of CNC's surfaces with methacrylate groups and, therefore, possible covalent bonding of the cellulose nanoparticles to the polymer network takes place. This influences mainly the compatibility and dispersion of CNC within the matrix, thus contributing to a smoother 3D printing process with less clogging of the nozzle, and improves the final stiffness and strength of the composites. With respect to the photoresponse of the tested materials, the stiffer behavior of the methaCNC composites, compared to the refCNC ones, brings a slight improvement of the speed of reverse actuation in dark, as well as, a slightly more pronounced photosoftening effect. Despite the fact that both concentrations of DR1 in all samples lead to materials presenting a similar amplitude and speed of photoactuation, the Azo05 samples show an improved stiffness in dark and an increased photosoftening compared to the Azo5 samples.

In order to underline the strength of our approach highlighting the advantage of using additive manufacturing in the production of photomechanical devices, a demonstrator consisting of a single module was successfully 3D printed with the methaCNC Azo05 composition. The device and its operation are illustrated in Figure 3.2-6. **S**uch a module is meant as an active part that closes an electronic circuit when illuminated and could be used, for instance, as a light sensor for circuits that need to operate only during the day, as phototracking structures for photovoltaic panels used to maximize solar energy harvest. Importantly, the device was printed in a single manufacturing platform and it was designed to directly fit on its support. When compared to a classical manufacturing technology, for example, molded films, our method reduces the number of manufacturing steps and the waste of residual materials, while ensuring a reliable alignment of the LC and CNC. The operational mode of the module consists in a 3D structure with a 200 µm thick actuating layer allowed to bend during illumination (Figure 3.2-6a). The active part, coated with 20 nm of Pt to ensure electrical conductivity, is in its original state (Figure 3.2-6c,d) as open circuit when in dark. During illumination with a 480 nm LED, the bending of the active part produces close contact with an electrode, hence closing the circuit (Figure 3.2-6e). Another red LED is connected to the circuit and switches on 22 s after the beginning of the actuation (Figure 3.2-6b), demonstrating the closure of the circuit. The difference in time observed between this demonstrator (22 s) and the previous filaments observation (<3 s) derives from the need of the actuator to generate enough pressure to close the circuit between the electrodes.

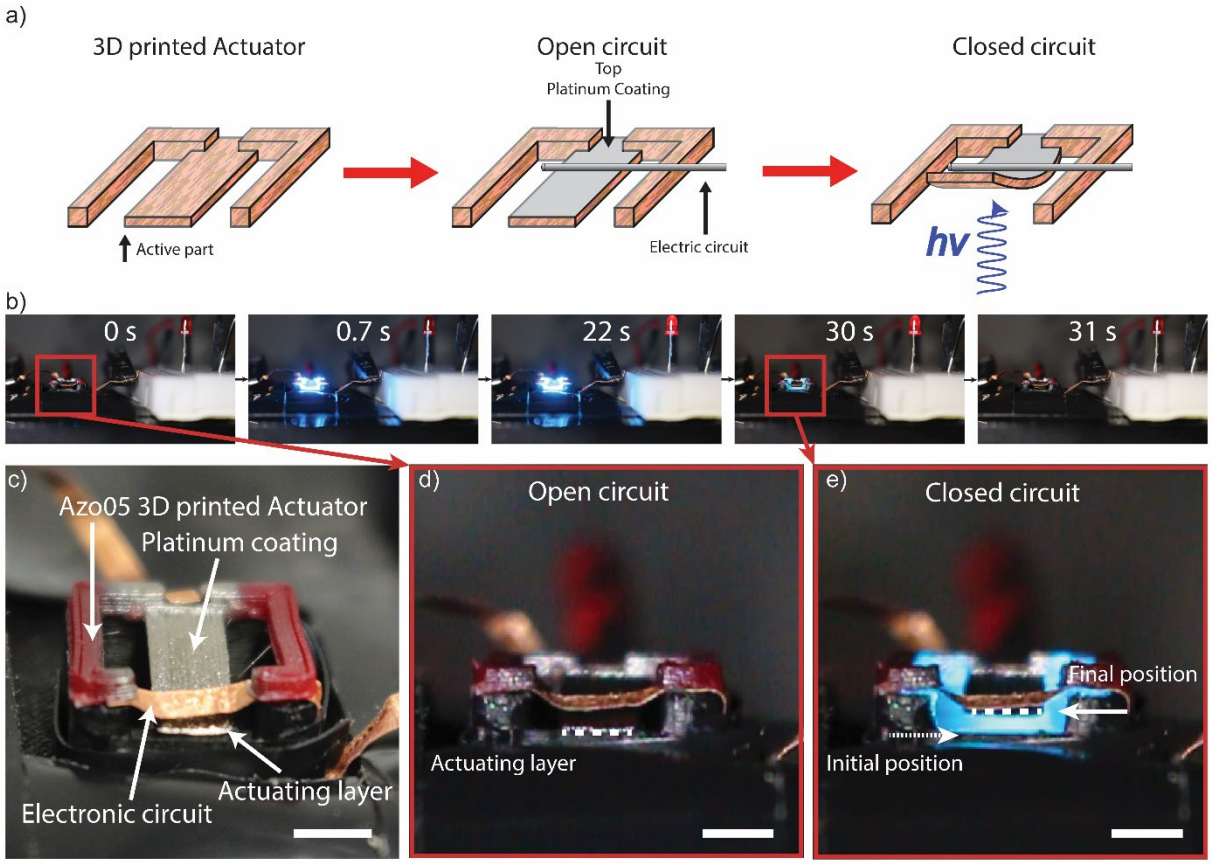

Figure 3.2-6 *Demonstrator showing a 3D printed actuator utilized as activation circuit. In dark the circuit stays open, while the electric circuit closes when illuminated. (a) Schematic illustration of the working principle of such printed device. (b) Defined frames showing the demonstrator in action. When the actuator is illuminated it starts moving and after 22 s the red LED switches on. At 30 s the light has been switched off and the actuator comes back to its original position and the circuit is open again. (c) A magnification of the Azo05 3D printed device. (d) and (e) Magnifications of the frames at 0 and 30 s, respectively, to show the movement of the actuating layer. Scale bars correspond to 3 mm.*

As soon as the 480 nm wavelength illumination stops, the actuated part recovers its original shape within 3 s. The operation of this photoresponsive module was successfully repeated more than 20 times (SI Video S2). Another device, presenting the opposite actuation has also been created and is illustrated in SI Figure S 3.2-13. Here, the Pt coating was applied at the bottom of the actuating part and the circuit was opening during illumination, demonstrating application of the material as a safe circuit. Although only on/off actuators were presented in this manuscript, the developed materials open the venue to application as sensors. Indeed, due to the demonstrated photothermal effect, the amplitude and the speed of actuation depend on the irradiation intensity [48],[54],[55]. Moreover, more complex devices and movements can be engineered and fabricated by additive manufacturing approaches. Here, the 3D printing control over the alignment of the LC mesogens and the CNC particles dictates the bending directions. As previously demonstrated by studies on 3D printed LCE, combining different directions in a single layer would produce more complex movements as twisting and curling [26],[28] allowing further advances in the production of photoresponsive soft materials.

3.2.4 Conclusion

We present an innovative approach for the manufacturing of 3D printed actuator devices composed of photoresponsive soft LCE nanocomposites with a relatively high solid content of cellulose nanocrystals. With the introduction of biocompatible and sustainable CNC in an uncured LCE ink, our DIW process

permits direct printing of structures with tailored geometries and mechanical properties, while the successive azobenzene doping leads to fully reversible photoactivated dynamic responses like rapid photosoftening and photomechanical actuation on the order of seconds. The main strength of such a two-step approach lies in combining the anisotropic mechanical tailoring of CNC with the fast and reliable photoresponse of dye-doped LCE as presented by our on/off actuators, which could be directly applied on their support holders. The high degree of control over the LC nematic director, offered by the extrusion printing, can be exploited to increase the complexity of the photoactuated movements, as well as the photosoftening by creating complex patterns and multiple layers assemblies. Moreover, optimization of the material's performance can be achieved chemically. Indeed, with the printed materials presented, we evaluated the effect of surface chemistry of CNC on the photoresponses of the composites. When comparing the presence of methacrylate groups on the cellulose surface with unmodified refCNC, it was shown that covalent bonding between matrix and particles promotes a faster shape recovery after actuation. Finally, 3D printing of cellulose-based nanocomposites combining photomechanical actuation with tailored and dynamic stiffness presents important potential for the fabrication of a wide range of devices, going from custom soft robots to vibration dampers or muscle-like prosthetics, where the customization of geometries, properties, and dynamic responses are needed.

3.2.5 Experimental Section

Materials. RefCNC, resulting from sulfuric acid hydrolysis of eucalyptus pulp, were supplied by University of Maine (Orono, ME). The matrix precursor poly(mercaptopropyl)methylsiloxane homopolymer (SMS 992) was purchased from Gelest. The liquid crystal mesogens and cross-linker, namely 4-methoxybenzoic acid 4-(6- acryloyloxyhexyloxy)phenyl and 1,4-bis-[4-(3-acryloyloxypropyloxy)-benzoyloxy]-2-methylbenzene were supplied by SYNTHON Chemicals Gmbh. N-ethyl-N-(2-hydroxyethyl)-4-(4-nitrophenylazo)aniline also called disperse red 1 (DR1, 95%), (hydroxyethyl)methacrylate (HEMA, 98%), methacrylic anhydride (94%), and pyridine were acquired from Sigma-Aldrich, while the dimethylformamide (DMF, ≥ 99.5% synthesis) was purchased from Roth AG.

MethaCNC Functionalization. Methacrylation of the refCNC's surface was obtained by grafting of methacrylic anhydride according to the procedure described by Siqueira et al. [32]. Briefly, freeze-dried refCNC were dispersed in DMF to obtain a 21 wt % gel. The gel was homogenized with two SpeedMixer (Speedmixer DAC 600, Hauschild & Co. KG) cycles at 1000 rpm for 1 min, 1500 rpm for 1 min, and 2000 rpm for 4 min. After resting overnight at 5 °C and mixing before utilization, 141 g of DMF were added to 15.7 g of refCNC gel in DMF. The solution was mixed with a magnetic stirrer in a glass reactor with condensation reflux up to homogenization (solution at 2 wt % of refCNC). The reagent was heated at 105 °C in nitrogen atmosphere and 188.9 g of methacrylic anhydride and 4.8 g of pyridine were added. The reaction continued for 5 h. Finally, the reactive mixture was quenched at 0 °C to stop the reaction. The modified material was then washed four times with a mixture of toluene/acetone/ethanol (4:1:1) by centrifugation at 5000 rpm and 5 °C for 25 min. After purification, the produced methaCNC were solvent exchanged in acetone with three centrifugation cycles at 5000 rpm for 5 min, in order to allow further use of the reaction product.

Ink Production. Inks suitable for Direct Ink Writing, with refCNC or methaCNC were prepared at 15 wt % of nanoreinforcements. Once a CNC/DMF dispersion was solvent exchanged with acetone by centrifugation (4 times, 5 min at 5000 rpm), both types of inks were produced in the following way: 4-methoxybenzoic acid 4-(6- acryloyloxyhexyloxy)phenyl (3.000g) , 1,4- B i s -[4- (3 - acryloyloxypropyloxy)benzoyloxy]-2-methylbenzene (0.827g), (mercaptopropyl)methylsiloxane homopolymer (1.241 g), and irgacure 819 (0.103g) were weighted into a beaker. RefCNC or methaCNC were successfully

added (0.912 g) from the acetone dispersions. The solution was stirred for 30 min and placed in an ultrasonic bath (TUC-150, TELSONIC) for 10 min before evaporating all the solvent by stirring the dispersion overnight at 40 °C. Finally, the obtained ink was homogenized with four speed mixer cycles: 1000 rpm for 1 min, 1500 rpm for 1 min, and 2000 rpm for 4 min.

3D Printing. A direct ink writing printer (3D-bioplotter "Manufacturer Series", EnvisionTEC, Germany) was used to print all the composite materials. Before printing, the inks were loaded into 30 mL UV shielding cartridges and air bubbles were removed by centrifugation at 3000 rpm for 10 min. Once the cartridge was loaded into the printer, the ink was pneumatically extruded with pressures ranging between 2.5 and 4 bar, through UV shielded tapered nozzles presenting an inner diameter of 0.25 mm. The filaments were extruded in air while films and structures were produced by depositing the filaments on hydrophobized glass slides at a speed of 10 mm s^{-1}. The extruded filaments and the produced structures were cured by UV illumination for 10 min. The illuminating setup was a self-made chamber composed of five monochromatic LEDs (410 nm wavelength, 3W). Finally, all the samples were postcured 15 min per side with a high pressure mercury lamp (UVASPOT 400/T, Dr Hönle) equipped with a UVC filter (H2 filter, Dr. Hönle) presenting maximum emission peak at 365 nm of wavelength.

Azobenzene Doping Process. In order to impart the photoresponsivity to the printed parts, the postcured materials were swollen in an acetone/DR1 solution for 24 h. Two solutions were used for the creation of Azo05 and Azo5 samples, one with 0.5 mg mL^{-1} of DR1 in acetone and another one with a concentration of 5 mg mL^{-1}, respectively. After the bath, the structures were extracted from the solutions, rinsed with pure acetone and kept overnight under vacuum in a desiccator for evaporating the remaining solvent.

Optical Microscopy. All images were recorded with an optical microscope (Zeiss, Axioplan) equipped with cross polarizer filters perpendicular to each other. The samples were illuminated in transmission mode and images were taken with a digital camera (Leica DVM 2500). Filaments and films were placed on a glass slide and oriented at 0° with respect to the light polarization. Observation of the birefringence effect was achieved by qualitatively comparing the samples at 0° with samples at 45° where transmitted light intensity should be maximal. This was achieved by rotating the sample stage. Quantification of the output light intensity was evaluated by integrating the pixel's gray values over an area of 2500 × 1900 pixels, having the long side oriented transversally to the filaments or films. Integration of gray value was carried out with ImageJ software.

Scanning Electron Microscopy (SEM). SEM images were taken in order to observe morphology of the printed filaments. Micrographs were acquired with an FEI Quanta 650 FEG ESEM with an accelerating voltage of 5 kV, a spot size of 3 or 3.5 and a working distance of 10 mm. Top view samples were directly glued on an aluminum sample holder with a double sided carbon tape. A 2 nm thick Pt coating was successively applied in order to ensure electrical conductivity and avoid charge concentration during measurements. Cross sections were obtained by embedding the filaments in a resin. The embedded samples were cured overnight at 60 °C. Once the resin cured, the sample was cut with a razor blade to enable observation of the cross section. A final 2 nm thick Pt coating was then deposited on the sample in order to avoid charge effects.

UV-vis Spectroscopy. The absorbance of DR1 in acetone solution was recorded with a UV-vis spectrophotometer (Cary 100E, Variant). The quartz cuvettes were filled with the acetone solutions with DR1 concentrations ranging from 0.1 to 0.0001 mg mL^{-1} and the spectra were recorded from 700 to 350 nm. Printed films where characterized with a UV-vis-NIR spectrophotometer (UV-3600, Shimadzu) equipped with an integrating sphere. 15 ×15 mm^2 samples were placed on a sample holder with an 8

mm diameter hole at the entrance of the integrating sphere. Three measurements per sample condition were taken.

Differential Scanning Calorimetry (DSC). Thermal properties of the printed materials were analyzed with a Q2000 DSC (TA Instruments) equipped with a mechanical cooler (RCS 90). Samples were loaded in aluminum closed pans (TZero Aluminum Hermetic) and hermetically sealed. The weight of each sample ranges between 8 and 11 mg. Each experiment was conducted in nitrogen atmosphere (50 mL min^{-1}), with three heating and cooling cycles from -80 to 100 °C at 10 °C min^{-1}.

Photoresponsive Differential Scanning Calorimetry (photo-DSC). Photo-DSC measurements were performed using a Q100 DSC from TA Instruments. The original setup was modified in order to use two 480 nm Opulent Creed LEDs connected in series (0.7 A, 7 V) as light sources for the reference pan and the sample pan. These light sources were adapted to the instrument and placed 45 mm away from 4 mg samples. Each sample was placed in an open aluminum pan. An empty aluminum pan was used as reference. After equilibration at 25 °C, an isotherm at 25 °C was held for 3 min in dark, then the LEDs were turned on for 5 min and a final isotherm was held for 3 more minutes without light. Three measurements were performed per sample condition, and the representative measurements are presented in this manuscript.

Characterization of Photoactuated Movements. Characterization of the movement generated during illumination was recorded with a Canon EOS 100 at 50 fps. A sample holder was 3D printed with a Prusa Imk3 in PLA. The filaments (200 μm thick) were placed vertically on the holder. The actuating light, an Opulent Creed LED at 480 nm (3W) was placed 2 mm away from the sample perpendicularly at a height of 5 mm from the tip of the filament. The samples were illuminated for 30 s and then allowed to rest for 30 s in dark. After recording of the photoactuation, during illumination and after illumination, the videos were analyzed with Image Analysis toolbox from Matlab software. A custom-made program was written to track the movement of the filament's tip as a function of time. Three samples per condition were tested and the results are presented with the average data and their standard deviation.

Rheology of Printing Inks. In order to establish the printability of the produced inks, their rheological behavior was characterized at room temperature with an MCR 301 Anton Paar rheometer with a 25 mm diameter plate-plate configuration presenting a gap of 0.5 mm. Storage and loss moduli were measured through oscillatory experiments with strain variations from 0.01 to 1000% at a frequency of 1 Hz with a logarithmic sweep. The apparent yield stress was defined as the shear stress where storage and loss moduli are equal ($\tan(\delta) = 1$), that is, by convention of the gelation point. Three samples per ink were measured, and the representative measurements are illustrated.

Dynamic Mechanical analysis (DMA). Several types of DMA measurements were conducted during this work. With the use of a RSA 3 analyzer from TA Instruments in tensile mode, the behavior of storage modulus in dark and under illumination at room temperature was observed. These tests were conducted with an initial clamp distance of 20 mm. The measurements were carried out with a frequency of 1 Hz, a strain of 0.04%, at 25 °C. In front of the clamp center, an Opulent Creed LED (480 nm, 3W) was placed at a distance of 10 mm from the filaments. A typical procedure consisted of a time sweep where 180 s were tested in dark and 180 s under light illumination, and the process was repeated twice in a row to ensure reversibility of the light irradiation influence. Tested samples presented a diameter ranging from 180 to 250 μm. Diameters were evaluated with optical microscopy observations. For each condition, three samples were tested, and the representative results are illustrated. Differently, the thermal behavior of viscoelastic properties in dark and under illumination was obtained using a Q800 DMA (TA Instruments) in tensile mode where an LED source (480 nm, 3W Opulent Creed) was inserted in the furnace chamber facing the samples at a distance of 10 mm. Temperature was increased from -20 to

80 °C with steps every 5 °C. At every step, after 5 min of equilibration, the samples' moduli were measured twice in dark at 1 Hz and 0.04 % strain followed by 1 min equilibration and successive 2 min of illumination. Again the moduli were measured twice at 1 Hz and 0.04% strain under illumination.

Microtensile Tests. Tensile tests on filaments were carried out in a custom-made microtensile test setup already reported by Burgert et al. [38]. Briefly, a linear table driven by a step motor and a load cell (5N in this case) are the main components of the apparatus. The step motor allowed to vary the speed from 1 μm s^{-1} to 1000 μm s^{-1}. The samples were glued with a cyanoacrylate glue from both sides on a rectangular 200 μm thick foil presenting three holes in the centers and one for each extremity. The holders were placed onto the moving table and fixed with pinholes at the extremities. The central holes were then cut in order to not measure the foil properties. The samples were stretched at a speed of 10 μm s^{-1}. The displacement of the table was used to calculate the sample's strain, which could be done due to the low stiffness of the tested materials. Each sample consisted of a filament with diameter ranging from 180 to 250 μm. The initial length of the filaments ranged between 4 and 6 mm and was considered to be the distance between each glue point. Both diameters and initial lengths were observed and recorded with an optical microscope. For measurements under illumination, a support for an Opulent Creed LED (480 nm, 3W) was 3D printed with a Prusa imk3 FDM in PLA and adapted to the set up in order to have a 10 mm distance from the samples. For each test and sample condition five samples were tested, and their representative measurements are illustrated.

Small Angle X-ray Scattering (SAXS). Measurements were carried out on a NANOSTAR system (Bruker AXS GmbH, Karlsruhe, Germany). The instrument was equipped with a pinhole collimation system allowing a beam size at sample position of about 400 μm in diameter. X-ray generation was sustained with a microfocused X-ray Cu source (wavelength Cu K α = 1.5406°A) and scattering patterns were recorded on a 2D MikroGap technology-based detector (VÅNTEC- 500 2D with 2048 × 2048 pixels and a pixel size of 68 × 68 μm) along with a custom-built semitransparent beamstop. In the SAXS configuration, with a sample to detector distance set at 107 cm and further calibrated with silver behenate powder sample, the resolved scattering vector modulus q covers a range between 0.06 and 2.1 nm^{-1}. The scattering patterns were recorded at room temperature under moderate vacuum condition (10^{-2} mbar) to limit air scattering. Samples were taped horizontally and the sample holder mounted vertically in the analytical chamber of the Nanostar. The intensity of the semitransparent beamstop for direct beam scans was used for transmission normalization. Background subtraction was done systematically for all samples by subtracting the scattering intensity of the direct beam to the normalized sample. The orientation analysis for refCNC and methaCNC samples was performed using fast fourier transformed analysis established by Bunk et al. [39].

Fourier Transform Infrared (FTIR) Spectroscopy. Degree of curing of both CNC inks was estimated with FTIR spectroscope equipped with a ZnSe attenuated total reflectance (ATR) cell. The instrument utilized was a Tensor 27 IR, Bruker. The measurements went from 600 to 4000 cm^{-1} with 32 scans and a resolution of 4 cm^{-1}. The quantity of unreacted C□C before and after polymerization was compared with three samples per each condition and type of particle. Cured samples consisted in single layer printed films with a thickness of 200 μm. To compare the relative degree of conversion we normalized the intensity of aliphatic C□C bond (band at 1637 cm^{-1}) by the C□O band's intensity at 1720 cm^{-1} as an internal standard and applied the following equation [40]:

$$DC = 100 * (1 - \frac{A_{cured}(\mathrm{C=C})/A_{cured}(C=O)}{A_{uncured}(\mathrm{C=C})/A_{uncured}(C=O)}) \quad (1)$$

3.2.6 Additional Information

Supporting Information

The Supporting Information is available free of charge at:

https://pubs.acs.org/doi/10.1021/acsami.2c02154.

Figures S1−S13 (PDF)

Video S1: Operation of this photoresponsive module-(MP4)

Video S2: Operation of this photoresponsive module-(MP4)

Acknowledgements

We thank A. Huch for the SEM imaging of both types of printed nanocomposites as filaments and films, Sandro Stucki for performing DSC analysis on all the composite compositions, Kevin De France for helping the operation of UV−vis spectrometry on printed films. We greatly acknowledge the financial support from the Swiss National Science Foundation (Grant No. 200021_178941/1). We gratefully acknowledge financial support from the Strategic Focus Area Advanced Manufacturing (SFA-AM) of the Swiss ETH domain, under the project D-Sense□Digital Manufacturing of 3D-Printed Wearable Sensors.

The authors declare no competing financial interest.

3.2.7 References

[1] Basir, S. N.; Yussof, H.; Zahari, N. I. Simulation Analysis of Mimosa Pudica Main Pulvinus Towards Biological Tactile Sensing Modelling. In *Procedia Computer Science*; Elsevier B.V., 2015; Vol. 76, pp 425–429. https://doi.org/10.1016/j.procs.2015.12.282.

[2] Forterre, Y.; Skotheim, J. M.; Dumals, J.; Mahadevan, L. How the Venus Flytrap Snaps. *Nature* **2005**, *433* (7024), 421–425. https://doi.org/10.1038/nature03185.

[3] Stehle, R.; Solzin, J.; Iorga, B.; Poggesi, C. Insights into the Kinetics of Ca 2+-Regulated Contraction and Relaxation from Myofibril Studies. *Pflugers Arch. Eur. J. Physiol.* **2009**, *458* (2), 337–357. https://doi.org/10.1007/s00424-008-0630-2.

[4] Navarro-Baena, I.; Kenny, J. M.; Peponi, L. Thermally-Activated Shape Memory Behaviour of Bionanocomposites Reinforced with Cellulose Nanocrystals. *Cellulose* **2014**, *21* (6), 4231–4246. https://doi.org/10.1007/s10570-014-0446-5.

[5] Bodaghi, M.; Damanpack, A. R.; Liao, W. H. Triple Shape Memory Polymers by 4D Printing. *Smart Mater. Struct.* **2018**, *27* (6). https://doi.org/10.1088/1361-665X/aabc2a.

[6] Sydney Gladman, A.; Matsumoto, E. A.; Nuzzo, R. G.; Mahadevan, L.; Lewis, J. A. Biomimetic 4D Printing. *Nat. Mater.* **2016**, *15* (4), 413–418. https://doi.org/10.1038/nmat4544.

[7] Li, Y.; Chen, H.; Liu, D.; Wang, W.; Liu, Y.; Zhou, S. PH-Responsive Shape Memory Poly(Ethylene Glycol)-Poly(ε-Caprolactone)-Based Polyurethane/Cellulose Nanocrystals Nanocomposite. *ACS Appl. Mater. Interfaces* **2015**, *7* (23), 12988–12999. https://doi.org/10.1021/acsami.5b02940.

[8] Hua, D.; Zhang, X.; Ji, Z.; Yan, C.; Yu, B.; Li, Y.; Wang, X.; Zhou, F. 3D Printing of Shape Changing Composites for Constructing Flexible Paper-Based Photothermal Bilayer Actuators. *J. Mater. Chem. C* **2018**, *6* (8), 2123–2131. https://doi.org/10.1039/c7tc05710e.

[9] Hiratani, T.; Kose, O.; Hamad, W. Y.; Maclachlan, M. J. Stable and Sensitive Stimuli-Responsive Anisotropic Hydrogels for Sensing Ionic Strength and Pressure. *Mater. Horizons* **2018**, *5* (6), 1076–1081. https://doi.org/10.1039/c8mh00586a.

[10] Lu, H.; Yu, K.; Liu, Y.; Leng, J. Sensing and Actuating Capabilities of a Shape Memory Polymer Composite Integrated with Hybrid Filler. *Smart Mater. Struct.* **2010**, *19* (6), 065014. https://doi.org/10.1088/0964-1726/19/6/065014.

[11] Pilz Da Cunha, M.; Van Thoor, E. A. J.; Debije, M. G.; Broer, D. J.; Schenning, A. P. H. J. Unravelling the Photothermal and Photomechanical Contributions to Actuation of Azobenzene-Doped Liquid Crystal Polymers in Air and Water. *J. Mater. Chem. C* **2019**, *7* (43), 13502–13509. https://doi.org/10.1039/c9tc04440j.

[12] Heidarian, P.; Kouzani, A. Z.; Kaynak, A.; Paulino, M.; Nasri-Nasrabadi, B. Dynamic Hydrogels and Polymers as Inks for Three-Dimensional Printing. *ACS Biomater. Sci. Eng.* **2019**, *5* (6), 2688–2707. https://doi.org/10.1021/acsbiomaterials.9b00047.

[13] Peterson, G. I.; Dobrynin, A. V.; Becker, M. L. Biodegradable Shape Memory Polymers in Medicine. *Adv. Healthc. Mater.* **2017**, *6* (21), 1–16. https://doi.org/10.1002/adhm.201700694.

[14] Kirillova, A.; Ionov, L. Shape-Changing Polymers for Biomedical Applications. *Journal of Materials Chemistry B*. Royal Society of Chemistry 2019, pp 1597–1624. https://doi.org/10.1039/c8tb02579g.

[15] Zeng, H.; Wasylczyk, P.; Wiersma, D. S.; Priimagi, A. Light Robots: Bridging the Gap between Microrobotics and Photomechanics in Soft Materials. *Adv. Mater.* **2018**, *30* (24), 1703554. https://doi.org/10.1002/adma.201703554.

[16] Shahsavan, H.; Aghakhani, A.; Zeng, H.; Guo, Y.; Davidson, Z. S.; Priimagi, A.; Sitti, M. Bioinspired Underwater Locomotion of Light-Driven Liquid Crystal Gels. *Proc. Natl. Acad. Sci. U. S. A.* **2020**. https://doi.org/10.1073/pnas.1917952117.

[17] Palagi, S.; Mark, A. G.; Reigh, S. Y.; Melde, K.; Qiu, T.; Zeng, H.; Parmeggiani, C.; Martella, D.; Sanchez-Castillo, A.; Kapernaum, N.; Giesselmann, F.; Wiersma, D. S.; Lauga, E.; Fischer, P. Structured Light Enables Biomimetic Swimming and Versatile Locomotion of Photoresponsive Soft Microrobots. *Nat. Mater.* **2016**, *15* (6), 647–653. https://doi.org/10.1038/nmat4569.

[18] Ube, T.; Ikeda, T. Photomobile Polymer Materials with Complex 3D Deformation, Continuous Motions, Self-Regulation, and Enhanced Processability. *Adv. Opt. Mater.* **2019**, *7* (16), 1900380. https://doi.org/10.1002/adom.201900380.

[19] Iamsaard, S.; Aßhoff, S. J.; Matt, B.; Kudernac, T.; Cornelissen, J. J. L. M.; Fletcher, S. P.; Katsonis, N. Conversion of Light into Macroscopic Helical Motion. *Nat. Chem.* **2014**, *6* (3), 229–235. https://doi.org/10.1038/nchem.1859.

[20] Lahikainen, M.; Zeng, H.; Priimagi, A. Design Principles for Non-Reciprocal Photomechanical Actuation. *Soft Matter* **2020**, *16* (25), 5951–5958. https://doi.org/10.1039/d0sm00624f.

[21] Finkelmann, H.; Nishikawa, E.; Pereira, G. G.; Warner, M. A New Opto-Mechanical Effect in Solids. *Phys. Rev. Lett.* **2001**, *87* (1), 015501/1-015501/4. https://doi.org/10.1103/PhysRevLett.87.015501.

[22] Van Oosten, C. L.; Harris, K. D.; Bastiaansen, C. W. M.; Broer, D. J. Glassy Photomechanical Liquid-Crystal Network Actuators for Microscale Devices ⋆. *Eur. Phys. J. E* **2007**, *23*, 329–336. https://doi.org/10.1140/epje/i2007-10196-1.

[23] Tibbits, S. 4D Printing: Multi-Material Shape Change. *Archit. Des.* **2014**, *84* (1), 116–121. https://doi.org/10.1002/ad.1710.

[24] Momeni, F.; M.Mehdi Hassani.N, S.; Liu, X.; Ni, J. A Review of 4D Printing. *Mater. Des.* **2017**, *122*, 42–79. https://doi.org/10.1016/J.MATDES.2017.02.068.

[25] Studart, A. R. Additive Manufacturing of Biologically-Inspired Materials. *Chem. Soc. Rev.* **2016**, *45* (2), 359–376. https://doi.org/10.1039/c5cs00836k.

[26] Kotikian, A.; Truby, R. L.; Boley, J. W.; White, T. J.; Lewis, J. A. 3D Printing of Liquid Crystal Elastomeric Actuators with Spatially Programed Nematic Order. *Adv. Mater.* **2018**, *30* (10), 1706164. https://doi.org/10.1002/adma.201706164.

[27] Davidson, E. C.; Kotikian, A.; Li, S.; Aizenberg, J.; Lewis, J. A. 3D Printable and Reconfigurable Liquid Crystal Elastomers with Light-Induced Shape Memory via Dynamic Bond Exchange. *Adv. Mater.* **2020**, *32* (1), 1905682. https://doi.org/10.1002/adma.201905682.

[28] Wang, Z.; Wang, Z.; Zheng, Y.; He, Q.; Wang, Y.; Cai, S. Three-Dimensional Printing of Functionally Graded Liquid Crystal Elastomer. *Sci. Adv.* **2020**, *6* (39), eabc0034. https://doi.org/10.1126/sciadv.abc0034.

[29] Zhang, C.; Lu, X.; Fei, G.; Wang, Z.; Xia, H.; Zhao, Y. 4D Printing of a Liquid Crystal Elastomer with a Controllable Orientation Gradient. *ACS Appl. Mater. Interfaces* **2019**, *11* (47), 44774–44782. https://doi.org/10.1021/acsami.9b18037.

[30] Hagaman, D. E.; Leist, S.; Zhou, J.; Ji, H. F. Photoactivated Polymeric Bilayer Actuators Fabricated via 3D Printing. *ACS Appl. Mater. Interfaces* **2018**, *10* (32), 27308–27315. https://doi.org/10.1021/acsami.8b08503.

[31] Ceamanos, L.; Kahveci, Z.; Lopez-Valdeolivas, M.; Liu, D.; Broer, D. J.; Sanchez-Somolinos, C. Four-Dimensional Printed Liquid Crystalline Elastomer Actuators with Fast Photoinduced Mechanical Response toward Light-Driven Robotic Functions. *ACS Appl. Mater. Interfaces* **2020**, *12* (39), 44195–44204. https://doi.org/10.1021/acsami.0c13341.

[32] Siqueira, G.; Kokkinis, D.; Libanori, R.; Hausmann, M. K.; Gladman, A. S.; Neels, A.; Tingaut, P.; Zimmermann, T.; Lewis, J. A.; Studart, A. R. Cellulose Nanocrystal Inks for 3D Printing of Textured Cellular Architectures. *Adv. Funct. Mater.* **2017**, *27* (12). https://doi.org/10.1002/adfm.201604619.

[33] Hausmann, M. K.; Rühs, P. A.; Siqueira, G.; Läuger, J.; Libanori, R.; Zimmermann, T.; Studart, A. R. Dynamics of Cellulose Nanocrystal Alignment. *ACS Nano* **2018**, *12*, 6926–6937. https://doi.org/10.1021/acsnano.8b02366.

[34] Müller, L. A. E.; Zimmermann, T.; Nyström, G.; Burgert, I.; Siqueira, G. Mechanical Properties Tailoring of 3D Printed Photoresponsive Nanocellulose Composites. *Adv. Funct. Mater.* **2020**, *2002914*, 1–9. https://doi.org/10.1002/adfm.202002914.

[35] Sultan, S.; Siqueira, G.; Zimmermann, T.; Mathew, A. P. 3D Printing of Nano-Cellulosic Biomaterials for Medical Applications. *Curr. Opin. Biomed. Eng.* **2017**, *2*, 29–34. https://doi.org/10.1016/j.cobme.2017.06.002.

[36] Dai, L.; Cheng, T.; Duan, C.; Zhao, W.; Zhang, W.; Zou, X.; Aspler, J.; Ni, Y. 3D Printing Using Plant-Derived Cellulose and Its Derivatives: A Review. *Carbohydrate Polymers*. 2019. https://doi.org/10.1016/j.carbpol.2018.09.027.

[37] Liu, J.; Gao, Y.; Wang, H.; Poling-Skutvik, R.; Osuji, C. O.; Yang, S. Shaping and Locomotion of Soft Robots Using Filament Actuators Made from Liquid Crystal Elastomer–Carbon Nanotube Composites. *Adv. Intell. Syst.* **2020**, *2* (6), 1900163. https://doi.org/10.1002/aisy.201900163.

[38] Burgert, I.; Frühmann, K.; Keckes, J.; Fratzl, P.; Stanzl-Tschegg, S. E. Microtensile Testing of Wood Fibers Combined with Video Extensometry for Efficient Strain Detection. *Holzforschung* **2003**, *57* (6), 661–664. https://doi.org/10.1515/HF.2003.099.

[39] Bunk, O.; Bech, M.; Jensen, T. H.; Feidenhans'L, R.; Binderup, T.; Menzel, A.; Pfeiffer, F. Multimodal X-Ray Scatter Imaging. *New J. Phys.* **2009**, *11* (12), 123016. https://doi.org/10.1088/1367-2630/11/12/123016.

[40] Barszczewska-Rybarek, I. M. Quantitative Determination of Degree of Conversion in Photocured Poly(Urethane-Dimethacrylate)s by Fourier Transform Infrared Spectroscopy. *J. Appl. Polym. Sci.* **2012**, *123* (3), 1604–1611. https://doi.org/10.1002/app.34553.

[41] Yang, H.; Liu, M. X.; Yao, Y. W.; Tao, P. Y.; Lin, B. P.; Keller, P.; Zhang, X. Q.; Sun, Y.; Guo, L. X. Polysiloxane-Based Liquid Crystalline Polymers and Elastomers Prepared by Thiol-Ene Chemistry. *Macromolecules* **2013**, *46* (9), 3406–3416. https://doi.org/10.1021/ma400462e.

[42] Yao, W.; Gao, Y.; Yuan, X.; He, B.; Yu, H.; Zhang, L.; Shen, Z.; He, W.; Yang, Z.; Yang, H.; Yang, D. Synthesis and Self-Assembly Behaviours of Side-Chain Smectic Thiol-Ene Polymers Based on the Polysiloxane Backbone. *J. Mater. Chem. C* **2016**, *4* (7), 1425–1440. https://doi.org/10.1039/c5tc04331j.

[43] Pelzl, G.; Hauser, A. Birefringence and Phase Transitions in Liquid Crystals. *Multinatl. J.* **1991**, *37* (1), 33–62. https://doi.org/10.1080/01411599108203447.

[44] Le, E. A.; Wang, W. C.; Liu, C. S.; Wang, C. W. Effect of Fiber Alignment on Optical Properties of Cellulose Nanocrystal Films. In *2014 International Symposium on Optomechatronic Technologies, ISOT 2014*; Institute of Electrical and Electronics Engineers Inc., 2014; pp 305–309. https://doi.org/10.1109/ISOT.2014.80.

[45) Cranston, E. D.; Gray, D. G. Birefringence in Spin-Coated Films Containing Cellulose Nanocrystals. *Physicochem. Eng. Asp.* **2008**, *325*, 44–51. https://doi.org/10.1016/j.colsurfa.2008.04.042.

[46] Poprawa-Smoluch, M.; Baggerman, J.; Zhang, H.; Maas, H. P. A.; De Cola, L.; Brouwer, A. M. Photoisomerization of Disperse Red 1 Studied with Transient Absorption Spectroscopy and Quantum Chemical Calculations. *J. Phys. Chem. A* **2006**, *110* (43), 11926–11937. https://doi.org/10.1021/jp054982b.

[47] Roppolo, I.; Chiappone, A.; Angelini, A.; Stassi, S.; Frascella, F.; Pirri, C. F.; Ricciardi, C.; Descrovi, E. 3D Printable Light-Responsive Polymers. *Mater. Horizons* **2017**, *4* (3), 396–401. https://doi.org/10.1039/c7mh00072c.

[48] Wani, O. M.; Zeng, H.; Priimagi, A. A Light-Driven Artificial Flytrap. *Nat. Commun.* **2017**, *8* (1), 1–7. https://doi.org/10.1038/ncomms15546.

[49] Camacho-Lopez, M.; Finkelmann, H.; Palffy-Muhoray, P.; Shelley, M. Fast Liquid-Crystal Elastomer Swims into the Dark. *Nat. Mater.* **2004**, *3* (5), 307–310. https://doi.org/10.1038/nmat1118.

[50] Lee, K. M.; White, T. J. Photochemical Mechanism and Photothermal Considerations in the Mechanical Response of Monodomain, Azobenzene-Functionalized Liquid Crystal Polymer Networks. *Macromolecules* **2012**, *45* (17), 7163–7170. https://doi.org/10.1021/ma301337e.

[51] Harrison, J. M.; Goldbaum, D.; Corkery, T. C.; Barrett, C. J.; Chromik, R. R. Nanoindentation Studies to Separate Thermal and Optical Effects in Photo-Softening of Azo Polymers. *J. Mater. Chem. C* **2015**, *3* (5), 995–1003. https://doi.org/10.1039/c4tc02336f.

[52] Kumar, K.; Schenning, A. P. H. J.; Broer, D. J.; Liu, D. Regulating the Modulus of a Chiral Liquid Crystal Polymer Network by Light. *Soft Matter* **2016**, *12* (13), 3196–3201. https://doi.org/10.1039/c6sm00114a.

[53] Yu, Y.; Nakano, M.; Ikeda, T. Directed Bending of a Polymer Film by Light. *Nature* **2003**, *425* (6954), 145–145. https://doi.org/10.1038/425145a.

[54] Pilz Da Cunha, M.; Van Thoor, E. A. J.; Debije, M. G.; Broer, D. J.; Schenning, A. P. H. J. Unravelling the Photothermal and Photomechanical Contributions to Actuation of Azobenzene-Doped Liquid Crystal Polymers in Air and Water. *J. Mater. Chem. C* **2019**, *7* (43), 13502–13509. https://doi.org/10.1039/c9tc04440j.

[55] Lahikainen, M.; Zeng, H.; Priimagi, A. Reconfigurable Photoactuator through Synergistic Use of Photochemical and Photothermal Effects. *Nat. Commun.* **2018**, *9* (1), 1–8. https://doi.org/10.1038/s41467-018-06647-7.

[56] Mehta, K.; Peeketi, A. R.; Liu, L.; Broer, D.; Onck, P.; Annabattula, R. K. Design and Applications of Light Responsive Liquid Crystal Polymer Thin Films. *Applied Physics Reviews*. American Institute of Physics Inc. December 1, 2020, p 41306. https://doi.org/10.1063/5.0014619.

[57] Gantenbein, S.; Masania, K.; Woigk, W.; Sesseg, J. P. W.; Tervoort, T. A.; Studart, A. R. Three-Dimensional Printing of Hierarchical Liquid-Crystal-Polymer Structures. *Nature*. Nature Publishing Group September 13, 2018, pp 226–230. https://doi.org/10.1038/s41586-018-0474-7.

[58] Bi, M.; He, Y.; Wang, Y.; Yang, W.; Qin, B.; Xu, J.; Wang, X.; Wang, B.; Dong, Y.; Gao, Y.; Li, C. Photo Actuation Performance of Nanotube Sheet Incorporated Azobenzene Crosslinked Liquid Crystalline Polymer Nanocomposite. *Polymers (Basel).* **2019**, *11* (4). https://doi.org/10.3390/polym11040735.

[59] Sánchez-Ferrer, A.; Finkelmann, H. Opto-Mechanical Effect in Photoactive Nematic Main-Chain Liquid-Crystalline Elastomers. *Soft Matter* **2013**, *9* (18), 4621–4627. https://doi.org/10.1039/c3sm27341e.

3.2.8 Supporting Information

Photo-responsive movement in 3D printed cellulose nanocomposites

Luca A. E. Müller, Adrien Demongeot, Joanne Vaucher, Yves Leterrier, Jonathan Avaro, Marianne Liebi, Antonia Neels, Ingo Burgert, Tanja Zimmermann, Gustav Nyström, Gilberto Siqueira**

DOI: 10.1021/acsami.2c02154

LC mesogen:
4-Methoxybenzoic acid 4-(6-acryloyloxyhexyloxy)phenyl

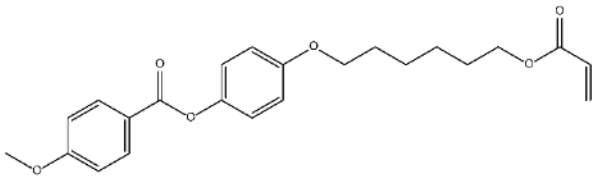

LC crosslinker:
1,4-Bis-[4-(3-acryloyloxypropyloxy)benzoyloxy]-2-methylbenzene

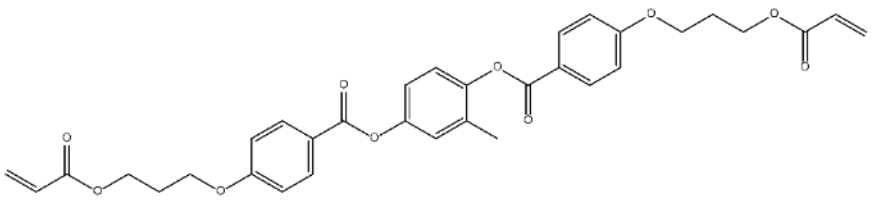

Main chain:
poly(mercaptopropyl)methylsiloxane (SMS992)

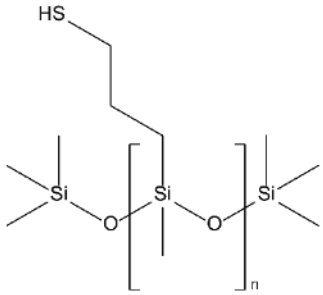

Photoinitiator:
Phenylbis(2,4,6-trimethylbenzoyl)phosphine oxide
Irgacure 819

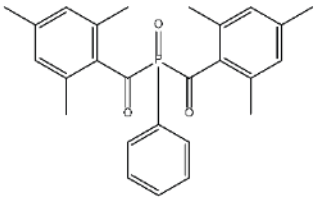

Figure S 3.2-1 *Schematic of the liquid crystalline matrix.*

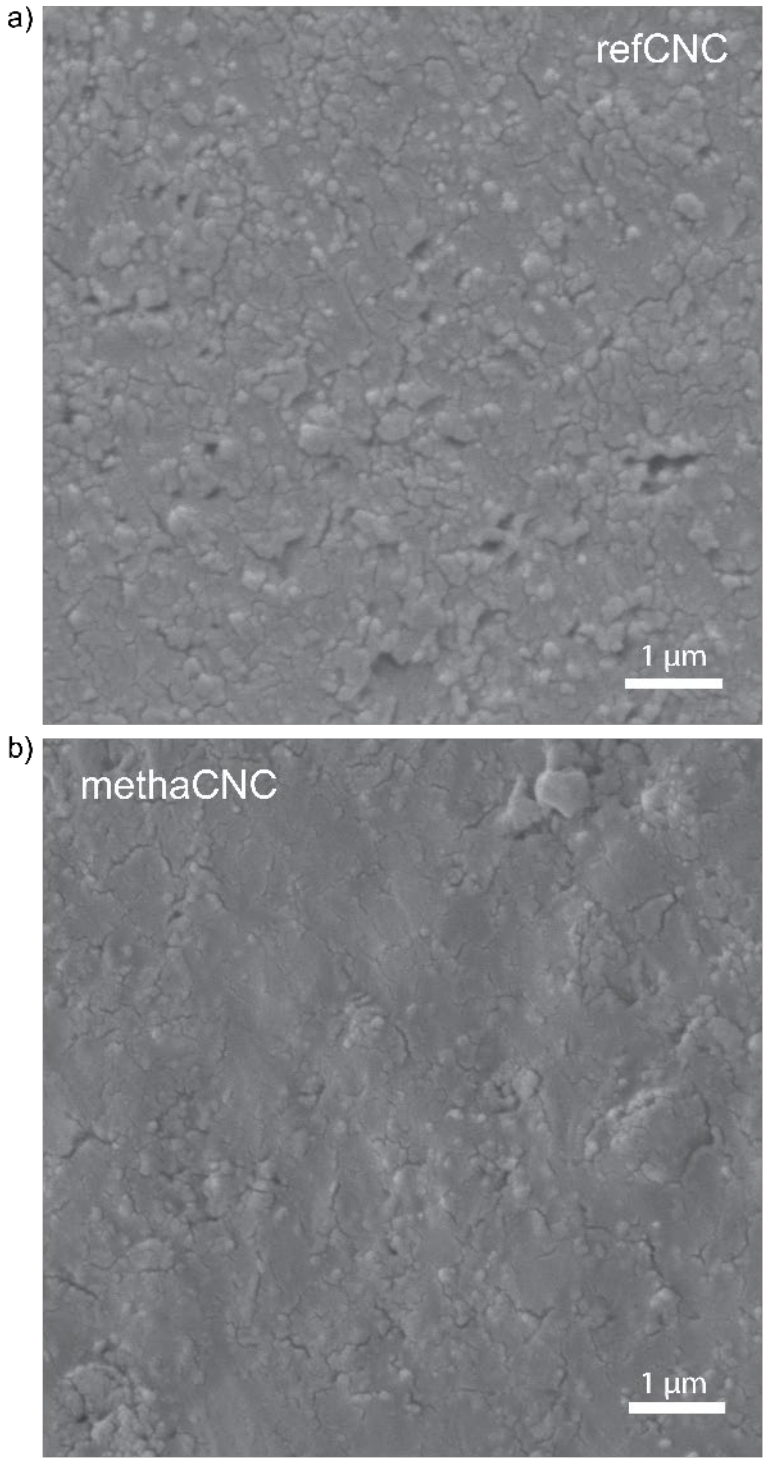

***Figure S 3.2-2**, SEM Cross section of refCNC (**a**) and methaCNC (**b**) filaments embedded in an epoxy resin. Materials with methaCNC show a smoother surface with a reduced presence of agglomerates.*

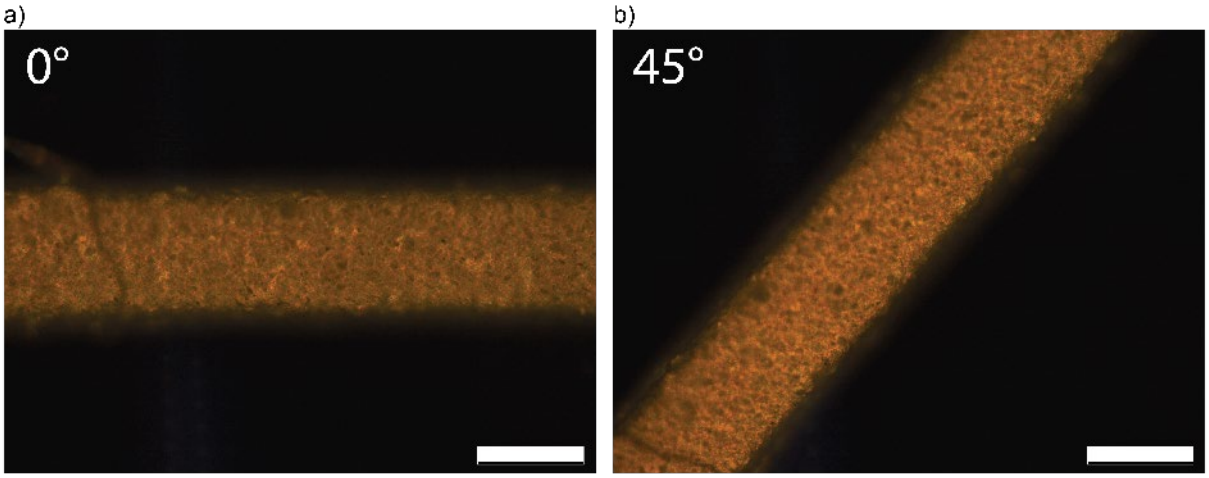

***Figure S 3.2-3**, 10X cross polarizer micrographs of methaCNC based printed filaments and cured at 60°C while the LC mesogens are in an isotropic state. Images show filaments with printing direction at 0° and 45° in respect to light polarization, for a) and b) respectively. The change in intensity between the two images is slightly noticeable and mainly attributed to the alignment of CNC. This sample did not show any photomechanical response after DR1 doping. Scale bars represent 200 µm.*

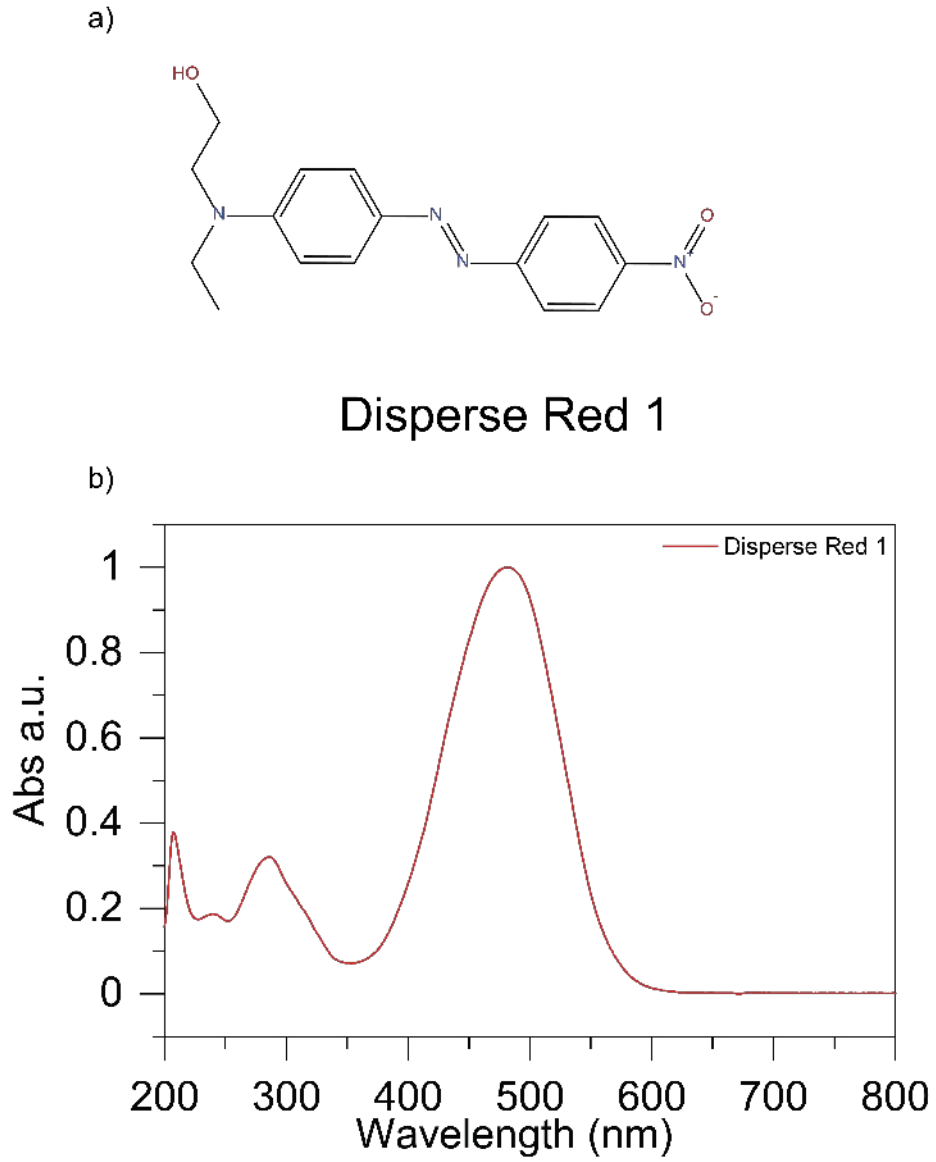

Figure S 3.2-4 *a) schematic representation of the Disperse Red 1 azobenzene molecular structure. b) UV-Vis observation of the absorption spectra of 10 µg ml^{-1} DR1 dissolved in acetone.*

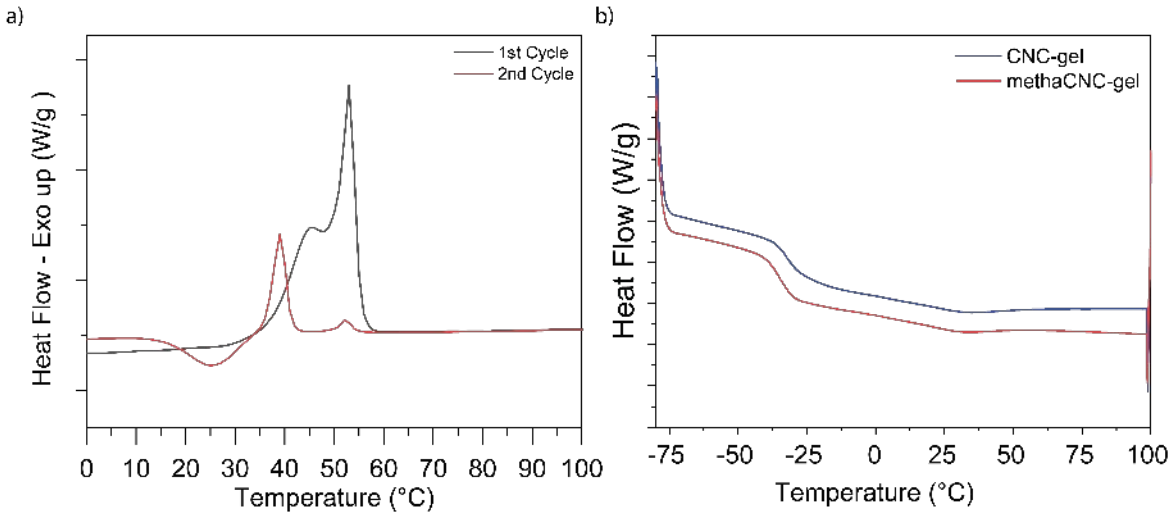

Figure S 3.2-5 *DSC measurement of the LC mesogen (4-Methoxybenzoic acid 4-(6-acryloyloxyhexyloxy)phenyl). The nematic to isotropic transition of the monomer occurs at 55°C a). DSC curves for uncured inks of 15 wt% refCNC and methaCNC b). The LC phase transition here occurs around 30°C.*

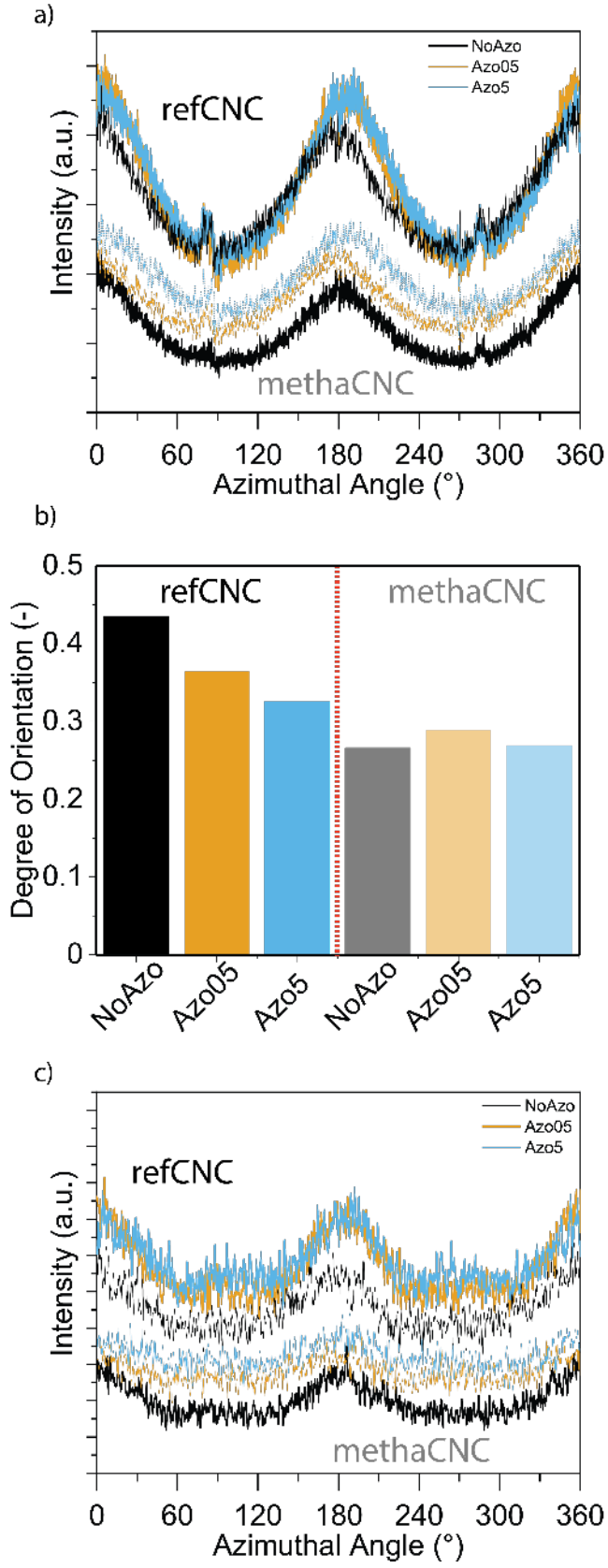

Figure S 3.2-6 *Orientation analysis carried out on printed composites from SAXS measurements. Azimuthal angle intensities for cellulose nanoparticles in the printed filaments (a), signal integrated from q=0.5 to q=1.17 nm^{-1} and their degree of orientation for measured samples in respect of CNC (b). (c) Azimuthal angles intensities for q between 1.17 to 2.32 nm^{-1} for both CNC and LC.*

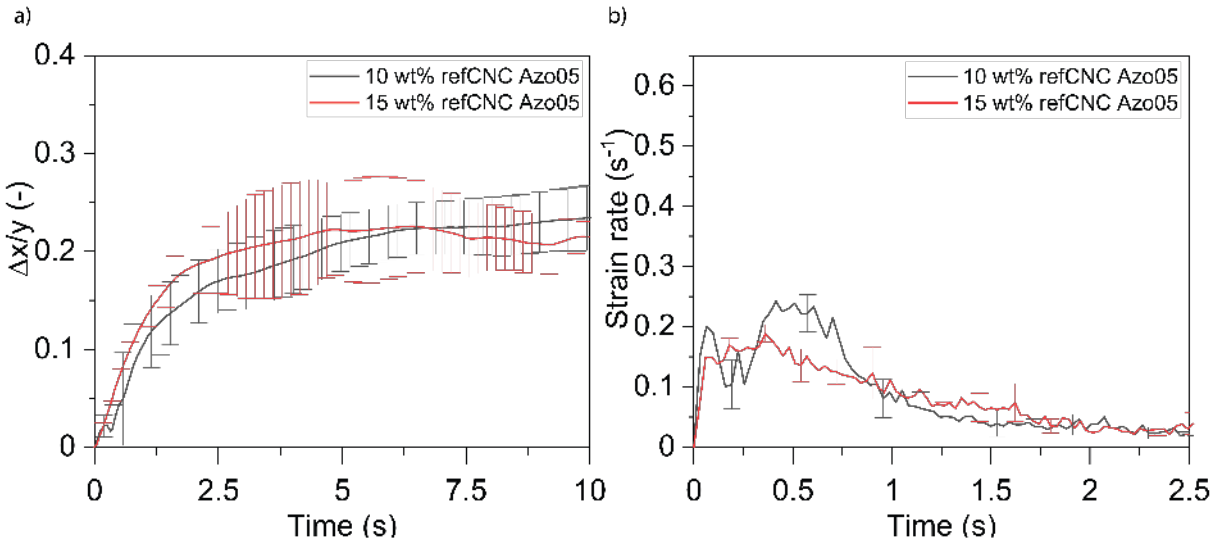

Figure S 3.2-7 *Analysis of the printed filaments photoactuated movements comparing 10 to 15 wt% refCNC Azo05.* ***a)*** *Measurements of the displacement of the filament tip normalized by the length y, in function of time for the photo-actuation.* ***b)*** *Measurements of the strain rate of the filament tip in function of time for the photo-actuation. For each experiment three samples were characterized.*

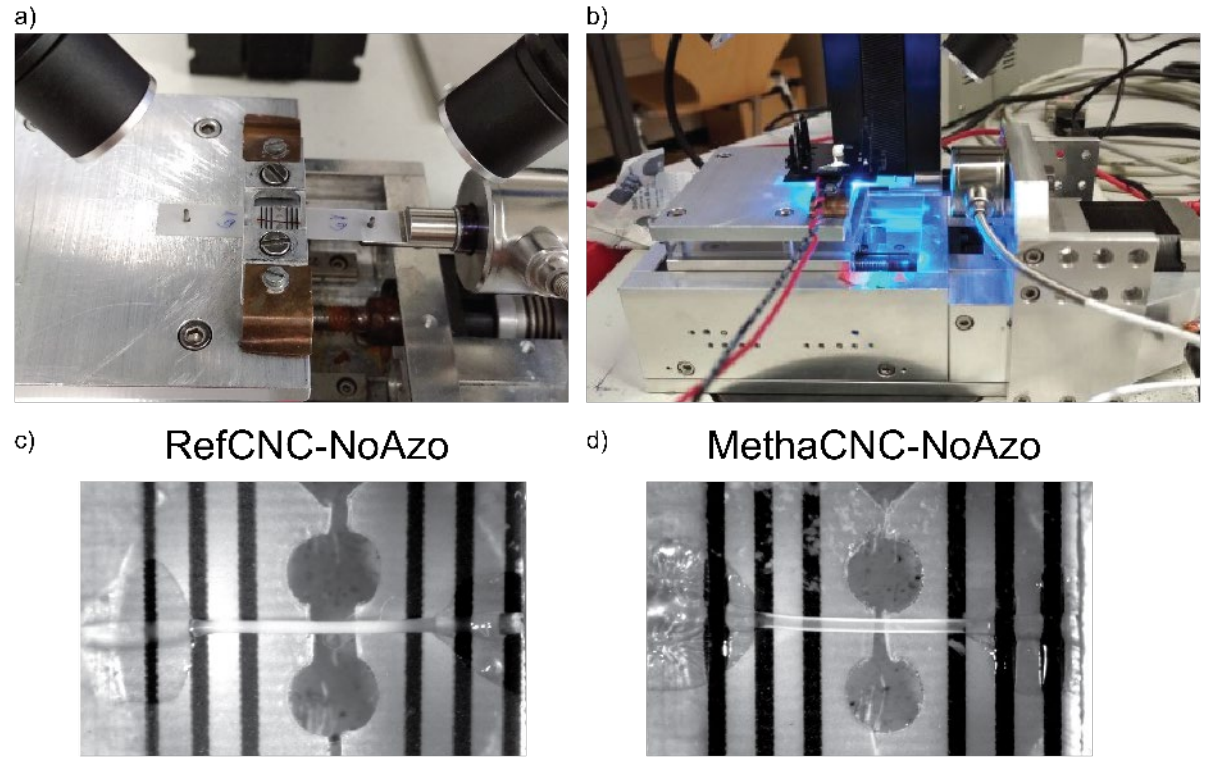

Figure S 3.2-8 *a) photograph of the microtensile test setup employed in this study. The sample is placed and glued onto a substrate in order to be tested. b) modified setup with the 480nm LED placed above the sample at a 5 mm distance. c) and d) respectively refCNC and methaCNC NoAzo samples placed and glued onto the substrate.*

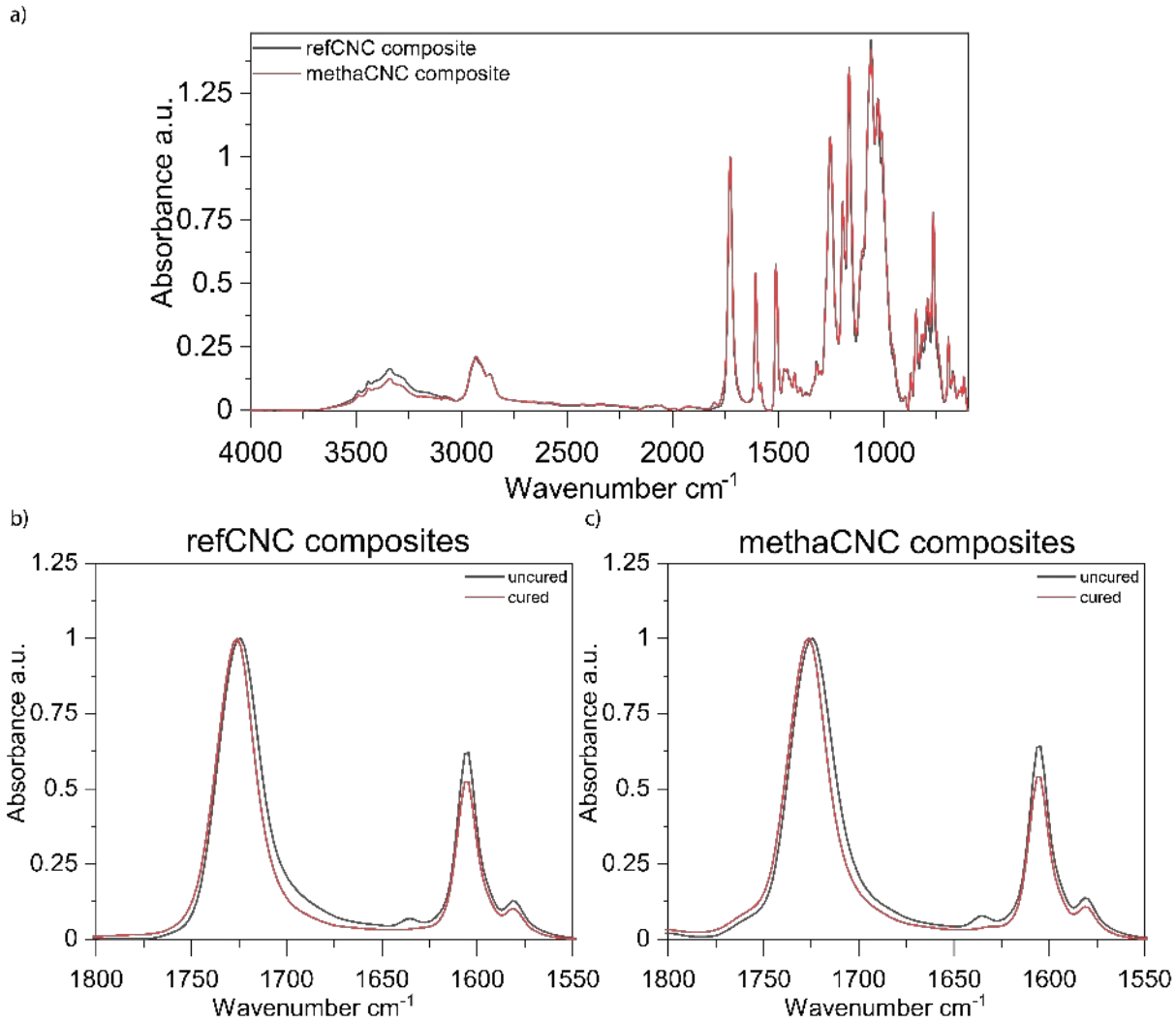

Figure S 3.2-9 *ATR-FTIR Spectra of refCNC and methaCNC composites. Full spectra of cured composites* ***(a)*** *and comparison of before and after curing in the region of interest for refCNC* ***(b)*** *and methaCNC* ***(c)*** *composites. The resulting relative degrees of conversion were 51.5 ± 6.3 % for refCNC and 51.3 ± 4.1 % for methaCNC composites.*

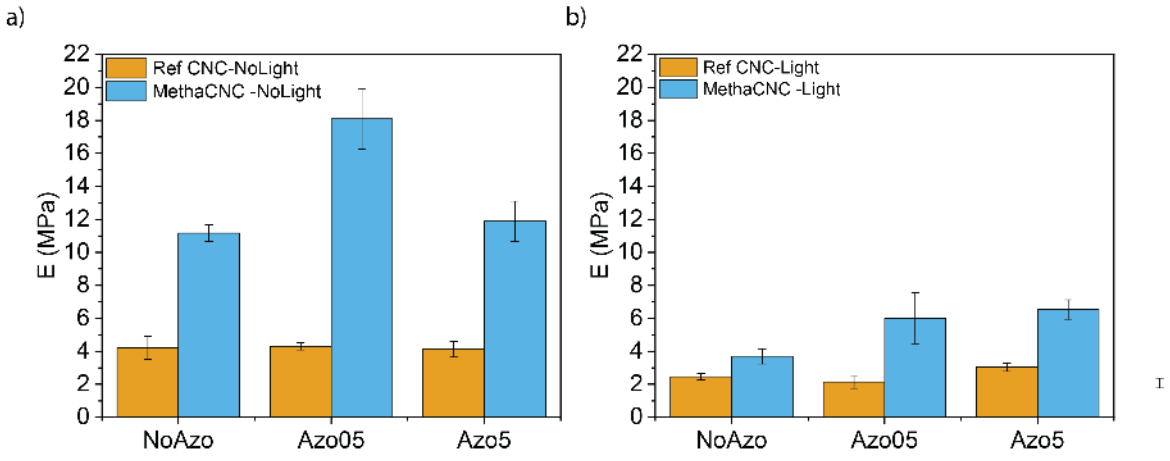

Figure S 3.2-10 *Young moduli of refCNC and MethaCNC 15 wt% composites extracted from the microtensile experiements.* ***(a)*** *Elastic moduli in dark.* ***(b)*** *Elastic moduli under illumination.*

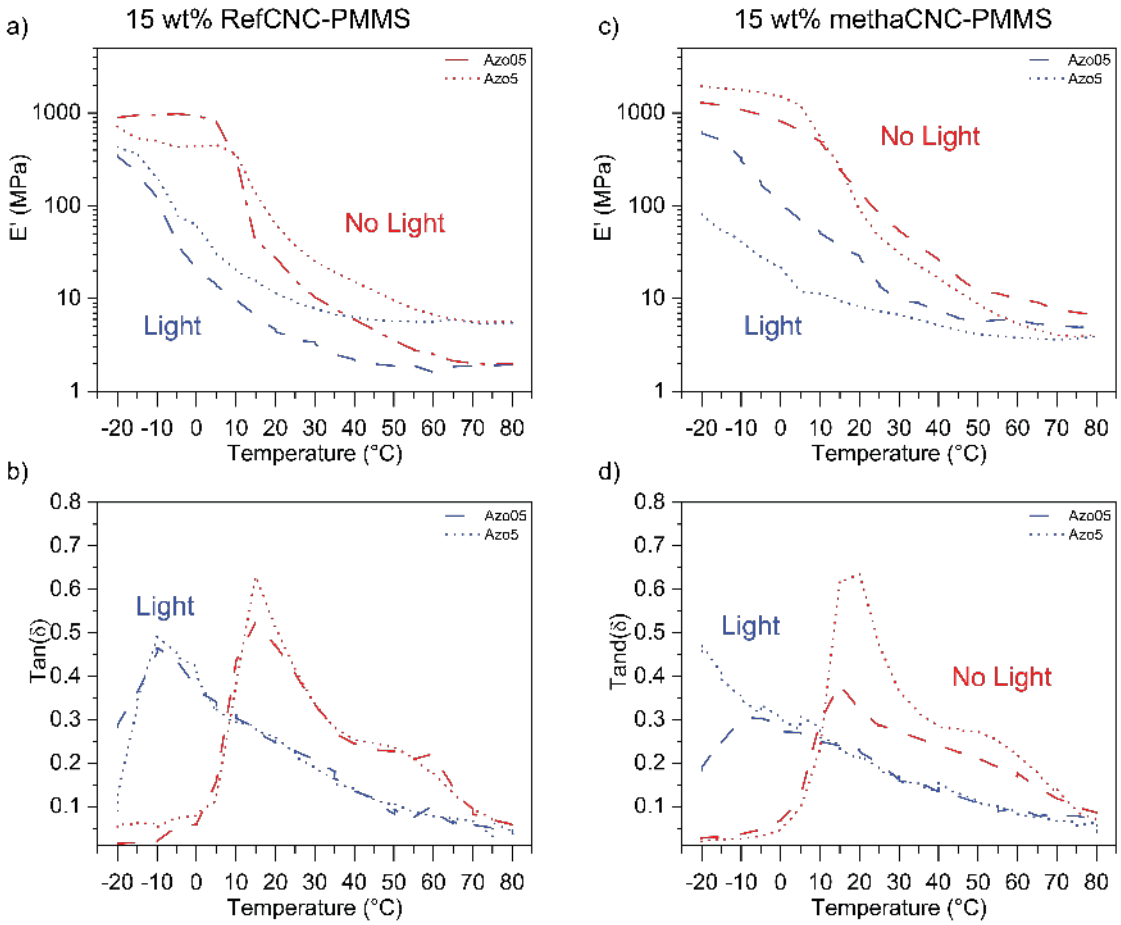

Figure S 3.2-11 *DMA experiments comparing storage modulus and tan(δ) in dark and under illumination of developed composites.* ***a)*** *and* ***b)*** *are the storage modulus and tan(δ) for composites with refCNC particles, respectively.* ***c)*** *and* ***d)*** *are the storage modulus and tan(δ) for composites with methaCNC particles, respectively.*

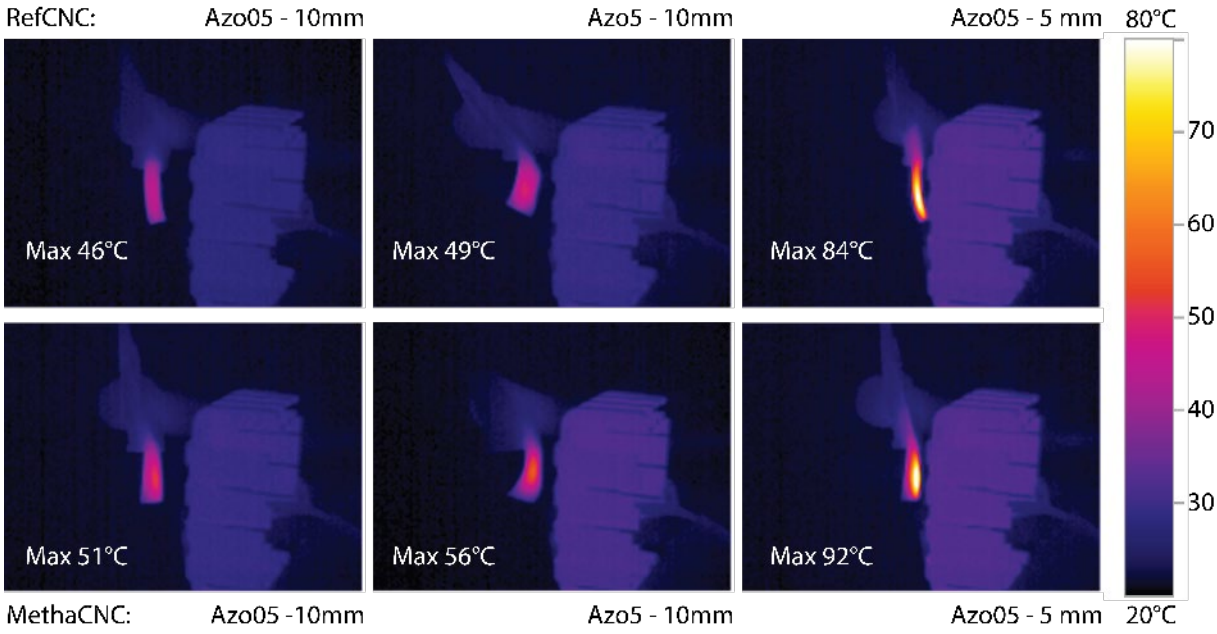

Figure S 3.2-12 *Thermal images of refCNC and MethaCNC composites at 10 mm from the LED light source and at 5 mm from the LED during illumination. The photogenerated heat is dependent on the light intensity. Reference samples for both CNC types showed a surface temperature of 25° and 32°C for 10 and 5 mm of distance respectively.*

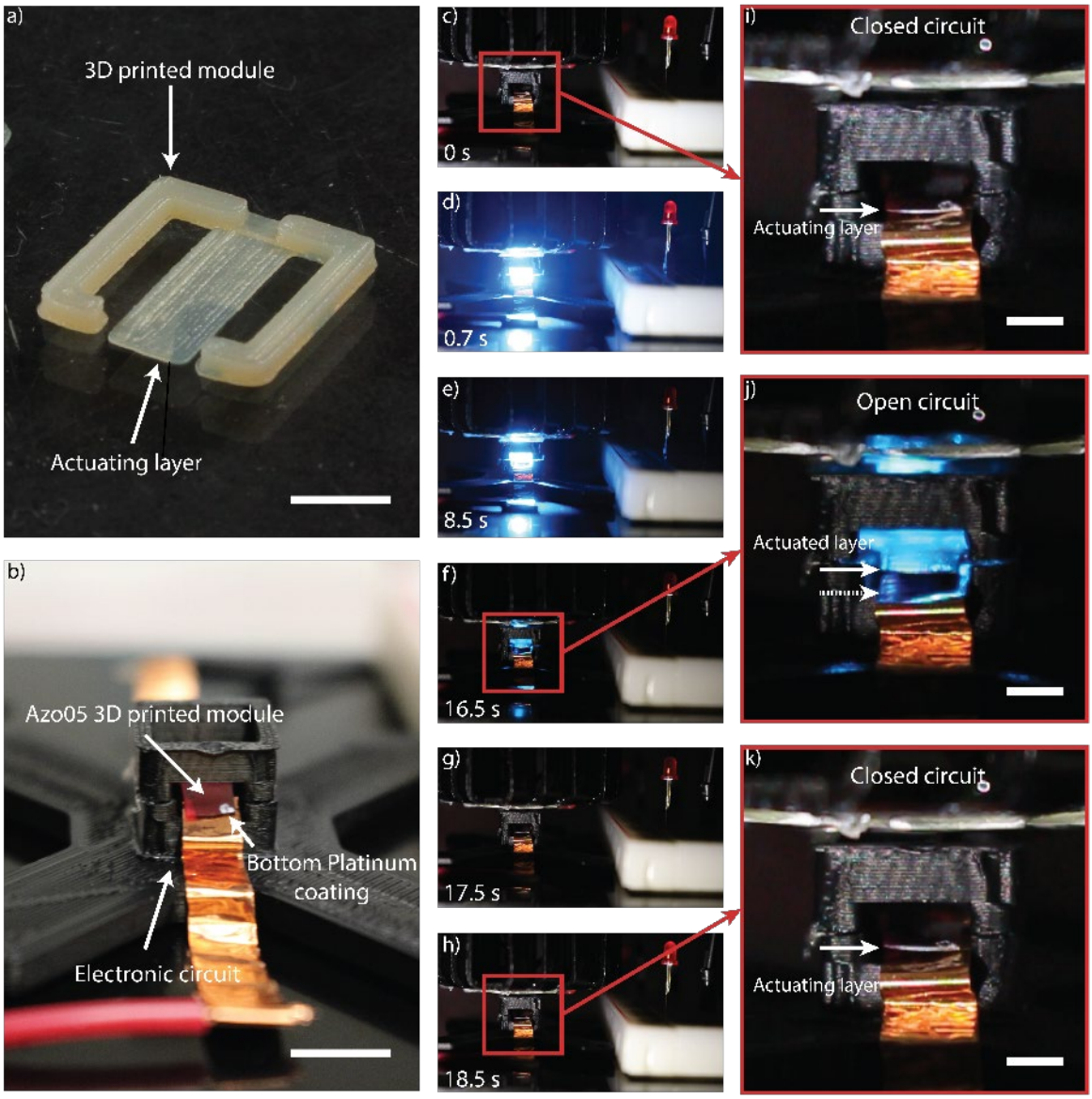

Figure S 3.2-13 *A 3D printed actuator utilized as safety circuit. When in dark the circuit stays closed, while when illuminated the electric circuit opens. a) 3D printed actuator before DR1 doping bath. b) Image of the incorporation of such module in the circuit after applying a 20 nm Pt layer at the bottom of the module. c-h) Defined frames showing the demonstrator in action. When the actuator is illuminated it starts moving and after 8.5 s the red LED switches off. At 17.5 s the light has been switched off and the actuator comes back to its original position and the circuit is closed again at 18.5 s. i) a magnification of the Azo05 3D printed device in its original position at time 0 s. j) and k) magnifications of the frames at 16.5s and 18.5 s respectively to show the movement*

3.3 Functionalized Cellulose Nanocrystals as Active Reinforcements for Light Actuated 3D Printed Structures

Luca A. E. Müller[+1,2], Anita Zingg[+1,2], Andrea Arcifa[3], Tanja Zimmermann[1], Gustav Nyström*[1,4], Ingo Burgert[2], Gilberto Siqueira*[1]

[+]Shared first co-authorship

[1]Cellulose and Wood Materials Laboratory, Empa, Swiss Federal Laboratories for Materials Science and Technology, 8600 Dübendorf, Switzerland

[2]Wood Materials Science, Institute for Building Materials, ETH-Zürich, 8093 Zürich, Switzerland

[3]Surface Science & Coating Technologies, Empa, Empa, Swiss Federal Laboratories for Materials Science and Technology, 8600 Dübendorf, Switzerland

[4]Department of Health Sciences and Technology, ETH Zürich, 8092 Zürich, Switzerland

*Corresponding authors: Gustav Nyström, Gilberto Siqueira

E-Mail addresses: gustav.nystroem@empa.ch , gilberto.siqueira@empa.ch

3.3.1 Abstract

Conventional manufacturing techniques allow the production of photoresponsive cellulose nanocrystals (CNC)-based composites that can reversibly modify their optical, mechanical, or chemical properties upon light irradiation. However, such materials are often limited to 2D films or simple shapes and do not benefit from spatial tailoring of mechanical properties resulting from CNC alignment. Herein, we propose the direct ink writing (DIW) of 3D complex structures that combine CNC reinforcement effects with photoinduced responses. After grafting azobenzene photochromes onto the CNC surfaces, up to 15 wt % of modified nanoparticles can be introduced into a polyurethane acrylate matrix. The influence of CNC on rheological properties allows DIW of self-standing 3D structures presenting local shear-induced alignment of the active reinforcements. The printed composites, with longitudinal elastic modulus of 30 MPa, react to visible-light irradiation with 30–50% reversible softening and present a shape memory behavior. The phototunable energy absorption of 3D complex structures is demonstrated by harnessing both geometrical and photoresponsive effects, enabling dynamic mechanical responses to environmental stimuli. Functionalized CNC in 3D printable inks have the potential to allow the rapid prototyping of several devices with tailored mechanical properties, suitable for applications requiring dynamic responses to environmental changes.

Keywords: *cellulose nanocrystals, 3D printing, photoresponsive, azobenzene, mechanical adaptation*

3.3.2 Introduction

Advancing sustainability in a technological world requires the development of lightweight devices that can reach peak mechanical performances while being composed of renewable and sustainable materials. As a result, in the last years, strong attention has been paid to biomimicry and bioinspiration since living

organisms can rely on biological materials exhibiting highly optimized performances [1]. Despite evolving with a limited palette of ingredients, such materials can often reach outstanding mechanical properties and demonstrate functional responses to external stimuli under demanding environmental conditions. A material like wood possesses highly anisotropic specific strength and stiffness [2], and the differential growth during wood formation by the tree can induce movements by the formation of reaction wood tissues [3],[4]. Trees and other plants can hence fulfill their biological functions and self-optimize their mechanical properties, preventing failure and securing survival. Such outstanding properties are achieved due to the intrinsic hierarchical structure of wood, which spans from the nanoscale of the cell wall to the macroscopic features of the bulk wood [5]. Many engineering design strategies of composite materials are inspired by features of biological materials and structures. These comprise localized orientation of natural building blocks commonly embedded in biopolymer matrices, localized density gradients of reinforcements, and matrices' compositional changes and gradients [6]. Although the influence of various parameters is well-known, the synthetic manufacture of materials with determined functional microstructures remains challenging and is still far from the astonishing intricacy and complexity of biological materials.

The development of additive manufacturing, and especially 3D-printing technologies, made it possible to harness the design strategies, mentioned above, for the production of customized high-performance devices. With a bottom-up layer-by-layer approach, 3D-printing technologies are versatile platforms providing high geometrical freedom, allowing the production of materials and devices exhibiting complex structures and controlled microstructures [1]. In this context, direct ink writing (DIW) has arisen as a reliable technique for the production of nanocellulose-based composites that possess spatially tailored mechanical properties [7-9]. Especially, building blocks such as cellulose nanocrystals (CNC) present great potential as biocompatible, renewable, and functional reinforcing agents in 3D-printed parts [10]. Acting as rheology modifiers, CNC allow suspensions to be processed by DIW, while their anisotropic rod-like shape confers a directional reinforcing effect. DIW is a filamentary technique, and it applies shear and extensional stresses to the suspension during extrusion, conferring a preferential particles' orientation along the printing direction. This leads to a high degree of CNC alignment [8] and provides high spatial control over the mechanical properties of the printed parts [11]. The development of such mechanically tailored CNC composites allows the creation of lightweight and highly optimized devices for applications subject to particular load conditions. Moreover, a combination of the spatially controlled mechanical properties with a dynamic change of physical and/or chemical properties as response to an external stimulus would further improve potential functionalization for a wide range of applications spanning from biomedical fields [12] to food packaging [13]. Nonetheless, the development of CNC-based composites fabricated by DIW is still in its infancy, and the triggering stimuli are mainly limited to humidity. It has been shown that CNC ink formulations can benefit from the alignment during printing and the hygroscopic nature of the nanoparticles, which leads to predetermined bending and curling, imitating cell wall dynamics in wood during hydration and dehydration cycles [14]. However, this approach has so far only been applied to soft hydrogels with Young's moduli of a few kPa.

Besides the renewable, biocompatible nature and the reinforcing behavior of CNC, such nanoparticles are also of great interest due to their surface chemistry, which allows for facile functionalization. The large available quantity of hydroxyl groups is suitable for covalently bonding specific chemical switches that confer adaptive properties in response to defined external stimuli such as heat, pH, solvent, and light [15], making these particles attractive as active functional reinforcements in 3D-printed composites. Among the different external stimuli, light is particularly attractive due to its contactless nature, which allows remote actuation with minimal impact on the material and its surroundings. In addition,

the actuating signal can be modulated both spatially and temporarily in order to obtain multiple responses [16]; hence, photoresponsive CNC-based nanocomposites have already been produced for several functionalities. By grafting coumarin [17] or benzophenone [18] moieties on the particle's surface, CNC composites can react to determined wavelengths and create covalent particle–matrix bonds resulting in localized photostiffening. This function was also successfully transferred to 3D-printed nanocomposites by introducing cinnamate moieties on the CNC surface and in the polymer network [19]. Other functionalization approaches, like the modification of CNC with azobenzene [20] photochromes, have resulted in composites films with reversible color changes when irradiated, facilitating optical storage applications. Azobenzene functionalization of other polymers has also been investigated to develop materials with different photoresponses. The use of the azobenzene *trans–cis* photoisomerization as switching event allowed multiple smart behaviors, such as phototriggered movements [21], changes in wettability [22], and gel–sol transitions [23]. These examples render CNC functionalization with azobenzene attractive for the production of 3D-printed reversible multiresponsive materials.

Hence, we propose here a way to manufacture 3D complex structures presenting both fast and reversible photoresponsive behaviors and tailored mechanical properties (Figure 3.3-1). By grafting the pseudo-stilbene Disperse Red 1 (DR1) [24] onto the surface of CNC, multipurpose active reinforcement particles that react to light with a wavelength of 475 nm can be produced. After modification, these active elements maintain their slender shape, and hence the ability to impart to Newtonian resins the rheological properties required for a successful DIW's filamentary extrusion and particle alignment. Polymer inks can then be printed in 3D complex shapes with optimized mechanical properties while demonstrating macroscopic photoresponsive behaviors, arising from the *trans–cis–trans* photoisomerization of DR1. As a proof of concept, we dispersed these functional CNC into a polyurethane acrylate matrix and printed a composite material that can undergo reversible softening and exhibits a shape memory effect when irradiated with the appropriate wavelength. With DIW, this material can be shaped into complex 3D structures that couple mechanical behaviors, arising from their geometry, with dynamic and reversible phototriggered mechanical responses. Such combination results in devices with mechanical properties tunable on demand and suitable for applications as dynamic dampers or energy absorbers.

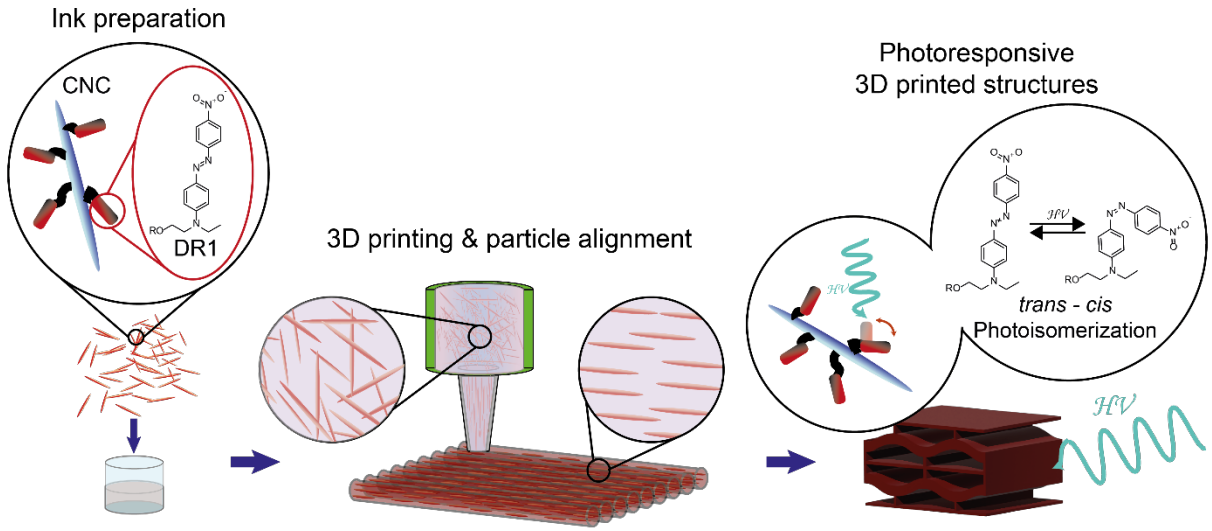

Figure 3.3-1 *Preparation of photoresponsive 3D-printed cellulose nanocomposites. The CNC are surface-modified with Disperse Red 1 (DR1). When introduced in a polymer resin, they create a printable ink that can be processed with DIW. 3D printing locally aligns the particles along the printing direction, conferring anisotropic mechanical properties to the printed objects. The final printed structure, after curing, displays photoresponsive behaviors due to the photoisomerization of DR1.*

These renewable functionalized particles have hence a great potential for the production of diverse smart mechanical structures, i.e., structures that react to an external stimulus. By allowing the additive manufacturing of diverse matrix materials while actively conferring reversible photoresponsive behaviors, these functionalized CNC substantially increase the design freedom by adding the temporal dimension to the structure's properties. Thus, lightweight devices for specific (dynamic) load cases can be produced and customized with fine-tuned mechanical properties that allow reacting to environmental changes.

3.3.3 Results and Discussion

3.3.3.1 Functionalization of CNC

We imparted functional and photoresponsive behaviors to cellulose nanocomposites by attaching DR1, an azobenzene molecule, to the surface of the CNC. To achieve such a chemical modification, cyanuric chloride was selected as a chemical linker, since the reaction undergoes two nucleophilic substitutions: one with the cellulose hydroxyl groups (−OH) and one with the DR1 ones (Figure S 3.3-1) allowing covalent bonding of the azobenzene on the CNC surface [25]. The chemical treatment could be carried out successfully, leading to strongly magenta colored CNC (Figure 3.3-2). Unmodified CNC (named CNC) and modified CNC (named CNC-DR1 for simplicity) were characterized qualitatively by ATR-FTIR and the results indicate a successful cellulose modification (Figure 3.3-2a). The appearance in the CNC-DR1 spectrum of IR bands at 854 cm^{-1} for the C–Cl bending and at 1500–1580 cm^{-1} for the C–N stretching vibrations [26] suggests the presence of the cyanuric chloride linker. Other new bands also appear in the region 1600–1750 cm^{-1} with a prominent peak at 1636 cm^{-1}, which substitutes the H–O–H vibration of adsorbed water observed in the CNC spectrum, and a second small peak at 1715 cm^{-1}, both attributed to the planar stretching vibrations of the triazine ring [27]. The sharpening of the 1636 cm^{-1} band occurred after CNC modification is assumed to occur due to the substitution of hydroxyl groups of the cellulose with the cyanuric chloride linker. The shoulder at 1610 cm^{-1} arises as a combination of triazine ring vibrations with the C═C stretching modes of the DR1 benzene rings [28]. Indeed, comparison of CNC-DR1 spectrum with the one of CNC that reacted only with the cyanuric chloride (CNC-Cy, Figure S 3.3-2) revealed that, when DR1 is employed for the reaction, the contribution of the C═C stretching makes the band at 1610 cm^{-1} appear stronger. Despite the differences observed between CNC and CNC-DR1 spectra, little differences subsist between the CNC-Cy and the CNC-DR1 IR spectra. The typical frequency bands at 1500–1550 cm^{-1} of the DR1 nitro group asymmetric stretching could not be clearly distinguished from the C–N stretching vibrations of the cyanuric chloride. To further confirm the DR1 presence on the surface of CNC-DR1, after the modification, additional proofs were qualitatively obtained by ToF SIMS, XPS, and NMR (Figure S 3.3-3). All measurements revealed the presence of DR1. From solid-state NMR (Figure S 3.3-3), the DR1 substitution fraction of accessible hydroxyl groups at the surface of CNC could be estimated at 0.7%, calculated according to the method employed by Xiao et al. [29]. Moreover, the substitution fraction of accessible hydroxyl on CNC-DR1 surface was estimated, considering one DR1 per triazine ring, at around 2.4%, by tracking the amount of nitrogen with elemental analysis (Table S 3.3-1).

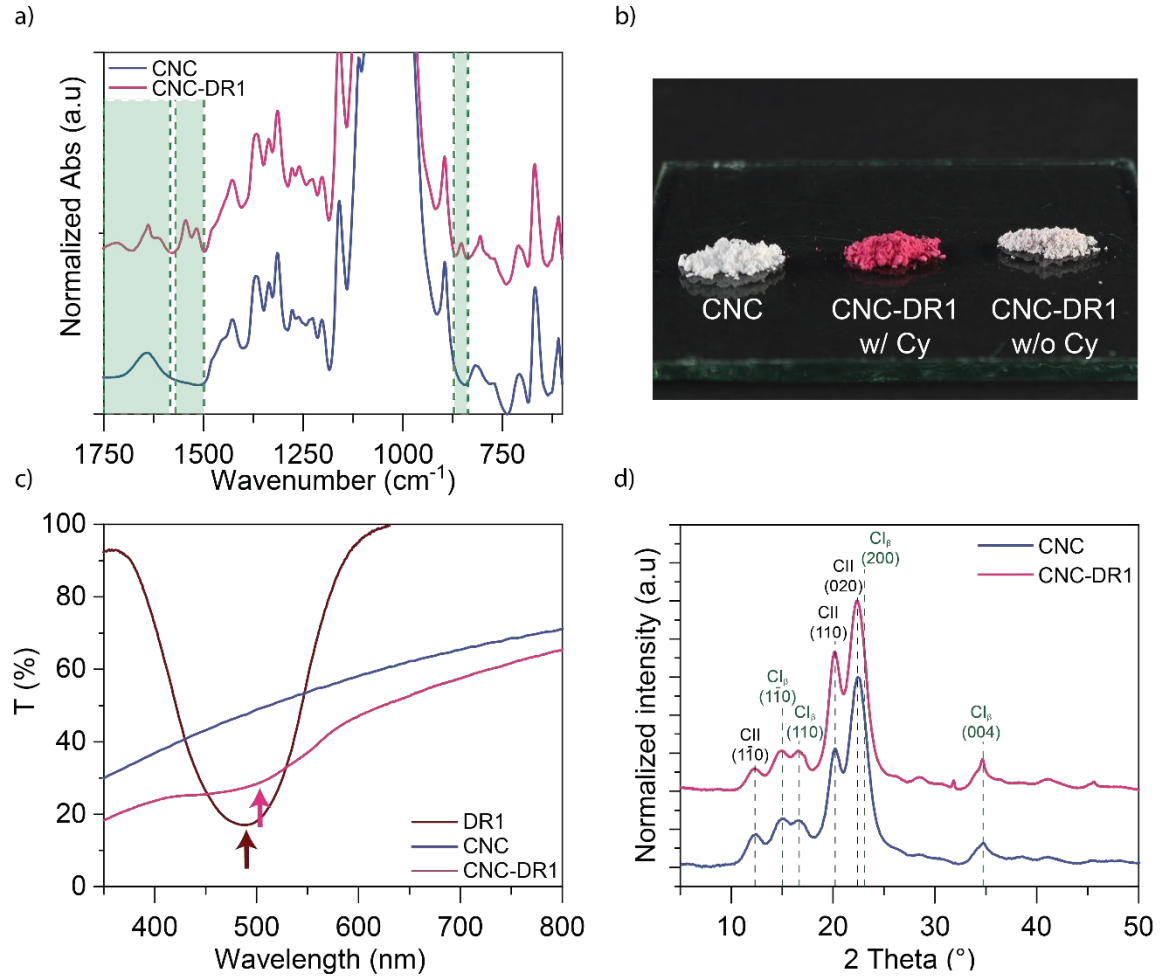

Figure 3.3-2 *Functionalization of CNC with azobenzene molecules. (a) Enlarged FTIR spectra between 1750 and 600 cm^{-1} of CNC (before) and CNC-DR1 (after functionalization), green regions highlight the appearance of new bands. (b) Photograph comparing dried CNC (left), washed with six cycles of centrifugation and acetone renewal, dried CNC-DR1 (middle) after six washing cycles, and dried CNC that underwent the modification with DR1 without cyanuric chloride (Cy) (right) after four washing cycles. (c) UV–vis spectra of CNC with and without modification and pure DR1 in acetone, the arrows indicate the maximum absorption peaks of the spectra with the respective colors. (d) XRD patterns comparison of CNC with CNC-DR1.*

The presence of DR1 on the CNC-DR1 surface can also be observed by the naked eye (Figure 3.3-2b) since CNC-DR1 powder dried from acetone assumes a strong magenta color, which is maintained after six washing cycles of the reaction product. Differently, repeating the reaction process, for CNC with DR1 alone, without the cyanuric chloride linker, led to a whitish powder that lost almost entirely the characteristic color of DR1 already after four washing cycles. This indirectly indicates a successful grafting of DR1, mediated by the cyanuric linker, on the CNC-DR1 surface.

The CNC's change of color is also observed in Figure 3.3-2c. Here, UV–vis spectra are illustrated comparing the transmission of 0.5 mg mL^{-1} of CNC particles (before and after modification) in acetone. Both particle suspensions show a similar behavior of increasing transmittance from 20–30% to around 60–70% with increasing wavelength. Such behavior is attributed to the light scattering observed from the two suspensions (Figure 3.3-2b). The lower transmittance of CNC-DR1 samples is due to a more homogeneous dispersion in acetone and a higher stability that promotes further scattering. Pristine CNC precipitate faster than CNC-DR1 when in acetone, resulting in lower concentrations in the light beam path during the measurement. However, the modified CNC show an absorption peak at 505 nm corresponding to the absorption region of DR1, while the unmodified particles present a constant increase in transmission as the wavelength increases. Interestingly, the maximum absorption of DR1 in acetone is

at 489 nm. The redshift that occurs in the CNC-DR1 suspension arises due to a stronger electron delocalization [30], further indicating a successful functionalization reaction.

Despite successfully accomplishing the chemical modification, the crystalline structure of the CNC may have been altered during the process [19]. To investigate the crystallinity in more detail, XRD was performed for both, CNC and CNC-DR1, as shown in Figure 3.3-2d. Comparing the two types of particles, it is observed that both XRD patterns are practically identical. The CNC pattern presents peaks at 14.91, 16.68, and 34.68° attributed to the crystallographic planes ($1\bar{1}0$), (110), and (004) of Cellulose I_β, respectively, and peaks at 12.25, 20.15, and 22.43° attributed to the crystallographic planes ($1\bar{1}0$), (110), and (020) of Cellulose II [31],[32]. As previously reported by Banerjee et al. [33] the coexistence of both Cellulose I_β and II polymorphs in the pristine CNC is a characteristic feature of these commercial particles. CNC-DR1 XRD pattern presents the same peaks, without shifts, nor the broadening of existing crystalline peaks of the cellulose particles that is usually attributed to a decrease of crystallite sizes [34]. Hence, the grafting process is not detrimental to the crystalline structure of CNC, which maintains a crystallinity index of 91%, as calculated according to the method described by Park et al. "XRD peak height method" [35]. Even though this method results in an overestimation of the crystallinity index, a relative comparison between cellulose particles seems reasonable.

After modification, CNC-DR1 must be incorporated into a polymer matrix in order to obtain a printable ink. The anisotropic shape of CNC plays an important role on the rheology of the suspension, as well as on the directional tailoring of the printed part's mechanical properties. To ensure a strong shear thinning behavior of the ink and successful alignment of the CNC during extrusion, the aspect ratio of the CNC needs to be preserved after modification. Hence, the morphology of modified and unmodified CNC was characterized with electron and atomic force microscopy (AFM) (Figure 3.3-3). These analyses confirm that the chemical treatment of CNC does not modify the morphology of single particles. Transmission electron microscopy (TEM) and AFM observations show the morphology of both CNC (Figure 3.3-3a,b) and CNC-DR1 (Figure 3.3-3d,e) single particles. By measuring the lengths and diameters of over 60 particles of each of the two CNC types from the AFM and TEM images, it was observed that unmodified CNC possess lengths of 117.9 ± 42.1 nm and widths of 4.7 ± 1.3 nm, while CNC-DR1 show an average length of 124.3 ± 44.1 nm and widths of 4.7 ± 1.4 nm. Despite the CNC morphology not being affected by the surface modification, a slight tendency of modified particles to agglomerate was noticed. Observation of isolated CNC-DR1 single particles was more sporadic than for CNC, often resulting in images with agglomerated elements similar to Figure 3.3-3e. This may arise from the formation of covalent bonds between CNC. Unreacted Cl of the cyanuric chlorine linkers could react with the free hydroxyls of the CNC surface, thus leading to the formation of such small clusters. To have a full overview of the morphological properties of CNC, scanning electron microscopy (SEM) observations were also carried out. Dry CNC (Figure 3.3-3c) and CNC-DR1(Figure 3.3-3f) films obtained from evaporation of the CNC/acetone suspensions with the same concentration, were observed by SEM. The CNC display the presence of thin filamentary agglomerated bundles as a result of a hornification process [36]. Similarly, CNC-DR1 also agglomerate, forming films with larger and bigger surface bundles and appear slightly less hornified.

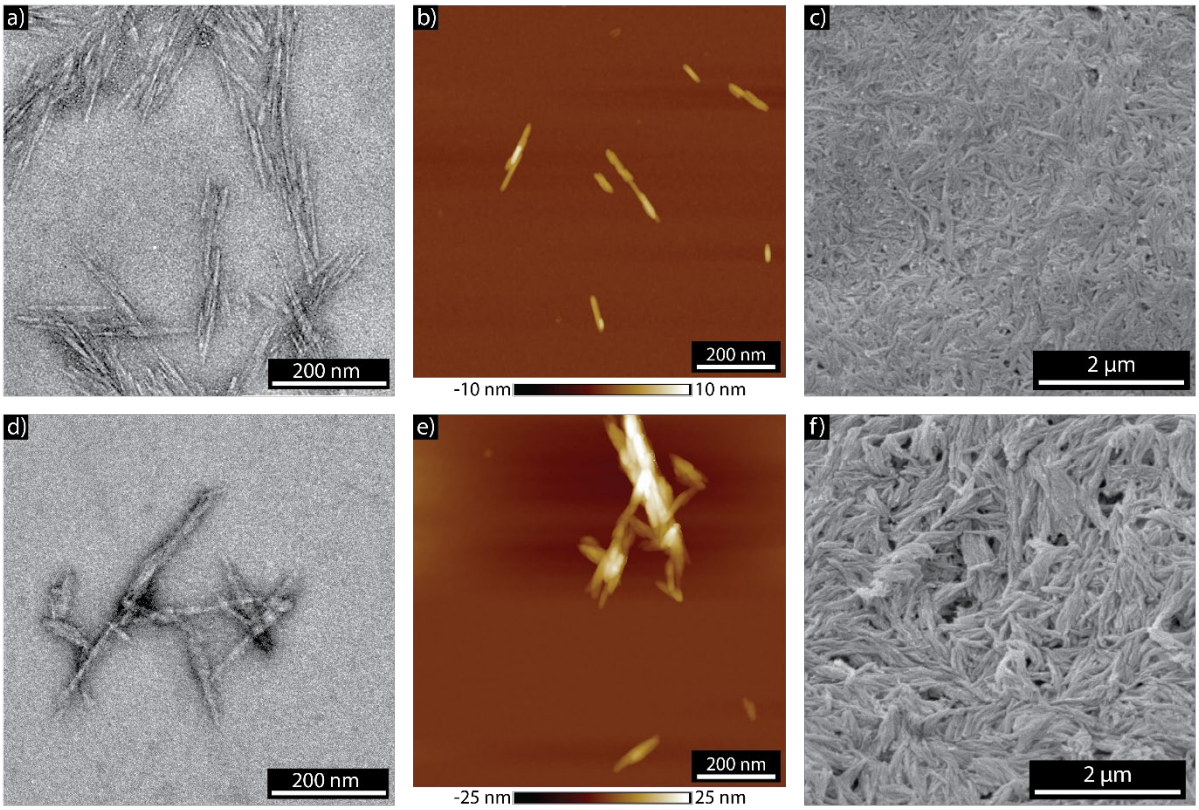

Figure 3.3-3 *Morphological characterization of the CNC before and after the chemical reaction. (a) and (d) TEM images of CNC and CNC-DR1, respectively. (b) and (e) AFM height measurements of CNC and CNC-DR1, respectively. (c) and (f) SEM images of CNC and CNC-DR1, respectively.*

3.3.3.2 Direct Ink Writing of 3D Structures

Modified CNC-DR1 and unmodified CNC particles were incorporated into a polyurethane acrylate (PUA) matrix composed of 49 wt % PUA, 49 wt % (hydroxyethyl)methacrylate (HEMA), and 2 wt % of photoinitiator Irgacure 819. 3D-printed composites must be manufactured by a DIW approach. Consequently, the inks need to meet specific rheological properties known as printability requirements [9],[19],[37]. More precisely, inks for DIW should present a storage modulus G' and a loss modulus G'' bigger than few kPa, an apparent yield stress τ_y bigger than 100 Pa while demonstrating a strong shear thinning behavior. In this work, three concentrations of CNC-DR1 were investigated by oscillatory rheology (Figure 3.3-4a), namely 10, 15, and 20 wt %. For all tested concentrations, the resulting inks feature a strong shear thinning behavior and rheological properties that fulfill the above-mentioned printability requirements. The storage and loss moduli of the tested inks display, at low shear stresses, a first plateau region where $G' > G''$ due to the formation of a percolating network by the nanocellulose particles [8]. The plateau region is followed by an initial drop of G' and an increase in G'' at higher shear stresses, until the dynamic yield stress where $G' = G''$ is reached, marking the transition from a solid-like response to a liquid-like behavior. Specifically, the yield stress defines the moment when the percolating network disrupts and the CNC particles align and order, inducing a strong shear thinning behavior [38], further confirmed with rotational rheology (Figure S 3.3-4). Increasing the concentration of CNC-DR1 in the polymer matrix enhances this rheological behavior, shifting both storage and loss moduli, and the dynamic yield stress to higher values. As the inks become more concentrated in CNC-DR1, from 10 to 20 wt %, the G' passes from $1.2 \cdot 10^5$ to $8.8 \cdot 10^6$ Pa and the τ_y increases from 844 to 7750 Pa. All three concentrations of CNC-DR1 in the PUA-HEMA ink formulations meet the printability criteria. The 15 wt % ink was the concentration of choice for the DIW printer employed during this study. This concentration allows maximizing the content of CNC in the system while allowing a wider

range of printing pressures to optimize the printing quality. On the contrary, an ink with 20 wt % concentration would require the maximum printing pressures of our system (ca. 5.5 bar) and it would be not possible to change this parameter.

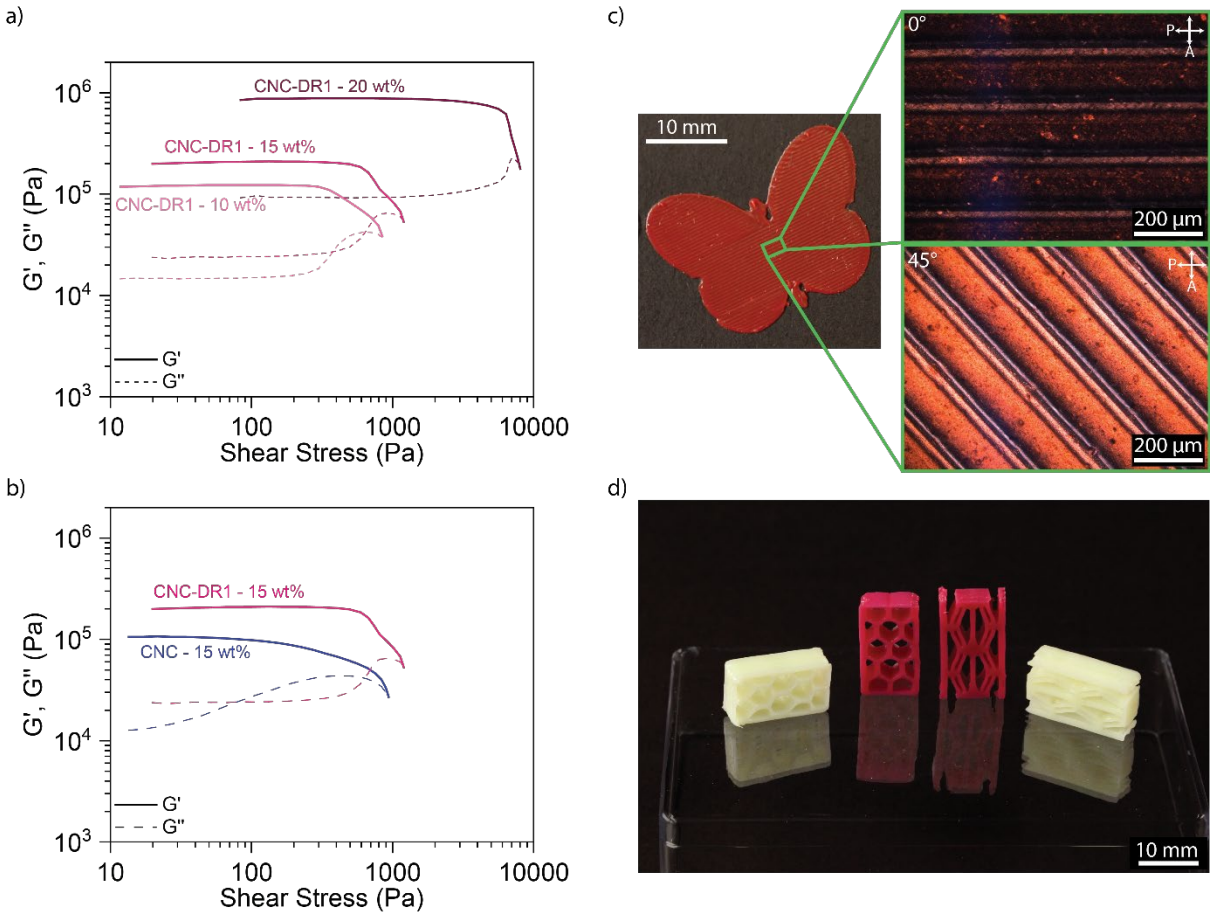

Figure 3.3-4 *Characterization of the printable inks and manufactured demonstrators. (a) Oscillatory rheology of CNC-DR1 inks with different particle concentrations and (b) comparison of rheological behavior with unmodified CNC. (c) Butterfly composed of a 3D-printed single layer of PUA-HEMA with 15 wt % of CNC-DR1 particles. The micrographs represent polarized optical microscopy observations of the layer with printing direction at 0° and 45° angle with the polarizer. (d) 3D-printed structures with 15 wt % of either unmodified CNC (white) or functionalized particles (red), manufactured by a single step of DIW.*

The 15 wt % CNC-DR1 ink shows slightly higher storage modulus and yield stress compared to the rheology of the unmodified CNC ink with the equivalent particles' concentration (Figure 3.3-4b). The ink with unmodified particles shows $G' = 10^5$ Pa and $\tau_y = 938$ Pa, while the CNC-DR1 ink presents $G' = 2 \cdot 10^5$ Pa and $\tau_y = 1202$ Pa probably arising from the presence of slightly aggregated clusters. These could decrease the maximum packing density allowed in the ink, which would result in higher viscosities for the same volume fraction of particles [39]. Hence, the surface chemistry of CNC-DR1 results in a stiffer ink below the yield stress, meaning that this ink is more suitable than the one with untreated CNC for printing self-standing structures. Indeed, the 15 wt % CNC-DR1 ink can easily be processed by DIW in several shapes and geometries. A custom butterfly shape (Figure 3.3-4c) was 3D-printed to investigate the shape fidelity of a single layer and control the post extrusion alignment of the cellulose particles. Comparisons of the initially designed dimensions of the butterfly's digital model with the dimensions of the final 3D-printed demonstrator showed a high shape fidelity for features that are bigger than 1 mm. Printed samples prepared with the CNC-DR1 ink revealed a strong alignment of the particles along the

printing direction, when observed with an optical microscope equipped with cross polarizer filters (Figure 3.3-4c). The well-known birefringence [40],[41] of CNC causes the strong change in intensity observed in the polarized microscopy images. CNC aligned to the light polarization (0°) allow undisturbed light transmission and its cancellation by the analyzer filter, leading to a dark image. On the other hand, when aligned at 45° to the light polarization, CNC birefringence promotes a strong light scattering, which maximizes the transmittance through the analyzer and produces the bright picture. The observed alignment of CNC-DR1 offers an interesting potential for optical applications, especially for wavelength selective polarization filter membranes. In fact, the CNC birefringence has previously been exploited for the inkjet printing of low concentrations (<2.6 wt %) sulfonated CNC suspensions, leading to materials that are promising for applications in optics as colorful polarization filters and in security printing for anticounterfeiting [42].

Moving from printing in 2D to manufacturing complex 3D structures was easily achieved in a single printing step for inks containing 15 wt % CNC-DR1. Here, this is demonstrated with the production of two honeycomb structures (Figure 3.3-4d) with a height of 5 mm, each produced with both types of CNC reinforcement particles.

3.3.4 Dynamic Response of Printed Materials and Structures

In order to understand both the effects of regular and photoresponsive DR1 modified CNC particles on the printed materials, the mechanical properties of 200 μm thick 3D-printed single layer composites were analyzed as a function of temperature and external illumination with an Opulent Cree LED at a wavelength of 475 nm (Figure 3.3-5). The first characterization compares CNC-DR1 with unmodified CNC printed films using thermal dynamic mechanical analysis (DMA) (Figure 3.3-5a). The comparison of 15 wt % CNC-DR1 with 15 wt % CNC composites shows that the surface modification introduced on the particles leads to stiffer materials. Both composites (CNC and CNC-DR1) have a glass transition temperature (T_g) of −55 °C and the difference in storage modulus increases after the materials reach the amorphous region, before decreasing again after 100 °C. Results of differential scanning calorimetry (DSC) measurements from −100 to 200 °C (Figure S 3.3-5) show that the T_g of both materials is around −59 °C, being in agreement with the results indicated by DMA measurements. Moreover, DSC analysis showed that both materials undergo melting at 123 °C with an onset temperature lying around 60 °C, thus explaining the strong final drop of storage moduli occurring after 80 °C in the DMA measurements. At 25 °C, CNC-DR1 composites demonstrate a clearly stiffer behavior with a storage modulus of 165 MPa compared to 66 MPa for unmodified CNC. The increase of the elastic properties of CNC-DR1 composites may stem from an interlocking of the CNC network, ensured by agglomerated CNC-DR1 (Figure 3.3-3e). During the reaction, cyanuric chloride groups might form covalent bonds with the cellulose's hydroxyl groups and promote such agglomeration. Furthermore, such an effect could also arise from the introduction of azobenzene's hard segments. In a previous work, we noticed that the presence of noncovalent bonded DR1 in liquid crystalline elastomer CNC composites promoted an increase in both, elastic modulus and strength of the materials [43].

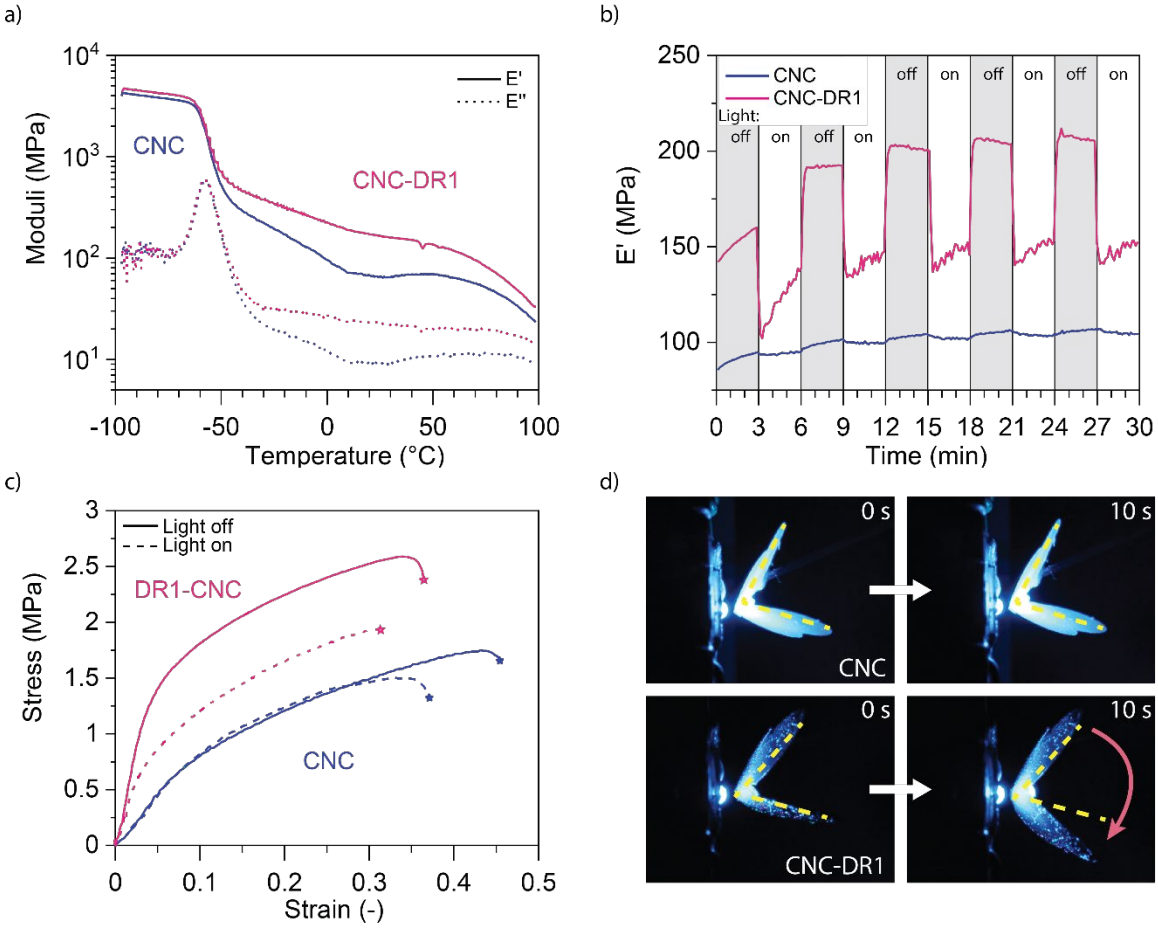

Figure 3.3-5 *Photoresponsive properties of the 3D-printed PUA-HEMA composites. (a) Thermal DMA operated between −100 and 100 °C in tensile mode. (b) Photoresponse of the storage modulus of the composites over time. The gray regions represent measurements in dark, while white regions are measurements under illumination. (c) Tensile tests at equilibrium for samples before or during illumination. (d) Shape memory effect observed on a PUA-HEMA 15 wt % CNC-DR1 printed butterfly. The folded butterfly recovers most of its initial shape after 10 s of illumination, while a butterfly composed of PUA-HEMA 15 wt % CNC does not present such a behavior under illumination.*

The photoresponsive effect of grafting the azobenzene to CNC surfaces was further studied with a DMA analysis under illumination. The printed CNC-DR1 composites display a reversible photosoftening when irradiated with light of 475 nm wavelength (Figure 3.3-5b). The dynamic softening was measured with a time sweep analysis in a DMA, during which an LED lamp (Opulent Cree, 3W) was set 5 mm away from the center of the sample. The light was then switched on and off every 3 min. These measurements show that the CNC-DR1 composites lose 32% of their storage modulus in less than 10 s after the light shines on them. This photoresponse is fully reversible. In contrast, the composites with unmodified CNC show only a slight reaction to the illumination that is attributed mainly to the heat generated from the illumination setup. The strong softening of CNC-DR1 composites arises from a photothermal effect generated by the strong light absorbance of DR1 moieties. During the illumination, DR1 molecules undergo fast *trans–cis–trans* conformational changes [24], generating temperatures reaching 200 °C in the near local molecular environment [44]. For the CNC-DR1 composites, an infrared camera (Figure S 3.3-6) revealed a maximum surface photogenerated temperature of 92.7 °C for the irradiated regions when the lamp is at a distance of 5 mm, confirming a strong photothermal effect of the CNC-DR1 particles. Instead, unmodified CNC composites did not show a photothermal effect, only a slight increase in temperature of 2 °C attributed to the heat irradiated from the illumination setup. The CNC-DR1 samples illuminated at 5 mm of distance show an average surface temperature around 60 °C for the whole irradiated region. This further suggests that the photosoftening arises from the increase in

temperature. The storage modulus of CNC-DR1 composites, obtained by thermal DMA experiments in Figure 3.3-5a, exhibits a drop of 33% when the temperature increase from room temperature to 60 °C. Such softening is comparable to the drop in modulus observed as a response to the irradiation.

After the dynamic observation of the current photosoftening, the effect of illumination at equilibrium conditions was also studied by microtensile tests [45] (Figure 3.3-5c), during which an LED lamp (Opulent Cree, 3W) was set 10 mm away from the center of the samples. Both unmodified CNC and CNC-DR1 composites were tested in dark and during irradiation. In dark, both composites demonstrate coherence with the DMA measurements. Unmodified CNC composites are weaker than CNC-DR1 ones, with elastic moduli measured in the dark around 10 and 30 MPa for CNC and CNC-DR1 composites, respectively. Irradiation did not lead to substantial differences in stress–strain behavior of the CNC composites compared to the samples tested in the dark, while irradiation of CNC-DR1 composites resulted in a loss in stiffness and strength. The elastic modulus of such composites strongly decreases from 30 to 16 MPa (Figure S 3.3-7) while the maximum strength slightly decreases from 2.3 to 1.8 MPa when samples were illuminated. The photoresponsive softening, being fully reversible, allows CNC-DR1 composites, which were illuminated with successive intervals of irradiation, to switch between mechanical behaviors in the dark and under illumination (Figure S 3.3-8).

The photogenerated heat produced from the CNC-DR1 reinforcements also proved to trigger the shape memory behavior of the PUA-HEMA matrix (Figure 3.3-5d). To clearly demonstrate this effect, we 3D-printed a butterfly using the 15 wt % CNC-DR1 ink and we folded and maintained its wings deformed until they kept an angle of 45°. Upon illumination with a 475 nm wavelength LED (Opulent Cree, 3W), the wings opened to 140° in less than 10 s, recovering 70% of the initial wing's opening before deformation. On the contrary, when irradiating another butterfly, folded in the same manner but composed of 15 wt % CNC in the PUA-HEMA matrix, the wings do not move or open even after 60 s of illumination (Figure S 3.3-9). Nonetheless, both CNC and CNC-DR1 composites react to temperature (Figure S 3.3-10) and display a thermally activated shape memory behavior, confirming the actuation of DR1 by a photothermal effect. Polyurethanes are known to exhibit a shape memory effect activated by temperature [46],[47]. This phenomenon arises in thermoset polyurethanes as the PUA-HEMA matrix of the current inks, due to the presence of cross-linked hard and other soft polymer segments. The former polymer segments define the permanent shape while the latter ones are responsible for the temporary shapes and the transition temperatures [48-50]. In particular, the PUA-HEMA matrix studied in this work demonstrates a very broad melting temperature (Figure S 3.3-5) indicating that the melting of the soft segments is responsible for the shape memory behavior.

At 15 wt % concentration, CNC-DR1 particles are providing printability to the uncured PUA-HEMA matrix. An increase in the elastic modulus and strength, a strong photosoftening, and a phototriggered shape memory behavior are the major effects on the cured composites. To highlight such properties and demonstrate the advantage of printing functional materials, two types of honeycomb structures were manufactured. These honeycombs were produced by 3D printing the 15 wt % CNC-DR1 PUA-HEMA ink with the goal to combine the geometry (3D printing) with functionality (photoresponse) and to give rise to targeted mechanical responses. First, hexagonal honeycombs were manufactured as examples of energy absorbing structures [51]. Second, we produced so-called negative stiffness structures composed of prismatic cells with two double curvature beams by DIW. The latter structures have the particularity to present energy absorption in a recoverable way [52]. The beams are designed to allow energy dissipation as they undergo a first mode buckling deformation displaying negative stiffness during such an event. These negative stiffness honeycombs have already demonstrated the influence of a well designed geometry for energy absorption and shock isolation applications [53],[54]. With the developed DIW

ink, both types of honeycomb could be easily printed and utilized to demonstrate photoresponsive dynamic energy absorbers.

Once the structures were printed, we carried out quasi static compression tests to characterize energy absorption features of the 3D-printed structures while illuminating them at selected deformations (Figure 3.3-6). This produces a distinct response to the compressive force, allowing to tune the quantity of energy absorbed by a defined structure. Indeed, the hexagonal honeycombs show a clear difference in their energy absorption capability when comparing samples compressed in the dark with samples compressed upon selective illumination (Figure 3.3-6a). The structures were compressed until 50% of their original size and released. The black curve represents the averaged mechanical behavior of the structures in the dark while the magenta curve shows what happens when the light irradiates the samples every 10% of strain intervals. In the dark, the hexagonal structure deforms linearly, before having a negative slope from 10% to 30%. After 30% of compressive strain, a second linear increase in force is observed due to the connection of the deformed cell walls, as can be observed in Figure 3.3-6b, occurring after 25% strain. When the functional composite structure undergoes irradiation intervals, the reversible photosoftening quickly arises under illumination. This generates a dynamic weakening of the structure that can be observed by the fast change of force-strain slope at 10% followed by a prompt strengthening at 20% strain, after stopping the irradiation. In the further course of the test, the illumination at 30% strain produces again a strong change in the mechanical properties of the composites. The slope of the force decreases from the nonilluminated condition and produces a continuous increase of force until the end of the cycle. Interestingly, both conditions led to the same result during unloading, the structures could recover only until 25% of compressive deformation.

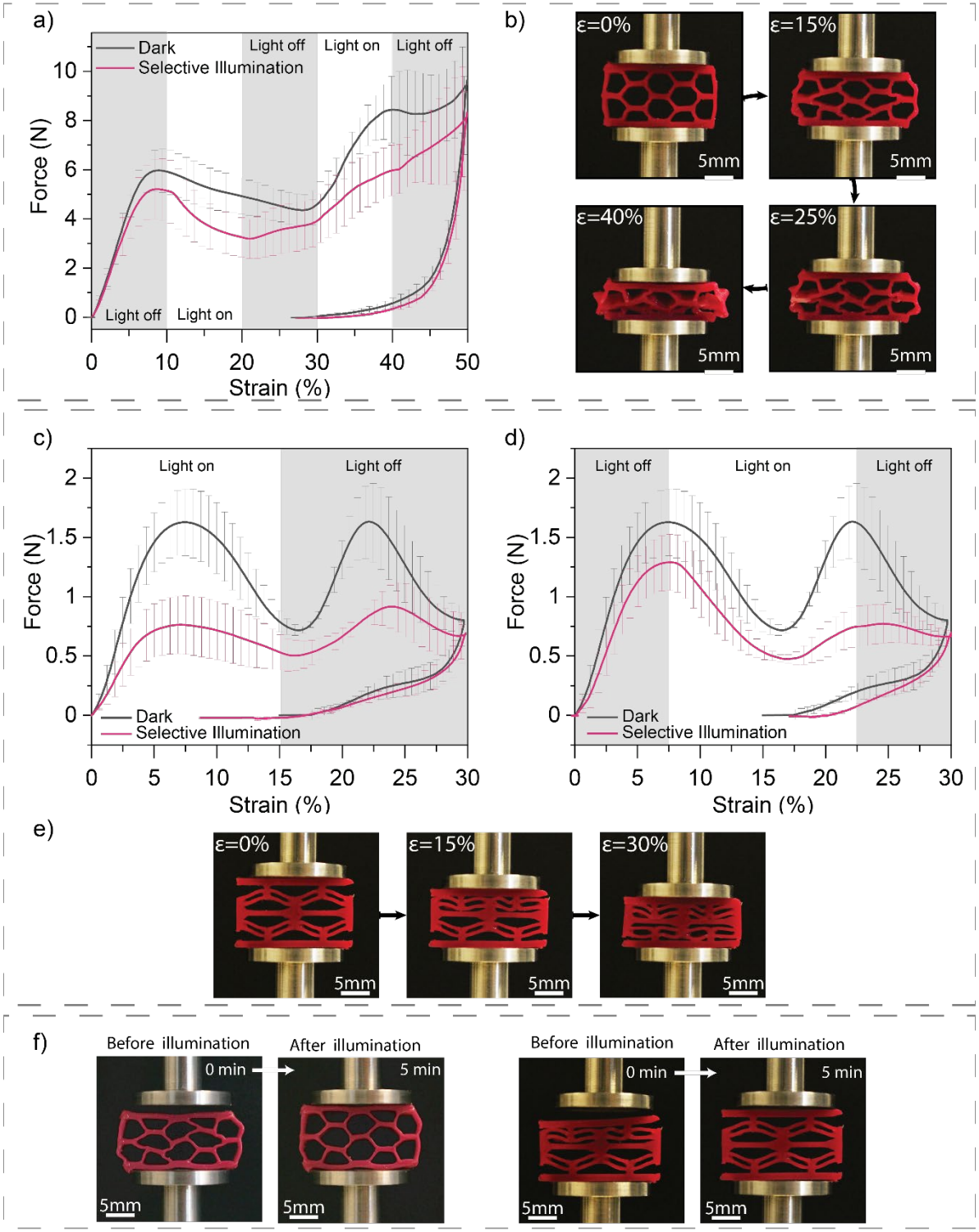

Figure 3.3-6 *Combination of 3D-printing complexity with dynamic response to light of 3D-printed cellular structures. (a) Compression tests, in dark or under selective illumination, of hexagonal honeycombs composed of PUA-HEMA with 15 wt % CNC-DR1. For selective illumination measurements, the light was off in the gray regions, while it was switched on for the white regions of the graph. (b) Images of deformed samples under compression for different strains. (c) and (d) Compression tests in dark or under selective illumination of negative stiffness structures composed of PUA-HEMA with 15 wt % CNC-DR1; for selective illumination measurements, (c and d) represent different illumination profiles, the light was off in the gray regions and it was on in the white regions of the graphs. (e) Deformation under compression of a tested negative stiffness structure. (f) Shape memory effect of compressed hexagonal honeycombs and negative stiffness structures after 5 min of illumination, both structures are composed of PUA-HEMA with 15 wt % CNC-DR1.*

The negative stiffness structures that were manufactured with 15 wt % of CNC-DR1 ink were loaded in the same compression experiments as the hexagonal honeycombs, but until 30% of compressive strain and different illumination profiles (Figure 3.3-6c and d). In the dark, the printed structures show a mechanical behavior with two maximum peaks of force around 1.5 N, representing the snapping of the double curvature beams of the prismatic cells (Figure 3.3-6e). Contrary to literature [52],[55], the composite structure does not seem to be recoverable, since during the unloading, it can recover only until 10–15% of strain with the slight presence of a snapping peak. Despite the fact that the process parameters have been optimized for both high resolution and CNC alignment (e.g., 250 μm nozzles diameter, 3.5 bar of pressure at 10 mm s^{-1}), unnoticeable defects might occur during printing of sharp corners, which could create local stress concentrations and lead to the formation of plastically deformed regions. Nonetheless, light irradiation provides important changes to the compressive behavior of the negative stiffness honeycombs. When irradiated from the beginning of the compressive loading (Figure 3.3-6c) to half of the deformation, the photosoftening completely weakens the negative stiffness structures, leading to a broad initial force peak (reaching 0.75 N) followed by a second peak in the dark where the mechanical resistance of the structures can only slightly recover from the initial illumination (0.90 N). On the contrary, when the illumination occurs at the maximum of the first force peak (Figure 3.3-6d) the softening of the negative stiffness structures leads to a marked change of slope followed by a strong decrease of the second force peak, which reaches again 0.75 N. During unloading the second double curvature cell does not snap back to its original position and remains blocked in its compressed state. This is also seen from the graph in Figure 3.3-6d where the recovery force peak is leveled out.

Certainly, both types of structures can benefit from the shape memory behavior previously observed, and recover their initial shape. After carrying out the compression, 5 min of illumination trigger the shape recovery of the tested hexagonal honeycomb and negative stiffness structures (Figure 3.3-6f). For the negative stiffness honeycomb, the recovery of the initial shape could be carried out three times. After the first shape recovery, the negative stiffness structure undergoes a slight decrease in the force threshold of the buckling deformation, decreasing from 1.6 to 1.3 N. However, the compression of the same part could be repeated two more times with minor shifts of the force peaks (Figure S 3.3-11), arising from buckling instabilities, but maintaining a similar resistance with force peaks varying between 1.15 and 1.3 N. Finally, the introduction of CNC-DR1 in the PU matrix allows for the material to be additively manufactured and confers both mechanical reinforcement as well as photoresponsive softening. Moreover, such material demonstrates to be suitable for the production of dynamic energy absorbers by 3D printing, which present customizability of the mechanical response and, interestingly, also improvement of recoverability of the compressed structures. Nevertheless, the greatest advantage of the modified CNC (CNC-DR1) lies in the possibility to be dispersed in other polymer matrices to exploit the photothermal effect for shape changing purposes, as could be the case for PNIPAM hydrogels [15], or to directly exploit the conformational changes of DR1 to trigger liquid crystalline elastomer shapemorphing [56].

3.3.5 Conclusion

We demonstrated an approach that allows the fabrication of composite materials with DIW while conferring photoresponsive behaviors to the obtained complex 3D-printed structures. Among the different photoresponses available by grafting DR1 azobenzenes on CNC, we harnessed the heat generated by the rapid *trans–cis–trans* photoisomerization to produce dynamic energy absorbers that can be functionally tuned by illumination, both spatially and temporally. The DR1 surface grafting on renewable CNC was confirmed by FTIR, NMR, XPS and UV–vis. The chemical modification led to a change in color

of the nanoparticles without modifying the crystalline structure or the morphology of the particles while maintaining their anisotropic shape. The modified nanoparticles could be introduced into a PUA matrix, strongly influencing its rheology and promoting the formation of gel-like inks that fulfill printability requirements, thus allowing the processing of 3D parts by DIW. The strong photothermal effect confers photosoftening ability and a shape memory effect to the 3D-printed structures. The strength of this approach lies in combining such photoresponses with the DIW ability to create 3D complex shapes, as honeycombs and negative stiffness structures, presenting local alignment of CNC. As a result, such devices could be printed in a single step and their mechanical behavior under compression forces could be tailored by temporally illuminating the structures during loading. The material produced in this work presents an interesting potential for the production of shock and vibration protection or dynamic energy absorbing devices that are operated in specific load conditions, for instance, as in prosthetics or in soft robotics. This demonstrates that adding functional responses to 3D-printed devices enhances the design freedom and adaptability of lightweight mechanically tailored structures. However, the potential of our CNC is not limited to the produced material, since CNC-DR1 would allow exploiting the azobenzene *trans–cis–trans* photoisomerization in other compatible polymer matrices. This could allow for 3D printing of devices with different photoresponses. By introducing such nanoparticles into liquid crystalline elastomers, the photomechanical effect would lead to dynamic and reversible shape changes. For instance, the use of a matrix including cyclodextrins in the polymer network would lead to gel–sol transitions. Furthermore, the development of these multipurpose active CNC enables to transfer material technologies that were formerly limited to 2D shape into 3D complex structures, in which geometrical effects, spatially tailored mechanical properties and photoresponses are combined. With this technology, highly customized devices with outstanding functional properties can be produced based on renewable materials, moving a step further toward independence from fossil fuel resources. Finally, by allowing and improving emulation of biological materials' structures and properties, the developed devices could also contribute to deepening the understanding of natural materials and their complexity.

3.3.6 Experimental Section

Materials: Cellulose nanocrystals (CNC) obtained from sulfuric acid hydrolysis of eucalyptus pulp were supplied by University of Maine (United States). The reagents Disperse Red 1 (DR1) (95%) and Cyanuric Chloride (≥98%) were acquired from Sigma-Aldrich and Fluka Chemie GmbH, respectively. The catalyst 2,4,6-trimethylpyridine was supplied by VWR (Acros Organics). The polymer matrix was composed of Polyurethane Acrylate (BR3741A) kindly supplied by Dymax and 2-hydroxyethyl methacrylate (HEMA) acquired from Sigma-Aldrich. The photoinitiator bis(2,4,6-trimethylbenzoyl)-phenylphosphineoxide (IRGACURE 819) was obtained from BASF. Finally, dimethyl sulfoxide (≥99.5%) was acquired by Sigma-Aldrich and used without further purification.

Functionalization of CNC: In order to graft the azobenzenes on the surface of the CNC, 1.5 g of DR1 were added into a 3-necks round-bottom flask containing a suspension of 3 g of CNC in 150 g of acetone. Four g of cyanuric chloride were successively dissolved in 30 g of acetone and added slowly to the cellulose suspension. Then, 2,4,6-trimethylpyridine (3.28 mL) was slowly poured in the suspension. The dispersion was continuously stirred and heated up to 55 °C in a nitrogen atmosphere for 15 h. The glass reactor was equipped with a condenser to avoid evaporation of the acetone. The reaction was stopped by quenching the suspension in an ice bath. The modified CNC were purified by 6 centrifugation cycles (Rotina-380, Hettich) at 5000 rpm for 5 min with renewal of the solvent. The solid content of the final suspension was determined by solvent evaporation.

Preparation of the inks: The inks that were investigated in this work contained 10, 15, or 20 wt % CNC (modified or unmodified) and the polyurethane-HEMA matrix. The matrix components were mixed with 49 wt % of the difunctional polyurethane acrylate oligomer (PUA), 49 wt % 2-hydroxyethyl methacrylate monomer (HEMA), and 2 wt % bis(2,4,6.trimethylbenzoyl)-phenylphosphineoxide (Irgacure 819) as photoinitiator. After mixing of the matrix components, the desired amounts of CNC were added as an acetone dispersion. The solvent was successively evaporated overnight, while continuously stirring the mixture at 40 °C. After this step, the ink was mixed 3 times in a SpeedMixer (DAC 150.1FVZ), with cycles composed of 1 min at 1000 rpm, 2 min at 1500 rpm, and 4 min at 2000 rpm. After mixing, the ink was transferred to a 30 mL UV shielding cartridge. The cartridge was centrifuged for 10 min at 3000 rpm to remove any air bubbles from the ink.

3D Printing of structures: 3D structures were printed using a conical nozzle with an inner diameter of 0.25 mm. The prepared cartridges were mounted on a direct ink writer (DIW) printer (3D-Bioplotter "Manufacturer Series", EnvisionTEC, Germany). All inks containing modified or unmodified CNC, were extruded with a printing speed of 10 mm/s and a pneumatic pressure ranging between 1 and 4 bar onto a previously hydrophobized glass slide. Each layer was illuminated for 10 s with three monochromatic LEDs (365 nm wavelength, 3 W) in air. The printed final structures were cured for 10 min in a nitrogen atmosphere using a custom-made illumination setup composed of 5 monochromatic LEDs (365 nm wavelength, 3 W).

Shape memory observation: The unfolding of the wings of a 3D-printed butterfly was characterized as follows: the wings of the butterfly were manually folded closed and maintained until no elastic response could be observed. Then, the materials were illuminated at a distance of 5 mm from an LED light (475 nm wavelength, 3 W). The movement of the demonstrator while illuminated was captured with a camera (EOS 100D, Canon) with an aperture of 9.0 and an exposure time of 100 ms.

Optical Microscopy: The images of the printed structures were taken with an optical microscope (Zeiss, Axioplan) equipped with a digital camera (Leica DFC 420). The microscope was also equipped with cross polarizer filters and the samples were rotated from 0° with respect to the polarizer to 45°.

Fourier-Transform Infrared Spectroscopy (FT-IR): The functionalization reactions were investigated with an FT-IR spectroscope (Tensor 27 IR, Bruker) equipped with a ZnSe crystal in attenuated total reflectance (ATR) mode. The samples were prepared by drying the suspensions for 48 h in a 60 °C oven to dry and evaporate the solvent. The FT-IR spectra were recorded from 4000 to 600 cm^{-1} with 64 scans per sample and a resolution of 4 cm^{-1}. Three spectra were recorded per sample; the spectra were baselined and averaged with OPUS scope software. Finally, each spectra was normalized by its maximum value to allow visualization and comparison of multiple spectra.

Ultraviolet-Visible (UV-Vis) Spectroscopy: Quartz glass cuvettes were filled with a DR1 solution with 10 μg mL^{-1} in acetone for the analysis of the pure azobenzene. Quartz cuvette containing 0.5 mg mL^{-1} of CNC (either unmodified or modified) in acetone. The cuvettes were shaken thoroughly before measuring the samples with an UV–vis spectrometer (Cary 1E, Varian). The spectra were recorded between 800 and 200 nm with a step size of 5 nm and the measurements were repeated 3 times for each sample. The representative measurements are illustrated in the manuscript.

Powder X-Ray Diffraction (XRD): Diffraction graphs were measured using an XRD system (Panalytical, X'pert Pro) equipped with Cu radiation ($K\alpha_1$ = 1.54056 Å and $K\alpha_2$ = 1.54439 Å). The samples were ground and placed on a zero-background silicon sample holder. The diffraction data was measured from 5 to 80 degrees with a step size of 0.026 degrees. The sample was rotated at a speed of 8 s per revolution during the measurement to increase the sampling statistic. The curves were baselined and

plotted for calculating the crystallinity index. The crystallinity index was determined based on the intensity method described by Park et al. [35] In this method, I_{002} peak intensity located at a 2 θ angle of around 22.5° and the amorphous peak intensity I_{AM} at approximately 18° are measured. The crystallinity index was calculated according to following eq (1):

$$Crystallinity\ index\ = \frac{(I_{002} - I_{AM})}{I_{002}} \quad (1)$$

Atomic Force Microscopy Scanning (AFM): Single particles were imaged with the Icon3 AFM (Bruker) in soft tapping mode using silicon tips (RTESPA-150, Bruker). Later, the images were flattened, and artifacts were removed with NanoScope analysis software from Bruker. The samples preparation for the AFM analysis was conducted based on the process described by Arcari et al. (56) Briefly, the modified and unmodified CNC were dispersed in Milli-Q water to reach a final concentration of 2 mg L^{-1}. Freshly cleaved mica was attached with double-sided tape to a glass slide. Twenty µL of an acqueous solution containing 0.05 vol % of (3-aminopropyl) triethoxysilane (APTES) were deposited on the mica to achieve a positive surface charge. After 60 s the mica was rinsed thoroughly with Milli-Q water and dried with a pressurized air gun. Successively, the mica was covered by the 2 mg/L CNC suspensions. After 30 s the mica was rinsed again thoroughly with Milli-Q water and dried with pressurized air. The samples were kept under vacuum in a desiccator before the measurements to prevent any contamination. Measurements of diameters of CNC were based on the vertical cantilever displacement, while length were extracted from the images with the NanoScope analysis software.

Scanning Electron Microscopy (SEM): The cellulose nanoparticles were imaged with a Nano-SEM 230 (FEI) SEM at a distance of 10 mm and an accelerating voltage of 5 kV. The samples were prepared by evaporating the acetone from the suspension in a 60 °C oven. The dried powders were sprinkled on a carbon tape stuck to aluminum sample holders. A 7 nm layer of platinum was sputtered on the samples as conductive layer. The samples were stored under vacuum in a desiccator before imaging.

Transmission Electron Microscopy (TEM): The modified and unmodified CNC were imaged with a JEM-2200FS (Jeol) TEM and an acceleration voltage of 200 kV. Samples were prepared and deposited on carbon coated-grids. The carbon-coated grid surface was made more hydrophilic by 10 s of oxygen plasma treatment. A 30 µL drop of 2 mg/L CNC water suspensions was deposited on Parafilm and the grid was laid on top of the drop for 30 s. Then, the grid was placed in a drop of 2 wt % of uranyl acetate for 30 s to stain the samples. The samples were dried and kept under vacuum in a desiccator before imaging. Analysis of lengths of CNC was conducted with the help of ImageJ software.

Nuclear Magnetic Resonance (NMR): The measurements were carried out on an AVIII HD 400 MHz wide-bore (Bruker) NMR spectrometer. For the liquid-state NMR, 30 mg of DR1 was weighed in a vial and 0.5 mL of deuterated chloroform was added to the vial. The solution was transferred to an NMR tube with a pipet. The solid-state cross-polarization magic angle spinning carbon-13 (^{13}C CP-MAS) NMR spectra were acquired between 400.2 and 100.6 MHz on an Avance III 400 MHz (Bruker) spectrometer at room temperature with a 4 mm MAS probe operating at a spinning speed of 10 kHz. Approximately 50–80 mg of the sample material were densely packed into 4 mm zirconia rotors. For the ^{13}C CP-MAS NMR experiments a 3.5 µs excitation pulse at 90° was applied on the ^{1}H channel. Further, the contact time was set to 1 ms (optimized for best signal-to-noise) with a ramp from 100 to 50% of the power level on the proton channel. During acquisition, 3 s recycle delays, and 71 kHz SPINAL 64 proton decoupling were applied. Appropriate numbers of 1500 to 16000 scans were recorded to yield reasonable signal-to-noise ratios.

Time of Flight Secondary Ion Mass Spectrometry (ToF SIMS): CNC films dried from an acetone suspension for both the unmodified and DR1 modified CNC were fixed on to the ToF-SIMS plate with aluminum tape and inserted into the vacuum chamber of the ToF-SIMS.5 from IONTOF GmbH, Germany. Depth profiling was carried out using a cesium ion sputter gun with an energy of 500 eV. An area of 500 × 500 μm was sputtered and an area of 50 × 50 μm^2 or 100 × 100 μm^2 was measured. Bi^{3+} ions at an energy of 25 keV and a cycle time of 100 μs were used in the analysis beam. Images were measured with a resolution of 256 × 256 pixels per measurement. A floodgun was used to counteract charging at the surface and the charge compensation was automatically adjusted for each sample.

X-ray Photoelectron Spectroscopy (XPS): he samples were prepared as dry film from slow evaporation of acetone/CNC or acetone/CNC-DR1 suspensions. The XPS spectra were acquired with a PHI Quantum spectrometer, equipped with an Al Kα monochromatic source (1486.7 eV), a hemispherical capacitor electron-energy analyzer, and a 16–channel plate detector. All the spectra were acquired with an emission angle of 45°, in fixed analyzer transmission mode, using a nominal X-ray beam-spot size of 150 μm. Given the insulating nature of the samples, all the acquisitions were carried out under dual-beam charge compensation. The peak maximum of the C 1s was used for BE referencing. Specifically, the BE value of the alkoxy group in cellulose [57] (2876.7 eV) was taken as reference value.

Nitrogen (N 1s) spectra were acquired at a pass energy of 23.5 eV, step size of 0.1 eV and duration of ca. 36 min while the X-ray beam was scanned over a 500 × 1000 μm^2 area during spectra acquisition, rather than focusing on a stationary point to limit X-ray induced degradation of nitro groups. Surveys spectra were acquired on previously not irradiated areas for a duration of ca. 15 min and used to carry out elemental quantitative analysis, according to the formula in eq (2):

$$x_a = \frac{I_a/_{RSF_a}}{\sum_i^n I_i/_{RSF_i}} \tag{2}$$

x_a is the atomic concentration of the element "*a*", and I_i is the intensity (area) of the selected peak of the element "*i*". RSFi is the associated relative sensitivity factor. The RSFs used in this work were derived from the analysis software of the XP-spectrometer. It should be noted that the approach based on eq (2) is strictly valid for materials that are homogeneous to a depth greater than the information depth of the technique.

Rheology: The rheological behavior of the printable inks was characterized with an MCR 301 (Anton Paar) rheometer at 20 °C. The measurements were carried out with a plate–plate geometry, using a disposable aluminum plate with a diameter of 25 mm and a gap of 0.5 mm between the plates. The storage (G') and loss (G'') modulus were determined by applying an oscillatory deformation between 0.01% and 1000% strain with a frequency of 1 Hz and a logarithmic sweep. Flow properties were measured with rotational increase of the shear rate in a logarithmic sweep. Three measurements per ink were performed and the representative measurement is reported in this work.

Differential Scanning Calorimetry (DSC): The thermal behavior of the composite materials was investigated using a DSC 8000 DSC by PerkinElmer with two heating cycles from −100 to 200 °C at a rate of 20 °C/min and one cooling cycle from 200 °C to −100 °C at a rate of 20 °C/min. Approximately 18 mg of the samples were placed in a pan and sealed tightly. All the measurements were carried out under nitrogen atmosphere.

Dynamic Mechanical Analysis (DMA): The mechanical properties of the printed composites were obtained with a DMA RSA 3 analyzer from TA Instruments. Printed films with a width of 3 mm and a

thickness of approximately 200 μm were mounted with the printing direction parallel to the tensile direction at a clamp distance of 20 mm and a prestrain of 20 g. The temperature sweeps were conducted starting from −100 to 100 °C at a rate of 3 °C/min with a strain of 0.04% and a frequency of 1 Hz, using a liquid nitrogen cooler. Light illumination tests were performed at room temperature (25 °C) by placing one LED lamp (475 nm, 3 W) at a distance of 5 mm from the center of the sample. Here, a time sweep with 0.04% of strain and a frequency of 1 Hz were applied. The LED lamp was switched on and off every 3 min until the end of the measurement, after 30 min. Three samples per condition were tested and the representative one is illustrated.

Microtensile tests: Tensile tests on the printed composites were carried out in a custom test setup reported by Burgert et al. [45]. In summary, a step motor on a linear table allowed to vary the speed from 1 μm s^{-1} to 1000 μm s^{-1} while the loading is measured with a 5 N load cell. The samples, films of 1 mm width and a thickness of 200 μm, were glued with a cyanoacrylate glue from both sides onto rectangular plastic foils containing three holes in the centers and one for each extremity. The holders were placed onto the moving table and fixed with pin holes at the extremities. In order to not measure the foil properties, the three holes were cut. The samples were stretched at a speed of 30 μm s^{-1}. To calculate the sample's strain, the displacement of the table was divided by the sample's length between the glued points of the sample (6 to 9 mm). Both diameters and initial length were observed and recorded with an optical microscope. For measurements under illumination, a support for the Opulent Cree LED (480 nm, 3W) was 3D-printed with a Prusa imk3 FDM in PLA and adapted to the set up in order to have a 10 mm distance from the samples. Five samples were tested for each test and sample's condition. All samples were tested with the printing direction parallel to the loading direction. The representative measurements are illustrated.

Compression tests: Compression Force-strain curves of the printed structures were obtained on a RSA3 3 analyzer from TA Instruments. The 2.5 mm thick hexagonal and negative stiffness honeycombs of 15 wt % CNC-DR1 were placed in the instrument in compression mode, using circular clamps with a diameter of 15 mm. The instrument was set to operate at a speed of 30 μm s^{-1} and at a compression of 50% and 30% strain for hexagonal and negative stiffness structures, respectively. The illumination was applied by the mean of two Opulent Cree LED (475 nm, 3 W) placed at 10 mm from the samples on each side (back and front). Five samples per condition where tested. The averaged measurements are illustrated with the standard deviation.

3.3.7 Additional Information

Supporting Information

The Supporting Information is available free of charge at:

https://pubs.acs.org/doi/10.1021/acsnano.2c05628.

- Schematic representation of DR1 grafting. FTIR, ToF SIMS, XPS, solid-state NMR, elemental analysis of CNC and modified CNC, rotational rheology of CNC and CNC-DR1 inks, thermal imaging, tensile tests, shape memory effect and cyclic compression tests of 3D-printed composites (PDF)

Corresponding Authors

*Gustav Nyström. E-mail: gustav.nystroem@empa.ch

*Gilberto Siqueira. E-mail: gilberto.siqueira@empa.ch

Acknowledgment

The authors thank A. Huch for the TEM and SEM imaging of CNC and modified paricles, Beatrice Fischer for carrying out the DSC experiments, Daniel Rentsch for analyzing the solid-state NMR samples, Ines Collings for performing the powder XRD measurements, and Rowena Crockett for the measurement and the interpretation ToF SIMS. The authors greatly acknowledge the financial support from the Swiss National Science Foundation (grant no. 200021_178941/1).

The authors declare no competing financial interest.

3.3.8 References

[1] A. R. Studart, "Additive manufacturing of biologically-inspired materials," *Chem. Soc. Rev.*, vol. 45, no. 2, pp. 359–376, Jan. 2016, doi: 10.1039/c5cs00836k.

[2] B. Kasal, "WOOD FORMATION AND PROPERTIES | Mechanical Properties of Wood," in *Encyclopedia of Forest Sciences*, Oxford: Elsevier, 2004, pp. 1815–1828.

[3] P. T. Martone *et al.*, "Mechanics without Muscle: Biomechanical inspiration from the plant world," in *Integrative and Comparative Biology*, 2010, vol. 50, no. 5, pp. 888–907, doi: 10.1093/icb/icq122.

[4] B. Clair and B. Thibaut, "Physical and Mechanical Properties of Reaction Wood," in *The Biology of Reaction Wood*, Heidelberg: Springer Series in Wood Science, 2014, pp. 171–200.

[5] C. Chen *et al.*, "Structure–property–function relationships of natural and engineered wood," *Nat. Rev. Mater.*, vol. 5, no. 9, pp. 642–666, Sep. 2020, doi: 10.1038/s41578-020-0195-z.

[6] B. Bar-On, F. G. Barth, P. Fratzl, and Y. Politi, "Multiscale structural gradients enhance the biomechanical functionality of the spider fang," *Nat. Commun.*, vol. 5, no. 1, pp. 1–8, May 2014, doi: 10.1038/ncomms4894.

[7] D. Kokkinis, M. Schaffner, and A. R. Studart, "Multimaterial magnetically assisted 3D printing of composite materials," *Nat. Commun.*, vol. 6, Oct. 2015, doi: 10.1038/ncomms9643.

[8] M. K. Hausmann *et al.*, "Dynamics of Cellulose Nanocrystal Alignment during 3D Printing," *ACS Nano*, vol. 12, no. 7, pp. 6926–6937, 2018, doi: 10.1021/acsnano.8b02366.

[9] G. Siqueira *et al.*, "Cellulose Nanocrystal Inks for 3D Printing of Textured Cellular Architectures," *Adv. Funct. Mater.*, vol. 27, no. 12, 2017, doi: 10.1002/adfm.201604619.

[10] C. Gauss, K. L. Pickering, and L. P. Muthe, "The use of cellulose in bio-derived formulations for 3D/4D printing: A review," *Composites Part C: Open Access*, vol. 4. Elsevier B.V., p. 100113, 01-Mar-2021, doi: 10.1016/j.jcomc.2021.100113.

[11] M. K. Hausmann *et al.*, "Complex-Shaped Cellulose Composites Made by Wet Densification of 3D Printed Scaffolds," *Adv. Funct. Mater.*, vol. 30, no. 4, p. 1904127, Jan. 2020, doi: 10.1002/adfm.201904127.

[12] A. Kirillova and L. Ionov, "Shape-changing polymers for biomedical applications," *Journal of Materials Chemistry B*, vol. 7, no. 10. Royal Society of Chemistry, pp. 1597–1624, 2019, doi: 10.1039/c8tb02579g.

[13] H. Yu, C. Yan, and J. Yao, "Fully biodegradable food packaging materials based on functionalized cellulose nanocrystals/poly(3-hydroxybutyrate-co-3-hydroxyvalerate) nanocomposites," *RSC Adv.*, vol. 4, no. 104, pp. 59792–59802, 2014, doi: 10.1039/c4ra12691b.

[14] O. Fourmann *et al.*, "3D printing of shape-morphing and antibacterial anisotropic nanocellulose hydrogels," *Carbohydr. Polym.*, vol. 259, p. 117716, May 2021, doi: 10.1016/j.carbpol.2021.117716.

[15] R. Nasseri, C. P. Deutschman, L. Han, M. A. Pope, and K. C. Tam, "Cellulose nanocrystals in smart and stimuli-responsive materials: a review," *Mater. Today Adv.*, vol. 5, p. 100055, Mar. 2020, doi: 10.1016/j.mtadv.2020.100055.

[16] S. Palagi *et al.*, "Structured light enables biomimetic swimming and versatile locomotion of photoresponsive soft microrobots," *Nat. Mater.*, vol. 15, no. 6, pp. 647–653, Jun. 2016, doi: 10.1038/nmat4569.

[17] M. V. Biyani, C. Weder, and E. J. Foster, "Photoswitchable nanocomposites made from coumarin-functionalized cellulose nanocrystals," *Polym. Chem.*, vol. 5, no. 18, pp. 5501–5508, Sep. 2014, doi: 10.1039/c4py00486h.

[18] M. V. Biyani, M. Jorfi, C. Weder, and E. J. Foster, "Light-stimulated mechanically switchable, photopatternable cellulose nanocomposites," *Polym. Chem.*, vol. 5, no. 19, pp. 5716–5724, 2014, doi: 10.1039/c4py00487f.

[19] L. A. E. Müller, T. Zimmermann, G. Nyström, I. Burgert, and G. Siqueira, "Mechanical Properties Tailoring of 3D Printed Photoresponsive Nanocellulose Composites," *Adv. Funct. Mater.*, vol. 2002914, pp. 1–9, 2020, doi: 10.1002/adfm.202002914.

[20] X. Liu, M. Li, X. Zheng, E. Retulainen, and S. Fu, "Dual light- and pH-responsive composite of polyazo-derivative grafted cellulose nanocrystals," *Materials (Basel).*, vol. 11, no. 9, Sep. 2018, doi: 10.3390/ma11091725.

[21] L. Ceamanos, Z. Kahveci, M. Lopez-Valdeolivas, D. Liu, D. J. Broer, and C. Sanchez-Somolinos, "Four-dimensional printed liquid crystalline elastomer actuators with fast photoinduced mechanical response toward light-driven robotic functions," *ACS Appl. Mater. Interfaces*, vol. 12, no. 39, pp. 44195–44204, Sep. 2020, doi: 10.1021/acsami.0c13341.

[22] N. Wagner and P. Theato, "Light-induced wettability changes on polymer surfaces," *Polym. (United Kingdom)*, vol. 55, no. 16, pp. 3436–3453, 2014, doi: 10.1016/j.polymer.2014.05.033.

[23] Y. Kim, D. Jeong, V. V. Shinde, Y. Hu, C. Kim, and S. Jung, "Azobenzene-grafted carboxymethyl cellulose hydrogels with photo-switchable, reduction-responsive and self-healing properties for a controlled drug release system," *Int. J. Biol. Macromol.*, vol. 163, pp. 824–832, Nov. 2020, doi: 10.1016/j.ijbiomac.2020.07.071.

[24] M. Poprawa-Smoluch, J. Baggerman, H. Zhang, H. P. A. Maas, L. De Cola, and A. M. Brouwer, "Photoisomerization of disperse red 1 studied with transient absorption spectroscopy and quantum chemical calculations," *J. Phys. Chem. A*, vol. 110, no. 43, pp. 11926–11937, Nov. 2006, doi: 10.1021/jp054982b.

[25] R. Tang, J. Wen, R. E. Stote, and Y. Sun, "Cyanuric Chloride-Based Reactive Dyes for Use in the Antimicrobial Treatments of Polymeric Materials," *ACS Appl. Mater. Interfaces*, vol. 13, no. 1, pp. 1524–1534, Jan. 2021, doi: 10.1021/acsami.0c18613.

[26] M. Prabhaharan, A. R. Prabakaran, S. Srinivasan, and S. Gunasekaran, "Experimental and theoretical spectroscopic analysis, HOMO-LUMO, and NBO studies of cyanuric chloride," *Spectrochim. Acta - Part A Mol. Biomol. Spectrosc.*, vol. 127, pp. 454–462, Jun. 2014, doi: 10.1016/j.saa.2014.02.040.

[27] Y. Sun, Z. Chen, and M. Braun, "Preparation and physical and antimicrobial properties of a cellulose-supported chloromelamine derivative," *Ind. Eng. Chem. Res.*, vol. 44, no. 21, pp. 7916–7920, 2005, doi: 10.1021/ie0504452.

[28] M. Cinar, A. Coruh, and M. Karabacak, "FT-IR, UV-vis, 1H and 13C NMR spectra and the equilibrium structure of organic dye molecule disperse red 1 acrylate: A combined experimental and theoretical analysis," *Spectrochim. Acta - Part A Mol. Biomol. Spectrosc.*, vol. 83, no. 1, pp. 561–569, 2011, doi: 10.1016/j.saa.2011.09.003.

[29] L. Xiao *et al.*, "Bio-based green composites with high performance from poly(lactic acid) and surface-modified microcrystalline cellulose," *J. Mater. Chem.*, vol. 22, no. 31, pp. 15732–15739, Aug. 2012, doi: 10.1039/c2jm32373g.

[30] A. Goulet-Hanssens, T. C. Corkery, A. Priimagi, and C. J. Barrett, "Effect of head group size on the photoswitching applications of azobenzene Disperse Red 1 analogues," *J. Mater. Chem. C*, vol. 2, no. 36, pp. 7505–7512, Sep. 2014, doi: 10.1039/c4tc00996g.

[31] A. D. French, "Idealized powder diffraction patterns for cellulose polymorphs," *Cellulose*, vol. 21, no. 2, pp. 885–896, Aug. 2014, doi: 10.1007/s10570-013-0030-4.

[32] J. Gong, J. Li, J. Xu, Z. Xiang, and L. Mo, "Research on cellulose nanocrystals produced from cellulose sources with various polymorphs," *RSC Adv.*, vol. 7, no. 53, pp. 33486–33493, Jun. 2017, doi: 10.1039/c7ra06222b.

[33] M. Banerjee, S. Saraswatula, A. Williams, and B. Brettmann, "Effect of Purification Methods on Commercially Available Cellulose Nanocrystal Properties and TEMPO Oxidation," *Processes*, vol. 8, no. 6, p. 698, Jun. 2020, doi: 10.3390/pr8060698.

[34] U. P. Agarwal, S. A. Ralph, C. Baez, R. S. Reiner, and S. P. Verrill, "Effect of sample moisture content on XRD-estimated cellulose crystallinity index and crystallite size," *Cellulose*, vol. 24, no. 5, pp. 1971–1984, 2017, doi: 10.1007/s10570-017-1259-0.

[35] S. Park, J. O. Baker, M. E. Himmel, P. A. Parilla, and D. K. Johnson, "Cellulose crystallinity index: Measurement techniques and their impact on interpreting cellulase performance," *Biotechnol. Biofuels*, vol. 3, 2010, doi: 10.1186/1754-6834-3-10.

[36] J. M. B. Fernandes Diniz, M. H. Gil, and J. A. A. M. Castro, "Hornification - Its origin and interpretation in wood pulps," *Wood Sci. Technol.*, vol. 37, no. 6, pp. 489–494, 2004, doi: 10.1007/s00226-003-0216-2.

[37] S. Sultan, G. Siqueira, T. Zimmermann, and A. P. Mathew, "3D printing of nano-cellulosic biomaterials for medical applications," *Curr. Opin. Biomed. Eng.*, vol. 2, pp. 29–34, 2017, doi: 10.1016/j.cobme.2017.06.002.

[38] F. Pinto and M. Meo, "Design and Manufacturing of a Novel Shear Thickening Fluid Composite (STFC) with Enhanced out-of-Plane Properties and Damage Suppression," *Appl. Compos. Mater.*, vol. 24, no. 3, pp. 643–660, Jun. 2017, doi: 10.1007/s10443-016-9532-1.

[39] I. M. Krieger and T. J. Dougherty, "A Mechanism for Non-Newtonian Flow in Suspensions of Rigid Spheres," *Trans. Soc. Rheol.*, vol. 3, no. 1, pp. 137–152, Mar. 1959, doi: 10.1122/1.548848.

[40] E. A. Le, W. C. Wang, C. S. Liu, and C. W. Wang, "Effect of Fiber Alignment on Optical Properties of Cellulose Nanocrystal Films," in *2014 International Symposium on Optomechatronic Technologies, ISOT 2014*, 2014, pp. 305–309, doi: 10.1109/ISOT.2014.80.

[41] E. D. Cranston and D. G. Gray, “Birefringence in spin-coated films containing cellulose nanocrystals,” *Physicochem. Eng. Asp.*, vol. 325, pp. 44–51, 2008, doi: 10.1016/j.colsurfa.2008.04.042.

[42] E. Eremeeva *et al.*, “Printing of Colorful Cellulose Nanocrystalline Patterns Visible in Linearly Polarized Light,” *ACS Appl. Mater. Interfaces*, vol. 12, no. 40, pp. 45145–45154, Oct. 2020, doi: 10.1021/acsami.0c11846.

[43] L. A. E. Müller *et al.*, “Photoresponsive Movement in 3D Printed Cellulose Nanocomposites,” *ACS Appl. Mater. Interfaces*, p. acsami.2c02154, Apr. 2022, doi: 10.1021/acsami.2c02154.

[44] J. Vapaavuori, A. Laventure, C. G. Bazuin, O. Lebel, and C. Pellerin, “Submolecular Plasticization Induced by Photons in Azobenzene Materials,” *J. Am. Chem. Soc.*, vol. 137, no. 42, pp. 13510–13517, Oct. 2015, doi: 10.1021/jacs.5b06611.

[45] I. Burgert, K. Frühmann, J. Keckes, P. Fratzl, and S. E. Stanzl-Tschegg, “Microtensile Testing of Wood Fibers Combined with Video Extensometry for Efficient Strain Detection,” *Holzforschung*, vol. 57, no. 6, pp. 661–664, Oct. 2003, doi: 10.1515/HF.2003.099.

[46] W. M. Huang, B. Yang, and Y. Q. Fu, *Polyurethane Shape Memory Polymers*. Boca Raton, London, Newyork: CRC Press, 2011.

[47] Y. C. Chien, W. T. Chuang, U. S. Jeng, and S. H. Hsu, “Preparation, Characterization, and Mechanism for Biodegradable and Biocompatible Polyurethane Shape Memory Elastomers,” *ACS Appl. Mater. Interfaces*, vol. 9, no. 6, pp. 5419–5429, 2017, doi: 10.1021/acsami.6b11993.

[48] F. Xie, L. Huang, J. Leng, and Y. Liu, “Thermoset shape memory polymers and their composites,” *J. Intell. Mater. Syst. Struct.*, vol. 27, no. 18, pp. 2433–2455, 2016, doi: 10.1177/1045389X16634211.

[49] D. Ratna and J. Karger-Kocsis, “Recent advances in shape memory polymers and composites: A review,” *J. Mater. Sci.*, vol. 43, no. 1, pp. 254–269, 2008, doi: 10.1007/s10853-007-2176-7.

[50] H. Chu *et al.*, “4D printing: A review on recent progresses,” *Micromachines*, vol. 11, no. 9, 2020, doi: 10.3390/MI11090796.

[51] L. J. Gibson and M. F. Ashby, *Cellular solids: Structure & properties*, vol. 9, no. 2. Oxford: Pergamon Press, 1989.

[52] D. M. Correa, C. C. Seepersad, and M. R. Haberman, “Mechanical design of negative stiffness honeycomb materials,” *Integr. Mater. Manuf. Innov.*, vol. 4, no. 1, pp. 165–175, Dec. 2015, doi: 10.1186/s40192-015-0038-8.

[53] D. A. Debeau, C. C. Seepersad, and M. R. Haberman, “Impact behavior of negative stiffness honeycomb materials,” *J. Mater. Res.*, vol. 33, no. 3, pp. 290–299, 2018, doi: 10.1557/jmr.2018.7.

[54] S. Chen *et al.*, “A novel gradient negative stiffness honeycomb for recoverable energy absorption,” *Compos. Part B Eng.*, vol. 215, p. 108745, Jun. 2021, doi: 10.1016/j.compositesb.2021.108745.

[55] D. M. Correa, T. Klatt, S. Cortes, M. Haberman, D. Kovar, and C. Seepersad, “Negative stiffness honeycombs for recoverable shock isolation,” *Rapid Prototyp. J.*, vol. 21, no. 2, pp. 193–200, Mar. 2015, doi: 10.1108/RPJ-12-2014-0182.

[56] M. Arcari *et al.*, “Nanostructural Properties and Twist Periodicity of Cellulose Nanofibrils with Variable Charge Density,” *Biomacromolecules*, vol. 20, no. 3, pp. 1288–1296, 2019, doi: 10.1021/acs.biomac.8b01706.

[57] H. Bennettand, G. J. O. Wiley, A. Benninghoven, K. T. F. Janssen, J. Tumpner, and H. W. Wer, “High Resolution XPS of Organic Polymers: The Scienta ESCA300 Database (Beamson, G.; Briggs, D.),” *J. Chem. Educ.*, vol. 70, no. 1, p. A25, Jan. 1993, doi: 10.1021/ed070pa25.5.

3.3.9 Supporting Information

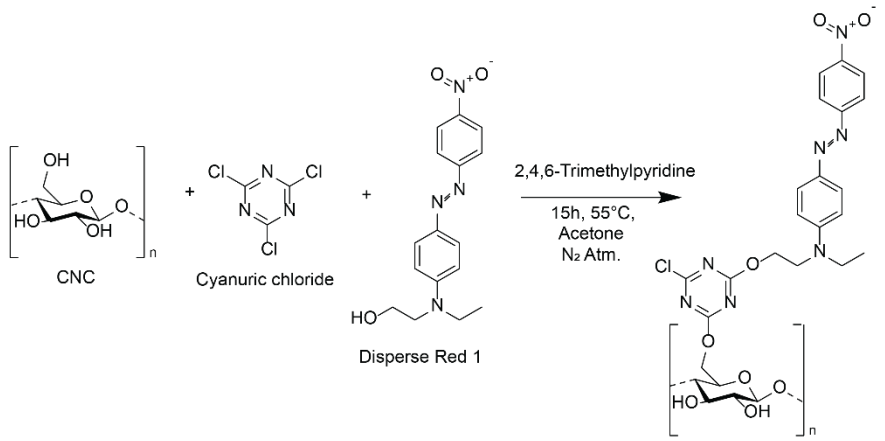

Figure S 3.3-1 *Schematic representation of the chemical modification of CNC. The grafting is represented here on C6, accounting for the higher probability that the reaction occurs in this position due to the reduced steric hinderance of this group. However, the reaction could also occur on the other OH groups of the AGU (Anhydroglucose Unit).*

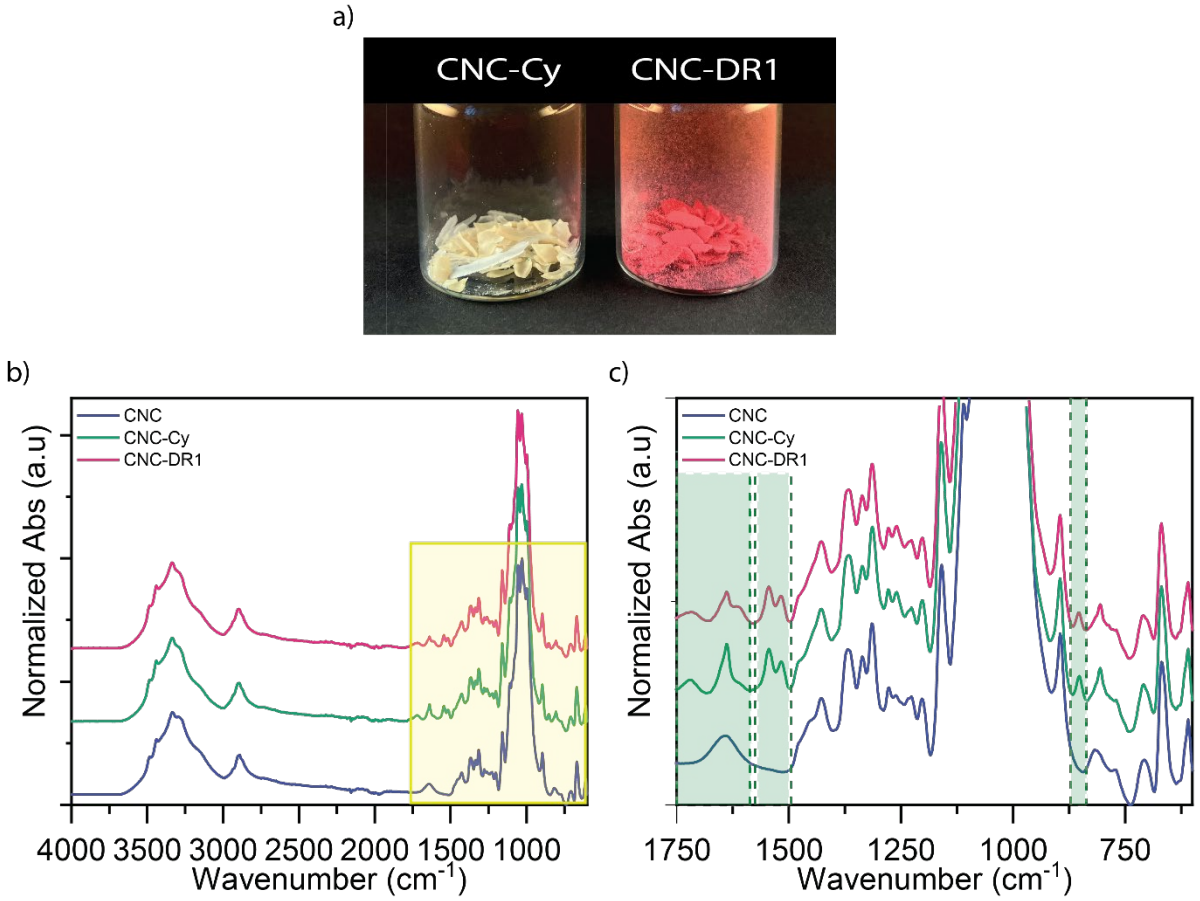

Figure S 3.3-2 *ATR-FTIR Spectra of the CNC before, intermediate and after modification.* ***(a)****Photograph of the two reaction products CNC-Cy (modified only with cyanuric chloride) and CNC-DR1.* ***(b)*** *Full spectra including CNC, CNC-Cy, and modified CNC-DR1.* ***(c)*** *Enlargement of the yellow region of the spectra in (b) between 1750 and 600 cm^{-1}, green boxes highlight the regions of interest in the spectra.*

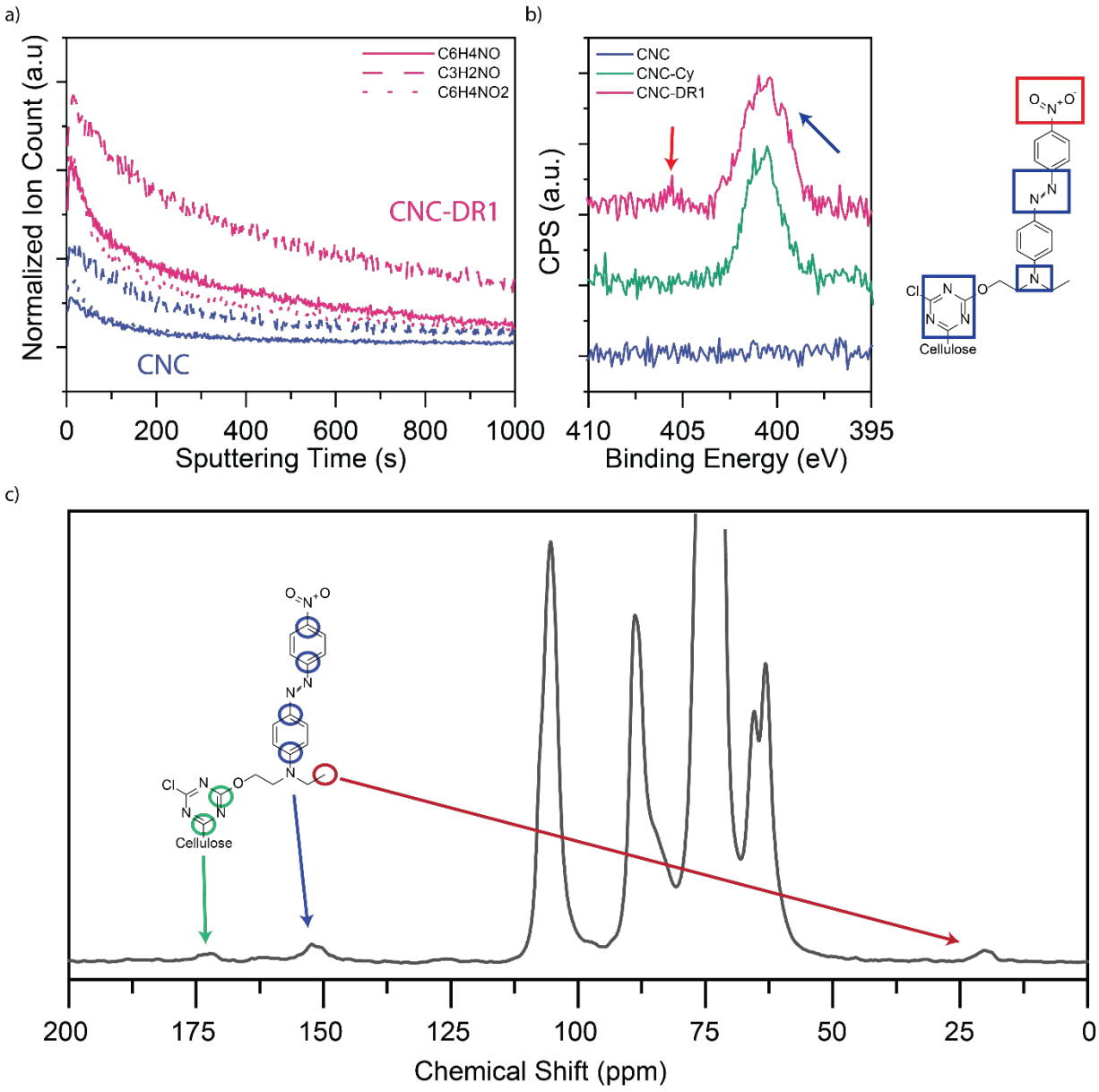

Figure S 3.3-3 *Chemical characterization of CNC-DR1.* ***(a)*** *DR1ToF-SIMS negative spectra of CNC-DR1 and CNC for the NO_2 group of DR1 Azobenzene.* ***(b)*** *XPS spectra of N1s signal for CNC, CNC-Cy, CNC-DR1 (left) and the grafted DR1 compound (right) the colored arrows indicates which peak corresponds to which N atoms in the compound.* ***(c)*** *Solid state C^{13} NMR spectra of CNC-DR1.*

Note on XPS: The DR1 is attached to the cellulose, since ref CNC samples do not show presence of N as contamination. Indeed, nitrogen seems to be present with 1% at. However, the N-O group tends to degrade under X-ray, becoming a N-H group. Longer acquisition times would be required to have a full quantification, but this would lead to destruction of the functional group and decreasing of the NO_2 peak at 405-406 eV.

Estimation of Substitution fraction of CNC accessible hydroxyls from Solid State NMR: The number of OH reacting with DR1 over the number of accessible OH was estimated from the NMR results in Figure S3 by applying the following equation:[1,2]

$$\omega = \frac{\frac{\int C_{Dr1}}{4}}{0.45 * 3 * \int C1_{CNC}} = 0.7\%$$

Where $\int C_{Dr1}$ corresponds to the area of the four aromatic carbons of DR1 at 152 ppm, while $\int C1_{CNC}$ corresponds to the area of the C1 of the anhydroglucose unite at 105 ppm. Each glucose unit bears 3 hydroxyl and for CNC with a transversal size of

around 5 nm, only around 45 % (estimated from Sugiyama et al.[3]) of the total amount of hydroxyl groups is accessible at the surface of the particles.

Table S 3.3-1 *Elemental analysis results for CNC and CNC-DR1 obtained with a LECO TruSpec Micro. Samples were dried 24 hours at 60 °C from acetone suspension prior measurement.*

Sample	%C	%H	%Cl	%N	DS	Substitution fraction of CNC accessible hydroxyls
CNC	39.45	5.75	0.61	<0.20	-	-
CNC-DR1	41.99	5.73	2.05	1.80	0.03	2.39 %

Degree of substitution from elemental analysis: The DS per anhydroglucose unit was estimated directly from %N of CNC-DR1 assuming the grafted molecules to be composed of a DR1 and a Cyanuric Chloride unit as illustrated in Figure S1 and that the reference CNC do not contain nitrogen since the measured value is below the detection limit of the instrument. The following equation was applied:[4]

$$DS = \frac{M_n * n_{AGU} - \%N * M_{AGU}}{\%N * M_{com} - M_N * n_N}$$

Where M_N is the nitrogen molecular weight, n_{AGU} the number of nitrogen atoms in an anhydroglucose unit (AGU), M_{AGU} the molecular weight of the AGU, M_{com} is the molecular weight of the grafted compound and n_N is the number of nitrogen atoms in the grafted compound. The substituted fraction of OH groups among those accessible at the surface was obtained by dividing the DS by a factor of 3 (three hydroxyls per AGU) and a factor of 0.45 (fraction of surface hydroxyls).[5]

Note on elemental analysis: The degree of substitution here calculated is likely an over estimation arising from the assumption that one DR1 and one cyanuric chloride are linked together (according to the presence of Cl in the final product and the C-Cl bending band observed from FTIR). However, being a one pot reaction, there is the possibility that more cyanuric chlorides are attached to CNC than DR1. The calculated value remains an estimation.

(1) Xiao, L.; Mai, Y.; He, F.; Yu, L.; Zhang, L.; Tang, H.; Yang, G. Bio-Based Green Composites with High Performance from Poly(Lactic Acid) and Surface-Modified Microcrystalline Cellulose. *J. Mater. Chem.* **2012**, *22* (31), 15732–15739. https://doi.org/10.1039/c2jm32373g.

(2) Gårdebjer, S.; Bergstrand, A.; Idström, A.; Börstell, C.; Naana, S.; Nordstierna, L.; Larsson, A. Solid-State NMR to Quantify Surface Coverage and Chain Length of Lactic Acid Modified Cellulose Nanocrystals, Used as Fillers in Biodegradable Composites. *Compos. Sci. Technol.* **2015**, *107*, 1–9. https://doi.org/10.1016/j.compscitech.2014.11.014.

(3) Sugiyama, J.; Vuong, R.; Chanzy, H. Electron Diffraction Study on the Two Crystalline Phases Occurring in Native Cellulose from an Algal Cell Wall. *Macromolecules* **1991**, *24* (14), 4168–4175. https://doi.org/10.1021/ma00014a033.

(4) Vaca-Garcia, C.; Borredon, M. E.; Gaseta, & A. *Determination of the Degree of Substitution (DS) of Mixed Cellulose Esters by Elemental Analysis*; 2001; Vol. 8.

(5) Siqueira, G.; Bras, J.; Dufresne, A. New Process of Chemical Grafting of Cellulose Nanoparticles with a Long Chain Isocyanate. *Langmuir* **2010**, *26* (1), 402–411. https://doi.org/10.1021/la9028595.

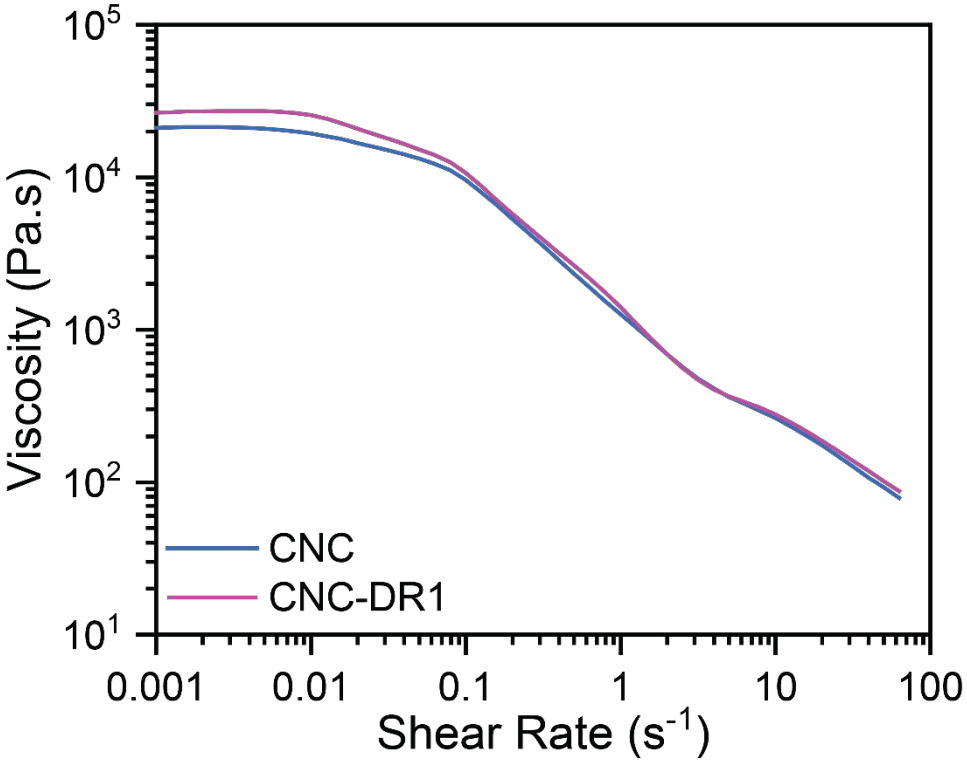

Figure S 3.3-4 *Shear thinning behavior of 15 wt% CNC or CNC-DR1 in PUA-HEMA inks. Rheology measurements obtained with a rotational experiment.*

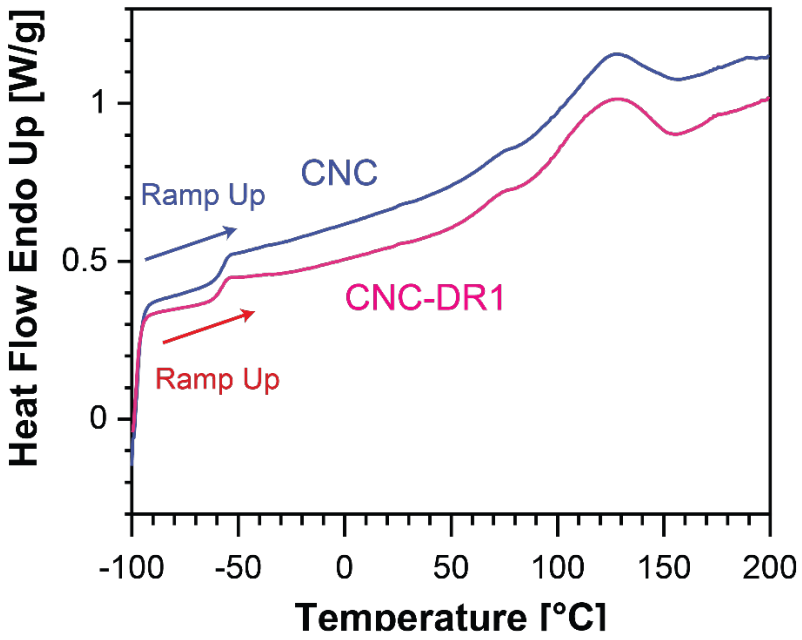

Figure S 3.3-5 *DSC analysis of composites with 15 wt% of particles in the PUA-HEMA matrix for both CNC and CNC-DR1. First heating cycle obtained at 20 °C min^{-1}.*

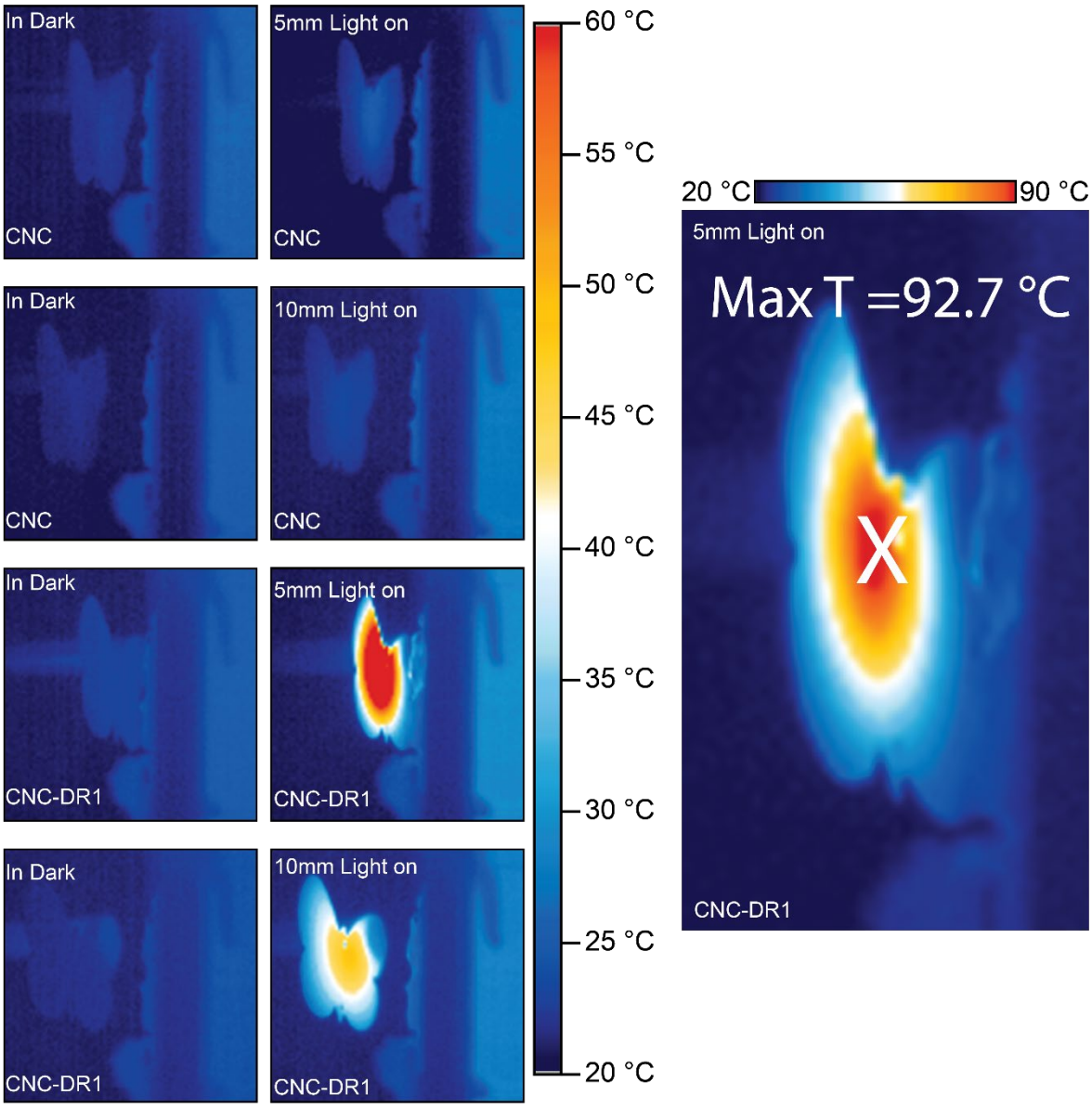

Figure S 3.3-6 *Thermographs of the printed composite materials in dark or under illumination. The enlargement (right image) is the CNC-DR1 composite illuminated at 5 mm distance with the adjusted scale.*

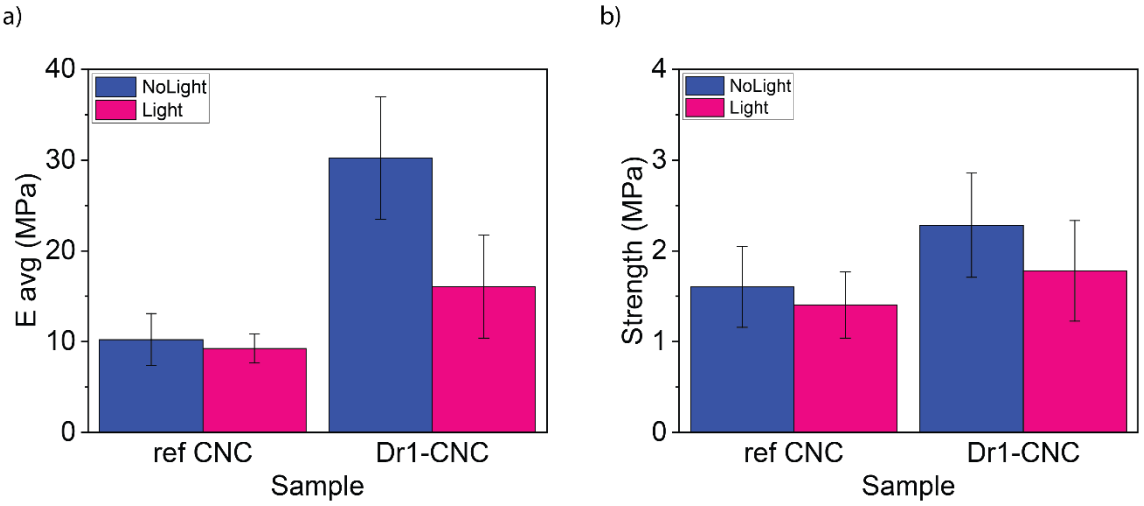

Figure S 3.3-7 *Mechanical properties of the tested composites.* ***(a)*** *Young moduli and* ***(b)*** *strength extracted from the micro-tensile tests.*

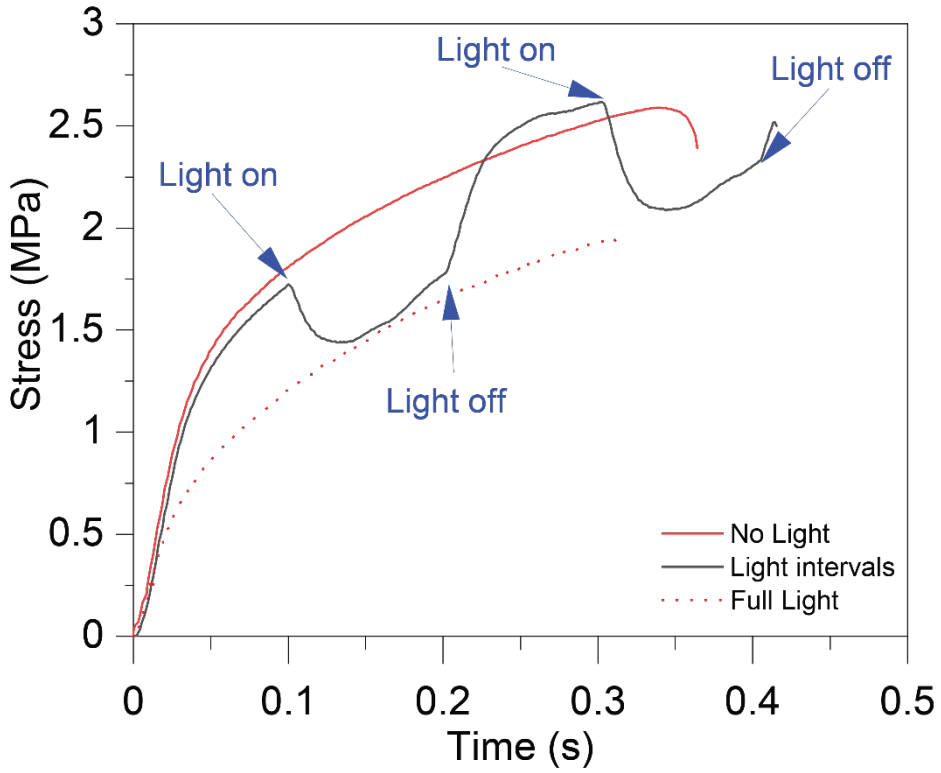

Figure S 3.3-8 *Microtensile tests of CNC-DR1 composites in dark, under illumination and under selective light intervals.*

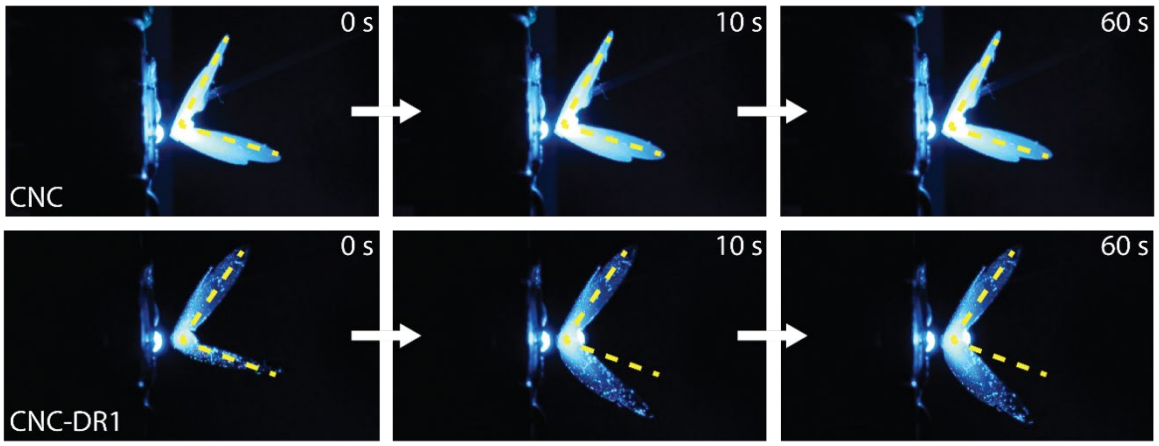

Figure S 3.3-9 *Comparison of the shape memory effect triggered by illumination for CNC* ***(a)*** *and unmodified CNC-DR1* ***(b)*** *printed composites.*

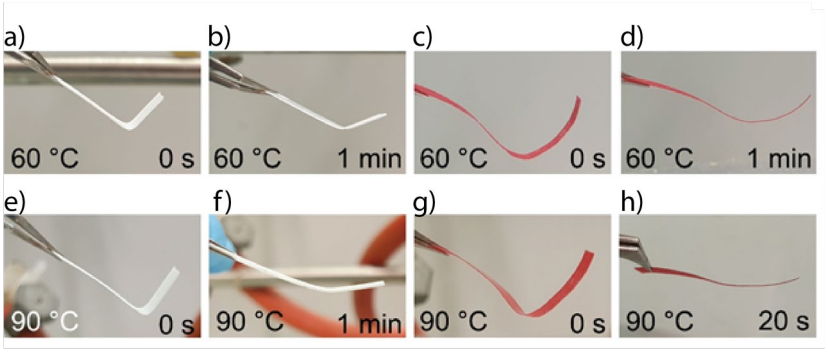

Figure S 3.3-10 *Thermally activated shape memory effect of the printed composites for CNC* ***(a,b,e,f)*** *and CNC-DR1* ***(c,d,g,h)****.*

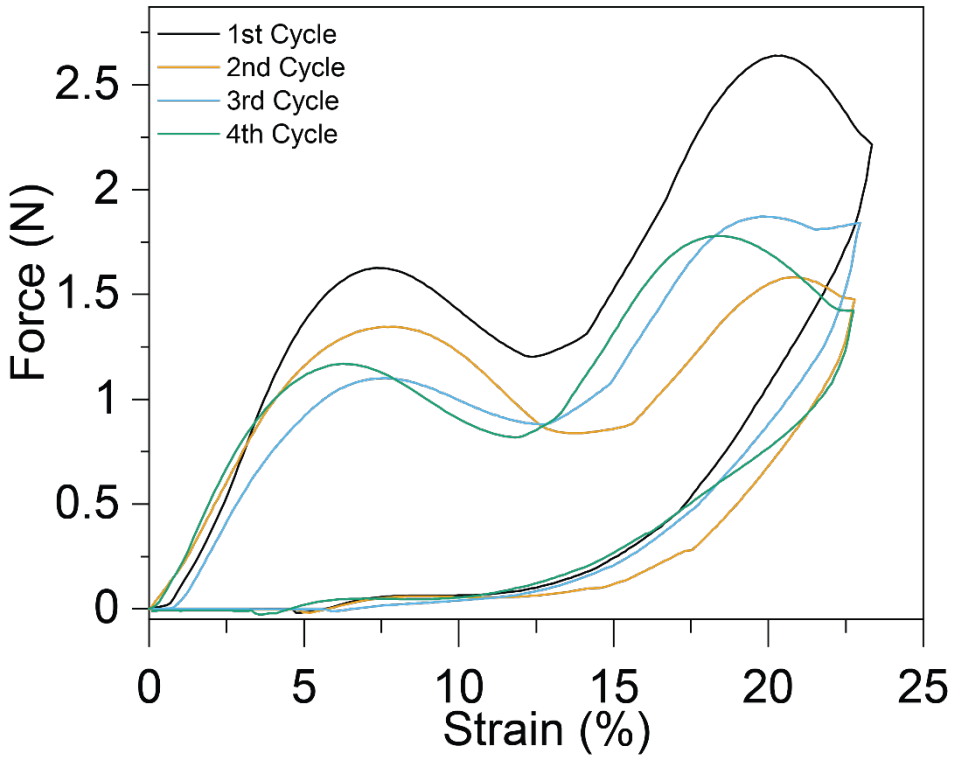

Figure S 3.3-11 *Compression of a CNC-DR1 composite printed as negative stiffness honeycomb. The sample was illuminated for 5 minutes after each cycle in order to recover its initial shape.*

4 General discussion and conclusion

For the first time, CNC composites with relatively high solid contents that display phototopatternable stiffening, *shape changing* ability and/or photosoftening could be manufactured in 3D shapes by additive manufacturing. Such behavior was obtained by combining the engineering of cellulose nanoparticles, as active reinforcing elements, and the design of suitable polymer matrices with the spatial control of composition and microstructure organization offered by DIW.

Focusing on particle-matrix interactions, local photostiffenings was achieved by introducing on demand crosslink density variations. Stiffening is hence observed as a consequence of the photoresponsive [2,2] cycloaddition of cinnamate moieties, grafted on the CNC, with the cinnamates of the primary polymer network. This secondary polymer network is triggered by light at a wavelength of 365 nm and the density of crosslinks is controlled by the illumination time. Spatially controlling the illumination leads to the formation of stiff and soft domains that allows tailoring the mechanical properties of polyurethane/CNC composites. The *shape changing* ability, as a reaction to light at 480 nm, was demonstrated by LCE/CNC composites, after doping the printed parts with an azobenzene dye. The DIW of the material allowed orienting the CNC to structure the liquid crystal mesogens of the polymer matrix in ordered nematic phases. The azobenzene dye can then act as a photoswitch that trigger, under illumination, the polymer order/disorder liquid crystalline phase transitions. This amplifies the azobenzene contractions during photoisomerization, leading to reversible macroscopic bending in diverse 3D printed structures. Design of CNC as active building blocks, by grafting of azobenzene dyes, permits DIW and, at the same time, confers multiple photoresponses to polymers. As an example, photosoftening is the primary reaction to light observed in a polyurethane acrylate embedding these active CNC. Such composites undergo photogenerated heating, resulting in a decrease of the Young's modulus and the triggering of the matrix's shape memory effect. With these engineered functions (photostiffening, *shape changing* and photosoftening), the different materials demonstrated a very large design freedom for 3D shapes, mechanical properties and responses. This allows the production of tailored devices for a wide range of applications, spanning from protective structures for sensors to dynamic energy absorption.

The light stimulated adaptable behaviors conferred to our 3D printed cellulose nanocomposites is seen as the main result of this thesis. The initial works on 3D printing of cellulose nanocrystals focused primarily on the capability of extrusion printing to orient particles and the consequent spatial control over CNC's anisotropic stiffness in the printed materials [1]–[3]. This led to lightweight printed structures achieving outstanding static mechanical properties, optimized for the load requirements [3]. Differently from previous works, here we were able to add dynamic responses to composites with specific microstructures. This allowed printing nanocellulose-based devices that display adaptable physical properties under illumination, suitable for utilization in environments presenting dynamic temporal light solicitations. Such photoresponsive devices have the potential to revolutionize several applications ranging from soft robotics to sensors. In soft robots, structural components can be lightened, while the device assemblies can be simplified, not requiring neither engines or contact power supplies [4]. A single material can be mechanically optimized and carry out the actuation with determined movements. Similarly, sensors, impact-resistant structures, and construction materials could also benefit from this principle. In short, smart photoresponsive materials based on cellulose nanocrystals can contribute to a high technological world by reducing energy consumptions in both device production (decrease of assembly steps) and operation (weight decrease and mechanical optimization). Moreover, the methods and approaches developed in this thesis could be applied even to other material compositions for the development of

new photoresponsive functions in renewable materials. Especially, the active reinforcement particles cin-CNC and CNC-DR1 could be used with other polymer matrices that satisfy the conditions required for the photoresponse in soft materials. This would promote the use of renewable cellulose nanoparticles outside of the boundaries of paper and food packaging applications, further expanding their market.

This thesis provides also new insights into the process-structure-property relationships of these photoresponsive cellulose nanocomposites. The influence of the functionalization of the cellulose nanoparticles and polymer matrices on the ink processing by DIW could be established. The effect of DIW on the physical properties and dynamic behaviors of the final 3D shaped composites could be revealed. Special attention has been paid to the synergy occurring between extrusion induced alignment of the particles with the resulting mechanical properties and photoresponse performances of the printed composites. The collection of these data allowed to furnish a guideline with methods and requirements for the fabrication of photoresponsive 3D printable cellulose nanocomposites. In the following sections these findings are reviewed and critically assessed.

4.1 Direct ink writing of functionalized CNC composite inks

4.1.1 Printing of high CNC solid content inks

The main challenge that is currently encountered in CNC based composites resides in achieving homogeneous dispersions of the hydrophilic nanoparticles into the often hydrophobic polymer matrices [5]. The surface energy discrepancy between matrix and fillers promotes high viscosities of the dispersion, complicating the compounding of dispersions and composite melts [5]. On the other hand, the large amount of hydroxyl groups on CNC surfaces promotes particle aggregation. The agglomerates lead to reduced stress-transfer and stress concentration sites, which subsequently decrease the stiffness and strength of the composite materials [6]–[8]. DIW of such materials has been impeded by these limiting factors, since incompatible matrices with CNC strongly limit the amount of particle solid content that allows printing. High concentrations result in inhomogeneous flows, high or prohibitive printing pressures (e.g.> 5 bar) and/or clogging of the nozzles due to agglomerates. Despite the fact that several methods, such as ultrasonication, magnetic stirring or chemical functionalization with surfactants [6], [8], [9], have been developed to increase homogeneity of CNC dispersions, 3D printing of high solid contents remains a major challenge and a hot topic [10]. Devices with high solid contents of CNC could present superior mechanical properties while decreasing the amounts of non-renewable components.

Functionalization of CNC with the selected photoswitches and their introduction in the polymer matrix face the same issues. However, the cinnamic moieties grafted on CNC, developed in Chapter 3.1, demonstrated to function not only as photoswitches, but also as compatibilizer and hydrophobizing agents. The dispersion of cin-CNC in the PUA-VCA leads to lower storage and loss moduli, as well as, yield stress for a determined concentration, when compared to unmodified CNC-polymer inks. The chemical treatment of cin-CNC and the appropriate choice of the polymer matrix did not hinder the DIW of the cin-CNC PUA-VCA inks, but improved the process. Further, the particle-polymer compatibility allows for the direct printing of materials with high concentrations of particles, reaching, at least, 30 wt%. Hausmann et al. [3] prepared CNC/CNF composites with nanocellulose content around 35-40 wt%. These values could be reached after a post printing densification process of a gel containing, initially, 20 wt% CNC and 1 wt% of CNF. The recent work of Latif et al. [10] demonstrated the printing of pastes containing 25.94 wt% of nanocellulose with a CNC:CNF ratio of 20:1. Interestingly, our ink with 30 wt% cin-CNC in PUA-VCA reaches a yield stress of few hundreds Pa. Being in the lower range of yield stress required for ensuring successful 3D printing with the employed DIW set-up [1], [11], 30

wt% is in the lower range of concentrations that could be printed. Even if this remains yet to be explored, our approach has the potential to increase further the amount of renewable particles in the photoresponsive 3D printed cin-CNC composites.

The functionalization of CNC with DR1, as demonstrated in (Chapter 3.3), without developing a compatible matrix do not allow to reach such high solid content values in the final composites. CNC-DR1 particles dispersed into the polyurethane display higher rheological properties than the suspension with the same concentration of pristine CNC. It would hence be unlikely to print CNC-DR1/polyurethane inks with solid content as high as 30 wt%. This also implies that despite the fact that a photoresponsive behavior can be conferred to commercially available matrices, it is important to select a compatible matrix in order to further increase the amount of modified CNC in the ink.

On the contrary, the approach of engineering a structured matrix as the LCE exposed in (Chapter 3.2) results in poor dispersion of unmodified particles. In this case, pristine CNC needed to be methacrylated in order to reduce the agglomeration and ease the printing process. Methacrylated CNC allows a reduction of the yield stress of one order of magnitude, hence demanding lower printing pressures than LCE inks with unmodified CNC. This further confirms the importance of compatibilizing the hydrophobic interactions between particles and matrix when a high solid content of CNC in the ink is desired.

When the solid content of nanoparticles is not a primary target, both approaches of utilizing CNC as active photoresponsive elements or introducing CNC in engineered light stimulated polymer matrices still allow to tune the rheology of Newtonian resins and create stable shear thinning gels that can be processed by commercial 3D printers. Importantly, the development of our materials demonstrates concepts and methods directed toward the optimization of the material's properties for a given manufacturing set-up. Another way for increasing the amount of particles during printing would require optimization of the printer set-up. Increasing further the printing pressure would allow processing of inks with higher solid contents.

4.1.2 Hierarchical structuring in photoresponsive composites

Once uniform and homogeneous CNC/polymer dispersions could be achieved, engineering and structuring of photoactive composites take place through DIW. Former studies already demonstrated DIW's ability to create structures with hierarchical porosity spanning from the mesoscale to the macroscale [12], [13], the ability to align nanoparticles [1], [14], [15] and molecules like liquid crystal mesogens [16], [17] at the nanoscale. These features make DIW able to spatially organize materials' microstructure in a hierarchical fashion to tailor the mechanical properties of the printed parts. By incorporating photoresponsive functions into printable inks, DIW can manufacture hierarchically structured materials that show light activated behaviors. Interestingly, the works presented in Chapter 3.1 and Chapter 3.2 did not only show a final photoresponsive effect after printing. They actively contributed to further increase the complexity of the microstructures achievable with DIW, by adding a level of hierarchy at the molecular scale.

In our cin-CNC inks (Chapter 3.1), the photopatternable stiffening introduces, at the molecular level, compositional changes into a single material, i.e a material presenting regions with different crosslink densities. Other approaches, such as the use of two different polymers ratios, in DIW could be previously obtained with direct mixing in the syringe, right before the nozzle as reported by Kokkinis et al. [18]. However, the spatial resolution of this method is limited by the inner diameter of the nozzle. On the contrary, the limit in resolution of our approach resides in the illumination set-up and can reach higher resolutions (<100 µm). Photopatterning is, in fact, conferring a high design freedom that can be used to

create a large variety of mechanical responses as a function of the photopattern designs employed. Our material presents hence the potential to use complex geometrical patterns that would further tailor printed material reactions to external stresses and deformations. For example, Guzzi et al. [19] recently produced a dual hydrogel combining hydroxypropyl cellulose, PEG-b-PLA nanoparticles and GelMA that can locally photostiffen. They achieved printing of 3D scaffolds embedding high resolution photopatterns by alternating DIW and DLP for each layer of the final structure. This allowed to prepare composite hydrogels that display variable Young's moduli and Poisson's ratios as a function of the employed geometrical patterns. Moreover, our cin-CNC composites demonstrated a Young modulus dependent of the light intensity and illumination time. These two parameters would allow the introduction of functional crosslink density gradients, as employed in grayscale stereolithography [20], [21]. Spatial control of illumination with different intensities allows local control over the crosslink density, further increasing the complexity of the hierarchical assembly and hence the tailoring of the mechanical properties.

Our work on the composite LCE (Chapter 3.2) shows, to the best of our knowledge, the first co-occurrence of relatively high solid content (15 wt%) of aligned CNC with LC mesogens. During extrusion, the shear and extensional forces align the CNC and LC mesogens of the engineered matrix along the printing directions, organizing hence LC mesogens at the molecular level. Liu et al. [22] printed soft actuators composed of carbon nanotube in an LCE matrix. They demonstrated that the addition of 2 wt% CNC had the effect to increase the order parameter of the nematically aligned LCE. The addition of CNC in our LCE not only allowed the printing of the material at room temperature, but it permitted to obtain LCEs with structured LC mesogens with enhanced actuation performances when increasing the amount of CNC. The ability of cellulose to act as an alignment layer has been demonstrated by Kang et al. [23] where LC cells of transparent rubbed cellulose films presented performances close to polyimide rubbed LC cells. In agreement with this result, our CNC particles promote the formation of more complex phases of the LCE inks, than simply uniaxially aligned mesogens. Consequently, our LCE composites contributes both to the field of hierarchical assembly and to the field of 3D printing of LCE by DIW. Imparting molecular control to LCE through ink extrusion allows controlling the properties and the stimuli responses of such materials. Many examples have shown the extrusion of uniaxially aligned nematic LC phases [16], [24], [25], and it remains an open challenge to reach complex phases as the cholesteric or chiral nematic. By controlling the printing parameters, such as temperature, layer height, and nozzle diameter, functionally graded LCE devices could be printed, presenting spatially controlled degrees of LC alignment varying from isotropic to nematic [17]. A recent effort has focused on the 3D printing of chiral nematic phases and successfully achieved such task. It was demonstrated that control of temperature and printing speed (1-2 mm/s) allowed the helical phase to be formed again after printing, leading to an iridescent LCE material [26].

Even though the actual LC phase of our material still needs to be fully characterized, printing of the LCE composites at room temperature is an evidence of an interplay between CNC orientation and the LC phase. The pure LCE is in its crystalline phase at room temperature, but when CNC are dispersed, the suspension behaves as a gel, indicating an amorphous state of the LC mesogens. This happens because the CNC decrease the crystalline to nematic temperature of uncured inks from 44 °C to 25 – 30 °C. From a technical point of view, better understanding of the interactions between CNC and LC feeds the hope of allowing the faster manufacturing of materials with highly organized structures in a near future. In other words, the control of LC mesogens with CNC would further optimize materials' structure with respect to the mechanical properties (hierarchical organization) and provide multiple stimuli responsive functionalities. In particular, a printed device composed of a single material could present iridescent colors changing as it is self-bending (or contracting, curling…). This would offer the possibility

either to obtain an optical read out of the movement or to modify its motion as the incoming light is transmitted with a different wavelength, producing oscillating movements as observed during self-shadowing [27]. As a consequence, a deeper insight into the role of CNC on the LC phase arrangement should be carried out and would be of great benefit to the field.

4.1.3 Manufacturing process limitations

With the technical advances detailed above, it is important to keep in mind that the processes of these materials by DIW are not exempt from limitations and challenges. From a general perspective, we demonstrated a step further toward the production of functional 3D materials based on renewable and biodegradable materials, as shown by our use of CNC. The current challenges in the production of CNC, like the high quantity of acid waste and the intensive energy demand linked to their isolation, rises concerns about the sustainability of these materials [28]–[31]. Even though such challenges are currently tackled, the nowadays use of CNC in our 3D printing materials is justified and limited mainly to niche applications such as biomedical, soft robotics, sensing and actuation, where shape and property customization, as well as, adaptability are required [32].

From an environmental perspective, the chemical treatments employed during this thesis still require use of toxic solvents. For instance, grafting of cinnamates on the CNC surface (Chapter 3.1) occurs in DMF, and due to its high boiling point recovery of the solvent for reuse is unfavourable. In order to solve this issue, our initial trials for the modification of CNC with DR1 (Chapter 3.3) involved the use of water as medium for the reaction and citric acid as a linker. Despite the grafting of DR1 with the CNC was successfully achieved, the process required a drying step that resulted in the agglomeration of the particles, rendering such nanofillers not suitable for printing anymore. The aggregated particles could not be homogenously redispersed and the ink did not reach the rheological properties required for DIW. Consequently, the chemical process was adapted by changing the citric aacid linker for cyanuric chloride and acetone was utilized, a common industrial solvent [33], as medium for the modification of CNC surfaces with DR1 (Chapter 3.3). Moreover, acetone was also used as base for production of the inks and doping of the printed LCE composites (Chapter 3.2). With respect to DMF, the lower boiling point of acetone (55 °C) would ensure an easier recycling of the solvent. Nevertheless, a revision of the chemical processes employed and a shift toward greener solvents is a current challenge. Solving this issue would strongly contribute to the development of a more sustainable process for the preparation of the proposed materials.

Addressing the production process, the achievable sizes of the printed parts are limited by the light penetration during the photopolymerization [34], which fixes the gel into a solid composite. Features with thicknesses up to one centimeter could be printed for all the materials, but the actual light's penetration depth remain yet to be investigated for each composite. Secondly, the radical photopolymerization of the PU matrices in Chapter 3.1 and Chapter 3.3 undergoes oxygen inhibition [35] and hence requires an oxygen free atmosphere during curing which increases the production costs of the parts. However, overcoming size limitations could be achieved by harnessing oxygen inhibition. Illuminating every layer for some seconds allows to cure the bulk of the material, while the surface remains inhibited by the oxygen. While a new layer is added, the inhibited surface can react with the added material. Finally, we are still far away from the astonishing complexity of natural materials since, for instance, CNC particles can not be aligned out-of plane with our approaches, limiting the spatial control of the particles' orientation into the printing plane.

4.2 Photoresponse as a function for adaptable systems

4.2.1 Light for contactless stimulation

The advantages of using light as a triggering stimulus has been already proven in the last decades [36]–[38]. Three main features of light emerges as particularly interesting: energy, temporal and spatial control, and tuneability of its physical properties. A mole of photons at 365 nm wavelength present 130 times more energy than kT at 25 °C [39]. This allows reactions and processes with unfavorable energetic barriers at room temperature, to overcome their activation energy and occur in rapid timescales. Initiation of such processes is triggered on demand by switching on the light source used, and can be stopped or reverted when switching off, thus conferring a temporal control over the process. With the current technologies of light sources [40], such as flood lamps, LEDs, and lasers, precise spatial control over the illuminated regions is granted. Commercial 3D printing technologies based on photopolymerization, like SLA and DLP can already reliably reach resolutions of few tens of micrometers. Hence, it is possible to decide when and where a phototriggered reaction or process is activated, which could lead to increased complexity of the material responses. As an example, Palagi et al. [41] produced a nematically aligned LCE with pendant azobenzene moieties that could swim mimicking the symplectic and antiplectic metachrony of ciliate protozoa. The locomotion of an LCE thread was obtained by structuring the light field, with a digital micromirror device, into a travelling wave pattern formed of transversal rectangles moving along the thread main axis. Additionally, the nature of light, as an electromagnetic radiation, allows its physical properties as wavelength or polarization to be adjusted to the required needs. Materials can be engineered to react with a different motions or responses for each wavelength and responses can occur contemporarily. Lahikainen et al. [42] demonstrated the occurrence of non-reciprocal photomechanical actuation in LCEs embedding two different azobenzenes reacting respectively to 365 and 550 nm of wavelength for the *trans-cis* isomerization with reversible *cis-trans* under visible light illumination. The arrangement of the photoswitches and the spatiotemporal control over the illumination sources resulted in different complex trajectories of the tip of rectangular films. The control over the polarization's direction of the actuating wave also demonstrated to induce controlled movement owning to the optical properties of azobenzenes. Polydomain LC azofilms produced by Yu et al. [43] presented bending in the direction of the polarization since azobenzenes absorb light with polarization parallel to the molecule, but not light with orthogonal polarization [44].

With such interesting features, light represents a stimulus with enormous design potential. Functions of photoresponsive materials and devices are engineered intrinsically, by incorporating photoswitches into the material structure, and extrinsically, by designing and structuring of the light's spatio-temporal and physical properties. The three photoresponsive materials explored in this work represent mainly approaches of intrinsic design. The light used for the actuation, coming from an high pressure mercury flood lamp and wide angle LEDs, were not spatially structured (outside the rudimentary use of the photomask for cin-CNC composites) nor polarized. Mainly the temporal control was exerted. Already, these materials showed the concrete potential of 3D printed photoresponsive and adaptable devices composed of single materials. The large design freedom of each material approach allows them to be suitable for a large range of applications in which the occurrence of the photoresponses at room temperature, fast and reliable actuation times, and reversibility of the responses are desired.

4.2.2 Photoresponsive performances of 3D printed CNC nanocomposites

4.2.2.1 cin-CNC composites

Cellulose nanocrystals played the role of active reinforcement that allowed the 3D printing of devices and contributed to the photoresponses and the mechanical performances of the printed devices. Looking at the ability to photostiffen of cin-CNC composites, the active reinforcements tailor the mechanical properties forming covalent bonds with the polymer matrix, enhancing the stress-transfer from the matrix to the particles. The triggering time for such response to occur was studied up to 90 minutes and led to a 3.4 times increase in the elastic modulus of the composites with 15 wt% of cin-CNC. The reported times correspond to the kinetics of the cinnamate dimerization, reported also for other cinnamate based polymers [45]–[47], while the stiffening observed is in agreement with 2D photostiffening CNC composites reported by Biyani et al. [48], [49]. This work demonstrates that the 3D printing does not influence the photoresponsive behavior of the material, but it rather increases the design freedom of the finished part. The cinnamate chemistry of cin-CNC is the limiting factor for the triggering time. Faster photostiffening could be achieved and further improved with the use of different reactive groups, as observed from benzophenone modified CNC that react in 2 min instead of 90 min [48]. Nonetheless, cinnamate chemistry presents an advantaging potential with respect to benzophenones. Cinnamate cycloaddition is a reversible reaction that has already been exploited for 2D materials for actuation of self-healing [50] or for shape memory effect [51]. For our cin-CNC composites, the ability of crosslinking demonstrates potential for self-healing. With intimate contact between two unstiffened fragmented composites, it should be possible to actuate crosslinking at their interface, closing the crack. The current state of the research on these materials did not allow to see these results yet. With respect to the shape memory effect, despite the shape fixing ability could be demonstrated in Chapter 3.1 for our cin-CNC composites, the reversible reaction was unsuccessfully tested in a follow-up study. Under UVC illumination (up to 6h) our cin-CNC composites did not show recovery from the fixed deformed shape. The lack of response to UVC of our materials might arise from the combination of strong UVC absorption of cinnamate groups and the UVC absorption of the PUA, which would localize the photoresponse to the surface of the tested samples. However, according to the previous studies on cinnamate materials [50], [51] our method of introducing cinnamate derivatives onto the CNC surface and into the polymer matrix has the potential to produce 3D printable composites expressing both self-healing and shape memory responses. The new materials might be obtained by applying our method to a matrix presenting UVC transparency like silicone elastomers [52] and by investigating the concentration of cinnamate moieties onto the CNC surface and into the matrix allowing such effects to arise. A combination of shape memory and self-healing effects in a cin-CNC composite would be advantageous. The material could be shaped in devices that are used in stretched fixed temporary shapes. When a crack is initiated, the stored elastic energy could be released by UVC illumination, with the actuation of the shape memory effect. The shape recovery from the stretched configuration would automatically result in crack closure. Once the crack is closed the UVB illumination healing of the structure would happen allowing partial recovery of the mechanical properties. Despite the downside that this new system would heal only once, the combination of these effects would allow to increase the lifetime of the printed devices. Further investigations in this direction are recommended. Materials produced with our 3D printing method have the potential to be freely shaped into geometries and designs for efficient use of this shape-memory assisted self-healing for customized structural applications.

4.2.2.2 LCE/CNC composites

3D printing of LCE with CNC resulted in soft actuators with multiple responses to illumination: *shape changing* and photosoftening. With respect to the printed materials performances, an increased amount of CNC permitted to obtain faster responses upon illumination, most probably due to increased ink's viscosity that allows enhanced alignment of the particles [2] and the LC mesogens [52]. Further optimization of the *shape changing* response was observed when the CNC were modified with methacrylated groups. Faster responses and slightly bigger deformations arise due to several factors. The increase in the dispersion quality of the CNC improves printing quality. The CNC's ability to create covalent bonds with the LCE tailors the mechanical properties increasing both stiffness and strength. This leads to a bigger storage of elastic energy during the deformation, which is released during recovery of the initial shape. Two further factors that deserve deeper investigation might explain the observed improvement in the photoactuation. First, the covalent bonding of methaCNC with the LCE network ensures strong interfaces that enhance stress-transfer. Consequently, the LCE network might "pull" the particles during its deformation, improving the local motion of methaCNC and amplifying the LCE phase transition deformation [53], [54]. Second, the current LC phase might have been also modified by the different surface chemistry of methacrylated CNC, resulting in a different order or phase of the LC mesogens. These features bring a strong potential to tackle further the challenge of making renewable LCE and further underline the need of understanding CNC – LC mesogen interactions.

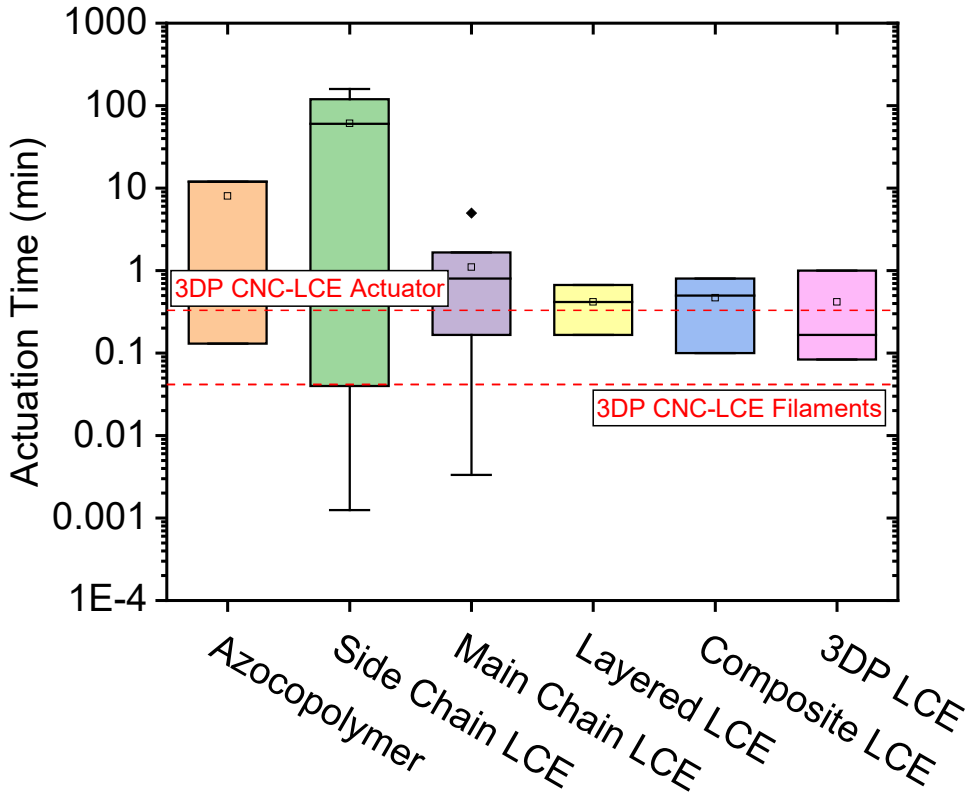

Figure 4.2-1 Comparison of actuation times of the different types of photomechanical LCE films. Data taken from [54]–[57], [60]–[81].

Comparing the performances of our LCE/methaCNC composite with the existing examples of 3D printed photoresponsive LCE is a complicated task since no standard is yet in place. The performances

of LCE are always reported in literature for different light intensities, different test setups and illumination sources, and for different properties. The bending angles achieved so far in our LCE/CNC composites are relatively small when compared to existing 2D LCE thin films. This is due to the presence of CNC and the thickness of the printed parts. Both factors contribute to decreasing the achievable deformation amplitude. CNC adds higher Young's moduli to our composites and decrease the relative concentration of LC mesogens. Hence, our materials require higher energy to achieve the deformation while they present a slightly smaller ability to generate such deformation. While, an increased thickness of LCE results in lower percentages of activated volume, due to the strong light absorption of azobenzenes. Current 3D printing of LCE approaches balance this last issue by printing LCE with main chain LC mesogens [55], [56] since they demonstrated larger actuated movements than side chain LCE (our materials). In our case, we opted for a side chain LCE because they present smectic and splayed phases that promote illumination orientation independent movements [57]. Another reason explaining a smaller bending observed in our materials might emerge from the dispersion of azobenzenes into the printed composites. Even though the doping process allows printing several layers of the materials in a single step and promotes a faster actuation [58], it still presents the drawback of having azobenzenes not being covalently attached to the polymer network nor to the particles. Azobenzenes that are not used as crosslinkers do not have the ability to achieve network pull-effects, i.e. the transfer of the photomechanical stress to the polymer network [54], [59]. Hence, the shrinking of dispersed azobenzene molecule during the *trans-cis* photoisomerization is not directly exerted on the polymer backbone of the LCE and act solely by creating disorder in the nematic LC phase, resulting in lower amplitudes of the bending.

Considering the actuation time of the different approaches applied for the formation of LCE with photomechanical ability, reported in literature so far, our materials lie in the faster actuation range (Figure 4.2-1). Deeper analysis of the photomechanical performances of the materials remains yet to be undertaken and standardized. The mainstream potential of a 3D printed LCE lies in the possibility to 3D print muscle-like prosthetics. As a consequence, a characterization of the work capability of our printed materials should be investigated as a function of the illumination power, as for instance carried out from Ceamanos et al. [55]. This investigation would allow to establish process and design parameters for the production of devices for real-world applications requiring force generation, such as muscle-like actuators and soft robots.

4.2.2.3 CNC-DR1 composites

CNC-DR1 were developed to confer photoresponsive features to polymer resins while allowing their processing by 3D printing. The example in Chapter 3.3 demonstrated that this goal was achieved. CNC-DR1 can confer to a polyurethane matrix a strong photosoftening (~50%) by harnessing the photothermal effect of DR1 and its increase in free volume during *trans-cis* photoisomerization. The actuation of the softening by illumination occurred in timescales of seconds, in agreement with what was observed for the LCE/CNC composites, and, as well, the response was completely reversible. As a secondary response, the CNC-DR1 isomerization could trigger the shape memory effect of the polyurethane matrix. This demonstrates the potential of CNC-DR1 to be used as photothermal reinforcing elements for other thermoplastic shape memory materials, such as PLA or PCL, where CNC already demonstrated the ability to improve by 20 % the shape fixity ratio [82]. This work demonstrates photosoftening effect in an arbitrarily chosen polymer matrix. However, a superficial choice of the matrix limits the possible responses to illumination that could be achieved with CNC-DR1. The engineering of a suitable matrix could in fact result in carefully optimized and diversified responses. Already, the introduction of CNC-DR1 in an LCE would allow both the 3D printing of composites with tailored mechanical properties and

the actuation of the *shape changing* ability to blue or green light. Comparing with the work on LCE/CNC composites in Chapter 3.2, the CNC-DR1 approach would allow to remove the azobenzene doping step and to reduce the use of solvents in the whole production process of LCE/CNC composites. In addition, covalently bonding DR1 to the CNC would avoid to have leaks of the dye, when the LCE is swollen in solvents where DR1 is soluble. This would render such composites more suitable for biomedical applications as implants and prosthetics. Another polymer matrix, could be engineered with oligomers bearing cyclodextrins leading to CNC-DR1 composites able to undergo gel-sol transitions upon illumination [83]. Thereby, enhanced recyclability could be obtained.

Looking from a wider perspective, CNC-DR1 present a feature that might promote the use of these active reinforcements to improve manufacturing of hierarchical materials with other 3D printing techniques such as SLA and DLP using vat polymerization. DR1 is a known azobenzene that undergo photoalignment and it is already used for LC alignment layers [44], [84], [85]. When linearly polarized light reaches these azobenzenes, they undergo *trans-cis-trans* isomerization until reaching a perpendicular alignment with the polarization direction, where they do not absorb light anymore. Owing to this property, there is the possibility to control remotely the alignment of the modified CNC without the use of shear. This would allow to obtain 3D printed high resolution parts with aligned particles without the use of magnetic fields [86]. When CNC-DR1 are dispersed in low viscosity resins, the isomerization of DR1 could be harnessed to control the position of the CNC leading to density gradients. Abid et al. [87] developed DR1 coated polymer nanoparticles that demonstrated controlled swimming from the light to the dark. Despite that preliminary experiments on photoalignment of CNC-DR1 into HEMA were not conclusive, the particles demonstrated the tendency to create density gradients when the light was focused on single locations (Figure 1.2-2).

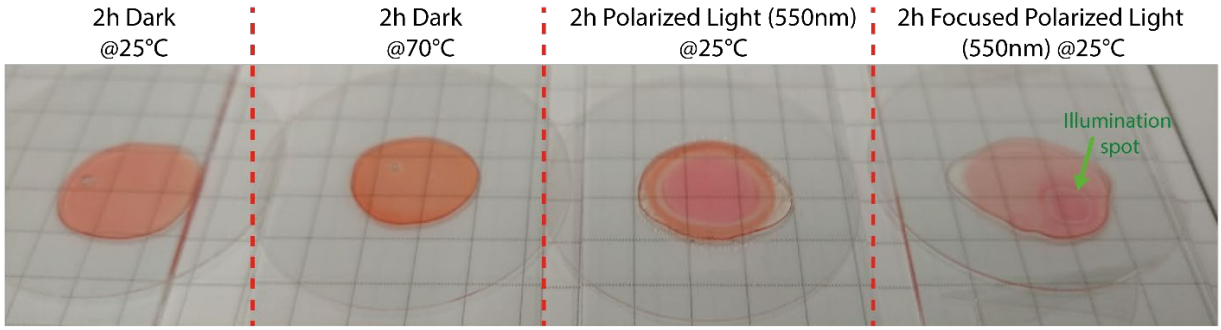

Figure 1.2-2 HEMA with 2 wt% CNC-DR1 samples illuminated with polarized light at 550 nm before UV curing. Focused light on the samples led to the creation of rings with particles that are more concentrated as indicated by the darker colour. All samples were polymerized with 10 minutes illumination with a 365 nm wavelength LED.

4.3 Limitations of 3D printed photoresponsive cellulose nanocomposites

The photoresponsive 3D printed cellulose nanocomposites developed in this thesis present a high degree of freedom and versatility in their design for tailoring geometry, mechanical properties and the light stimulated responses. However, these materials still suffer from some challenges related to their photoresponsive behaviors in view of real world applications.

The illumination of the samples is not homogeneous and depends on the light source applied. Lasers show a Gaussian distribution of power, while diffusing LEDs are not extraneous to power distribution inhomogeneities [88]. Consequently, the in-plane activation of the photoresponses is locally dependent

on the power distribution of the light source. With respect to out-of-plane light's power distribution, light penetrates materials with exponential decrease of its intensity according to Beer-Lambert law [89]. This limits the maximum printable sizes of efficient devices. For a given illumination set-up, printed materials with dimensions bigger than the actuated volume will not show an effective photoresponsive actuation. The activated volume will be mainly concentrated at the surface of the materials. The cin-CNC composites in Chapter 3.1 can overcome this limitation and be used to produce structures with bulk photostiffened domains, if selective illumination is applied every layer and the layer height doesn't surpass the effective light absorption volume, as shown by by Guzzi et al. [19]. But, the potential reversible reaction of cinnamate moieties would be highly limited at the surface of the final printed part, due to the high absorption of light in the UVC region, occurring in polymer matrices. With the same logic, the possibility to print LCE/CNC from Chapter 3.2 in devices with active parts composed of a stack of several layers remains an open challenge. In particular, azobenzene derivatives show a strong absorption coefficient which limits the light absorption to tens of microns [90], [91], originating hence the deformation gradient that promotes the LCE bending. Further decreasing the diameter of the printing nozzle could solve this issue and lead to complex deformations obtained by stacking layers with different filament alignments. But, the overall size of the 3D printed parts would still be limited. Using CNC-DR1 to produce photoresponsive materials (Chapter 3.3) shares the same maximum printing size limitations due to the strong absorption of DR1.

The wide availability of sunlight is an advantage of using light as a stimulus, since materials can be engineered to use directly this energy in their operation. At the same time, sunlight present a wide spectrum of wavelengths and the presence of UV and blue to green light could result in unwanted stimulation of our materials, depending on the application. The cin-CNC composites would photostiffen if not protected properly and the photopattern would disappear, leaving a single stiff domain. Instead, a structure composed of CNC-DR1 would undergo unwanted softening during the day and stiffening during the night. In fact, dark conditions are required to use these materials if the temporal control over the illumination is required. On the other hand, this constraint can be taken into account during the design of the active device. For instance, as demonstrated by the LCE/CNC actuator in Chapter 3.2, an actuator can be built to close an electric circuit either during the day or during the night. This allows limiting the operation of the circuit during one of these time spans.

Production of photoresponsive materials with low elastic moduli (few tens of MPa) and high chain mobility allowed demonstration of both their production and light activated performance. Despite that our materials are suitable for soft robotic, gripping and sensing applications, structural applications require hard and stiff smart materials. Solar panel structures, for instance could highly benefit from structural materials that can support their weight and move in order to allow the solar cell to automatically follow the sun. In particular, photoresponsive shape morphing of stiff and rigid materials is still a main challenge in the field, since increasing the Young modulus generally decreases the actuated deformation [92].

4.4 Towards future devices and applications

The development of technologies and methods allowing 3D printing of photoresponsive smart devices is still in its infancy and is mainly limited by the availability of printable stimuli responsive materials. These new photoactive materials, developed during this research, represent further progress in the evolution of the field. The introduction of CNC in the inks both allowed the DIW process and contributed to the tailoring of the mechanical properties of the printed structures, as well as, to the performances of

their photoresponses. As a result, our smart photoresponsive devices combine the geometric design freedom of additive manufacturing with light stimulated responses, showing a great potential for mechanically customized structures, actuators, vibration and shock absorbing applications.

The versatility of the demonstrated DIW approaches represent an important strength of this thesis. Highly customized shapes can be easily created with this additive manufacturing process and the control over the hierarchy of the structure permits to adapt and customize a single material device, not only, for a wide range of load cases and stimulation conditions, but also for a large palette of applications. Indeed, the tuneable mechanical properties, fast response times coupled with a non-contact stimulation make our cellulose composites very promising for room temperature applications in the soft robotics or biomedical fields for which high temperatures or contact stimulation can be harmful. The composites bearing cin-CNC could be used as structures for protection of sensors or also impact protection in soft robots or external prostheses. Spatial geometries and gradients of Young's modulus can be introduced varying the light intensity or the illumination time of the photopatterning, thus, creating functionally graded materials suitable for such applications [93]. As another example, our LCE/CNC composites have, as well, the potential to be used in energy harvesting applications and micro transportation where first concepts of light driven engines [94] and photo-induced locomotion [27] have already been proposed with 2D LCE films. Shaping such devices with DIW would simplify the production process, removing assembly steps that were previously required. Moreover, manufacturing of lightweight locomotive devices or soft robots can be achieved without incorporation of gears, hinges and hydraulic systems, since the material directly transforms the energy of light into motion.

The enormous freedom of device design, brought by the DIW, is not restrained to a single material. Multi-material printing is also an advantageous possibility of this process that allows two main features: introduction of particle density variations and production of multi-responsive devices. We observed for each type of composites that there is a range of CNC concentrations allowing DIW of self-standing structures. Thus, with a multi-material approach it is possible to integrate in the same part, inks with different solid contents (within the printable range), and control locally the concentration of particles in the final structure. This adds a further design parameter, for instance, for controlling and optimizing the mechanical properties of cin-CNC printed composites on top of other functional gradients [93]. Interestingly, it was observed in Chapter 3.2 that increasing the CNC content in the LCE promotes faster and larger movements. Printing of an actuating layer with a determined pattern variation of particle content is another way to control the actuated movements that should be explored. On the other hand, printing of multi-responsive devices and structures can be achieved by integrating more than one of our photoresponsive materials in a single structure. Based on the same polyurethane acrylate matrix, cin-CNC and CNC-DR1 composites present a strong chemical compatibility, ensuring also the covalent crosslinking between the different materials during curing. This allows for single step multi-material printing of devices with modular parts where the ability of photopatterning stiffened domains brings optimized tailoring of the mechanical properties while photosoftening or shape memory regions act as active, adaptable components. For instance, the main frame of the negative stiffness structures of Chapter 3.3 could be printed with photopatterned cin-CNC composites, while the active double curvature beams are composed of CNC-DR1 composites. The photoresponsive softening would hence influence the mechanical behavior of the structure only during loading in one in-plane direction (transverse to the active prismatic cell), while the stress in the other direction and the out-of-plane would be supported by the cin-CNC composite. With the same principle applied by Mao et al. [95] for the creation of sequential self-folding shape memory polymers, LCE/CNC could also be integrated in soft robotic cin-CNC/CNC-DR1 composite multi-material structures as hinges allowing, at the same time, the bending of determined device regions and the softening of others with the same illumination. With an attentive exploration of other

existing stimuli responsive printable materials, our materials could also easily be integrated in devices presenting multi-stimuli triggering multiple responses [96], [97].

The concepts and the manufacturing methods developed so far also provide strategies that can be applied for the production of new enlightened smart materials presenting intricate photoresponses. A possible development path might start from producing an ink with the introduction of cin-CNC and CNC-DR1 in an LCE matrix bearing also cinnamate groups. In this way, a 4D material could be printed similar to the examples demonstrated by Lu et al. [56]. The material would then exploit the photostiffening of cin-CNC/cinnamate groups at 365 nm of wavelength to be deformed and fixed in a particular geometry in order to store elastic energy into the system. Such energy could then increase the complexity of the movements actuated by the CNC-DR1, or amplify the shape change amplitude or the stress development upon illumination with light at 480 nm. Such adaptable behavior conferred by the photoresponses could allow for inspiration from plants movements [98] for the creation of efficient grippers, sensors and actuators that are non-sensitive to water. Another development could be directed toward the creation of fully renewable smart materials, by replacing the non renewable polyurethanes and silicones with other bio-based polymer matrices such as epoxies and urethanes obtained from biomass [99], [100].

The hierarchical organization demonstrated in our works with the chemical gradients of cin-CNC, the alignment of anisotropic CNC and organization of LC could be used to promote the understanding of microstructure functions. By modeling and emulating biological microorganisms and plants, it would be possible to study and deepen the understanding on the design of their structure, their organization, as well as the related movements. Biological hierarchical materials such as stomatopod dactyl club [101], [102] or spider fangs [103] could be analyzed numerically and the simulated results could be validated by applying a combination of self-assembly and 3D printing for the production of devices with the correspondent hierarchical features. This would allow to extract the main general design principles of the materials and to apply these findings to engineer new materials and devices with outstanding adaptable properties.

In summary, the materials presented in this thesis and the developed strategies of manufacturing processes contribute to the development of 3D printing technologies, and have the potential to further expand the printable material market [104], [105]. The freedom and versatility in the design of these materials is an asset brought by DIW that confers ease of manufacturing, fast prototyping and production of devices and structures with custom and personalized geometries. These features reduce the amount of time consuming assembly steps and the material waste, hence, decreasing manufacturing costs. The large range of possible applications of our materials demonstrates the value of such approaches and will motivate the spreading of our materials into the market. Moreover, by substituting and decreasing the amount of synthetic polymers, originating from non-renewable sources, with the abundant cellulose nanocrystals a first step toward sustainable development of photoresponsive smart materials was achieved.

4.5 References

[1] G. Siqueira *et al.*, "Cellulose Nanocrystal Inks for 3D Printing of Textured Cellular Architectures," *Adv. Funct. Mater.*, vol. 27, no. 12, 2017, doi: 10.1002/adfm.201604619.

[2] M. K. Hausmann *et al.*, "Dynamics of Cellulose Nanocrystal Alignment during 3D Printing," *ACS Nano*, vol. 12, no. 7, pp. 6926–6937, 2018, doi: 10.1021/acsnano.8b02366.

[3] M. K. Hausmann *et al.*, "Complex-Shaped Cellulose Composites Made by Wet Densification of 3D Printed Scaffolds," *Adv. Funct. Mater.*, vol. 30, no. 4, p. 1904127, Jan. 2020, doi: 10.1002/adfm.201904127.

[4] D. Rus and M. T. Tolley, "Design, fabrication and control of soft robots," *Nature*, vol. 521, no. 7553. Nature Publishing Group, pp. 467–475, 27-May-2015, doi: 10.1038/nature14543.

[5] J. Shojaeiarani, D. S. Bajwa, and S. Chanda, "Cellulose nanocrystal based composites: A review," *Composites Part C: Open Access*, vol. 5. Elsevier B.V., p. 100164, 01-Jul-2021, doi: 10.1016/j.jcomc.2021.100164.

[6] H. Kargarzadeh *et al.*, "Recent developments on nanocellulose reinforced polymer nanocomposites: A review," *Polymer*, vol. 132. Elsevier Ltd, pp. 368–393, 06-Dec-2017, doi: 10.1016/j.polymer.2017.09.043.

[7] Y. Wu *et al.*, "Characterization of an antimicrobial poly(lactic acid) film prepared with poly(ε -caprolactone) and thymol for active packaging," *Polym. Adv. Technol.*, vol. 25, no. 9, pp. 948–954, Sep. 2014, doi: 10.1002/pat.3332.

[8] S. Chanda and D. S. Bajwa, "A review of current physical techniques for dispersion of cellulose nanomaterials in polymer matrices," *Reviews on Advanced Materials Science*, vol. 60, no. 1. Walter de Gruyter GmbH, pp. 325–341, 01-Jan-2021, doi: 10.1515/rams-2021-0023.

[9] M. Girard, D. Vidal, F. Bertrand, J. R. Tavares, and M. C. Heuzey, "Evidence-based guidelines for the ultrasonic dispersion of cellulose nanocrystals," *Ultrason. Sonochem.*, vol. 71, p. 105378, Mar. 2021, doi: 10.1016/j.ultsonch.2020.105378.

[10] M. Latif, Y. Jiang, B. Kumar, J. M. Song, H. C. Cho, and J. Kim, "High Content Nanocellulose 3D-Printed and Esterified Structures with Strong Interfacial Adhesion, High Mechanical Properties, and Shape Fidelity," *Adv. Mater. Interfaces*, p. 2200280, May 2022, doi: 10.1002/admi.202200280.

[11] J. E. Smay, J. Cesarano, and J. A. Lewis, "Colloidal inks for directed assembly of 3-D periodic structures," *Langmuir*, vol. 18, no. 14, pp. 5429–5437, Jul. 2002, doi: 10.1021/la0257135.

[12] S. Sultan and A. P. Mathew, "3D printed scaffolds with gradient porosity based on a cellulose nanocrystal hydrogel," *Nanoscale*, vol. 10, no. 9, pp. 4421–4431, Mar. 2018, doi: 10.1039/c7nr08966j.

[13] D. Wang, D. Chen, and Z. Chen, "Recent Progress in 3D Printing of Bioinspired Structures," *Front. Mater.*, vol. 7, p. 286, Nov. 2020, doi: 10.3389/fmats.2020.00286.

[14] A. R. Studart, "Additive manufacturing of biologically-inspired materials," *Chem. Soc. Rev.*, vol. 45, no. 2, pp. 359–376, Jan. 2016, doi: 10.1039/c5cs00836k.

[15] M. K. Hausmann *et al.*, "Dynamics of Cellulose Nanocrystal Alignment," *ACS Nano*, vol. 12, pp. 6926–6937, 2018, doi: 10.1021/acsnano.8b02366.

[16] C. Zhang, X. Lu, G. Fei, Z. Wang, H. Xia, and Y. Zhao, "4D Printing of a Liquid Crystal Elastomer with a Controllable Orientation Gradient," *ACS Appl. Mater. Interfaces*, vol. 11, no. 47, pp. 44774–44782, Nov. 2019, doi: 10.1021/acsami.9b18037.

[17] Z. Wang, Z. Wang, Y. Zheng, Q. He, Y. Wang, and S. Cai, "Three-dimensional printing of functionally graded liquid crystal elastomer," *Sci. Adv.*, vol. 6, no. 39, p. eabc0034, Sep. 2020, doi: 10.1126/sciadv.abc0034.

[18] D. Kokkinis, F. Bouville, and A. R. Studart, "3D Printing of Materials with Tunable Failure via Bioinspired Mechanical Gradients," *Adv. Mater.*, vol. 30, no. 19, p. 1705808, May 2018, doi: 10.1002/adma.201705808.

[19] E. A. Guzzi *et al.*, "Hierarchical biomaterials via photopatterning-enhanced direct ink writing," *Biofabrication*, vol. 13, no. 4, p. 044105, Oct. 2021, doi: 10.1088/1758-5090/ac212f.

[20] I. Valizadeh, A. Al Aboud, E. Dörsam, and O. Weeger, "Tailoring of functionally graded hyperelastic materials via grayscale mask stereolithography 3D printing," *Addit. Manuf.*, vol. 47, p. 102108, Nov. 2021, doi: 10.1016/j.addma.2021.102108.

[21] X. Kuang *et al.*, "Grayscale digital light processing 3D printing for highly functionally graded materials," *Sci. Adv.*, vol. 5, no. 5, 2019, doi: 10.1126/sciadv.aav5790.

[22] J. Liu, Y. Gao, H. Wang, R. Poling-Skutvik, C. O. Osuji, and S. Yang, "Shaping and Locomotion of Soft Robots Using Filament Actuators Made from Liquid Crystal Elastomer–Carbon Nanotube Composites," *Adv. Intell. Syst.*, vol. 2, no. 6, p. 1900163, Jun. 2020, doi: 10.1002/aisy.201900163.

[23] H. Kang, J. C. Lee, B. U. Nam, and J. W. Bae, "Liquid crystal alignment behavior on transparent cellulose films," *RSC Adv.*, vol. 5, no. 48, pp. 38654–38659, Apr. 2015, doi: 10.1039/c5ra03713a.

[24] A. Kotikian, R. L. Truby, J. W. Boley, T. J. White, and J. A. Lewis, "3D Printing of Liquid Crystal Elastomeric Actuators with Spatially Programed Nematic Order," *Adv. Mater.*, vol. 30, no. 10, p. 1706164, Mar. 2018, doi: 10.1002/adma.201706164.

[25] E. C. Davidson, A. Kotikian, S. Li, J. Aizenberg, and J. A. Lewis, "3D Printable and Reconfigurable Liquid Crystal Elastomers with Light-Induced Shape Memory via Dynamic Bond Exchange," *Adv. Mater.*, vol. 32, no. 1, pp. 1–6, 2020, doi: 10.1002/adma.201905682.

[26] J. A. H. P. Sol, H. Sentjens, L. Yang, N. Grossiord, A. P. H. J. Schenning, and M. G. Debije, "Anisotropic Iridescence and Polarization Patterns in a Direct Ink Written Chiral Photonic Polymer," *Adv. Mater.*, vol. 33, no. 39, p. 2103309, Oct. 2021, doi: 10.1002/adma.202103309.

[27] A. H. Gelebart *et al.*, "Making waves in a photoactive polymer film," *Nature*, vol. 546, no. 7660, pp. 632–636, 2017, doi: 10.1038/nature22987.

[28] P. Kaur *et al.*, "Nanocellulose: Resources, Physio-Chemical Properties, Current Uses and Future Applications," *Frontiers in Nanotechnology*, vol. 3. Frontiers Media S.A., p. 82, 15-Nov-2021, doi: 10.3389/fnano.2021.747329.

[29] D. Trache *et al.*, "Nanocellulose: From Fundamentals to Advanced Applications," *Frontiers in Chemistry*, vol. 8. Frontiers Media S.A., p. 392, 06-May-2020, doi: 10.3389/fchem.2020.00392.

[30] F. Piccinno, R. Hischier, S. Seeger, and C. Som, "Predicting the environmental impact of a future nanocellulose production at industrial scale: Application of the life cycle assessment scale-up framework," *J. Clean. Prod.*, vol. 174, pp. 283–295, Jan. 2018, doi: 10.1016/j.jclepro.2017.10.226.

[31] F. Foroughi, E. Rezvani Ghomi, F. M. Dehaghi, R. Borayek, and S. Ramakrishna, "A Review on the Life Cycle Assessment of Cellulose: From Properties to the Potential of Making It a Low Carbon Material," 2021, doi: 10.3390/ma14040714.

[32] D. Mohan, Z. K. Teong, A. N. Bakir, M. S. Sajab, and H. Kaco, "Extending cellulose-based polymers application in additive manufacturing technology: A review of recent approaches," *Polymers*, vol. 12, no. 9. MDPI AG, 01-Sep-2020, doi: 10.3390/POLYM12091876.

[33] D. R. Joshi and N. Adhikari, "An Overview on Common Organic Solvents and Their Toxicity," *J. Pharm. Res. Int.*, vol. 28, no. 3, pp. 1–18, Jun. 2019, doi: 10.9734/jpri/2019/v28i330203.

[34] J. H. Lee, R. K. Prud'homme, and I. A. Aksay, "Cure depth in photopolymerization: Experiments and theory," 2001.

[35] S. C. Ligon, B. Husár, H. Wutzel, R. Holman, and R. Liska, "Strategies to reduce oxygen inhibition in photoinduced polymerization," *Chemical Reviews*, vol. 114, no. 1. American Chemical Society, pp. 577–589, 08-Jan-2014, doi: 10.1021/cr3005197.

[36] M. Kathan and S. Hecht, "Photoswitchable molecules as key ingredients to drive systems away from the global thermodynamic minimum," *Chemical Society Reviews*, vol. 46, no. 18. Royal Society of Chemistry, pp. 5536–5550, 21-Sep-2017, doi: 10.1039/c7cs00112f.

[37] M. M. Russew and S. Hecht, "Photoswitches: From molecules to materials," *Adv. Mater.*, vol. 22, no. 31, pp. 3348–3360, 2010, doi: 10.1002/adma.200904102.

[38] A. Goulet-Hanssens, F. Eisenreich, and S. Hecht, "Enlightening Materials with Photoswitches," *Adv. Mater.*, vol. 32, no. 20, p. 1905966, May 2020, doi: 10.1002/adma.201905966.

[39] S. Chatani, C. J. Kloxin, and C. N. Bowman, "The power of light in polymer science: photochemical processes to manipulate polymer formation, structure, and properties," *Polym. Chem.*, vol. 5, no. 7, p. 2187, 2014, doi: 10.1039/c3py01334k.

[40] S. Kitsinelis, *Light Sources. Technologies and Applications*. 2011.

[41] S. Palagi *et al.*, "Structured light enables biomimetic swimming and versatile locomotion of photoresponsive soft microrobots," *Nat. Mater.*, vol. 15, no. 6, pp. 647–653, Jun. 2016, doi: 10.1038/nmat4569.

[42] M. Lahikainen, H. Zeng, and A. Priimagi, "Design principles for non-reciprocal photomechanical actuation †," 2020, doi: 10.1039/d0sm00624f.

[43] Y. Yu, M. Nakano, and T. Ikeda, "Directed bending of a polymer film by light," *Nature*, vol. 425, no. 6954, pp. 145–145, Sep. 2003, doi: 10.1038/425145a.

[44] O. Yaroshchuk and Y. Reznikov, "Photoalignment of liquid crystals: Basics and current trends," *J. Mater. Chem.*, vol. 22, no. 2, pp. 286–300, Jan. 2012, doi: 10.1039/c1jm13485j.

[45] L. Wu, C. Jin, and X. Sun, "Synthesis, Properties, and Light-Induced Shape Memory Effect of Multiblock Polyesterurethanes Containing Biodegradable Segments and Pendant Cinnamamide Groups," *Biomacromolecules*, vol. 12, no. 1, pp. 235–241, Jan. 2011, doi: 10.1021/bm1012162.

[46] H. Du and J. Zhang, "The synthesis of poly(vinyl cinnamates) with light-induced shape fixity properties," *Sensors Actuators, A Phys.*, vol. 179, pp. 114–120, 2012, doi: 10.1016/j.sna.2012.02.001.

[47] D. Tunc, C. Le Coz, M. Alexandre, P. Desbois, P. Lecomte, and S. Carlotti, "Reversible cross-linking of aliphatic polyamides bearing thermo- and photoresponsive cinnamoyl moieties," *Macromolecules*, vol. 47, no. 23, pp. 8247–8254, 2014, doi: 10.1021/ma502083p.

[48] M. V. Biyani, M. Jorfi, C. Weder, and E. J. Foster, "Light-stimulated mechanically switchable, photopatternable cellulose nanocomposites," *Polym. Chem.*, vol. 5, no. 19, pp. 5716–5724, 2014, doi: 10.1039/c4py00487f.

[49] M. V. Biyani, C. Weder, and E. J. Foster, "Photoswitchable nanocomposites made from coumarin-functionalized cellulose nanocrystals," *Polym. Chem.*, vol. 5, no. 18, pp. 5501–5508, Sep. 2014, doi: 10.1039/c4py00486h.

[50] P. Sinha Roy *et al.*, "Bio-based photo-reversible self-healing polymer designed from lignin," *Green Chem.*, vol. 23, no. 24, pp. 10050–10061, Dec. 2021, doi: 10.1039/d1gc02957f.

[51] A. Lendlein, H. Jiang, O. Jünger, and R. Langer, "Light-induced shape-memory polymers," *Nature*, vol. 434, pp. 879–882, 2005, doi: 10.1038/nature03438.1.

[52] A. E. Özçam, K. Efimenko, and J. Genzer, "Effect of ultraviolet/ozone treatment on the surface and bulk properties of poly(dimethyl siloxane) and poly(vinylmethyl siloxane) networks," *Polymer (Guildf).*, vol. 55, no. 14, pp. 3107–3119, Jun. 2014, doi: 10.1016/j.polymer.2014.05.027.

[53] M. del Pozo, J. A. H. P. Sol, A. P. H. J. Schenning, and M. G. Debije, "4D Printing of Liquid Crystals: What's Right for Me?," *Advanced Materials*, vol. 34, no. 3. John Wiley and Sons Inc, p. 2104390, 01-Jan-2022, doi: 10.1002/adma.202104390.

[54] L. Braun, T. Linder, T. Hessberger, and R. Zentel, "Influence of a Crosslinker Containing an Azo Group on the Actuation Properties of a Photoactuating LCE System," *Polymers (Basel).*, vol. 8, no. 12, p. 435, Dec. 2016, doi: 10.3390/polym8120435.

[55] M. Pilz Da Cunha, E. A. J. Van Thoor, M. G. Debije, D. J. Broer, and A. P. H. J. Schenning, "Unravelling the photothermal and photomechanical contributions to actuation of azobenzene-doped liquid crystal polymers in air and water," *J. Mater. Chem. C*, vol. 7, no. 43, pp. 13502–13509, Nov. 2019, doi: 10.1039/c9tc04440j.

[56] H. Finkelmann, E. Nishikawa, G. G. Pereira, and M. Warner, "A New Opto-Mechanical Effect in Solids," *Phys. Rev. Lett.*, vol. 87, no. 1, 2001, doi: 10.1103/PhysRevLett.87.015501.

[57] C. L. Van Oosten, C. W. M. Bastiaansen, and D. J. Broer, "Printed artificial cilia from liquid-crystal network actuators modularly driven by light," *Nat. Mater.*, vol. 8, no. 8, pp. 677–682, 2009, doi: 10.1038/nmat2487.

[58] W. Wang, X. Sun, W. Wu, H. Peng, and Y. Yu, "Photoinduced Deformation of Crosslinked Liquid-Crystalline Polymer Film Oriented by a Highly Aligned Carbon Nanotube Sheet," *Angew. Chemie Int. Ed.*, vol. 51, no. 19, pp. 4644–4647, May 2012, doi: 10.1002/anie.201200723.

[59] S. Guo, K. Matsukawa, T. Miyata, T. Okubo, K. Kuroda, and A. Shimojima, "Photoinduced Bending of Self-Assembled Azobenzene-Siloxane Hybrid," *J. Am. Chem. Soc.*, vol. 137, no. 49, pp. 15434–15440, 2015, doi: 10.1021/jacs.5b06172.

[60] T. Ube, K. Minagawa, and T. Ikeda, "Interpenetrating polymer networks of liquid-crystalline azobenzene polymers and poly(dimethylsiloxane) as photomobile materials," *Soft Matter*, vol. 13, no. 35, pp. 5820–5823, 2017, doi: 10.1039/C7SM01412K.

[61] M. Kondo *et al.*, "Photomechanical properties of azobenzene liquid-crystalline elastomers," *Liq. Cryst.*, vol. 36, no. 10–11, pp. 1289–1293, 2009, doi: 10.1080/02678290903138711.

[62] M. Bi *et al.*, "Photo actuation performance of nanotube sheet incorporated azobenzene crosslinked liquid crystalline polymer nanocomposite," *Polymers (Basel).*, vol. 11, no. 4, 2019, doi: 10.3390/polym11040735.

[63] T. Ube, K. Takado, and T. Ikeda, "Photomobile materials with interpenetrating polymer networks composed of liquid-crystalline and amorphous polymers," *J. Mater. Chem. C*, vol. 3, no. 31, pp. 8006–8009, Aug. 2015, doi: 10.1039/c5tc01489a.

[64] H.-K. Kim *et al.*, "Reversible Photo-Mechanical Switching Behavior of Azobenzene-Containing Semi-Interpenetrating Network under UV and Visible Light Irradiation," *Macromol. Chem. Phys.*, vol. 206, no. 20, pp. 2106–2111, Oct. 2005, doi: 10.1002/macp.200500241.

[65] M. Camacho-Lopez, H. Finkelmann, P. Palffy-Muhoray, and M. Shelley, "Fast liquid-crystal elastomer swims into the dark," *Nat. Mater.*, vol. 3, no. 5, pp. 307–310, 2004, doi: 10.1038/nmat1118.

[66] C. Li, C. W. Lo, D. Zhu, C. Li, Y. Liu, and H. Jiang, "Synthesis of a photoresponsive liquid-crystalline polymer containing azobenzene," *Macromol. Rapid Commun.*, vol. 30, no. 22, pp. 1928–1935, 2009, doi: 10.1002/marc.200900421.

[67] J. Cviklinski, A. R. Tajbakhsh, and E. M. Terentjev, "UV isomerisation in nematic elastomers as a route to photo-mechanical transducer," *Eur. Phys. J. E*, vol. 9, no. 5, pp. 427–434, 2002, doi: 10.1140/epje/i2002-10095-y.

[68] K. M. Lee, D. H. Wang, H. Koerner, R. A. Vaia, L.-S. Tan, and T. J. White, "Photomechanical Response of Pre-strained Azobenzene-Functionalized Polyimide Materials," *Macromol. Chem. Phys.*, vol. 214, no. 11, pp. 1189–1194, Jun. 2013, doi: 10.1002/macp.201200340.

[69] D. E. Hagaman, S. Leist, J. Zhou, and H. F. Ji, "Photoactivated Polymeric Bilayer Actuators Fabricated via 3D Printing," *ACS Appl. Mater. Interfaces*, vol. 10, no. 32, pp. 27308–27315, Aug. 2018, doi: 10.1021/acsami.8b08503.

[70] L. Ceamanos, Z. Kahveci, M. Lopez-Valdeolivas, D. Liu, D. J. Broer, and C. Sanchez-Somolinos, "Four-dimensional printed liquid crystalline elastomer actuators with fast photoinduced mechanical response toward light-driven robotic functions," *ACS Appl. Mater. Interfaces*, vol. 12, no. 39, pp. 44195–44204, Sep. 2020, doi: 10.1021/acsami.0c13341.

[71] X. Lu *et al.*, "4D-Printing of Photoswitchable Actuators," no. 10, Mar. 2021, Accessed: 23-Apr-2021. [Online]. Available: https://onlinelibrary.wiley.com/doi/10.1002/ange.202012618.

[72] O. M. Wani, H. Zeng, and A. Priimagi, "A light-driven artificial flytrap," *Nat. Commun.*, vol. 8, no. 1, pp. 1–7, May 2017, doi: 10.1038/ncomms15546.

[73] C. L. Van Oosten, K. D. Harris, C. W. M. Bastiaansen, and D. J. Broer, "Glassy photomechanical liquid-crystal network actuators for microscale devices ⋆," *Eur. Phys. J. E*, vol. 23, pp. 329–336, 2007, doi: 10.1140/epje/i2007-10196-1.

[74] A. Sánchez-Ferrer, A. Merekalov, and H. Finkelmann, "Opto-Mechanical Effect in Photoactive Nematic Side-Chain Liquid-Crystalline Elastomers," *Macromol. Rapid Commun.*, vol. 32, no. 8, pp. 671–678, Apr. 2011, doi: 10.1002/marc.201100005.

[75] A. Sánchez-Ferrer and H. Finkelmann, "Opto-mechanical effect in photoactive nematic main-chain liquid-crystalline elastomers," *Soft Matter*, vol. 9, no. 18, pp. 4621–4627, May 2013, doi: 10.1039/c3sm27341e.

[76] T. Ikeda, M. Nakano, Y. Yu, O. Tsutsumi, and A. Kanazawa, "Anisotropic Bending and Unbending Behavior of Azobenzene Liquid-Crystalline Gels by Light Exposure," *Adv. Mater.*, vol. 15, no. 3, pp. 201–205, Feb. 2003, doi: 10.1002/adma.200390045.

[77] M. Kondo *et al.*, "Effect of concentration of photoactive chromophores on photomechanical properties of crosslinked azobenzene liquid-crystalline polymers," *J. Mater. Chem.*, vol. 20, no. 1, pp. 117–122, Dec. 2010, doi: 10.1039/b917342k.

[78] F. Cheng, Y. Zhang, R. Yin, and Y. Yu, "Visible light induced bending and unbending behavior of crosslinked liquid-crystalline polymer films containing azotolane moieties," *J. Mater. Chem.*, vol. 20, no. 23, pp. 4888–4896, Jun. 2010, doi: 10.1039/b926903g.

[79] T. Yoshino, M. Kondo, J. Mamiya, M. Kinoshita, Y. Yu, and T. Ikeda, "Three-Dimensional Photomobility of Crosslinked Azobenzene Liquid-Crystalline Polymer Fibers," *Adv. Mater.*, vol. 22, no. 12, pp. 1361–1363, Mar. 2010, doi: 10.1002/adma.200902879.

[80] J. Lv, W. Wang, W. Wu, and Y. Yu, "A reactive azobenzene liquid-crystalline block copolymer as a promising material for practical application of light-driven soft actuators," *J. Mater. Chem. C*, vol. 3, no. 26, pp. 6621–6626, Jun. 2015, doi: 10.1039/C5TC00595G.

[81] M. Camacho-Lopez, H. Finkelmann, P. Palffy-Muhoray, and M. Shelley, "Fast liquid-crystal elastomer swims into the dark," *Nat. Mater.*, vol. 3, no. 5, pp. 307–310, 2004, doi: 10.1038/nmat1118.

[82] R. C. P. Verpaalen, M. Pilz da Cunha, T. A. P. Engels, M. G. Debije, and A. P. H. J. Schenning, "Liquid Crystal Networks on Thermoplastics: Reprogrammable Photo-Responsive Actuators," *Angew. Chemie Int. Ed.*, vol. 59, no. 11, pp. 4532–4536, Mar. 2020, doi: 10.1002/anie.201915147.

[83] I. Navarro-Baena, J. M. Kenny, and L. Peponi, "Thermally-activated shape memory behaviour of bionanocomposites reinforced with cellulose nanocrystals," *Cellulose*, vol. 21, no. 6, pp. 4231–4246, Dec. 2014, doi: 10.1007/s10570-014-0446-5.

[84] Y. Kim, D. Jeong, V. V. Shinde, Y. Hu, C. Kim, and S. Jung, "Azobenzene-grafted carboxymethyl cellulose hydrogels with photo-switchable, reduction-responsive and self-healing properties for a controlled drug release system," *Int. J. Biol. Macromol.*, vol. 163, pp. 824–832, Nov. 2020, doi: 10.1016/j.ijbiomac.2020.07.071.

[85] A. R. K. Nassrah, I. Jánossy, and T. Tóth-Katona, "Photoalignment at the nematic liquid crystal–polymer interface: The importance of the liquid crystalline molecular structure," *J. Mol. Liq.*, vol. 312, p. 113309, Aug. 2020, doi: 10.1016/j.molliq.2020.113309.

[86] T. Tóth-Katona and I. Jánossy, "Photoalignment at the nematic liquid crystal-polymer interface: Experimental evidence of three-dimensional reorientation," *J. Mol. Liq.*, vol. 285, pp. 323–329, Jul. 2019, doi: 10.1016/j.molliq.2019.04.074.

[87] D. Kokkinis, M. Schaffner, and A. R. Studart, "Multimaterial magnetically assisted 3D printing of composite materials," *Nat. Commun.*, vol. 6, Oct. 2015, doi: 10.1038/ncomms9643.

[88] J. P. Abid *et al.*, "Light-driven directed motion of azobenzene-coated polymer nanoparticles in an aqueous medium," *Langmuir*, vol. 27, no. 13, pp. 7967–7971, Jul. 2011, doi: 10.1021/la200682p.

[89] M. Herath, J. Epaarachchi, M. Islam, L. Fang, and J. Leng, "Light activated shape memory polymers and composites: A review," *European Polymer Journal*, vol. 136. Elsevier Ltd, p. 109912, 05-Aug-2020, doi: 10.1016/j.eurpolymj.2020.109912.

[90] R. V. Beblo and L. M. Weiland, "Light activated shape memory polymer characterization," *J. Appl. Mech. Trans. ASME*, vol. 76, no. 1, pp. 1–8, Jan. 2009, doi: 10.1115/1.2999447.

[91] T. Ikeda, J. Mamiya, and Y. Yu, "Photomechanics of Liquid-Crystalline Elastomers and Other Polymers," *Angew. Chemie Int. Ed.*, vol. 46, no. 4, pp. 506–528, Jan. 2007, doi: 10.1002/anie.200602372.

[92] Z. Mahimwalla, K. G. Yager, J. I. Mamiya, A. Shishido, A. Priimagi, and C. J. Barrett, *Azobenzene photomechanics: Prospects and potential applications*, vol. 69, no. 8. 2012.

[93] M. Pilz Da Cunha, M. G. Debije, and A. P. H. J. Schenning, "Bioinspired light-driven soft robots based on liquid crystal polymers," *Chemical Society Reviews*, vol. 49, no. 18. Royal Society of Chemistry, pp. 6568–6578, 21-Sep-2020, doi: 10.1039/d0cs00363h.

[94] Z. Liu, M. A. Meyers, Z. Zhang, and R. O. Ritchie, "Functional gradients and heterogeneities in biological materials: Design principles, functions, and bioinspired applications," *Progress in Materials Science*, vol. 88. Elsevier Ltd, pp. 467–498, 01-Jul-2017, doi: 10.1016/j.pmatsci.2017.04.013.

[95] M. Yamada *et al.*, "Photomobile polymer materials: Towards light-driven plastic motors," *Angew. Chemie - Int. Ed.*, vol. 47, no. 27, pp. 4986–4988, 2008, doi: 10.1002/anie.200800760.

[96] Y. Mao, K. Yu, M. S. Isakov, J. Wu, M. L. Dunn, and H. Jerry Qi, "Sequential Self-Folding Structures by 3D Printed Digital Shape Memory Polymers," *Sci. Rep.*, vol. 5, no. 1, pp. 1–12, Sep. 2015, doi: 10.1038/srep13616.

[97] M. Nadgorny and A. Ameli, "Functional Polymers and Nanocomposites for 3D Printing of Smart Structures and Devices," *ACS Appl. Mater. Interfaces*, vol. 10, no. 21, pp. 17489–17507, 2018, doi: 10.1021/acsami.8b01786.

[98] M. Rafiee, R. D. Farahani, and D. Therriault, "Multi-Material 3D and 4D Printing: A Survey," *Adv. Sci.*, vol. 7, no. 12, p. 1902307, Jun. 2020, doi: 10.1002/advs.201902307.

[99] H. Mano and M. Hasebe, "Rapid movements in plants," *J. Plant Res.*, vol. 134, no. 1, pp. 3–17, Jan. 2021, doi: 10.1007/s10265-020-01243-7.

[100] H. Li, Y. Liang, P. Li, and C. He, "Conversion of biomass lignin to high-value polyurethane: A review," *Journal of Bioresources and Bioproducts*, vol. 5, no. 3. KeAi Communications Co., pp. 163–179, 01-Aug-2020, doi: 10.1016/j.jobab.2020.07.002.

[101] S. Hirose, T. Hatakeyama, and H. Hatakeyama, "Novel Epoxy Resins Derived from Biomass Components," *Procedia Chem.*, vol. 4, pp. 26–33, Jan. 2012, doi: 10.1016/j.proche.2012.06.004.

[102] J. C. Weaver *et al.*, "The stomatopod dactyl club: A formidable damage-tolerant biological hammer," *Science (80-.).*, vol. 336, no. 6086, pp. 1275–1280, Jun. 2012, doi: 10.1126/science.1218764.

[103] L. K. Grunenfelder *et al.*, "Ecologically Driven Ultrastructural and Hydrodynamic Designs in Stomatopod Cuticles," *Adv. Mater.*, vol. 30, no. 9, p. 1705295, Mar. 2018, doi: 10.1002/adma.201705295.

[104] B. Bar-On, F. G. Barth, P. Fratzl, and Y. Politi, "Multiscale structural gradients enhance the biomechanical functionality of the spider fang," *Nat. Commun.*, vol. 5, no. 1, pp. 1–8, May 2014, doi: 10.1038/ncomms4894.

[105] V. Butorin, *Economic Consequences of 3D Printing*. 2014.

[106] C. Weller, R. Kleer, and F. T. Piller, “Economic implications of 3D printing: Market structure models in light of additive manufacturing revisited,” *Int. J. Prod. Econ.*, vol. 164, pp. 43–56, Jun. 2015, doi: 10.1016/j.ijpe.2015.02.020.

5 Outlook

The development of our 3D printed photoresponsive materials bears huge potential for biomedicine, soft robotics, sensing and actuators as future applications. Despite the significant contribution of this study going all the way from the development of the basic concepts to the fabrication of first demonstrators, there are several possibilities to continue this exciting research. Here, three main research paths are proposed as ways to continue and further improve the phenomena and processes discussed in this thesis. These three research topics are:

1) Optimization of processes and chemistries toward fully renewable materials.
2) Investigation on CNC – LC mesogen arrangements and crystalline phases.
3) Technology transfer toward vat polymerization 3D printing techniques with aligned nanoparticles.

Optimization of processes and chemistries toward fully renewable materials. In the current context, moving toward increased renewability and sustainability to minimize the dependence on petroleum based polymers represents an important goal. This work demonstrated the production of smart photoresponsive materials based on cellulose nanocrystals. As main challenge, the chemical procedures employed in this work still rely on the use of organic solvents as DMF and acetone. As an alternative, Cyrene, a dipolar aprotic solvent presenting low toxicity, has emerged as a suitable candidate to replace DMF and other dipolar solvents like DMSO [1]. Synthetized from cellulose, Cyrene is a renewable and sustainable option that already demonstrated to be a suitable medium for carbon-carbon reactions, nucleophilic substitutions, step growth polymerizations and synthesis of substituted amides and ureas [2]. The high miscibility of Cyrene in water could allow easy separation of reaction products and a subsequent recovery of the solvent by water distillation. The chemical reactions for the production of cin-CNC and CNC-DR1 could be occurring in Cyrene, broadening the use of this green alternative. However, the incompatibility of Cyrene with strong oxidizing/reducing agents or acids and bases might be limiting the esterification reaction of CNC. Careful investigation on the behavior of the two chemical reactions in the presence of Cyrene is required. Moreover, in order to further improve the safety of the processes, the use of pyridine for cin-CNC modification (Chapter 3.1), cyanuric chloride and collidine for CNC-DR1 preparation (Chapter 3.3) could be revisited and substituted with safer chemicals. For instance, L-tartaric acid has proven to act as an organocatalyst and it allows the esterification of bacterial CNF with acetic and propionic acids [3]. Such a molecule shows potential to be used for the grafting of cinnamic acid on CNC. Alternatively, the use of citric acid is well established for the modification of cellulose [4]–[8] and can be achieved without the use of catalysts [8]. Despite having already tried using citric acid as a linker for the azobenzene on CNC, citric acid remain a potential substitute to the previous toxic linker (cyanuric chloride) and catalyst (collidine). In this case, the process should be optimized to avoid the drying steps that resulted in the strong agglomeration of our reacted particles. There is hence the potential to improve safety and environmental impact of both CNC modification reactions, developed during this thesis. Future works could investigate the above mentioned approaches and compare them to previous procedures in order to establish the yields, advantages and drawbacks.

The growing research on bio-based polymers, particularly on polyurethanes [9]–[13] has increased the possibilities of using polymer matrices derived from renewable resources. This offers renewable alternatives to substitute the synthetic matrices that were employed in this thesis. The recent work of Khasraghi et al. [14] demonstrated a procedure to produce UV curable polyurethane acrylates from PCL-

diol polyols, hexamethylene diisocynate and HEMA. The resulting polymers demonstrated efficient thermal shape memory effects characterized by shape fixity ratios over 98 % and shape recovery ratios over 99 %. With the advantage of being bio-based, biocompatible and biodegradable, such polyurethane acrylate represents a suitable candidate to improve the renewability of our composites. Our active reinforcements particles (cin-CNC) would allow to combine photostiffening with the thermal response to produce multiway shape memory composites [15]. On the other hand, the low transition temperatures characteristic of this new materials (from 30 to 50 °C) would allow using CNC-DR1 as a photoresponsive trigger of the polymer's shape memory effect. Furthermore, the use of bio-based molecular liquid crystals emerging from cellulose, such as hydroxypropyl cellulose monomers, or from DNA, spider silk or polypeptides [16] also offer alternatives that might replace the polysiloxane side chain LC mesogens utilized in Chapter 3.2 while maintaining the shape changing ability.

Investigation on CNC – LC mesogen arrangements and crystalline phases. With respect to increasing the amount of renewable materials in *shape changing* CNC composites, fundamental understanding of the relationships between CNC and LC mesogens remains the main challenge of our material. A deeper investigation on the influence of dispersed CNC on the behavior and structural arrangements of LC mesogens is of particular importance to demonstrate the potential of using such particles for both hierarchical structuring and improvement of photoresponsive *shape changing* ability. Understanding the relationships between these elements could pave the way for further amplifying the *trans-cis-trans* photoisomerization of the azobenzenes. In photoresponsive materials, the order and the structure of the environment of photoswicthing unit (azobenzenes) influences the macroscopic expression of the photoresponse; the more ordered and structured is the environment, the more amplified is the photoisomerization [17].

We attempted to characterize the organization of CNC and LC mesogens in our LCE/CNC composite in static conditions, in dark, but only the order of CNC could be resolved. The actual nematic structure of the LC mesogens, which promotes the light orientation independent bending, remains to be fully determined. In addition, the spatial behavior of both LC and CNC nanodomains as a function of illumination time remains unknown. As a consequence, currently under investigation, LCE/CNC composites produced by 3D printing will be analyzed with time-dependent high resolution X-ray spectroscopy at the Paul Scherrer Institute (PSI). The planned experiments have two main goals: determination of both the LC phase and the CNC orientation distribution, and kinetic observation of the printed structures during light triggered experiments. It should be possible to obtain such information by mapping, as a function of illumination time, the orientation's distribution of the LC and CNC over the composite filaments' diameter, as well as, to discriminate the signal of both elements from high resolution SAXS scans. Such experiments will help to understand the influence of CNC on the alignment and the structuring of LC mesogens (during printing), and the influence of LC mesogen phase transition on the CNC orientation (during actuation). Studying the mobility and dynamics of the CNC rearrangement in the actuated soft LCE could contribute to move toward smart materials containing higher amounts of CNC. Thus, the biocompatibility and the renewability of the smart material could improve. Systems composed of optimal CNC/LC ratio could be produced targeting the optimization of the photoactuated behaviors. The results obtained from this X-ray analysis can be combined with 3D printing process parameters, such as printing speed, nozzle size and printing temperature, to obtain a process window defining the guidelines for the printing of LCE/CNC composites. In this way, the photoresponses of LCE/CNC composites can be highly tuned, and suitable devices for specialized applications spanning from soft robots to biomedical muscle-like prosthetics could be produced.

Technology transfer toward vat polymerization 3D printing techniques with aligned nanoparticles. The field of 3D printing of CNC composites is in continuous development and not only limited to

DIW technologies. Vat polymerization 3D printing technologies as SLA and DLP, reach higher resolution and allow for structuring more complex 3D shapes. These technologies can already benefit from the reinforcing properties of CNC, when these particles are introduced in UV polymerizable inks. Palaganas et al. [18] introduced up to 1.2 wt % of CNC into a PEGDA matrix for the production of complex 3D geometries by SLA. The resulting material showed improved physicochemical and thermal properties resulting in increased toughness and wettability. Similarly, by incorporating up to 5 wt% of CNC into a matrix of PEGDA and 1,3-diglycerolate diacrylate, Li et al. [19] allowed DLP printing of structures with enhanced elastic modulus. Focusing on renewability, functionalized all-cellulose based hydrogels could be produced with DLP, by incorporating methacrylated CNC in acrylated carboxymethyl cellulose. These examples underline the potential of using CNC in vat polymerization techniques. When compared to DIW, SLA and DLP techniques do not allow yet to exploit the anisotropy of CNC to spatially tailor the mechanical properties of the printed parts, since the CNC could not be aligned. Furthermore, movements as responses to an external stimulus like light still have not been demonstrated. As mentioned in the previous Chapter 4, CNC-DR1 have a sure potential to confer photoresponsive behavior to the printed materials as well as to control density gradients of particles in low viscosity resins. Additionally, owing to the capability of DR1 to photoalign [20], it might be possible to control either alignment of CNC-DR1 (in the best case) or to use CNC-DR1 to control the orientation of surrounding LC mesogens. In order to achieve such a goal, a careful investigation focusing on the reaction to linearly polarized light of both particles and possible LC mesogens as a function of DR1 degree of substitution would be required. The possibilities of developing cellulose-based high resolution 3D printed parts presenting controlled hierarchical structures and light stimulated responses would greatly benefit biomedical applications. Thus, it is worth the effort to pursue the work of this thesis in this direction.

Finally, it is important to note that the above-mentioned future research directions are a suggestion for tackling the main challenges and interrogations of the presented work. However, the wide possibilities brought on with the development of our materials, as the high design freedom and the fine-tuning of mechanical and photoresponsive properties, pave the way to a large range of future applications of nanocelluloses in the additive manufacturing field. Optimization of each single material developed during this thesis, with respect to mechanical and photoresponsive behaviors and the 3D printing process, is also an interesting pathway to further pursue the production of personalized devices for targeted real case-applications. Indeed, research is a never ending journey.

5.1 References

[1] R. A. Sheldon, "The greening of solvents: Towards sustainable organic synthesis," *Current Opinion in Green and Sustainable Chemistry*, vol. 18. Elsevier B.V., pp. 13–19, 01-Aug-2019, doi: 10.1016/j.cogsc.2018.11.006.

[2] D. Kong and A. V. Dolzhenko, "Cyrene: A bio-based sustainable solvent for organic synthesis," *Sustainable Chemistry and Pharmacy*, vol. 25. Elsevier B.V., p. 100591, 01-Apr-2022, doi: 10.1016/j.scp.2021.100591.

[3] J. A. Ávila Ramírez, C. J. Suriano, P. Cerrutti, and M. L. Foresti, "Surface esterification of cellulose nanofibers by a simple organocatalytic methodology," *Carbohydr. Polym.*, vol. 114, pp. 416–423, Dec. 2014, doi: 10.1016/j.carbpol.2014.08.020.

[4] B. Martel, M. Weltrowski, D. Ruffin, and M. Morcellet, "Polycarboxylic acids as crosslinking agents for grafting cyclodextrins onto cotton and wool fabrics: Study of the process parameters," *J. Appl. Polym. Sci.*, vol. 83, no. 7, pp. 1449–1456, 2002, doi: 10.1002/app.2306.

[5] B. Martel, D. Ruffin, M. Weltrowski, Y. Lekchiri, and M. Morcellet, "Water-soluble polymers and gels from the polycondensation between cyclodextrins and poly(carboxylic acid)s: A study of the preparation parameters," *J. Appl. Polym. Sci.*, vol. 97, no. 2, pp. 433–442, 2005, doi: 10.1002/app.21391.

[6] M. Rehan, S. A. Mahmoud, H. M. Mashaly, and B. M. Youssef, "β-Cyclodextrin assisted simultaneous preparation and dyeing acid dyes onto cotton fabric," *React. Funct. Polym.*, vol. 151, no. March, p. 104573, 2020, doi: 10.1016/j.reactfunctpolym.2020.104573.

[7] Y. Zhou, Y. Hu, W. Huang, G. Cheng, C. Cui, and J. Lu, "A novel amphoteric B-cyclodextrin-based adsorbent for simultaneous removal of cationic/anionic dyes and bisphenol A," *Chem. Eng. J.*, vol. 341, no. 130, pp. 47–57, 2018, doi: 10.1016/j.cej.2018.01.155.

[8] X. Cui, T. Honda, T. A. Asoh, and H. Uyama, "Cellulose modified by citric acid reinforced polypropylene resin as fillers," *Carbohydr. Polym.*, vol. 230, no. November 2019, 2020, doi: 10.1016/j.carbpol.2019.115662.

[9] S. Wendels and L. Avérous, "Biobased polyurethanes for biomedical applications," *Bioactive Materials*, vol. 6, no. 4. KeAi Communications Co., pp. 1083–1106, 01-Apr-2021, doi: 10.1016/j.bioactmat.2020.10.002.

[10] S. Tang *et al.*, "Current trends in bio-based elastomer materials," *SusMat*, vol. 2, no. 1, pp. 2–33, Feb. 2022, doi: 10.1002/sus2.45.

[11] A. Noreen, K. M. Zia, M. Zuber, S. Tabasum, and A. F. Zahoor, "Bio-based polyurethane: An efficient and environment friendly coating systems: A review," *Progress in Organic Coatings*, vol. 91. Elsevier, pp. 25–32, 01-Feb-2016, doi: 10.1016/j.porgcoat.2015.11.018.

[12] R. Morales-Cerrada, R. Tavernier, and S. Caillol, "Fully bio-based thermosetting polyurethanes from bio-based polyols and isocyanates," *Polymers (Basel).*, vol. 13, no. 8, Apr. 2021, doi: 10.3390/polym13081255.

[13] H. Chaudhuri and N. Karak, "Water dispersed bio-derived transparent polyurethane: Synthesis, properties including chemical resistance, UV-aging, and biodegradability," *Prog. Org. Coatings*, vol. 146, p. 105730, Sep. 2020, doi: 10.1016/j.porgcoat.2020.105730.

[14] S. S. Khasraghi, A. Shojaei, and U. Sundararaj, "Bio-based UV curable polyurethane acrylate: Morphology and shape memory behaviors," *Eur. Polym. J.*, vol. 118, pp. 514–527, Sep. 2019, doi: 10.1016/j.eurpolymj.2019.06.019.

[15] M. Bodaghi, A. R. Damanpack, and W. H. Liao, "Triple shape memory polymers by 4D printing," *Smart Mater. Struct.*, vol. 27, no. 6, 2018, doi: 10.1088/1361-665X/aabc2a.

[16] K. Joseph, K. Y. Sandhya, and A. Saritha, "Liquid Crystalline Polymers from Renewable Resources: Synthesis and Properties," in *Liquid Crystalline Polymers: Volume 1-Structure and Chemistry*, Springer International Publishing, 2015, pp. 273–306.

[17] A. Goulet-Hanssens, F. Eisenreich, and S. Hecht, "Enlightening Materials with Photoswitches," *Adv. Mater.*, vol. 32, no. 20, p. 1905966, May 2020, doi: 10.1002/adma.201905966.

[18] N. B. Palaganas *et al.*, "3D Printing of Photocurable Cellulose Nanocrystal Composite for Fabrication of Complex Architectures via Stereolithography," *ACS Appl. Mater. Interfaces*, vol. 9, no. 39, pp. 34314–34324, Oct. 2017, doi: 10.1021/acsami.7b09223.

[19] V. C. F. Li, X. Kuang, A. Mulyadi, C. M. Hamel, Y. Deng, and H. J. Qi, "3D printed cellulose nanocrystal composites through digital light processing," *Cellulose*, vol. 26, no. 6, pp. 3973–3985, Apr. 2019, doi: 10.1007/s10570-019-02353-9.

[20] T. Tóth-Katona and I. Jánossy, “Photoalignment at the nematic liquid crystal-polymer interface: Experimental evidence of three-dimensional reorientation,” *J. Mol. Liq.*, vol. 285, pp. 323–329, Jul. 2019, doi: 10.1016/j.molliq.2019.04.074.